

Heteronuclear Recoupling Methods in Solid-State NMR

Heteronuclear Recoupling Methods in Solid-State NMR

Dissertation
zur Erlangung des Grades

„Doktor der Naturwissenschaften“

am Fachbereich Chemie und Pharmazie
der Johannes Gutenberg-Universität
in Mainz

Kay Saalwächter
geboren in Aachen

Mainz 2000

Die vorliegende Arbeit wurde unter der Betreuung von Prof. H. W. Spiess in der Zeit vom November 1997 bis April 2000 am Max-Planck-Institut für Polymerforschung in Mainz angefertigt.

Dekan: Prof. Dr. W. Tremel

Erster Berichterstatter:

Zweiter Berichterstatter:

Dritter Berichterstatter:

Tag der mündlichen Prüfung: 14.7.2000

Vorwort

Heteronukleare Doppelquanten-NMR Spektroskopie in Festkörpern galt es im Rahmen dieser Arbeit zu realisieren. Zahlreiche Vorarbeiten auf dem Gebiet der homonuklearen Doppelquanten-NMR waren gemacht, und die Einbeziehung einer weiteren Spinspezies sollte im Rahmen bekannter Konzepte ohne große Probleme möglich sein. Dennoch ist die zeitliche Abfolge der Ideen, die in diese Arbeit eingegangen sind, ein Beispiel dafür, daß sich entscheidende Fortschritte oft erst durch einen Blick über den Zaun zum Nachbarn einstellen.

Weniger die direkte Übernahme etablierter Methoden (eben der homonuklearen *Doppel-*Quantentechniken), sondern vielmehr die Neuinterpretation eines schon bekannten, spezifisch heteronuklearen Konzeptes brachte den gewünschten Erfolg. Es zeigte sich zudem, daß die Aufnahme von Spektren mit gleichem Informationsgehalt unter der Hinzunahme von *Null-*Quanten, also die Messung von heteronuklearen Multiquantenkohärenzen (HMQ) als Summe der beiden, mit der doppelten spektralen Intensität möglich ist.

Vom Standpunkt der homonuklearen Doppelquanten-NMR im Festkörper war dies nicht von vornherein selbstverständlich; überraschend war, daß es sich dabei keineswegs um ein neues Konzept handelt, sondern im Gebiet der NMR in Lösungen seit mehr als zwanzig Jahren zum „common sense“ zählt. Diese Arbeit stellt daher auch einen Beitrag zur Vereinheitlichung zweier Teilgebiete dar, die sich erst in jüngster Zeit wieder einander anzunähern begonnen haben. Zahlreiche Anwendungen in den Biowissenschaften, insbesondere das Studium der Struktur von Proteinen in ihrer natürlichen Umgebung, also mitunter teilimmobilisiert in Doppellipidschichten („soft matter“), führten zu einem verstärkten Bedarf, Konzepte der Festkörperspektroskopie, insbesondere die Ausnutzung anisotroper Wechselwirkungen, auf die NMR in Lösungen zu übertragen. Die Annäherung erfolgt hier nun aus einer ganz anderen Richtung, nämlich aus der Anwendbarkeit von sehr einfachen Konzepten der NMR

in Lösungen auch auf starre Festkörper. Ermöglicht wurde dies durch technische Neuerungen der letzten drei Jahre, insbesondere die fortschreitende Entwicklung der schnellen Probenrotation am magischen Winkel. Die Flexibilität in der Manipulation der beobachteten heteronuklearen Zweispinkohärenzen durch einzelne Pulse, wie sie in der Optimierung der hier zu besprechenden Techniken ausgenutzt wurde, war so bereits in den frühesten Arbeiten zur Multiquanten-Korrelationsspektroskopie an organischen Verbindungen in Lösung realisiert.

Ein ausgesprochen festkörpertypischer Aspekt ist dagegen, daß diese Arbeit nicht auf heteronukleare Zweispinkohärenzen beschränkt ist, sondern daß die erwähnten Techniken aus der Flüssig-NMR zur Anregung von heteronuklearen Multiquantenkohärenzen mit im Prinzip beliebig vielen beteiligten Spins verwendet werden können, ohne daß die Einfachheit des zugrundeliegenden Konzepts geopfert wird. Vielleicht kann diese Arbeit einen Beitrag zur gegenseitigen Befruchtung zweier Teilgebiete liefern, die sich vor allem in Bezug auf ihre jeweilige Fachterminologie und weniger in den grundlegenden Konzepten unterscheiden.

Contents

Vorwort	I
Introduction	1
1 Quantum-Mechanical Description of Pulsed NMR Experiments	5
1.1 The Density Operator	6
1.1.1 Time Evolution	7
1.1.2 Representations of the Density Operator	9
1.1.3 Series Expansions and Average-Hamiltonian Theory	13
1.2 RF-Pulses and Signal Detection	15
1.3 NMR Interactions	18
1.3.1 Chemical Shift and Secular Averaging	19
1.3.2 Spin-Spin Couplings and Second Averaging	21
1.3.3 Quadrupolar Coupling	27
1.3.4 Quadrupolar and Dipolar Time Evolution	29
1.4 Spatial Averaging by Magic-Angle Spinning	30
1.4.1 Hamiltonians under MAS	31
1.4.2 Spinning-Sideband Patterns	35

2	Heteronuclear Correlation: REDOR and Multiple-Quantum Coherences	39
2.1	Principles of REDOR	40
2.1.1	Average REDOR Hamiltonian	41
2.1.2	The Conventional REDOR Experiment	43
2.2	REDOR as a Multiple-Quantum Technique	46
2.2.1	Similarities between REDOR and Back-to-Back	52
2.2.2	Rotor Encoding and Multiple-Quantum Spinning-Sideband Patterns	55
3	Recoupled Polarization-Transfer Methods	60
3.1	The REPT-HMQC Experiment	61
3.1.1	Influence of Remote Protons	69
3.1.2	Sensitivity to Experimental Imperfections	71
3.2	Generalized REPT Techniques	73
3.2.1	CSA and Dipolar Correction Terms	77
3.2.2	Rotor Encoding of Heteronuclear Dipolar Order	80
3.3	Multi-Spin Systems	82
3.3.1	Spectral Editing Applications	91
3.3.2	Labeling Effects in HETCOR Spectra	94
3.3.3	Influence of Homonuclear Couplings	97
3.4	Comparison of the REPT Variants	101

4	Symmetric Dipolar Heteronuclear Multiple-Spin Correlation	103
4.1	DIP-HMSC of IS-Pairs and RELM	103
4.2	DIP-HMSC in Systems with Multiple I-Spins	106
4.3	Heteronuclear Spin Counting	111
4.3.1	Principles of Spin Counting	111
4.3.2	Experimental Results	114
4.4	^{13}C - ^1H DIP-HMS Shift Correlation Spectra	118
4.5	^{13}C - ^1H Dipolar Couplings from Build-up Curves and Sideband Patterns	123
4.6	DIP-HMS Spinning-Sideband Spectra	127
4.7	Conclusions and Comparison with REPT	132
5	HMQ Correlation Spectroscopy involving Quadrupolar Nuclei	134
5.1	The Excitation Problem	135
5.2	^2H - ^{13}C HMQC Spectroscopy	138
5.2.1	Theoretical Description	138
5.2.2	Evolution of $L = 1$ Spins Under Finite Pulses	141
5.2.3	Simulated and Experimental Results	145
6	Relaxation-Induced Dipolar Exchange with Recoupling	149
6.1	Circumventing the Excitation Problem	149
6.2	Experimental Procedure	153
6.3	Theoretical Description	153
6.3.1	Coupling to $L = \frac{1}{2}$	154

6.3.2	Coupling to $L = 1$	156
6.3.3	Couplings to Multiple L-spins	158
6.4	Experimental Demonstration	160
6.4.1	^{13}C - ^{14}N Distances in L-Alanine	160
6.4.2	^{13}C - ^2H Distances in CD_3 -Methylmalonic Acid	164
6.5	Concluding Discussion	167
7	Applications	169
7.1	Structure and Dynamics of Discotic Hexabenzocoronene Mesophases	170
7.1.1	DSC and X-Ray Results	172
7.1.2	Core Dynamics in the HT Mesophases	173
7.1.3	Sidechain Dynamics of HBC- PhC_{12} in the LT Phases	176
7.1.4	Summary and Discussion of the Results	179
7.2	Hydrogen Bonds in Poly(vinyl alcohol)	182
7.2.1	Selection of the Crystalline Components	183
7.2.2	^2H -REDOR Measurements	186
7.2.3	^2H -WISE and Static ^2H Spectra	189
7.2.4	Discussion of the Experimental Results	191
	Summary	195
	Appendix	199
A	Tensor Algebra	199
B	Phenomenological Description of T_1 Relaxation for Spin-1 Nuclei	202

C	Numerical Procedures	204
C.1	Powder Averaging	204
C.2	Multiple Tensors	206
C.3	Density Matrix Simulations	207
C.4	Transformation of Time-domain Data	209
D	Description of the Sample Substances	210
D.1	L-Alanine	210
D.2	L-Tyrosine·HCl	210
D.3	Ammonium Formate	211
D.4	Methylmalonic Acid	214
D.5	Poly(vinyl alcohol)	215
E	Experimental Details	216
E.1	Instrumentation	216
E.2	REPT Experiments	217
E.3	DIP-HMSC Experiments	217
E.4	² H-WISE and RIDER	221
	Abbreviations and Acronyms	223
	Bibliography	225
	Zusammenfassung	237

Introduction

Nuclear magnetic resonance (NMR) spectroscopy has proven itself as an indispensable tool for structural and dynamical studies in liquids and solids alike. Since the advent of one- and two-dimensional Fourier-transform methods, as pioneered by Ernst in the mid 1960's and 1970's, respectively, solution-state NMR methods, in particular homonuclear (COSY — *correlation spectroscopy*) and heteronuclear correlation methods (e.g., HETCOR, HC-COSY), have become invaluable to synthetic chemists. When routine identification and structural characterization of small organic molecules is required, NMR spectroscopy is paralleled by no other analytical method. Moreover, using the NOESY (*nuclear Overhauser-enhanced spectroscopy*) technique to establish through-space correlations, NMR has become the standard tool for structural studies of moderately sized proteins in their natural state, i.e. in solution.

In contrast to its solution-state counterpart, solid-state NMR has not yet gained widespread popularity. Solid-state NMR is still considered a theoretically challenging field, with complicated experiments, requiring a highly skilled spectroscopist. The reason for this notion is not, as commonly assumed, the difficulty in obtaining the desired spectral information, or a lack of it, but its overabundance: this is for instance represented by the multitude of orientation-dependent dipolar splittings between individual spins. In contrast, the rapid tumbling of molecules in solution completely averages out the anisotropic interactions, and the resulting spectra are simplified to a large degree.

However, the field of protein structure studies represents an example of the convergence of solid-state and solution-state techniques in recent research. Dipolar-induced relaxation, as utilized in the NOESY techniques, is so far the most widely used mechanism by which distance information can be assessed in a dissolved protein. The parameter space for ever

larger proteins is so big that it became desirable to obtain additional distance constraints. This is achieved by harnessing the dipolar interaction directly by dissolving the protein in solutions of lyotropic liquid crystals, disc-shaped micelles (“bicelles”) in particular. These interfere with the rapid isotropic molecular tumbling, and as a consequence, weak residual dipolar couplings become directly observable.

In the solid state, the homonuclear dipolar coupling, which is the dominant interaction in ^1H spectroscopy, leads to very broad lines, which obscure the chemical-shift information. From the earliest days, the concern of NMR in the solid state has been to invent techniques to overcome this problem. From the large variety of ingenious techniques for resolution enhancement, one technique stands out as the most widely used approach towards line-narrowing: rapid sample spinning at the magic angle, MAS. If the sample is spun fast enough, the anisotropic interactions are essentially averaged out, and the resulting spectra are dominated by the isotropic interactions. This method has gained particular importance on account of the recent development of MAS probeheads capable of spinning frequencies up to 35 kHz. In our group, much progress has been made towards using proton chemical shifts and dipolar proximities, as accessible by homonuclear double-quantum spectroscopy, to obtain structural and dynamical information in solids.

The aim of this work was to extend the homonuclear multiple-quantum (MQ) methodology, namely the probing of proximities or the determination of specific dipolar coupling constants by means of investigating the MQ build-up process or analyzing spinning-sideband patterns in the MQ dimension of two-dimensional experiments, to the heteronuclear case. In the latter case, the accessibility of similar dynamical and structural information with the increased site-resolution of ^{13}C chemical shifts was expected to significantly enhance our methodology. In this thesis, it will be shown that relatively simple concepts from solution-state MQ NMR exploiting the indirect spin-spin coupling become applicable once the spin system under investigation is dominated by specific heteronuclear dipolar couplings. In ^1H systems in particular, the strong homonuclear dipolar couplings can largely be averaged out by very-fast MAS. The heteronuclear couplings can then be selectively re-introduced by means of recoupling pulse sequences, which are applied in the free evolution intervals of the original solution-state experiments.

In 1989, Gullion and Schaefer introduced a very elegant experiment with which the weak dipolar coupling constants between two heteronuclei can be determined under MAS condi-

tions. It was termed REDOR, for *rotational echo, double resonance*, and it represents the undoubtedly most elementary and robust approach towards recoupling of the heteronuclear dipolar coupling. The main theme of this work will be to explore the possibility of using the remarkably simple concept of REDOR, as reviewed in Chapter 2 of this thesis, as a building block for a variety of spectroscopic techniques, each being suited to face different challenges of heteronuclear correlation in solids.

For the correlation of ^1H and ^{13}C chemical shifts as well as dipolar couplings, where techniques applicable to samples naturally abundant in ^{13}C are highly desirable, the large dipolar couplings and different spin topologies in the common building blocks of organic substances, namely CH, CH_2 , and CH_3 units, are expected to dominate the spectra. Additionally, the high magnetogyric ratio of the proton and its high concentration demands specific attention as far as the influence of surrounding protons and homonuclear couplings among the protons on the spectra is concerned. Another point of interest is the possible determination of long-range couplings to quaternary carbon atoms and the dependence of these results on different structural arrangements. On the other hand, when correlations between pairs of less abundant heteronuclei are to be established, other problems may arise, such as the failure of finite pulses to uniformly excite spins covering large ranges of resonance frequencies, for example quadrupolar nuclei or spins with extremely large chemical shift anisotropies.

It is thus not surprising that this variety of aspects demands different techniques in order to address specific problems such as peak assignment via high-resolution chemical-shift correlation, spectral editing, or the use of dipolar couplings for the study of dynamical processes. However, it will be shown that the mentioned combination of different simple concepts, some of which are adopted directly from solution-state NMR, with REDOR as a means to recouple the heteronuclear dipolar interaction under MAS, is a versatile approach towards the correlation of ^{13}C and ^1H (Chapters 3 and 4), and can also be used to correlate ^{13}C with quadrupolar spins such as ^2H (Chapter 5) or even ^{14}N (Chapter 6). In the last case, the most drastic measure to tackle the excitation problem of quadrupolar nuclei is discussed, namely the complete omission of pulses on one of the two heteronuclei under investigation.

The concluding Chapter 7 contains applications of some of the techniques discussed in the body of this work, which show that the new heteronuclear concepts are indeed applicable to the investigation of structure and dynamics in complex organic systems such as discotic liquid crystals, or hydrogen bonds in poly(vinyl alcohol).

Chapter 1

Quantum-Mechanical Description of Pulsed NMR Experiments

Since the pioneering works of Bloch and Purcell [Bloch 46, Purcell 46], who in 1946 presented the first experimental evidence of nuclear magnetic resonance, the way of performing NMR experiments has changed entirely. The initially used slow-passage (or continuous-wave, CW) methods have more or less completely been replaced by Fourier transform (FT) techniques, where the response of the spin system to strong radio frequency (rf) pulses is measured in a time-resolved fashion. The frequency spectrum is subsequently generated by a Fourier transformation. This way of performing NMR experiments not only opens up the possibility of applying various digital data manipulation techniques, such as resolution enhancement and noise reduction via window functions [Ernst 87, Schmidt-Rohr 94], but also allows for a well-defined manipulation of the spin system with more complicated pulsing schemes prior to the detection. This led to the development of the standard tools in NMR, such as two-dimensional spectroscopy, multiple-quantum methods [Ernst 87], and resolution-enhancement techniques in solid-state NMR [Haeberlen 68].

The quantum mechanics of spin systems is well developed, and a variety of monographs on the topic exists. Starting with basic quantum mechanics of angular momentum, as for instance presented in [Sakurai 85], and texts specifically devoted to the application of group theory and tensor algebra [Rose 59], the texts of Abragam [Abragam 61] and Slichter [Slichter 96] present the foundations of NMR from a physicist's point of view. The work of

Ernst, Bodenhausen, and Wokaun [Ernst 87] covers the whole range of modern application-oriented NMR, from the basic quantum-mechanical treatment to the description of imaging techniques. Finally, Mehring's book [Mehring 83] is particularly suited to meet the needs of the solid-state NMR spectroscopist, and Schmidt-Rohr and Spiess [Schmidt-Rohr 94] present the most up-to-date compendium of applications to the investigation of structure and dynamics in solid polymers.

This chapter comprises a review of the theoretical tools needed to describe the dynamics of spin systems subject to rf-pulses in strong external magnetic fields, with particular emphasis on the calculation of spectra, either by numerical means or by a full analytical treatment.

1.1 The Density Operator

The spectroscopic information in an NMR experiment is always measured as an *ensemble average* over the individual spins. Thus the spin system is most conveniently represented by the density operator,

$$\hat{\rho}(t) = \sum_{ij} \overline{c_i^*(t)c_j(t)} |i\rangle\langle j|, \quad (1.1)$$

where the $|i\rangle$ are the eigenstates of the nuclear spin Hamiltonian \hat{H} in a suitable Hilbert space basis. The matrix elements of this self-adjoint ($\hat{\rho}^+ = \hat{\rho}$) operator,

$$\hat{\rho}_{ij}(t) = \langle i|\hat{\rho}(t)|j\rangle = \overline{c_i^*(t)c_j(t)}, \quad (1.2)$$

have a probabilistic interpretation. The diagonal elements, $\hat{\rho}_{ii} = P_{ii}$, give the probability of finding the spin system in state $|i\rangle$, whereas the off-diagonal elements are the complex amplitudes of coherent superpositions of eigenstates, averaged over the ensemble. These coherences are either transverse modes of magnetization or multiple-quantum coherences, depending on whether they are associated with a change in the magnetic quantum number of just one spin by ± 1 or involve multiple transitions, respectively.

The expectation value of an operator \hat{A} for an arbitrary pure state, $|\Psi\rangle = \sum_i c_i |i\rangle$, is $\langle \Psi | \hat{A} | \Psi \rangle$. It follows that the ensemble-averaged expectation value for a spin system in a mixed state is calculated as

$$\langle \hat{A} \rangle = \text{Tr} \{ \hat{A} \hat{\rho} \}. \quad (1.3)$$

1.1.1 Time Evolution

From the time-dependent SCHRÖDINGER equation and the definition of the density operator (Eq. 1.1), the time dependence of the density operator can be shown to be ¹

$$\frac{d}{dt} \hat{\rho}(t) = -i[\hat{H}(t), \hat{\rho}(t)]. \quad (1.4)$$

This important result is termed the LIOUVILLE-VON NEUMANN equation, and it serves as the basis for numerical as well as analytical approaches for the calculation of the time evolution of a spin system in an NMR experiment. In its most general form, the solution of this differential equation reads

$$\hat{\rho}(t) = \hat{U}(t) \hat{\rho}(0) \hat{U}^{-1}(t), \quad (1.5)$$

where $\hat{U}(t)$ is called the *propagator*. For constant Hamiltonians, $\hat{H} \neq f(t)$, it is simply

$$\hat{U}(t) = \exp \{ -i\hat{H}t \}. \quad (1.6)$$

Complications arise, however, if \hat{H} is a function of time. Eq. (1.6) can nevertheless be used if \hat{H} is piecewise constant in time, as is often the case when the effects of pulse sequences are to be calculated. The time evolution can then be evaluated sequentially. This is also the approach used in numerical calculations, where the time evolution is subdivided into intervals, Δt , small enough to allow the use of an approximately constant Hamiltonian. In such cases Δt has to be chosen at least one order of magnitude smaller than the inverse of the largest interaction present (in frequency units).

¹Throughout this thesis, energies will be given in angular frequency units, thus \hbar does not appear in Eq. (1.4).

For non-constant Hamiltonians, the propagator reads

$$\hat{U}(t) = \hat{T} \exp \left\{ -i \int_0^t \hat{H}(t') dt' \right\}. \quad (1.7)$$

The DYSON time-ordering operator, \hat{T} , makes sure that the exponential of the integral is evaluated in the correct order, i. e. with increasing time. As a consequence, there is no closed analytical form for Eq. (1.7) when the Hamiltonian does not commute with itself at different times, $[\hat{H}(t'), \hat{H}(t'')] \neq 0$. One then has to resort to approximations, such as series expansions of Eqs. (1.4) or (1.7).

In Eq. (1.5), a known starting point has been assumed for the evolution of the density matrix, i.e. $\hat{\rho}(0)$. For a spin ensemble in thermal equilibrium, this initial state is given by a BOLTZMANN distribution of the individual spins among the energy levels of the system. For most NMR applications, it is sufficient to restrict oneself to the strongest interaction. The ZEEMAN interaction exceeds most of the other interactions by orders of magnitude; its Hamiltonian is

$$\hat{H}_0 = - \sum_i \gamma_i B_0 \hat{I}_z^{(i)} = \sum_i \omega_{L,i} \hat{I}_z^{(i)}, \quad (1.8)$$

where γ_i is the magnetogyric ratio of spin i and $\omega_{L,i}$ is called its LARMOR frequency. From statistical mechanics, one obtains for the density matrix:

$$\hat{\rho}(0) = \frac{\exp \left\{ -\hat{H}_0 \hbar/kT \right\}}{\text{Tr} \left\{ \exp \left\{ -\hat{H}_0 \hbar/kT \right\} \right\}} = \frac{\exp \left\{ -\sum_i \omega_{0,i} \hat{I}_z^{(i)} \hbar/kT \right\}}{\text{Tr} \left\{ \exp \left\{ -\sum_i \omega_{0,i} \hat{I}_z^{(i)} \hbar/kT \right\} \right\}}. \quad (1.9)$$

Since the individual z-angular momentum operators, $\hat{I}_z^{(i)}$, commute, the exponential of the sum can be factorized, and the trace operation for the partition function in the denominator can be evaluated for each spin individually. Moreover, for temperatures $T > 1$ K and proton Larmor frequencies of a few hundred MHz, the TAYLOR expansion of the operators can be truncated to terms of first order:²

$$\hat{\rho}_0 = \frac{1}{\prod_i (2I_i + 1)} \left(\hat{\mathbb{1}} - \sum_i \frac{\omega_{0,i} \hbar}{kT} \hat{I}_z^{(i)} \right) \quad (1.10)$$

²Recently, an interesting experimental demonstration of the effects of higher-order contributions to the equilibrium density matrix was published by Callaghan and coworkers [Minot 99].

The unity operator, $\hat{\mathbb{1}}$, commutes with any other operator describing internal interactions, consequently it does not evolve in time and can be neglected. We see that the initial state is given by a sum of the individual z-angular momentum operators, with relative weights determined by the different LARMOR frequencies.

1.1.2 Representations of the Density Operator

In principle, the density operator describes the entire quantum-mechanical system in question. Throughout this thesis, we are only concerned with individual spins coupled among each other. The influence of the surroundings, or the “lattice”, and its effects with respect to relaxation, will only be dealt with in a semiclassical fashion (Appendix B). Thus, it is appropriate to restrict the wave functions to functions of the magnetic spin quantum numbers, m_i , only. The most intuitive choice for the representation of the basis is to use a product of N individual spin eigenfunctions of the ZEEMAN Hamiltonian, $\prod_i^N |m_i\rangle = |m_1 m_2 \dots m_N\rangle$. The dimension of the Hilbert space is then always finite and equals $\prod_i^N (2I_i + 1)$. The matrix elements of the angular momentum operators in the Zeeman basis are given by

$$(\hat{I}_z)_{m'm} = \langle m' | \hat{I}_z | m \rangle = m \delta_{m'm}, \quad (1.11)$$

$$(\hat{I}_x)_{m'm} = \pm i (\hat{I}_y)_{m'm} = \frac{1}{2} \sqrt{I(I+1) - m(m \pm 1)} \delta_{m'm \pm 1}. \quad (1.12)$$

For $I = \frac{1}{2}$, these are the elements of the PAULI spin matrices. By taking a linear combination of the operators in Eq. (1.12), one obtains shift operators

$$\hat{I}_{\pm} = \frac{1}{\sqrt{2}} (\hat{I}_x \pm i \hat{I}_y), \quad (1.13)$$

which increase or decrease the magnetic spin quantum number in steps of 1,

$$\hat{I}_{\pm} |m\rangle = \sqrt{2(I \mp m)(I \pm m + 1)} |m \pm 1\rangle \quad \text{for } |m \pm 1| \leq I. \quad (1.14)$$

In a multi-spin system, the matrix representations of single-spin angular momentum operators are given by outer matrix (or tensor-) products

$$\hat{I}_{\alpha}^{(i)} = \hat{\mathbb{1}}_1 \otimes \hat{\mathbb{1}}_2 \otimes \dots \otimes \hat{\mathbb{1}}_{i-1} \otimes \hat{I}_{\alpha} \otimes \hat{\mathbb{1}}_{i+1} \dots \otimes \hat{\mathbb{1}}_N, \quad (1.15)$$

where $\hat{\mathbb{I}}_j$ are unity operators, with matrix representations of appropriate dimension $2I_j + 1$. Outer products of matrices $\underline{\mathbf{A}} = \underline{\mathbf{B}} \otimes \underline{\mathbf{C}}$ are evaluated by using $B_{i,j}\underline{\mathbf{C}}$ as “sub-matrices” of the new, expanded matrix $\underline{\mathbf{A}}$ at position (i, j) . The matrix representation of a particular shift operator $\hat{I}_{\pm}^{(i)}$ is interesting in that it has only one non-zero element at the position which connects the two product functions which differ only in the magnetic quantum number of constituent spin i :

$$\hat{I}_{\pm} |m_1 \dots m_i \dots m_N\rangle \sim |m_1 \dots m_i \pm 1 \dots m_N\rangle. \quad (1.16)$$

It is thus a *single-transition* operator, which acts in the subspace spanned by the wave function of this one spin. Also, product operators of the form $\hat{I}_{\alpha}^{(i)} \hat{I}_{\beta}^{(j)}$ act in the product subspace of spin i and j . When dealing with matrix representations of these operators, these intuitive rules are exactly obeyed by the matrix algebra.

In the foregoing section, it was shown that the density operator in thermal equilibrium can be *represented* by the weighted sum of single-spin z-angular momentum operators. That is to say, the complete set of single-spin angular momentum operators, $\{\hat{I}_{\alpha}^{(i)}\}$, forms a basis for the representation of the density operator. The space spanned by these operators is called the LIOUVILLE space, and we will see that the propagator (Eq. (1.7)), along with the prescription of applying it in bilinear form (unitary transformation according to Eq. (1.5)), forms an operator in LIOUVILLE space, also referred to as a *superoperator*.

$$\hat{\rho}(t) = \hat{U}(t) \hat{\rho}(0) = e^{i\hat{H}t} \hat{\rho}(0) \quad (1.17)$$

In particular, $\hat{U}(t)$ is called a unitary transformation superoperator. These superoperators form an algebra, a set of relatively simple rules for the calculation of the time evolution of spin systems. As an example, let us consider an initial state of transverse magnetization of a single spin, $\hat{\rho}(0) = \hat{I}_y$, as generated by a 90° -pulse. It will evolve in time under a constant Hamiltonian, \hat{H} . By using the definition of an operator- (or matrix-) exponential by its TAYLOR expansion, and collecting different powers of t , one obtains from Eqs. (1.5) and (1.6)

$$\hat{\rho}(t) = \hat{\rho}(0) - \frac{it}{1!} [\hat{H}, \hat{\rho}(0)] + \frac{(it)^2}{2!} [\hat{H}, [\hat{H}, \hat{\rho}(0)]] - \frac{(it)^3}{3!} [\hat{H}, [\hat{H}, [\hat{H}, \hat{\rho}(0)]]] + \dots \quad (1.18)$$

This result is known as the BAKER-HAUSDORFF lemma. If the operators in \hat{H} and $\hat{\rho}(0)$ commute cyclically, it follows that

$$[\hat{H}, [\hat{H}, \hat{\rho}(0)]] = \omega^2 \hat{\rho}(0). \quad (1.19)$$

Since the third order term in Eq. 1.18 then reduces to $[\hat{H}, [\hat{H}, [\hat{H}, \hat{\rho}]]] = [\hat{H}, \omega^2 \hat{\rho}(0)]$, all higher orders collapse accordingly, and we get

$$\begin{aligned} \hat{\rho}(t) &= \hat{\rho}(0) \left(1 + \frac{(i\omega t)^2}{2!} + \frac{(i\omega t)^4}{4!} + \dots \right) - \frac{1}{\omega} [\hat{H}, \hat{\rho}(0)] \left(\frac{(i\omega t)^1}{1!} + \frac{(i\omega t)^3}{3!} + \dots \right) \\ &= \hat{\rho}(0) \cos(\omega t) - i \frac{1}{\omega} [\hat{H}, \hat{\rho}(0)] \sin(\omega t). \end{aligned} \quad (1.20)$$

For the last line, the TAYLOR series for the sine and cosine functions were used. If the Hamiltonian is just the ZEEMAN Hamiltonian $\omega_L \hat{I}_z$, and $\hat{\rho}(0) = \hat{I}_y$, we obtain the familiar result

$$\hat{\rho}(t) = \hat{I}_y \cos(\omega_L t) - \hat{I}_x \sin(\omega_L t). \quad (1.21)$$

This is due to the cyclic commutation of the angular momentum operators:

$$[\hat{I}_\alpha, \hat{I}_\beta] = i \varepsilon_{\alpha\beta\gamma} \hat{I}_\gamma, \quad (1.22)$$

where $\varepsilon_{\alpha\beta\gamma}$ equals +1 for cyclic permutations of $\alpha\beta\gamma$ ($\alpha, \beta, \gamma \in \{x, y, z\}$), -1 for anticyclic ones, and 0 otherwise. In particular, we have used: $[\hat{I}_z, \hat{I}_y] = -i\hat{I}_x$. We see that the external magnetic field, B_0 , as represented by the ZEEMAN Hamiltonian, leads to a *precession* of magnetization in the transverse plane. Eq. (1.21) is the quantum-mechanical equivalent of the solution for the classical BLOCH equations (neglecting relaxation). The ensemble-averaged expectation values of the angular momentum operators behave exactly like classical magnetization. The analogy will not be pursued any further, because it is not applicable to multi-spin coherences.

The physics of Eq. (1.21) is of much greater importance for its implications for the calculation of the time evolution of coupled spin systems. For weakly coupled systems it is possible to find sets of three cyclically commuting operators (and *products* thereof) for any initial state

and any single one- or two-spin NMR interaction. Calculation of the time evolution of the spin system then reduces to rotations in three-dimensional Cartesian subspaces of the LIOUVILLE space, where the sign of the precession and its frequency are obtained by evaluating just one commutator, as described in Eq. (1.20). The set of rules derived for the most common types of interactions in NMR is known as product operator theory, and has been developed by Ernst and coworkers [Sørensen 83]. The action of a unitary transformation superoperator is often written in a shorthand notation (here for the evolution of \hat{I}_y under the ZEEMAN Hamiltonian):

$$\hat{I}_y \xrightarrow{\omega_L t \hat{I}_z} \hat{I}_y \cos(\omega_L t) - \hat{I}_x \sin(\omega_L t) \quad (1.23)$$

This equation describes the LARMOR precession of magnetization, which leads to a voltage in the receiver coil of the NMR probe, which is then subject to amplification, digitization and Fourier transformation. The signal is, however, not sampled with its LARMOR frequency but with a much lower frequency corresponding to the internal interactions such as chemical shifts and spin-spin couplings. This is achieved by mixing the signal with the reference carrier frequency prior to digitization such that only the frequency differences from the carrier are measured. This is not only feasible from an experimental point of view but also has interesting theoretical implications. The ZEEMAN interaction is large enough compared to most internal interactions to justify treating the internal interactions as first order perturbations of the ZEEMAN levels. The transformation ³

$$\hat{\rho}^* = \exp \left\{ i \sum_i \omega_{L,i} t \hat{I}_z^{(i)} \right\} \hat{\rho} \exp \left\{ -i \sum_i \omega_{L,i} t \hat{I}_z^{(i)} \right\} \quad (1.24)$$

represents a transition into the interaction picture, where the time dependence due to the largest interaction is transferred to the wave functions, or the density matrix, and to terms in the Hamiltonian which do not commute with the ZEEMAN term. The sum indicates that for different spin species the reference frames may rotate with different LARMOR frequencies, resulting in a density matrix in a multiply rotating frame, $\hat{\rho}^*$. Time evolution due to the remaining interactions are then automatically treated as first order perturbations, if the

³In practice, the rotating frame transformation is performed using the reference carrier frequency, which does not necessarily match $\omega_{L,i}$ exactly. See Sections 1.2 and 1.3.1 for details.

corresponding internal Hamiltonians are transformed accordingly:

$$\hat{H}_{int}^* = \exp \left\{ i \sum_i \omega_{L,i} t \hat{I}_z^{(i)} \right\} \hat{H}_{int} \exp \left\{ -i \sum_i \omega_{L,i} t \hat{I}_z^{(i)} \right\} \quad (1.25)$$

This result can directly be derived by requiring Eq. (1.4) to be valid also for $\hat{\rho}^*$ and \hat{H}^* . This transformation leads to substantial simplifications of the interaction Hamiltonians, termed secular averaging. This will be discussed in more detail in Section 1.3.1. From now on, even though not mentioned explicitly, the symbol $\hat{\rho}$ will always refer to the density operator in the rotating frame. It will also be referred to as the *density matrix* of the system. By using the proper secular-averaged Hamiltonians, the treatment of the time evolution is thus formally in accord with the Schrödinger picture.

1.1.3 Series Expansions and Average-Hamiltonian Theory

The time evolution of the density matrix as calculated from product-operator theory is based on the assumption of a constant Hamiltonian with components that commute with each other. Only then does the propagator $\hat{U} = \exp \{ -i(\hat{H}_1 + \hat{H}_2)t \}$ factorize to $\hat{U} = \exp \{ -i\hat{H}_1 t \} \exp \{ -i\hat{H}_2 t \}$, and the evolution due to the different contributions can be evaluated by independent transformations. The solution by consecutive independent transformations is, in turn, not possible if the constituent Hamiltonians, $\{ \hat{H}_i \}$, do not commute. However, in such cases Eq. (1.18) may be used to calculate the *initial behavior* of the time evolution. For a calculation of the long-time evolution (which is required to obtain a free-induction decay (FID) for the calculation of a spectrum by Fourier transformation), one usually has to resort to numerical solutions of the LIOUVILLE-VON NEUMANN equation (1.4).

If \hat{H} is a function of time and does not contain non-commuting contributions for a specific time t , the problem might still be tractable analytically. For piecewise constant Hamiltonians (e.g. pulse sequences), the problem can be solved by consecutive evaluation for the fixed intervals τ_i . This has already been alluded to in section 1.1.1. If the pulse sequence is *cyclic*, with a given cycle time $t_c = \sum_i \tau_i$, it is in many cases possible to calculate an *average Hamiltonian*, \bar{H} , for one cycle of the sequence.

$$\hat{U}(t_c) = e^{-i\hat{H}_1 \tau_1} e^{-i\hat{H}_2 \tau_2} \dots e^{-i\hat{H}_n \tau_n} = e^{-i\bar{H} t_c} \quad (1.26)$$

Since any \bar{H} commutes with itself (it is not time-dependent), the propagator for N cycles simply reads $\hat{U}(Nt_c) = \exp\{-i\bar{H}Nt_c\}$. However, \bar{H} cannot be calculated as simple sum of the $\hat{H}_i\tau_i/t_c$, because generally $[\hat{H}_i, \hat{H}_j] \neq 0$. The construction of \bar{H} can be either based on symmetry principles, as elaborated in detail in [Haeberlen 76], or determined by brute-force application of the BAKER-CAMPBELL-HAUSDORFF relation,

$$e^{\hat{B}}e^{\hat{A}} = e^{\hat{B}+\hat{A}+\frac{1}{2}[\hat{A},\hat{B}]+\frac{1}{12}([\hat{B},[\hat{B},\hat{A}]]+[[\hat{B},\hat{A}],\hat{A}])+\dots}, \quad (1.27)$$

which gives a prescription of how to evaluate a product of exponentials of non-commuting operators. The average Hamiltonian is then conveniently written as sum of different orders,

$$\bar{H} = \bar{H}^{(0)} + \bar{H}^{(1)} + \bar{H}^{(2)} + \dots, \quad (1.28)$$

where the order i indicates the overall power of t_c , and the number of nested commutators involved. Indeed, the zeroth-order average Hamiltonian then reads

$$\bar{H}^{(0)} = \frac{1}{t_c} \sum_i \hat{H}_i\tau_i, \quad (1.29)$$

while higher-order terms involve increasing amounts of algebra. For instance,

$$\bar{H}^{(1)} = -\frac{1}{2t_c} \sum_i \sum_{j < i} [\hat{H}_i\tau_i, \hat{H}_j\tau_j]. \quad (1.30)$$

As with the BAKER-HAUSDORFF lemma (Eq. (1.18)), substantial simplifications may arise for the higher-order terms if the involved operators commute cyclically. Still, for this treatment it has been assumed that the \hat{H}_i are constant during the interval τ_i . If the time dependence of a continuously changing Hamiltonian $\hat{H}(t)$ is periodic, however, the problem can be treated in the limit of $\tau_i \rightarrow 0$ and $n \rightarrow \infty$. Eq. (1.26) can then be used to calculate the zeroth-order contribution to \bar{H} , because the commutators $[\hat{H}(t), \hat{H}(t + \Delta t)]$ vanish for infinitely small time. The full average Hamiltonian (in these cases also called the “effective” Hamiltonian) can again be written as a sum. The higher-order contributions can be calculated from an application of

Eq. (1.27) to the definition of the propagator (Eq. 1.7) in the limit of $\Delta t \rightarrow 0$. Eq. (1.28) is then called the Magnus expansion, and the first three contributions are

$$\bar{H}^{(0)} = \frac{1}{t_c} \int_0^{t_c} dt \hat{H}(t), \quad (1.31)$$

$$\bar{H}^{(1)} = -\frac{i}{2t_c} \int_0^{t_c} dt_1 \int_0^{t_1} dt_2 [\hat{H}(t_1), \hat{H}(t_2)], \quad (1.32)$$

$$\begin{aligned} \bar{H}^{(2)} = & -\frac{1}{6t_c} \int_0^{t_c} dt_1 \int_0^{t_1} dt_2 \int_0^{t_2} dt_3 ([\hat{H}(t_1), [\hat{H}(t_2), \hat{H}(t_3)]] \\ & + [\hat{H}(t_3), [\hat{H}(t_2), \hat{H}(t_1)]]). \end{aligned} \quad (1.33)$$

This result is most useful for magic-angle spinning, where t_c has the natural meaning of one rotor period, τ_R . Often, it is sufficient to restrict oneself to the zeroth order. Then, $\bar{H} = \bar{H}^{(0)}$ is called the average Hamiltonian.

1.2 RF-Pulses and Signal Detection

The equilibrium polarization of an ensemble of spins, as represented by Eq. (1.10), is invariant under the action of the ZEEMAN Hamiltonian. The power of modern pulsed FT NMR lies in the possibility of manipulating this polarization by rf-pulses in a variety of ways, the most straightforward of which is the application of a 90° -pulse, which puts the magnetization into the transverse plane. Quantum-mechanically, a coherent superposition of states is created. The manipulation of coherence states, as represented by angular momentum operators, by rf-irradiation will be discussed in the following.

Upon continuous rf-irradiation, the sample experiences an oscillating magnetic field of magnitude B_1 . The irradiation can be described as a standing wave, thus the time-dependence of the rf-Hamiltonian is given by

$$\hat{H}_{rf} = -\gamma_I \mathbf{B}_1 \hat{\mathbf{I}} e^{i\mathbf{q}\mathbf{r}} e^{i\omega_{rf}t}. \quad (1.34)$$

The B_1 -field experienced by the I-spins corresponds to an effective angular precession frequency $\omega_1 = -\gamma_I B_1$. This definition implies that the action of pulses is described by mathematically positive rotations, i.e., the effective B_1 -field of a pulse described by the Hamiltonian $\omega_1 t \hat{I}_x$ (x-pulse) is oriented along the $-x$ direction [Ernst 87]. \mathbf{qr} is the phase of the rf-signal. Upon transition into the rotating frame (secular approximation, see Section 1.3.1), the oscillating z-component of the B_1 -field can be neglected, because the applied rf-power is usually limited to an effective precession frequency of 50–200 kHz, which is significantly less than the LARMOR frequency. Also, the field is usually applied in the transverse plane. In MAS probeheads, however, the effective rf-power corresponds to the projection of the \mathbf{B}_1 -vector (which is along the magic angle, because the long axis of the coil coincides with the rotor axis) onto the transverse plane; thus the effective field is only 82% of the full coil amplitude. Assuming an initial x-phase for the rf-signal ($\mathbf{qr} = 0$), we obtain for the combined ZEEMAN- and rf-Hamiltonians in the rotating frame (which is now taken to be rotating with ω_{rf} rather than ω_L , see Eq. (1.25)):

$$\begin{aligned} \hat{H}_0^* + \hat{H}_{rf}^* &\stackrel{rot.}{=} (\omega_L - \omega_{rf}) \hat{I}_z + 2\omega_1 \cos \omega_{rf} t [\hat{I}_x \cos \omega_L t - \hat{I}_y \sin \omega_L t] \\ &= (\omega_L - \omega_{rf}) \hat{I}_z + \omega_1 [\hat{I}_x \cos(\omega_{rf} + \omega_L)t - \hat{I}_y \sin(\omega_{rf} + \omega_L)t] \\ &\quad + \omega_1 [\hat{I}_x \cos(\omega_{rf} - \omega_L)t + \hat{I}_y \sin(\omega_{rf} - \omega_L)t] \end{aligned} \quad (1.35)$$

$$\stackrel{(\omega_{rf} \approx \omega_L)}{\cong} (\omega_L - \omega_{rf}) \hat{I}_z + \omega_1 \hat{I}_x + \omega_1 [\hat{I}_x \cos 2\omega_L t - \hat{I}_y \sin 2\omega_L t] \quad (1.36)$$

The factor of two in the first line accounts for the fact that only half of the applied power can account for on-resonance excitation of the irradiated nucleus, the other half is represented by rf-components counter-rotating with respect to the LARMOR precession. These components (Eq. (1.36) in square brackets) also vanish in the secular approximation, thus the effect of an rf-pulse can be described by a rotation around the x- (or y-) axis in the rotating frame. Nevertheless, the second-order contribution of the Magnus expansion reads

$$\bar{H}_{rf}^{(1)} = \omega_1^{(1)} \hat{I}_z, \quad (1.37)$$

where first-order frequency correction $\omega_1^{(1)}$ is called the BLOCH-SIEGERT shift. The dependence of $\bar{H}_{rf}^{(1)}$ on \hat{I}_z (z-rotation) means that the signal experiences a phase-change by $\omega_1^{(1)} \tau_p$ during a pulse of duration τ_p . This is usually a non-detectable quantity, but it gains importance

in double-resonance experiments, especially between nuclei close in frequency (e.g. ^1H and ^{19}F), where strong long-time irradiation on one channel (e.g. decoupling) leads to a phase change of the signal on the *other* channel.

The first term in Eq. (1.36) describes the off-resonance field contribution to the pulse, if the applied rf-frequency does not exactly match the LARMOR frequency of the irradiated nucleus. It follows that in this case the effective field is not along an axis in the transverse plane, but that the effective precession takes place around an axis tilted away from the transverse plane by an angle $\tan^{-1} \frac{\omega_L - \omega_{rf}}{\omega_1}$, with an effective frequency of $\omega_{eff} = \sqrt{(\omega_L - \omega_{rf})^2 + \omega_1^2}$. The deviation of ω_{eff} from ω_1 is usually small, but gains importance if internal interactions of the spin system, which are to be considered additionally to ω_L , cover very large frequency ranges (see Chapter 5).

After the excitation of single spin species in thermodynamic equilibrium by a 90° y-pulse, $\hat{I}_z \xrightarrow{\pi/2\hat{I}_y} \hat{I}_x$, the subsequent LARMOR precession of the transverse magnetization leads to the induction of a weak voltage in the rf-coil. As mentioned in Section 1.1.2, this signal is mixed with the reference carrier frequency to obtain the response in the rotating frame, i.e., the free induction decay (FID). The carrier has, for technical reasons, the same frequency as the rf-irradiation (it is produced by the same source). Thus, the first term in Eq. (1.36) describes the frequency of this precession, which is referred to as the frequency offset, $\omega_{off} = \omega_L - \omega_{rf}$. With a phase-sensitive detector, x- and y-components of the precessing magnetization can be separated, amplified, and digitized. Quantum-mechanically, the transverse magnetization is an *observable*, and following Eq. (1.3), its expectation value can be calculated as

$$\langle \hat{I}_+ \rangle = \text{Tr} \{ \hat{I}_+ \hat{\rho} \} = \frac{1}{\sqrt{2}} \left(\text{Tr} \{ \hat{I}_x \hat{\rho} \} + i \text{Tr} \{ \hat{I}_y \hat{\rho} \} \right) = \frac{1}{\sqrt{2}} \left(\langle \hat{I}_x \rangle + i \langle \hat{I}_y \rangle \right), \quad (1.38)$$

where the expectation value of the shift-operator \hat{I}_+ is shown to give the full complex time-domain signal. The Fourier transform of $\langle \hat{I}_+ \rangle(t)$ thus yields a spectrum with full phase information. In *two-dimensional* spectroscopy, the amplitude (or the phase) of the detected signal can be modulated by introducing another time dimension, t_1 , at some point in the pulse sequence. If the spectroscopic information in this indirect dimension is to be acquired in a sign-sensitive fashion, a phase cycling of a part of the pulse sequence with respect to the indirect dimension generally has to be implemented such that for subsequent time increments in the indirect dimension (called “slices”), the modulation is only due to the cosine or the sine

component of the indirectly detected signal. Various schemes exist with respect to the timing of the indirectly detected cosine and sine contributions relative to the t_1 incrementation. Techniques such as TPPI (*time-proportional phase incrementation*) or the STATES (hypercomplex) method, along with numerous practical hints, are presented in [Schmidt-Rohr 94].

1.3 NMR Interactions

The theoretical framework presented so far is applicable to spin quantum mechanics in general. However, this work is concerned with solid-state NMR. In this section, the main NMR interactions, which are ultimately responsible for the features in the spectra, will be presented. At this point, we have to deal with the goods and evils of solid-state NMR, that is, with the over-abundance of spectral information, and with ways of describing it. The *anisotropy* of interactions, their orientational dependence with respect to the static magnetic field, \mathbf{B}_0 , requires an appropriate formalism. We will thus review some basic features of tensor algebra. In its most general form, the Hamiltonian for an internal interaction of the spin system can be written as a bilinear product

$$\hat{H}_{int} = \hat{\mathbf{V}}^{(i)} \underline{\mathbf{A}} \hat{\mathbf{U}}^{(j)}, \quad (1.39)$$

with $\underline{\mathbf{A}}$ as the tensor describing the space part and $\hat{\mathbf{V}}$ and $\hat{\mathbf{U}}$ as vector operators, e.g. $(\hat{V}_x \hat{V}_y \hat{V}_z)^T$. These vector operators can be spin angular momentum operators of like or unlike spins, describing homonuclear and heteronuclear couplings, respectively. They can even be operators of the same spin (quadrupolar coupling), or one of them can represent the Cartesian vector of the magnetic field, \mathbf{B}_0 (chemical shift interaction). The second rank tensor $\underline{\mathbf{A}}$ is most intuitively represented by a (3×3) -matrix in Cartesian space. Such a matrix can always be decomposed into three contributions:

$$\begin{aligned} \underline{\mathbf{A}} &= A_{\parallel} + \begin{pmatrix} 0 & B & C \\ -B & 0 & D \\ -C & -D & 0 \end{pmatrix} + \begin{pmatrix} E & G & H \\ G & F & I \\ H & I & -E - F \end{pmatrix} \\ &= A_0 + (A_{1-1} \ A_{10} \ A_{1-1})^T + (A_{2-2} \ \dots \ A_{22})^T \end{aligned} \quad (1.40)$$

A represents the isotropic part, the second term is the traceless and antisymmetric (3 components), and the third the traceless, symmetric part of the tensor (5 components). The second line indicates the transition into the *irreducible spherical representation* of this tensor. It consists of a scalar, and two vectors of dimension 3 and 5, respectively. The reason for this change of the reference frame is the favorable transformation behavior of spherical tensor components. They transform exactly like spherical harmonics $Y_{L,m}$, with the familiar multiplicity of $2L + 1$, and values for m ranging in integer steps from $-L \dots +L$. To appreciate the use of the spherical representation, Eq. (1.39) can be rewritten in terms of a scalar product of spherical tensors:

$$\hat{H}_{int} = \sum_L \sum_{m=-L}^L (-1)^m A_{Lm} \hat{T}_{L-m}, \quad (1.41)$$

where \hat{T}_{L-m} is an *irreducible spherical spin tensor operator* of rank L and order $-m$. The spin operators for all important interactions in solid-state NMR can be represented by linear combinations of irreducible tensor operators. Furthermore, rotations in real space (affecting $\underline{\mathbf{A}}$) and in spin space (as brought about by pulses, the description of which is based on the transformation properties of angular momentum operators) occur without changing the rank, L , of a tensor. Instead of arduous matrix multiplications one is then just left with linear combinations among the $2L + 1$ components, which leads to a much more economic formalism. The relations for the transformation between the Cartesian and spherical representations of tensors, along with the equations describing their behavior under rotations, are summarized in Appendix A.

1.3.1 Chemical Shift and Secular Averaging

In atoms and molecules, the external magnetic field, B_0 , is locally influenced by the electron clouds surrounding the nuclear spins. This is phenomenologically accounted for by introducing a *chemical-shift tensor* $\underline{\sigma}$, with the Hamiltonian of the chemical shift interaction being given by

$$\begin{aligned} \hat{H}_{CS} &= -\gamma_I \mathbf{B} \underline{\sigma} \hat{\mathbf{I}} \\ &= -\gamma_I B_0 (\sigma_{zx} \hat{I}_x + \sigma_{zy} \hat{I}_y + \sigma_{zz} \hat{I}_z), \end{aligned} \quad (1.42)$$

where the common convention $\mathbf{B}_0 = (0 \ 0 \ B_0)^T$ was used. This Hamiltonian may serve as an instructive example for the simplification of an interaction Hamiltonian upon transition into the rotating frame. By applying Eq. (1.25), we obtain a sum of time-dependent and time-independent terms

$$\begin{aligned}\hat{H}_{CS}^* &= H_{CS}^{sec} + H_{CS}^{nonsec}(t) \\ &= -\gamma_I B_0 \sigma_{zz} \hat{I}_z - \gamma_I B_0 e^{\omega_L t \hat{I}_z} (\sigma_{zx} \hat{I}_x + \sigma_{zy} \hat{I}_y) e^{-\omega_L t \hat{I}_z}.\end{aligned}\quad (1.43)$$

The time-independent terms are called the *secular* parts of the Hamiltonians. The time-dependent, non-secular parts of the Hamiltonian do not contribute to the spectrum to first order. This can be rationalized by the fact that they oscillate rapidly, i.e. with the LARMOR frequency, ω_L , or powers thereof,⁴ and that signal variations are sampled at a much lower rate. Average Hamiltonian theory justifies this argument because, if the cycle-time is chosen to be $2\pi/\omega_L$, all but the secular parts will vanish for \bar{H}_0 . The secular Hamiltonian might also be viewed as a “direction cosine” of the interaction Hamiltonian with respect to the z-axis. If not noted otherwise, any Hamiltonian \hat{H} will henceforth be in the secular approximation. Thus,

$$\hat{H}_{CS}^{(i)} = \omega_{L,i} \sigma_{zz,i} \hat{I}_z^{(i)} \quad (1.44)$$

for a single spin.

The tensor element σ_{zz} is a function of the orientation of the molecular segment with respect to the magnetic field. In its principal axes frame (PAS), the chemical shift tensor is diagonal,

$$\begin{aligned}\underline{\sigma}^{PAS} &= \begin{pmatrix} (\sigma_x + \sigma_{iso}) & 0 & 0 \\ 0 & (\sigma_y + \sigma_{iso}) & 0 \\ 0 & 0 & (\sigma_z + \sigma_{iso}) \end{pmatrix} \\ &= \sigma_{iso} \mathbb{1} + \frac{\delta_{CS}}{\omega_L} \begin{pmatrix} -\frac{1+\eta_{CS}}{2} & 0 & 0 \\ 0 & -\frac{1-\eta_{CS}}{2} & 0 \\ 0 & 0 & 1 \end{pmatrix},\end{aligned}\quad (1.45)$$

⁴ $H_{CS}^{nonsec}(t)$ can be expanded using the BAKER-HAUSDORFF lemma (Eq. 1.18), where the nested commutators produce powers of $\omega_L t$ in the higher-order terms.

where we have used the definitions of the anisotropy parameter, $\delta_{CS} = \omega_L \sigma_z$, and the asymmetry parameter, $\eta_{CS} = \frac{\sigma_y - \sigma_x}{\sigma_z}$. The $\sigma_\alpha = \sigma_{\alpha\alpha}^{PAS} - \sigma_{iso}$ are the components of the traceless, symmetric part of the chemical shift tensor,⁵ and the trace $\sigma_{iso} = \frac{1}{3}(\sigma_{xx}^{PAS} + \sigma_{yy}^{PAS} + \sigma_{zz}^{PAS})$ is the orientation-independent isotropic chemical shift, which is usually given in ppm of the LARMOR frequency of the given nucleus such that its magnitude is independent of the B_0 field. In order to relate the principal values of the chemical shift tensor to the chemical shift observed in the laboratory frame, $\sigma_{zz}^{LAB}(\Omega_{PL})$ ($= \sigma_{zz}$ in Eq. (1.44)), unitary rotations must be used, where $\Omega_{PL} = (\alpha_{PL}, \beta_{PL}, \gamma_{PL})$ is the set of Euler angles describing the transformation from the principal axes frame (P) to the laboratory frame (L). This is presented in more detail in Appendix A. In particular, for the case of just one spin, where there is no need to specify relative tensor orientations, we obtain a simple dependence on the polar angles ($\theta = \beta_{PL}, \phi = \alpha_{PL}$) of the B_0 -field in the PAS:

$$\sigma_{zz}^{LAB} = \sigma_{iso} + \frac{\delta_{CS}}{\omega_L} \frac{1}{2} (3 \cos^2 \theta - 1 + \eta_{CS} \sin^2 \theta \cos 2\phi). \quad (1.46)$$

In terms of spherical tensor operators, the space parts are given in the Appendix, Eqs. (A.9)–(A.14), and the corresponding non-vanishing tensor operators in the secular approximation are obtained by comparing their definitions (Eqs. (A.3)–(A.8)) with Eq. (1.42): $\hat{T}_{00}^{CS} = \sqrt{\frac{3}{2}} \hat{T}_{20}^{CS} = \hat{I}_z$. Since one of the constituents of the Hamiltonian is the B_0 -field vector, the tensor operators are only linear in the spin operators.

It should further be mentioned that the isotropic chemical shift cannot be distinguished from the frequency offset in the rotating frame, $\omega_{off} = \omega_L - \omega_{rf}$, for cases where the carrier frequency, ω_{rf} (and thus the frequency of the rotating frame), is different from the LARMOR frequency. Therefore, the chemical-shift information has to be referenced using calibration compounds with known isotropic chemical shifts.

1.3.2 Spin-Spin Couplings and Second Averaging

In this section, we shall first consider homonuclear spin-spin interactions only. We will then see that the heteronuclear interactions follow naturally from the homonuclear treatment by

⁵In order to remove the arbitrariness in assigning the three σ_α to the three different eigenvalues of $\underline{\sigma}$, we follow the convention $|\sigma_y| \leq |\sigma_x| \leq |\sigma_z|$ [Spiess 78], which leads to $0 \leq \eta_{CS} \leq 1$ and identifies σ_z with the unique principal axis in the case of $\eta_{CS} = 0$.

introducing the concept of second averaging.

Spins exhibit magnetic dipole moments, which are essentially proportional to the expectation value of their spin angular momentum, $\mu_i \sim \gamma_i \langle m | \hat{\mathbf{I}} | m \rangle$. A dipole moment creates a local magnetic field, with which the dipole moments of adjacent spins can interact. For each pair of spins, the resulting shift of the energy levels can be described by the dipolar Hamiltonian

$$\hat{H}_D^{(ij)} = -\frac{\mu_0 \hbar \gamma_i \gamma_j}{4\pi r_{ij}^3} \left(\frac{3 (\hat{\mathbf{I}}^{(i)} \cdot \mathbf{r}_{ij}) (\hat{\mathbf{I}}^{(j)} \cdot \mathbf{r}_{ij})}{r_{ij}^2} - \hat{\mathbf{I}}^{(i)} \cdot \hat{\mathbf{I}}^{(j)} \right), \quad (1.47)$$

which is obtained from the classical energy formula found in electrodynamics textbooks [Jackson 75] by replacing the classical magnetic dipole moments, μ_i , by their quantum-mechanical operator counterparts. Adapting the bilinear product representation,

$$\hat{H}_D^{(ij)} = \hat{\mathbf{I}}^{(i)} \underline{\mathbf{D}}^{(ij)} \hat{\mathbf{I}}^{(j)}, \quad (1.48)$$

it is found that the dipolar coupling tensor,

$$\underline{\mathbf{D}}^{(ij)} = -D_{ij} \left(\frac{3 \mathbf{r}_{ij} \mathbf{r}_{ij}}{r_{ij}^2} - \mathbf{1} \right), \quad (1.49)$$

is traceless and symmetric. In its principal axis system, we can write

$$\underline{\mathbf{D}}^{(ij),PAS} = -2D_{ij} \begin{pmatrix} -\frac{1}{2} & 0 & 0 \\ 0 & -\frac{1}{2} & 0 \\ 0 & 0 & 1 \end{pmatrix}, \quad (1.50)$$

with the dipolar coupling constant

$$D_{ij} = \frac{\mu_0 \hbar \gamma_i \gamma_j}{4\pi r_{ij}^3} = -\frac{1}{2} \delta_D \quad (1.51)$$

in units of angular frequency. From the dipolar asymmetry parameter, δ_D , using Eq. (A.12), we can straightforwardly derive the only non-vanishing spherical tensor element

$$A_{20}^{D_{ij},PAS} = -\sqrt{6} D_{ij}. \quad (1.52)$$

By expanding Eq. (1.48) and sorting out the various dyadic products of spin operators, one arrives at the famous “dipolar alphabet” [Abragam 61]. In the secular approximation, several of these terms are again averaged to zero, and one is left with the dipolar Hamiltonian

$$\hat{H}_D^{(ij)} = A_{20}^{Dij} \hat{T}_{20}^{(ij)}. \quad (1.53)$$

The introduction of tensor operators according to the definitions given in Appendix A is equivalent to the introduction of a unique quantization axis (the z-axis, which is defined by the ZEEMAN interaction). This choice is convenient because the secular averaging can easily be performed within that specific representation. For a single *homonuclear* spin pair, the interaction depends only on the azimuthal angle θ :

$$\begin{aligned} \hat{H}_D^{(ij)} &= -D_{ij} \frac{1}{2} (3 \cos^2 \theta - 1) \left(2\hat{I}_z^{(i)} \hat{I}_z^{(j)} - \hat{I}_x^{(i)} \hat{I}_x^{(j)} - \hat{I}_y^{(i)} \hat{I}_y^{(j)} \right) \\ &= -D_{ij} P_2(\cos \theta) \left(2\hat{I}_z^{(i)} \hat{I}_z^{(j)} - \hat{I}_+^{(i)} \hat{I}_-^{(j)} - \hat{I}_-^{(i)} \hat{I}_+^{(j)} \right) \end{aligned} \quad (1.54)$$

The dependence of the dipolar splitting on the second LEGENDRE polynomial $P_2(\cos \theta)$ is the reason for the appearance of the famous PAKE pattern in static dipolar powder spectra of a spin pair (see Fig. 1.1, lower or upper left, grey line). Eq. (1.13) was used to introduce the shift operators, the appearance of which allows for a qualitative description of the action of the homonuclear dipolar coupling. These so-called “flip-flop” terms are responsible for the non-vanishing commutator $[\hat{T}_{20}^{(ij)}, \hat{I}_z^{(i)}] = -\frac{1}{\sqrt{3}} \hat{T}_{10}^{(ij)}$. Yet, the total z-angular momentum, $\hat{I}_z = \sum_i \hat{I}_z^{(i)}$, using the general relationship

$$[\hat{T}_{Lm}, \hat{I}_z] = m \hat{T}_{Lm}, \quad (1.55)$$

is proven to commute with $\hat{T}_{20}^{(ij)}$. This means that for a homonuclear two-spin system with equal polarizations, we will *observe* a simple shift of the energy levels $\sim D_{ij}$ and an independent evolution of each spin in the local field of the other. However, for different polarizations, magnetization exchange will become observable because mutual spin-flips occur. This is the basis of the phenomenon of spin diffusion, which links a homonuclear spin system together to form a “spin-bath” with a “spin-temperature” assigned to it. Without flip-flop exchange between the spins, such a thermodynamic interpretation would not be possible since local perturbations could not spread and explore the full phase space to reach an equilibrium.

Another spin-spin interaction is the scalar J-coupling, which is essentially orientation independent (neglecting the very weak J-anisotropy of light elements) and operates via the bond electrons between nuclei. Since the coupling constants, J_{ij} , are comparably small, it is of only minor importance in solid-state NMR. Its scalar nature demands a simple dependence on spin tensor operators of rank zero only:

$$\begin{aligned}\hat{H}_J^{(ij)} &= \hat{\mathbf{I}}^{(i)} J_{ij} \hat{\mathbf{I}}^{(j)} = J_{ij} \hat{T}_{00}^{(ij)} \\ &= J_{ij} \left(\hat{I}_z^{(i)} \hat{I}_z^{(j)} + \hat{I}_x^{(i)} \hat{I}_x^{(j)} + \hat{I}_y^{(i)} \hat{I}_y^{(j)} \right) \\ &= J_{ij} \left(\hat{I}_z^{(i)} \hat{I}_z^{(j)} + \hat{I}_+^{(i)} \hat{I}_-^{(j)} + \hat{I}_-^{(i)} \hat{I}_+^{(j)} \right)\end{aligned}\quad (1.56)$$

As to the flip-flop parts of the Hamiltonian, the J-coupling exhibits features similar to dipolar couplings. A distinct difference between J and dipolar coupling is the isotropic nature of the homonuclear J-coupling Hamiltonian, which means that J-coupling alone cannot account for the discrimination between two magnetically equivalent spins. Thus, whereas for dipolar coupling a splitting is observed for a single configuration of two like spins with the same chemical shift (brought about by the broken isotropic symmetry with respect to the unique z-axis), the signal of a J-coupled homonuclear spin pair with equal shifts is just a single line (Fig. 1.1, lower traces).

The aforementioned non-commutativity of $\hat{T}_{20}^{(ij)}$ (and $\hat{T}_{00}^{(ij)}$) with $\hat{I}_z^{(i)}$ has another important implication, which is connected to the interplay of dipolar couplings and chemical shifts. Average Hamiltonian theory suggests that in a system where one of two or more internal interactions exceeds the others by orders of magnitude,⁶ $|\hat{H}_s| \gg |\hat{H}_{int}|$, a formal **second averaging** of the Hamiltonian can be performed, with the consequence that only components of the Hamiltonian “parallel” to the strong interaction will survive. This is similar to the secular approximation, where the ZEEMAN interaction was responsible for the “first” averaging, i.e. the transition into the rotating frame of reference. The transformed Hamiltonian for the weaker interactions reads

$$\hat{H}_{int}^*(t) = e^{i\hat{H}_s t} \hat{H}_{int} e^{-i\hat{H}_s t}.\quad (1.57)$$

The density operator has to be transformed accordingly in analogy to Eq. (1.24). The average Hamiltonian and higher-order corrections are calculated using Eqs. (1.31)–(1.33), with the

⁶The Euclidian operator norm is defined by $|\hat{A}| = \sqrt{\text{Tr} \{ \hat{A} \hat{A}^\dagger \}}$.

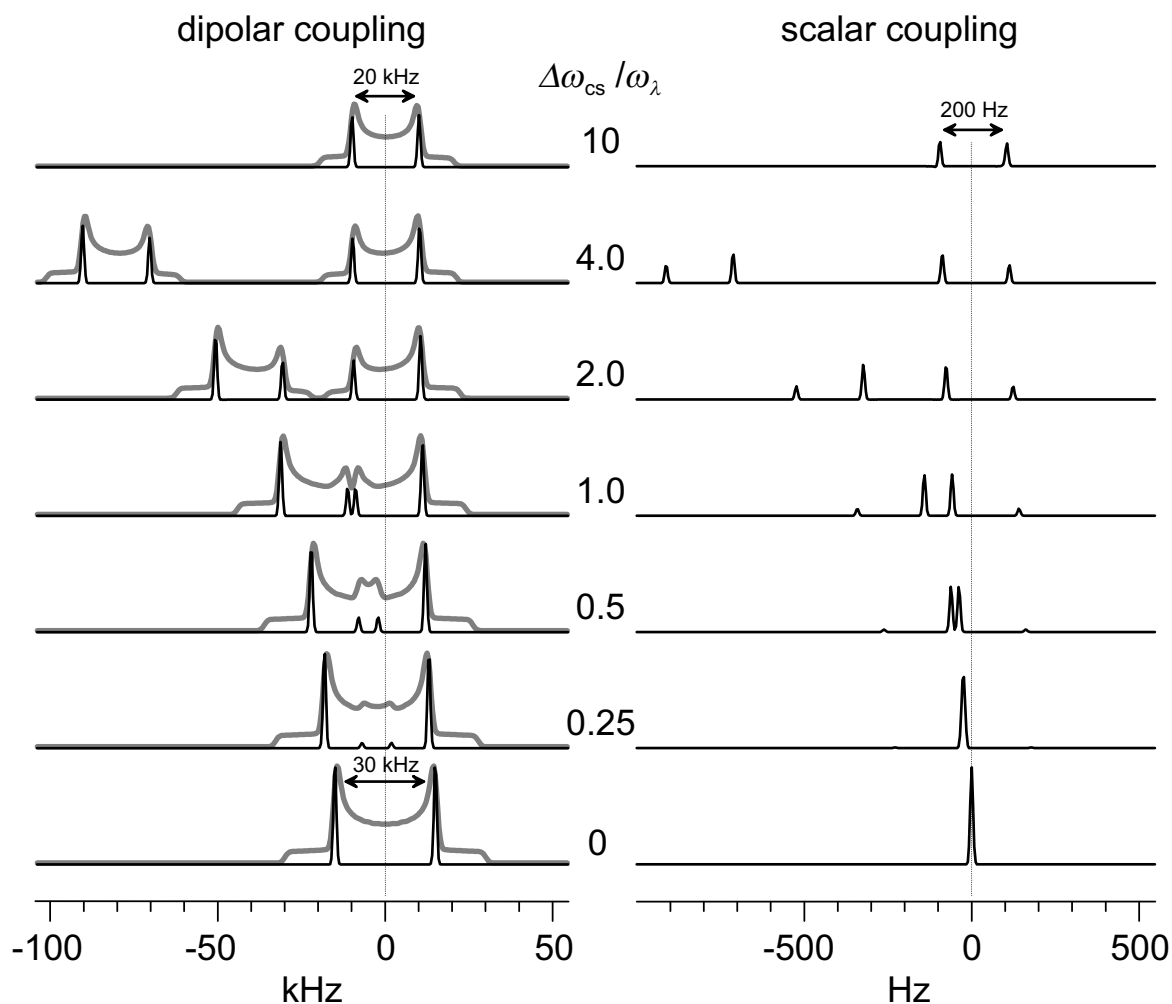


Figure 1.1: Effect of isotropic chemical shifts on homonuclear dipolar and J -splittings. The coupling constants, ω_{cpl} , used in the simulations were 20 kHz and 200 Hz, respectively. For the dipolar coupling, the spectra correspond to a single crystallite (at an angle $\theta = 90^\circ$), while the grey background traces are powder patterns. In the top slices, the offset parts of the doublets are outside the shown spectral range.

cycle time t_c being defined as the inverse of the characteristic frequency of \hat{H}_s . The most important case is the evolution under offsets, or isotropic chemical shifts, with $\hat{H}_s \sim \hat{I}_z^{(i)}$.⁷

The effects of isotropic chemical shifts on a homonuclear spin pair are explored in Fig.

⁷In certain average Hamiltonians, offset evolution might also occur with respect to a quantization axis which is not $\parallel z$, as a result of cyclic pulses sequences, which create so-called “toggling frame” Hamiltonians [Haeberlen 76].

1.1 for the cases of a dipolar-coupled and a J-coupled pair. For the situation with no chemical shift difference, a dipolar splitting of $\frac{3}{2}D_{ij} = 30$ kHz is observed for the orientation $\theta = 90^\circ$. This is also the splitting between the singularities of the PAKE pattern (grey background traces). The factor of $\frac{3}{2}$ arises from the spin part of the Hamiltonian; for an explanation see p. 29. Upon increasing the chemical shift of one of the two coupling partners, as described by the Hamiltonian $\Delta\omega_{cs}\hat{I}_z^{(i)}$, we see an increasing influence of the evolution due to the non-vanishing commutator $[\hat{T}_{20}^{(ij)}, \hat{I}_z^{(i)}] = -\frac{1}{\sqrt{3}}\hat{T}_{10}^{(ij)}$. We do *not* simply observe two doublets separated by $\Delta\omega_{cs}$. Rather, the effects of the chemical shifts lead to higher-order corrections of the dipolar Hamiltonian. For rather large $\Delta\omega_{cs}$, the situation for the individual spins can be described by a *second-averaged* dipolar Hamiltonian, as described above. The flip-flop terms in the coupling Hamiltonians are the ones which do not survive the second averaging. Thus, the observed dipolar splitting is now $D_{ij} = 20$ kHz.

Similarly, in the limit of large $\Delta\omega_{cs}$, J-splittings can be observed because the isotropy of the J-coupling Hamiltonian is lost after second averaging. Upon decreasing $\Delta\omega_{cs}$, higher-order corrections, which lead to the well-known ‘‘roofing effects’’, have to be taken into account. In Fig. 1.1 we see that the roofing effects are in opposite directions for dipolar and J-splittings.

The limiting case for large $\Delta\omega_{cs}$ is exactly the situation encountered for *heteronuclear* couplings, with the only difference that the averaging, which in the homonuclear case is manifested as second averaging of the homonuclear dipolar Hamiltonian by a chemical shift, is already taken into account within the secular approximation. In the heteronuclear case with the vastly different LARMOR frequencies of different nuclei and the notion of a multiply rotating frame, the flip-flop terms have already been removed. Thus, the secular Hamiltonians for heteronuclear spin-spin interactions are the same as for a homonuclear coupling that is second-averaged by a large chemical shift difference. Associating $\hat{\mathbf{S}}$ with the angular momentum operators of the second spin species, we have

$$\hat{H}_D^{(IS)} = -D_{IS}P_2(\cos\theta)2\hat{I}_z\hat{S}_z, \quad (1.58)$$

$$\hat{H}_J^{(IS)} = J_{IS}\hat{I}_z\hat{S}_z, \quad (1.59)$$

as the Hamiltonians for heteronuclear dipolar and J-coupling, respectively. If Eq. (1.58) is used to describe homonuclear dipolar interactions second-averaged by a chemical shift

difference, it is referred to as being in the “weak coupling limit”, and the observed dipolar splitting between the horns of the PAKE pattern changes from $\frac{3}{2}D_{ij}$ to D_{ij} .

The cross-polarization (CP) experiment is an instructive example of the *reintroduction* of flip-flop terms into heteronuclear spin-spin interaction Hamiltonians. The CP pulse sequence [Pines 72, Pines 73] is used to enhance the polarization of low-gamma nuclei by transferring magnetization from the protons. After an initial 90° -pulse on the protons, spin-lock rf-fields are applied on both channels.⁸ Speaking in terms of average Hamiltonian theory, the spin-lock rf-fields create a toggling frame dipolar Hamiltonian, with new “effective” quantization axes in the transverse plane of each rotating frame (the specific direction for each channel is dependent on the phase of the rf-field, while the relative phase of the spin-lock on the two channels does not matter). If the HARTMANN-HAHN condition is met, i.e. $B_{1,I}\gamma_I = B_{1,S}\gamma_S \Rightarrow \omega_{1,I} = \omega_{1,S}$, the two spin species experience a common frequency with respect to the quantization axis, hence flip-flop terms are energy-conserving and will appear in the effective dipolar Hamiltonian. As a result, the low-gamma nuclei are thermodynamically linked to the proton spin bath, and polarization transfer occurs until spin-temperature equilibration. For the case of just two heteronuclear spins, the polarization is transferred back and forth between the nuclei in an oscillatory fashion. The initial 90° -pulse ensures that the polarization of the protons at the start of the spin-lock is along the toggling frame quantization axis.

1.3.3 Quadrupolar Coupling

Spins with $I > \frac{1}{2}$ exhibit quadrupole moments, which interact with the local electric field gradient in the molecule. The bilinear Hamiltonian reads

$$\hat{H}_Q = \hat{I} \underline{\mathbf{Q}} \hat{I}, \quad (1.60)$$

with $\underline{\mathbf{Q}}$ being the quadrupolar interaction tensor. It is related to the local field gradient tensor, $\underline{\mathbf{V}}$, via the nuclear quadrupole moment, eQ (e is the elementary charge):

$$\underline{\mathbf{Q}} = \frac{eQ}{2I(2I-1)\hbar} \underline{\mathbf{V}} \quad (1.61)$$

⁸A spin-lock is an rf-pulse applied *along* the direction of a transverse coherence, which is then “locked” in that direction and does not precess.

In terms of spherical tensor operator formalism, the quadrupolar Hamiltonian in the secular approximation reads

$$\begin{aligned}\hat{H}_Q^{(i)} &= A_{20}^{Q_i} \hat{T}_{20} \\ &= A_{20}^{Q_i} \frac{1}{\sqrt{6}} \left(3\hat{I}_z^{(i)} \hat{I}_z^{(i)} - \hat{\mathbf{I}}^{(i)} \hat{\mathbf{I}}^{(i)} \right) \\ &= A_{20}^{Q_i} \frac{1}{\sqrt{6}} \left(3\hat{I}_z^{(i)2} - I(I+1) \right).\end{aligned}\quad (1.62)$$

As opposed to the case of dipolar couplings, the quadrupolar interaction tensor can be asymmetric. Its non-vanishing irreducible components in the principal axes system are

$$A_{20}^{Q,PAS} = \sqrt{\frac{3}{2}} \delta_Q = \sqrt{\frac{2}{3}} \omega_Q, \quad (1.63)$$

$$A_{2\pm 2}^{Q,PAS} = -\frac{1}{2} \delta_Q \eta_Q = -\frac{1}{3} \omega_Q \eta_Q. \quad (1.64)$$

Introducing $V_{zz}^{PAS} = eq$ as the z-principal value of the field-gradient tensor, the angular dependency of the quadrupolar interaction can be written in exact analogy to the chemical shift interaction (Eq. (1.46)) as

$$Q_{zz} = \delta_Q \frac{1}{2} (3 \cos^2 \theta - 1 + \eta_Q \sin^2 \theta \cos 2\phi). \quad (1.65)$$

For the case of deuterons ($I = 1$), V_{zz} is mainly determined by the electron distribution along the C²H-bond. The approximate axial symmetry of CH-bonds leads to negligible asymmetry parameters, η_Q , in most cases. Due to the dependence on $P_2(\cos \theta)$, the static lineshape is again a PAKE pattern, with a splitting between the horns of ⁹

$$\omega_Q/2\pi = \frac{3}{2} \delta_Q^{I=1} \frac{1}{2\pi} = \frac{3}{2} \frac{eQeq}{2\hbar} \frac{1}{2\pi}. \quad (1.66)$$

The factor of $\frac{3}{2}$ arises from the spin part of the Hamiltonian, in analogy to the homonuclear dipolar coupling. For ²H in aliphatic bonds, $\omega_Q/2\pi$ is 125 kHz. The value is increased by 20 to 30 kHz for O²H deuterons, where lower values are assumed when the deuteron is part of a hydrogen bond (see Section 7.2).

⁹Often, the coupling parameter given is the “quadrupole coupling constant” (QCC) $\frac{eQeq}{h} = \delta_Q/\pi$ in frequency units.

For the above considerations, it was assumed that the quadrupolar interaction can be treated as a first-order perturbation to the ZEEMAN Hamiltonian, i.e. within the secular approximation. This represents a good approximation only for small ω_Q . Light nuclei with $I = 1$ exhibit small quadrupole moments, eQ ; as a result, ^2H or ^6Li can usually be treated in first order. In many cases, however, the quadrupolar interaction reaches several percent of the ZEEMAN interaction, thus a first-order treatment is generally no longer feasible, and the inclusion of second-order terms, for instance using perturbation theory, cannot be circumvented. This is the case even for $I = 1$ nuclei (e.g. ^{14}N), when the z-principal value of the field gradient tensor (eq) is very large. Second-order contributions to the lineshape are most apparent for half-integer quadrupolar nuclei, where the shape of the “central transition”, which is sharp for vanishing second-order contributions, sensitively depends on these. ^7Li ($I = \frac{3}{2}$) is an exception in a sense that in its compounds it exhibits quadrupolar coupling constants small enough for a treatment in first order. Another prominent example of a first-order $I > 1$ spin is ^{27}Al ($I = \frac{5}{2}$) in alum, where the highly symmetric crystal environment leads to a very small field gradient tensor. For heavier elements such as Cl, Br, I, or transition metals, the quadrupolar coupling can be comparable to or even larger than the ZEEMAN interaction.

1.3.4 Quadrupolar and Dipolar Time Evolution

The “quadrupolar frequency”, $\omega_Q = \frac{3}{2}\delta_Q$, which was introduced in Eq. (1.63), appears as the argument of the trigonometric functions describing the rotation in the product operator subspace $(\hat{I}_x, i(\hat{T}_{21} + \hat{T}_{2-1}), \sqrt{\frac{2}{3}}\hat{T}_{20})$, which in turn is the basis for the description of the quadrupolar time evolution:

$$\hat{I}_x \xrightarrow{\omega_Q t \sqrt{\frac{2}{3}}\hat{T}_{20}} \hat{I}_x \cos \omega_Q t + i(\hat{T}_{21} + \hat{T}_{2-1}) \sin \omega_Q t \quad (1.67)$$

Since $(\hat{T}_{21} + \hat{T}_{2-1})$ does not represent observable magnetization, the cosine-dependence of \hat{I}_x leads to the observation of a doublet with signal positions at $\pm\omega_Q$, if the z-principal axis of the tensor points along the magnetic field (outer wings of the Pake spectrum). Eq. (1.67) is equivalent to the description of homonuclear dipolar couplings, where the observed splitting is $\pm\frac{3}{2}D_{ij}$:

$$\hat{I}_x \xrightarrow{-\frac{3}{2}D_{ij}t \sqrt{\frac{2}{3}}\hat{T}_{20}} \hat{I}_x \cos \frac{3}{2}D_{ij}t - i(\hat{T}_{21} + \hat{T}_{2-1}) \sin \frac{3}{2}D_{ij}t \quad (1.68)$$

According to Eq. (1.52), $A_{20}^{D_{ij},PAS} = -\sqrt{6}D_{ij}$. Therefore $\hat{H}_D^{(ij)} = -\sqrt{6}D_{ij}\hat{T}_{20}^{(ij)}$. An additional factor of $\frac{1}{2}$ enters because the dipolar evolution takes place in the composite subspace $(\hat{I}_x^{(i)} + \hat{I}_x^{(j)}, 2i(\hat{T}_{21}^{(ij)} + \hat{T}_{2-1}^{(ij)}), 2\sqrt{\frac{2}{3}}\hat{T}_{20}^{(ij)})$. For the total angular momentum of a 2-spin system (assuming equal polarizations), $\hat{I}_\alpha = \hat{I}_\alpha^{(1)} + \hat{I}_\alpha^{(2)}$ ($\alpha \in \{x, y, z\}$), the tensor operators have to be calculated by inserting this sum into the definitions (Eqs. (A.3)–(A.8)). For instance, the tensor operator in the composite subspace, \hat{T}_{20} , equals $\hat{T}_{20}^{(ij)} + \hat{T}_{20}^{(ji)} = 2\hat{T}_{20}^{(ij)}$ [Friedrich 98b]. For heteronuclear dipolar couplings, the appropriate subspace is $(\hat{I}_x, 2\hat{I}_y\hat{S}_z, 2\hat{I}_z\hat{S}_z)$.

1.4 Spatial Averaging by Magic-Angle Spinning

The plethora of information contained in solid-state NMR spectra demands techniques for spectral simplification, line-narrowing in particular, in order to extract the different components of the NMR interactions discussed in the last section. One possibility is to remove anisotropic components by manipulation of the spatial part of the NMR Hamiltonian (the A_{Lm} terms in Eq. (1.41)) and then to selectively re-introduce the orientation dependence, or anisotropy, into the spectrum by controlled manipulation of the spin-system using rf-pulses and the concept of multi-dimensional spectroscopy [Schmidt-Rohr 94]. Among the most important techniques to achieve the goal of removing the anisotropic information is rapid spinning of the sample about an axis inclined by the magic angle (54.7°) from the z-axis of the laboratory frame ($\parallel B_0$). The technique was introduced in the 1950's by Andrew and Lowe [Andrew 58, Lowe 59], and considerable technical progress has been made towards ever higher spinning frequencies.

The majority of the data presented in this work relies on the condition of so-called *very-fast* magic-angle spinning, i.e., on spinning frequencies exceeding 20 kHz. Since about two years ago, commercial MAS equipment supporting rotors with a diameter of 2.5 mm has become available. Such equipment allows for spinning frequencies of up to 35 kHz, and is routinely used in our group.

In the last section, it became obvious that the frequencies depending on the anisotropic part of most NMR interactions are proportional to the second LEGENDRE Polynomial, $P_2(\cos\theta)$ (Eqs. (1.46), (1.54), and (1.65)), which vanishes for $\theta = 54.7^\circ$. This angle is called the *magic angle*, and is often referred to with the symbol β_M ; it is the angle between the edge

of a cube and its body diagonal. If the sample is spun around the magic angle rapidly enough, the orientation dependence of the interaction in question is reduced to the direction cosine of the interaction tensor with respect to the $(1, 1, 1)$ direction, which is zero for all interactions discussed above. The principle is depicted in Fig. 1.2, where the intercept between the graphical representation of $P_2(\cos \beta)$ and the z-axis is proportional to the interaction frequency.

The condition for “rapid” spinning is to be taken from average Hamiltonian theory (AHT), where the time-dependence imposed on the interaction Hamiltonians, \hat{H}_λ , by the sample-spinning must be fast enough to justify the application of a time-independent average Hamiltonian. Only for a spinning frequency $\omega_R \gg \omega_\lambda$ are the anisotropies completely averaged out. Application of AHT requires “stroboscopic detection”, with a rate corresponding to the sample spinning frequency or an integer multiple thereof. For slower spinning, a time-dependence of the MAS Hamiltonian has to be considered explicitly. This, however, does not present a serious problem, since the higher-order terms in the Magnus expansion, Eqs. (1.32), (1.33),..., vanish for the case of a single interaction. Only the space-parts of the Hamiltonians are rendered time-dependent by the MAS, hence the Hamiltonian still commutes with itself at different times. One is left with a zeroth-order average Hamiltonian in the secular approximation, which describes the evolution under an interaction λ and sample rotation for arbitrary times:

$$\bar{H}_{\lambda, \text{MAS}}(t) = \frac{1}{t} \int_0^t \hat{H}_\lambda(t) dt = \hat{T}_{00} A_{00}^{\lambda, \text{LAB}} + \hat{T}_{20} \frac{1}{t} \int_0^t A_{20}^{\lambda, \text{LAB}}(\omega_R t) dt \quad (1.69)$$

1.4.1 Hamiltonians under MAS

In the last section, representations of anisotropic NMR interactions were given in terms of irreducible spherical tensors. This formalism will now prove its usefulness, as the derivation of the time dependence of the spatial part of the interaction Hamiltonians is sketched. Three Euler angle transformations are necessary to transform the interaction tensor, which is usually defined in its principal axes system (PAS), to the laboratory frame (LAB):

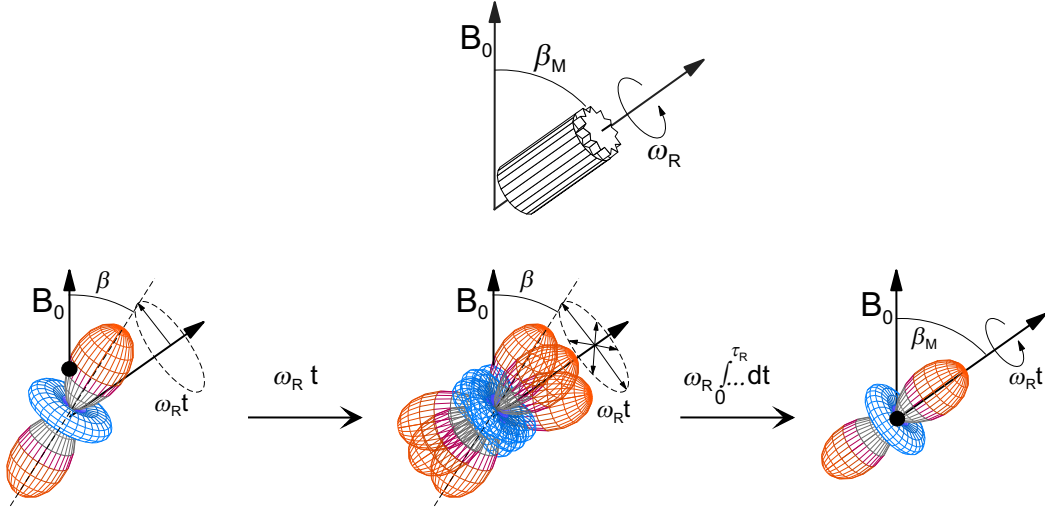


Figure 1.2: Principle of averaging of NMR interactions proportional to $P_2(\cos\beta)$ by magic-angle spinning.

$$\begin{array}{ccccccc}
 & (\alpha_{PC}, \beta_{PC}, \gamma_{PC}) & & (\alpha_{CR}, \beta_{CR}, \gamma_{CR}) & & (\omega_{Rt}, \beta_M, 0) & \\
 \text{PAS} & \Longrightarrow & \text{Crystal} & \Longrightarrow & \text{Rotor} & \Longrightarrow & \text{LAB} \\
 & \text{tensor orientation} & & \text{powder average} & & \text{MAS} &
 \end{array}$$

The time dependence enters the picture in the last transformation from the rotor to the laboratory frame, where the Euler angle α_{RL} depends on the rotor position (phase), $\alpha_{RL} = \omega_{Rt}$. Restricting ourselves to interaction tensors of rank two, Eq. (A.18) can be used to perform the transformations. For the three subsequent rotations we obtain

$$A_{20}^{\lambda, \text{LAB}}(t) = \sum_{m=-2}^2 A_{2-m}^{\lambda, R} e^{im\omega_{Rt}} d_{-m0}^{(2)}(\beta_M) \quad (1.70)$$

$$= \sum_{m=-2}^2 \left[\sum_{m'=-2}^2 A_{2-m'}^{\lambda, C} \mathcal{D}_{-m'-m}^{(2)}(\Omega_{CR}) \right] e^{im\omega_{Rt}} d_{-m0}^{(2)}(\beta_M) \quad (1.71)$$

$$\begin{aligned}
 &= \sum_{m=-2}^2 \left[\sum_{m'=-2}^2 \left[\sum_{m''=-2}^2 A_{2-m''}^{\lambda, \text{PAS}} \mathcal{D}_{-m''-m'}^{(2)}(\Omega_{PC}) \right] \mathcal{D}_{-m'-m}^{(2)}(\Omega_{CR}) \right] \\
 &\quad \times e^{im\omega_{Rt}} d_{-m0}^{(2)}(\beta_M). \quad (1.72)
 \end{aligned}$$

The integral over the time t , as required by Eq. (1.69), can easily be carried out for each of the above equations. The full treatment involving all three independent transformations is only necessary if more than one interaction is to be considered, i.e. when relative orientations of different tensors are to be specified. Otherwise, one can transform directly from the PAS into the rotor frame, and one can start with Eq. (1.71) (with $\underline{\mathbf{A}}^{\lambda,C} = \underline{\mathbf{A}}^{\lambda,PAS}$) to evaluate the time dependence. For the case of the chemical-shift anisotropy, using the definitions from tensor algebra as presented above and in Appendix A, the time-dependent average Hamiltonian is then calculated to be

$$\bar{H}_{CS,MAS}(t) = (\omega_{iso}t + \Phi_{CS}(t)) \hat{I}_z \frac{1}{t}, \quad \text{where} \quad (1.73)$$

$$\begin{aligned} \Phi_{CS}(t) = & \frac{C_1}{\omega_R} \{ \sin(\gamma + \omega_R t) - \sin \gamma \} + \frac{C_2}{2\omega_R} \{ \sin(2\gamma + 2\omega_R t) - \sin 2\gamma \} \\ & - \frac{S_1}{\omega_R} \{ \cos(\gamma + \omega_R t) - \cos \gamma \} - \frac{S_2}{2\omega_R} \{ \cos(2\gamma + 2\omega_R t) - \cos 2\gamma \}, \end{aligned} \quad (1.74)$$

$$\text{and} \quad C_1 = -\frac{\delta_{CS}}{\sqrt{2}} \sin 2\beta \left(1 + \frac{\eta_{CS}}{3} \cos 2\alpha\right), \quad (1.75)$$

$$C_2 = \frac{\delta_{CS}}{2} \sin^2 \beta - \frac{\delta_{CS}\eta_{CS}}{6} (1 + \cos^2 \beta) \cos 2\alpha, \quad (1.76)$$

$$S_1 = \frac{\sqrt{2}\delta_{CS}\eta_{CS}}{3} \sin \beta \sin 2\alpha, \quad (1.77)$$

$$S_2 = \frac{\delta_{CS}\eta_{CS}}{3} \cos \beta \sin 2\alpha. \quad (1.78)$$

For first-order quadrupolar couplings, Eq. (1.74) can also be used, with the modified Hamiltonian $\hat{H}_{Q,MAS}(t) = \frac{3}{2}\Phi_Q(t) \sqrt{\frac{2}{3}}\hat{T}_{20} \frac{1}{t}$.

For the case of a single dipolar-coupled spin pair, the only non-vanishing tensor element is $A_{20}^{D_{ij},PAS} = -\sqrt{6}D_{ij} = \frac{\sqrt{6}}{2}\delta_D$ ($\eta_D = 0$), and we obtain a simpler expression:

$$\bar{H}_{D,MAS}^{ij}(t) = \frac{3}{2}\Phi_{D_{ij}}(t) 2\sqrt{\frac{2}{3}}\hat{T}_{20}^{(ij)} \frac{1}{t} \left(\stackrel{het.}{=} \Phi_{D_{ij}}(t) 2\hat{I}_z \hat{S}_z \frac{1}{t} \right), \quad \text{where} \quad (1.79)$$

$$\begin{aligned} \Phi_{D_{ij}}(t) = & \frac{D_{ij}}{\omega_R} \frac{1}{\sqrt{2}} \sin 2\beta \{ \sin(\gamma + \omega_R t) - \sin \gamma \} \\ & - \frac{D_{ij}}{\omega_R} \frac{1}{4} \sin^2 \beta \{ \sin(2\gamma + 2\omega_R t) - \sin 2\gamma \}. \end{aligned} \quad (1.80)$$

Compared to the chemical-shift case, a factor of $\frac{1}{2}$ has been absorbed into the integrated phase, $\Phi_{D_{ij}}(t)$, in order to have the Hamiltonians in a more convenient form.

The evolution of an initial state $\hat{\rho}(0) = \hat{I}_x$ is, therefore, of the general form

$$\hat{I}_x \xrightarrow{\hat{H}_{\lambda, MAS}(t)t} \hat{I}_x \cos \Phi_{\lambda} + \hat{W} \sin \Phi_{\lambda}, \quad \text{where} \quad (1.81)$$

$$\begin{aligned} \Phi_{csa} &= \omega_{isot} t + \Phi_{CS}, \quad \hat{W} = \hat{I}_y, \\ \Phi_{quad} &= \frac{3}{2} \Phi_Q, \quad \hat{W} = i(\hat{T}_{21} + \hat{T}_{2-1}), \\ \Phi_{dip, hom} &= \frac{3}{2} \Phi_{D_{ij}}, \quad \hat{I}_x = \hat{I}_x^{(i)} + \hat{I}_x^{(j)}, \quad \hat{W} = 2\hat{I}_y^{(i)} \hat{I}_z^{(j)} + 2\hat{I}_y^{(j)} \hat{I}_z^{(i)}, \\ \Phi_{dip, het} &= \Phi_{D_{ij}}, \quad \hat{W} = 2\hat{I}_y \hat{S}_z. \end{aligned}$$

The acquired phase angles, Φ_{λ} , are functions of time and also depend on the Euler angles, (α, β, γ) , transforming the interaction tensor from the PAS to the rotor frame. (α, β) are identical to the polar angles (ϕ, θ) of the rotor axis in the PAS, and the dependence on α enters only for non-axially symmetric interaction tensors. γ describes the *initial rotor phase*, as is obvious from Eqs. (1.74) and (1.80) because the time-dependence, ω_{Rt} , always appears relative to this angle.

When pulse sequences are to be calculated, the lower limit for the integration in Eq. (1.69), i.e. the initial rotor phase, needs to be different from zero in many cases. We define

$$\Phi_{\lambda}(t_1; t_2) = \Phi_{\lambda}(t_2) - \Phi_{\lambda}(t_1) \quad (1.82)$$

as the acquired MAS phase for an interaction λ , generalized for an arbitrary initial rotor phase, i.e. $\Phi_{\lambda}(t_1; t_2) \sim (t_2 - t_1)^{-1} \int_{t_1}^{t_2} A_{20}^{\lambda, LAB}(t) dt$.

The normalized time-domain signal in a one-pulse experiment,

$$\begin{aligned} S_{MAS}(t) &= \frac{\langle \text{Tr} \{ \hat{I}_+ \hat{\rho}(t) \} \rangle}{\text{Tr} \{ \hat{I}_+ \hat{\rho}(0) \}} \\ &\stackrel{dip, quad}{=} \langle \cos \Phi_{\lambda}(t) \rangle, \\ &\stackrel{csa}{=} \left\langle e^{-i\omega_{isot} t} e^{-i\Phi_{CS}(t)} \right\rangle, \end{aligned} \quad (1.83)$$

has a directly observable imaginary component only for evolution under the chemical shift. $\langle \dots \rangle = \frac{1}{8\pi^2} \int_0^{2\pi} \int_0^{\pi} \int_0^{2\pi} \dots d\alpha \sin\beta d\beta d\gamma$ denotes the powder average to be taken over a sphere covered by the polar angles (α, β) , and over the range of initial rotor phases, γ .

An interesting point not yet discussed is the way the time dependence due to the sample rotation enters the Hamiltonian. Eq. (1.70) suggests a way of rewriting the MAS Hamiltonian in terms of five Fourier components, $\omega_\lambda^{(m)} = A_{2-m}^{\lambda,R} d_{-m0}^{(2)}(\beta_M)$:

$$\hat{H}_{\lambda,MAS}(t) = \hat{T}_{20} \sum_{m=-2}^2 \omega_\lambda^{(m)} e^{im\omega_R t} \quad (1.84)$$

The time dependence thus enters as trigonometric functions of $\omega_R t$ and $2\omega_R t$, which is a direct consequence of the representation of interactions by *second*-rank tensors. This time-dependence is a mere *rotor modulation* of the Hamiltonian, and if the latter is to be manipulated by rf-pulses, these time-symmetry properties often provide an intuitive way to understand such manipulations.

1.4.2 Spinning-Sideband Patterns

From Eq. (1.84), it can directly be inferred that the time-domain signal for a single anisotropic interaction, as described by Eq. (1.83), is *periodic* with respect to the rotor period, $\tau_R = \frac{2\pi}{\omega_R}$. Moreover, the dependence of the signal on $\cos \Phi(\omega_R t, 2\omega_R t)$ ($+i \sin \Phi(\omega_R t, 2\omega_R t)$) leads to the appearance of spectral components which oscillate at integer multiples of ω_R . Upon Fourier transformation, spectra are obtained with signals appearing at $\pm n\omega_R$. In Fig. 1.3, powder-averaged solutions to Eq. (1.83) are depicted for a dipolar-coupled spin pair, and for a spin evolving under the influence of CSA. The frequency range of each spinning-sideband pattern is approximately equal to the span of the static tensors (upper traces), but the rotor modulation of the Hamiltonian can indeed create spectral intensity *outside* the static spectral range. In the course of this work we will see that it is even possible to carry out two-dimensional experiments where spinning-sidebands patterns covering *arbitrary* frequency ranges in the indirect dimension may be detected.

The sideband manifold in the time domain may be written as

$$S_{MAS}(t) = \left\langle \sum_{n=-\infty}^{\infty} \xi_n e^{in\omega_R t} \right\rangle = \sum_{n=-\infty}^{\infty} \bar{\xi}_n e^{in\omega_R t} \quad (1.85)$$

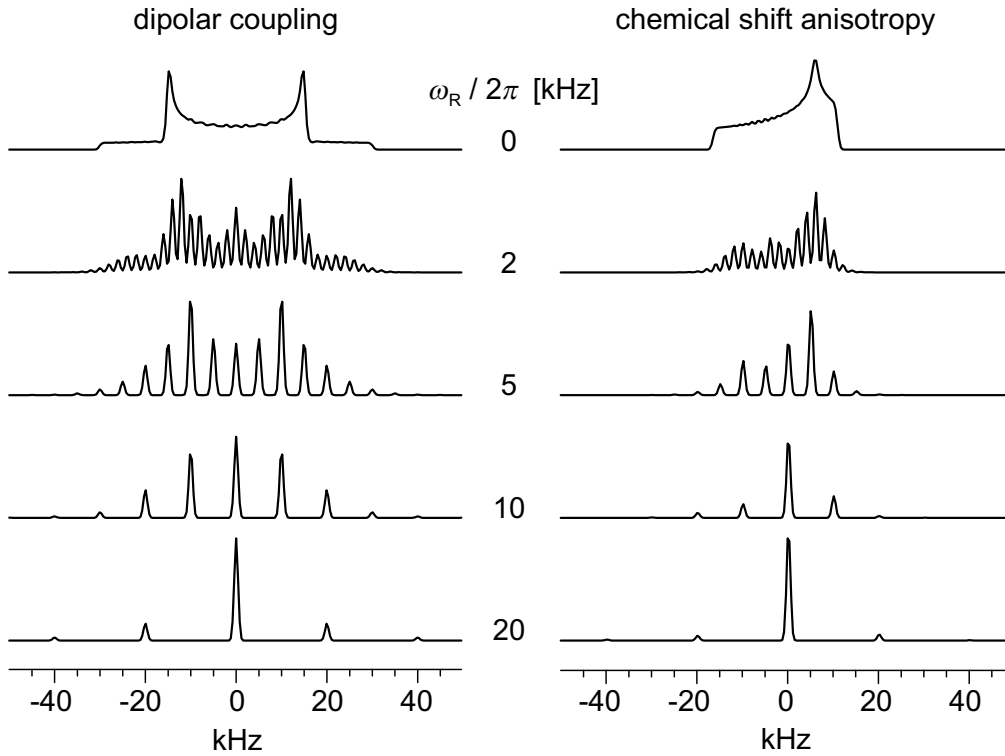


Figure 1.3: Simulated MAS spectra for a homonuclear dipolar spin pair ($D_{ij} = 20$ kHz) and a nucleus exhibiting chemical shift anisotropy ($\delta/2\pi = 20$ kHz, $\eta = 0.5$).

with the sideband intensities,

$$\bar{\xi}_n = \frac{1}{\tau_R} \left\langle \int_0^{\tau_R} S_{MAS}(t) e^{-in\omega_R t} dt \right\rangle, \quad (1.86)$$

to be determined by Fourier transformation. Using Eq. (1.83) for $S_{MAS}(t)$, it can be shown that the $\bar{\xi}_n$ can be written in terms of integrals of products of Bessel functions of different orders. Graphical representations of calculated intensity ratios $\bar{\xi}_{\pm n}/\bar{\xi}_0$ can be used to determine the tensor parameters δ and η from spinning-sideband patterns in MAS spectra, as was shown in the seminal paper of Herzfeld and Berger [Herzfeld 80].

The pure dipolar spectra presented in the left column of Fig. 1.3 are somewhat artificial, in that they can only be observed directly in solids with a highly isolated homonuclear spin pair. The usual situation encountered in ^1H spectra of solids is that the static spectrum is a broad, featureless line, which only starts to break up into spinning sidebands (of still appreciable linewidth) at spinning speeds above 5–10 kHz. The explanation for this behavior is that

the protons are part of a many-body coupling network, with multiple strong dipolar couplings present in the Hamiltonian. The treatment presented above was based on the existence of an average Hamiltonian, Eq. (1.69), with vanishing higher order terms in the Magnus expansion. For a spin system with multiple homonuclear couplings, $\hat{H}_{MAS}(t) = \sum_{ij} A_{20}^{Dij}(t) \hat{T}_{20}^{(ij)}$, the commutator $[\hat{H}_{MAS}(t), \hat{H}_{MAS}(t')]$ does not vanish any more, and higher order terms cannot be neglected. Such a system is said to behave *homogeneously* [Maricq 79].

For inhomogeneously evolving systems, $[\hat{H}_{MAS}(t), \hat{H}_{MAS}(t')] = 0$ leads to a time-domain signal that is periodic with respect to the sample rotation and, thus, to a set of infinitely sharp spinning sidebands (if relaxation is neglected). For a dipolar MAS Hamiltonian of a homonuclear multi-spin system, this condition is met only if the spatial dependence, $A_{20}^{Dij}(t)$, differs by a proportionality factor for different pairs (ij) . This is the case if all spins are positioned on a single line. In all other cases, the higher order terms have a non-negligible influence on the intensities and the linewidths of the spinning sidebands. In a recent paper [Filip 99], a rigorous analytical treatment of the time-domain signal of homogeneously evolving dipolar-coupled multi-spin systems under MAS, based on FLOQUET theory and perturbation expansions, was presented. Summarizing the essential results, it was found that the signal can be written as

$$S_{MAS}^{hom}(t) = \sum_n \langle I_n W_n(t) \rangle e^{in\omega_R t}, \quad (1.87)$$

where $W_n(t)$ is the “decay function” for the n^{th} sideband, describing its linewidth. $W_n(t)$ can be written in terms of a moment expansion [Vleck 48, Abragam 61], where the perturbation expansion for the second moment (which describes the largest contribution to the linewidth) depends on expectation values derived from *three-, four-, and higher spin correlations*, scaled by $1/\omega_R^2$, $1/\omega_R^4$, $1/\omega_R^6$, etc. For sufficiently high MAS speeds, higher-spin correlations are suppressed, leading to narrow spinning sidebands. In the limit of very fast MAS, the system is found to behave inhomogeneously again. The perturbation expansion for the relative sideband intensities can be ordered according to the number of spins, $i = 2 \dots N$, involved in the correlations:

$$I_n/I(0) = \delta_{n0} + \frac{2}{N} \sum_{i_2} [\xi_n(i_2) - \delta_{n0}] + \frac{1}{N} \sum_{i_3} f(i_3) + \frac{1}{N} \sum_{i_4} f(i_4) + \dots \quad (1.88)$$

The $f(i_m)$ are complicated functions, where expectation values due to spin correlations of order m , which are in turn functions of the geometry of the spin system, enter with increasing

powers of $1/\omega_R$. In particular, the leading terms are $\sim 1/\omega_R^{2(m-1)}$, which means that for fast spinning, these higher-spin correlations are suppressed. This leaves only the first two terms in Eq. (1.88), the second of which contains a sum over *all pair interactions*. The ξ_n are exactly the intensities for spinning sidebands in the spin-pair case, Eq. (1.85). Thus, the sideband intensities in a spectrum of a multi-spin system can be analyzed in terms of sums of sideband intensities from all possible pairs. It was shown that this approximation holds already for spinning speeds on the order of the strongest dipolar interaction in the system, i.e., for conditions where the spinning sidebands start to be well-separated [Schnell 99]. Since $\xi_n \sim \frac{D_{ij}^2}{\omega_R^2}$, Eq. (1.88) suggests the introduction of an *effective dipolar coupling constant*,

$$D_{eff} = \sqrt{\sum_{i<j} D_{ij}^2}, \quad (1.89)$$

which is experimentally accessible by fitting the fast-MAS sideband pattern of a multi-spin system with the analytical solution for a spin pair (Eq. (1.83)).

Finally, for the case of a heterospin, S, coupled to a multitude of I-spins, and neglecting homonuclear couplings among these, the time evolution of the S-spin is inhomogeneous, since the all heteronuclear dipolar couplings commute: $[2\hat{I}_z^{(i)}\hat{S}_z, 2\hat{I}_z^{(j)}\hat{S}_z] = 0$. This leads to a particularly simple theoretical description of heteronuclear MAS experiments, and the flavor of this advantage can be appreciated in the following chapters.

Chapter 2

Heteronuclear Correlation: REDOR and Multiple-Quantum Coherences

Reviewing the survey of theoretical tools presented in the last chapter can lead to a certain ambivalence about the utility of solid-state NMR techniques. On the one hand, anisotropic interactions are to be averaged in order to achieve well-resolved spectra, which is the prime requisite for spectral *selectivity*. On the other hand, interesting spectroscopic information is contained in these anisotropic interactions. In particular, the exploitation of the dipolar coupling, with its dependence on the internuclear distance, $D_{ij} \sim 1/r_{ij}^3$, and thus its use for structure determination in solids, is the major topic of this work.

The removal of the influence of dipolar couplings on spectra by magic-angle spinning, as discussed in the last sections, is the basis of the methods that will be presented. But how can one make use of an interaction which is averaged out in the course of the experiment? The answer to this question is one of the most fascinating aspects of time-domain NMR spectroscopy. It is the possibility to manipulate the spin-system response by two entirely different mechanisms: (i) Manipulation of the space part of the Hamiltonian (c.f. Eq. (1.41)), which is the basis of MAS, and (ii) manipulation of the spins by rf-irradiation. By applying suitable pulse schemes with timings synchronized to the sample rotation, it is indeed possible to re-introduce interactions selectively. This concept of *recoupling* may be applied to any of the internal NMR interactions. In our group, interest has focused on the development and application of techniques which recouple the homonuclear dipolar interaction, in particular

in ^{31}P and ^1H systems [Feike 96, Feike 98, Graf 96, Graf 98b, Schnell 98]. This has been done mostly within the framework of *multiple-quantum* (MQ) spectroscopy, where the well-localized character of MQ coherences provides the necessary selectivity for applications.

This thesis deals with the exploitation of *heteronuclear dipolar couplings*. Selective recoupling of this interaction can be achieved by very simple means, and a great body of work has been published on this topic. The REDOR (*rotational echo, double resonance*) technique has gained widespread popularity and certainly represents the most straightforward way to achieve the goal of heteronuclear recoupling. Nevertheless, the formal framework in which REDOR was originally presented, i.e. in terms of “dipolar dephasing”, is not particularly well-suited to the generality of the concept and its use as building block in more sophisticated experiments. In this chapter, the REDOR technique will be reviewed and explained more fully in the framework of MQ spectroscopy. We will see that, ultimately, most of the theoretical framework and methodology of homonuclear MQ techniques under recoupling conditions, namely the analysis of *MQ spinning-sideband patterns*, not only applies to the heteronuclear case but is even enriched by the possibility of independent manipulation of the different spin species.

2.1 Principles of REDOR

Although its principles are quite simple, REDOR is a surprisingly new technique. It was introduced by Gullion and Schaefer in 1989 [Gullion 89b, Gullion 89a]; for a recent review see [Gullion 97]. A variety of modifications exist, all of which are concerned with retrieving the important spectral information, i.e., the heteronuclear dipolar coupling. For this short review, we will describe the one way which has established itself as the approach used in most of the published applications: the application of a $\tau_R/2$ -spaced π -pulse train with fixed timings, and the concept of acquiring a “dephased” and a “reference” spectrum by inclusion or omission of (a) specific π -pulse(s).

The pulse sequence for the experiment is depicted in Fig. 2.1. REDOR is commonly applied for distance determination between two different kinds of low-gamma nuclei, at least one of which usually has to be isotopically enriched. Compounds with pairwise enrichment also may be used, and, in both cases, the enriched compound has to be diluted in a

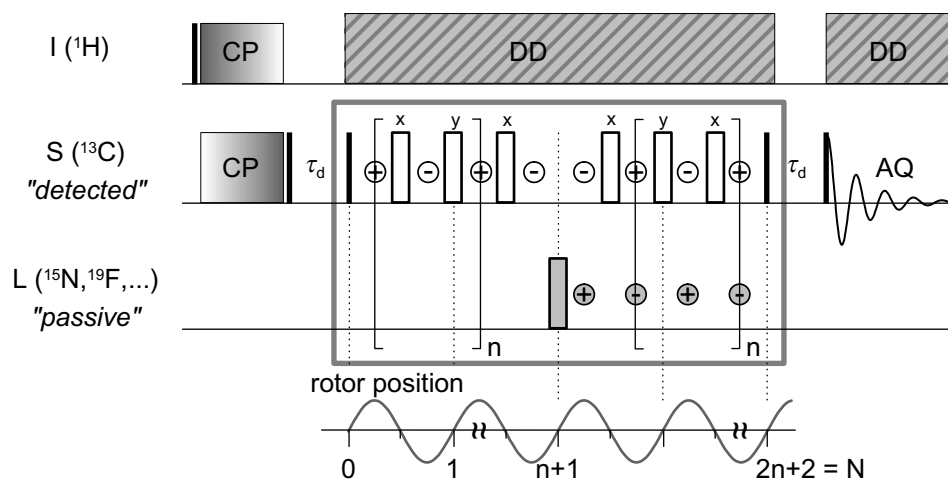


Figure 2.1: Pulse sequence for the REDOR experiment.

natural-abundance background in order to avoid perturbing influences by spins in neighboring molecules. Obviously, REDOR is really a triple-resonance method. In a CP step, initial proton magnetization is used to enhance the polarization of one of the heterospin species, usually termed the “observed” or “detected” spin. For the rest of the experiment, the protons have to be dipolar decoupled. The L-spin species, to which in the variant discussed here only one π -pulse is applied in the middle of the experiment, is called the “passive spin”. The two z-filters, with dephasing delays, τ_d , were not part of the original experiment but are commonly used throughout this thesis. They not only facilitate the design of phase cycles but also provide an efficient way of purging unwanted signal contributions. This is especially important in the two-dimensional applications presented below. The theoretical foundations of REDOR will be discussed only with respect to the building block in the large grey box of Fig. 2.1, for which a z-magnetization of the S-spins is taken as the initial and final state of the system.

2.1.1 Average REDOR Hamiltonian

For the time being, we will restrict the discussion of REDOR to the case of an isolated S-L spin pair, with spin operators $\hat{\mathbf{S}}$ and $\hat{\mathbf{L}}$. Cases of multiple couplings will be discussed in Chapters 3 and 4. The theoretical treatment will follow the sequence in Fig. 2.1, where the signs between the pulses indicate the sign of the dipolar interaction Hamiltonian. At first we will consider the dipolar evolution for the first full rotor period, with a π -pulse at the end of each half.

After an initial 90° -pulse on the S-spins, the resulting transverse magnetization (\hat{S}_y) evolves under the heteronuclear dipolar coupling under MAS, described in analogy to Eq. (1.81). If the free evolution period were an integer multiple of the rotor period, τ_R , there would be no net evolution, since $\Phi_{DSL}(\tau_R) = 0$. The application of properly spaced π -pulses, however, inverts the sign of the spin-part of the Hamiltonian after every second interval of length $\tau_R/2$, such that the evolution is effectively reversed for every other interval. This coincides with the rotor modulation of the Hamiltonian (in particular, with the Fourier component oscillating with ω_R , see Eqs. (1.79) and (1.84)). Obviously, intervals marked with a \oplus coincide with positive lobes of the sine-oscillation of the MAS, and vice versa, such that a non-zero integral $\int_0^t \hat{H}(t)_{MAS} dt$ remains after a full rotor period. In terms of product operator notation, we derive for the evolution over a full rotor period:

$$\hat{S}_y \xrightarrow{\Phi 2\hat{S}_z\hat{L}_z} \hat{S}_y \cos \Phi - 2\hat{S}_x\hat{L}_z \sin \Phi \quad (2.1)$$

$$\xrightarrow{\pi\hat{S}_x} -\hat{S}_y \cos \Phi - 2\hat{S}_x\hat{L}_z \sin \Phi \quad (2.2)$$

$$\xrightarrow{\Phi' 2\hat{S}_z\hat{L}_z} -\hat{S}_y (\cos \Phi \cos \Phi' + \sin \Phi \sin \Phi') - 2\hat{S}_x\hat{L}_z (\sin \Phi \cos \Phi' - \cos \Phi \sin \Phi') \\ \stackrel{(\Phi' = -\Phi)}{=} -\hat{S}_y \cos 2\Phi - 2\hat{S}_x\hat{L}_z \sin 2\Phi \quad (2.3)$$

$$\xrightarrow{\pi\hat{S}_x} \hat{S}_y \cos 2\Phi - 2\hat{S}_x\hat{L}_z \sin 2\Phi \quad (2.4)$$

For clarity, we have introduced the shorthand notations $\Phi = \Phi_{DSL}(0; \frac{1}{2}\tau_R)$ and $\Phi' = \Phi_{DSL}(\frac{1}{2}\tau_R; \tau_R)$, with $\Phi_{DSL}(t_1; t_2)$ being defined in Eq. (1.82), p. 34. The equality $\Phi' = -\Phi$ used in Eq. (2.3) corresponds to the effective inversion of the space part of the Hamiltonian by MAS. The second π -pulse in Eq. (2.4) was included in order to complete the full cycle of dipolar evolution under REDOR conditions. A comparison of Eq. (2.1) with Eq. (2.4) suggests the introduction of an average REDOR Hamiltonian,

$$\bar{H}_{SL} = \bar{\Phi} 2\hat{S}_z\hat{L}_z \frac{1}{\tau_R}, \text{ where} \quad (2.5)$$

$$\bar{\Phi} = 2\Phi = 2\Phi_{DSL}(0; \frac{1}{2}\tau_R) = \frac{-D_{SL}}{\omega_R} 2\sqrt{2} \sin 2\beta \sin \gamma \quad (2.6)$$

Formally, the average Hamiltonian is calculated by evaluating the propagator over the whole sequence, i.e. $(e^{i\pi\hat{S}_x} e^{i\Phi 2\hat{S}_z\hat{L}_z} e^{-i\pi\hat{S}_x}) e^{-i\Phi 2\hat{S}_z\hat{L}_z} = e^{-i\bar{H}_{SL}\tau_R}$. Here, the two π -pulses were chosen

to have opposite phase, in order to formally arrive at an inverted toggling frame Hamiltonian for the second evolution period (bracketed term).

In fact, neither the phase nor the channel where the π -pulses are applied has any influence on the average REDOR Hamiltonian. This can easily be proven by applying π -pulses of arbitrary phases in Eqs. (2.1)–(2.4). This freedom in the placement and choice of phase for these pulses enables one to implement π -pulse trains which are compensated for offsets, chemical-shift anisotropy, and pulse imperfections. In all experiments presented in this work, (xy-4) phase cycling has been used, i.e., the phases of the π -pulses alternate between x and y (see Fig. 2.1). Even though higher phase cycling schemes such as (xy-8) or (xy-16) exist [Gullion 90], we did not measure any substantial improvements for these sequences with longer cycle lengths. This may be due to the fact that the B_1 field strength we used in our probes was typically $\omega_1/2\pi = 125$ kHz, which corresponds to relatively short pulses of 4 μ s length. (xy-4) can conveniently be implemented in the loop structures of a pulse program, without the necessity of using different pulse programs for longer cycle times.

2.1.2 The Conventional REDOR Experiment

Using the average REDOR Hamiltonian, we obtain for initial \hat{S}_y -magnetization and a total evolution time of N rotor periods (including the π -pulse on the L-spins, marked grey in Fig. 2.1):

$$\hat{S}_y \xrightarrow{N\bar{\Phi}2\hat{S}_z\hat{L}_z} \hat{S}_y \cos N\bar{\Phi} - 2\hat{S}_x\hat{L}_z \sin N\bar{\Phi} \quad (2.7)$$

The final 90° -pulse stores the y-component along z, and the antiphase term is left to dephase. In the variant of the pulse sequence without the z-filter, \hat{S}_y is detected directly, and $2\hat{S}_x\hat{L}_z$ does not represent observable magnetization (nor would it evolve into such magnetization since the heteronuclear dipolar coupling is suppressed by MAS). The powder-averaged signal is thus

$$S_N/S_0 = \langle \cos N\bar{\Phi} \rangle, \quad (2.8)$$

which is called the “dephased signal”. This is the signal that is detected if the single L-spin π -pulse (grey pulse in Fig. 2.1) is applied. Only then does the average REDOR Hamiltonian

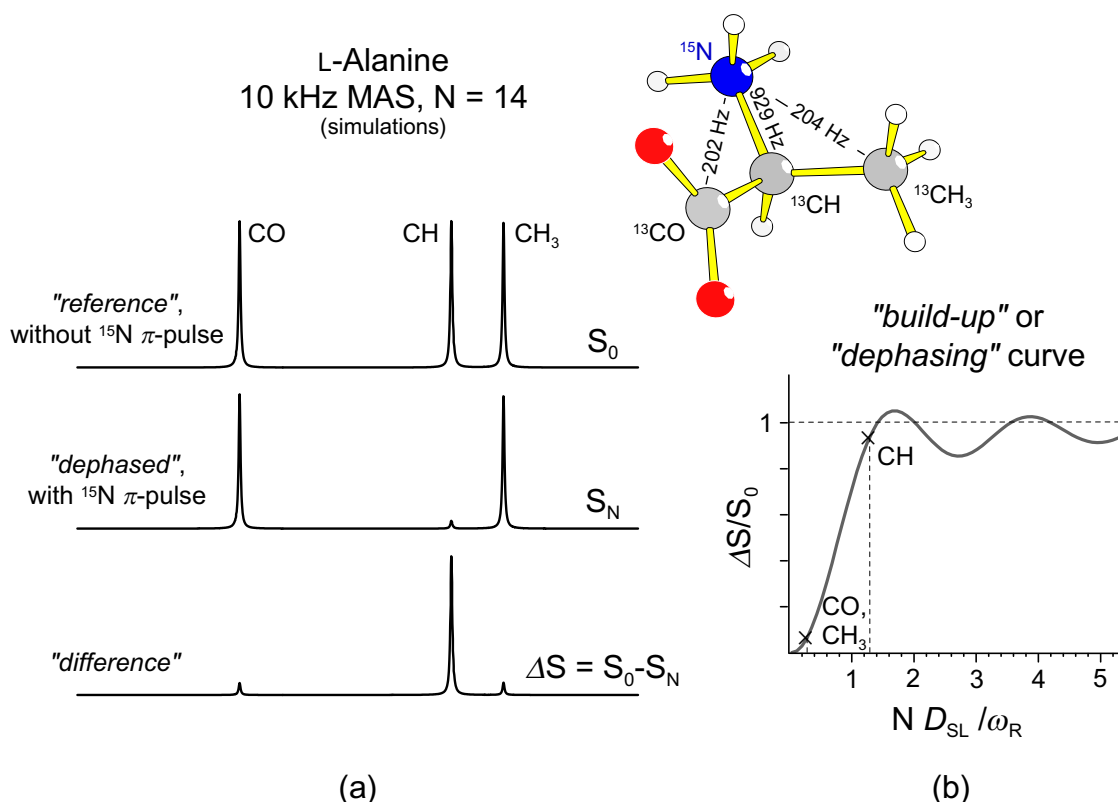


Figure 2.2: Simulated REDOR spectra, (a), based on the structural parameters of L-alanine. From the REDOR difference, (ΔS), and reference, (S_0), intensities, points on the universal dephasing curve for $\Delta S/S_0$, (b), can be obtained.

apply for the whole N cycles (grey \oplus and \ominus during the second $N/2$ cycles). Yet, \hat{S}_y usually suffers losses due to relaxation and imperfect π -pulses. The remedy is to acquire a “reference spectrum”, S_0 , where the central π -pulse on the L-spins is left out. Then, the dipolar interaction is completely refocused (as can easily be seen by following the \ominus and \oplus between the S-spin pulses), and the acquired signal is proportional to the integral S-spin signal, subject to pulse imperfections and relaxation losses, etc., but free of dipolar dephasing. Taking the ratio S_N/S_0 thus eliminates the adverse effects.

In particular, the complete refocusing also applies to the chemical shift anisotropy, the time dependence of which under MAS has essentially the same symmetry properties as the dipolar coupling (Eq. (1.73)). The CSA is also *recoupled* during a π -pulse train spaced by $\tau_R/2$, but shifting one pulse per rotor period, or just the central pulse of a whole REDOR train, to the other channel, removes its influence *completely*. Actually, in the original version

of REDOR, and in the applications presented in the following chapters, *all but the central* π -pulse are placed on the passive spin channel, since there, the pulses do not interfere with the evolution of transverse magnetization, viz., offsets. The placement of π -pulses presented here is of advantage when low rf-power and large offsets on the L-spin channel create excitation problems [Garbow 91] (see also Chapter 5).

It is customary to calculate a normalized “difference spectrum”, with intensities

$$\Delta S/S_0 = (S_0 - S_N)/S_0 = 1 - \langle \cos N\bar{\Phi} \rangle. \quad (2.9)$$

In Fig. 2.2, simulated REDOR dephased, reference, and difference spectra are depicted, which are calculated using Eqs. (2.8) and (2.9), and including the chemical shifts for the three carbons in L-alanine, with ^{13}C - ^{15}N couplings based on a neutron diffraction study [Lehmann 72]. From Fig. 2.8a, it is clear the the relative peak intensities of $\Delta S/S_0$ are a good measure for the relative distance of the three carbons to the ^{15}N atom. In 2.8b, a master curve for $\Delta S/S_0$ is depicted, with the position of the values from the simulated spectra indicated.

Clearly, the density of experimentally accessible points on such a master curve is determined by the ratio of D_{SL}/ω_r and thus by the upper limit for the rotor frequency. Nevertheless, theoretical master curves with sufficiently small point spacings can be calculated by scaling D_{SL} or ω_R . The results of various measurements of $\Delta S/S_0$ as a function of N can be fitted to such a theoretical curve, where values for any $\frac{\Delta S}{S_0}(ND_{SL}/\omega_R)$ can be obtained by interpolation. In principle, a single measurement of $\Delta S/S_0$, with a value $ND_{SL}/\omega_R < 1.68$, should be sufficient to determine the dipolar coupling, thus the internuclear distance (“one-shot experiment”). One serious restriction to this approach is that the reference measurement gives signals from *all* carbons in the sample, no matter whether they have a coupling partner or not. Thus, for a sample with incomplete labeling, this fraction has to be known, and S_0 has to be corrected accordingly. Also, the positions of the first local maxima and minima — if experimentally accessible — are a reliable measure for the dipolar coupling, when the absolute y-scaling is not known.

The universal dephasing curve in Fig. 2.2b, also termed the “build-up curve”, bears a striking resemblance to multiple-quantum build-up curves encountered in homonuclear MQ spectroscopy [Graf 98a, Schnell 99]. The measurement of MQ build-up behavior has for instance been the basis for a very recent confirmation of fundamental scaling laws in polymer

dynamics [Graf 98b]. In fact, there is more than just a formal resemblance between these kinds of experiments. In the following section, it will be shown that, for isolated spin pairs without CSA, the REDOR sequence is indeed the heteronuclear *equivalent* of the homonuclear recoupling sequence BABA (for *back-to-back*) [Feike 96].

2.2 REDOR as a Multiple-Quantum Technique

In order to motivate the interpretation of REDOR as a heteronuclear multiple-quantum technique, a new variant of the REDOR experiment is introduced. In Fig. 2.3, it is shown that by dividing the central π -pulse on the L-spins into two $\pi/2$ -pulses, the second of which is phase-switched relative to the first by 180° on alternate scans, alternating effective flip angles of 180° or 0° can be realized. If the receiver phase also alternates its sign in every other scan, intensities in the resulting spectrum will automatically be the REDOR difference intensities, ΔS . The sequence may be called “internal difference” REDOR.

This experiment was published by Sandström et al. [Sandström 99] and was used in ^{13}C - ^2H systems, where excitation problems for the quadrupolar nucleus ^2H are so severe that the number of pulses on the L-spin channel has to be minimized. Although there is no experimental advantage in using this sequence as opposed to conventional REDOR (the reference spectrum still has to be acquired in a separate experiment, which leads to an effectively longer total experiment time), it serves as the basis for a two-dimensional heteronuclear correlation experiment which will be discussed in Chapter 5. Here, the sequence just serves as a gedankenexperiment.

But where does the MQ aspect of the experiment manifest itself? A straightforward product-operator calculation, including the first “half” of the divided central π -pulse, reveals:

$$\hat{S}_y \xrightarrow{\frac{N}{2}\bar{\Phi} 2\hat{S}_z\hat{L}_z} \hat{S}_y \cos \frac{N}{2}\bar{\Phi} - 2\hat{S}_x\hat{L}_z \sin \frac{N}{2}\bar{\Phi} \quad (2.10)$$

$$\begin{aligned} &\xrightarrow{\frac{\pi}{2}\hat{L}_x} \hat{S}_y \cos \frac{N}{2}\bar{\Phi} + 2\hat{S}_x\hat{L}_y \sin \frac{N}{2}\bar{\Phi} \quad (2.11) \\ &= \hat{S}_y \cos \frac{N}{2}\bar{\Phi} + i \left(\underbrace{-\hat{S}_+\hat{L}_+ + \hat{S}_-\hat{L}_-}_{\text{DQ}} + \underbrace{\hat{S}_+\hat{L}_- - \hat{S}_-\hat{L}_+}_{\text{ZQ}} \right) \sin \frac{N}{2}\bar{\Phi} \end{aligned}$$

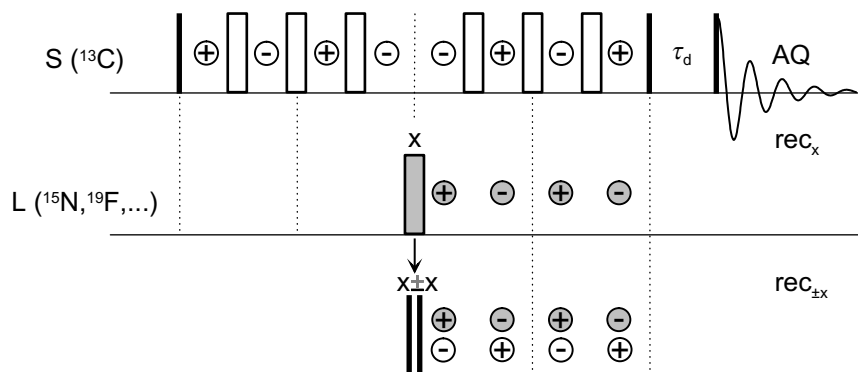


Figure 2.3: The idea of “internal difference” REDOR [Sandström 99].

The antiphase component $2\hat{S}_x\hat{L}_z$ is seen to be converted into a mixture of heteronuclear zero- (HZQ) and double-quantum (HDQ) coherence. $2\hat{S}_x\hat{L}_y$ is therefore referred to as *heteronuclear multiple-quantum* (HMQ) coherence, and for reasons given below, we will henceforth *not* distinguish between the two types of constituent coherences.

As is known from homonuclear multiple-quantum spectroscopy [Ernst 87], zero-quantum coherences evolve with *difference* of the chemical shifts of the spins involved, whereas double-quantum coherences evolve with the *sum* of the constituent chemical shifts. If interactions between multiple-quantum coherences and other spins are to be discussed, this effective chemical-shift evolution is important in that it may modulate such interactions. This can, for instance, be discussed in terms of second averaging (see also Section 1.3.2). As a consequence, *homonuclear* ZQ and DQ coherences behave differently, e.g., they differ in their relaxation times. The evolution of heteronuclear ZQ and DQ coherences also takes place as the difference or the sum, respectively, of the chemical shifts of the spins involved. For interactions between an HZQ or HDQ coherence and other spins, however, the picture changes entirely. The interaction picture (i.e. the secular approximation) demands a description of the I and S-spins in different rotating frames, thus interactions between each of these spins and some other spin (whether of type I or S) are *different*, and can be evaluated for each spin individually. There is no such thing as a second averaging applied to the MQ coherence as a single entity, because there are no interactions which are common to both constituent spins. As the ultimate consequence, within the secular approximation **heteronuclear zero- and double-quantum coherences are**, apart from their different precessional behavior, **equivalent**. Furthermore, the possibility of independently manipulating the involved spins

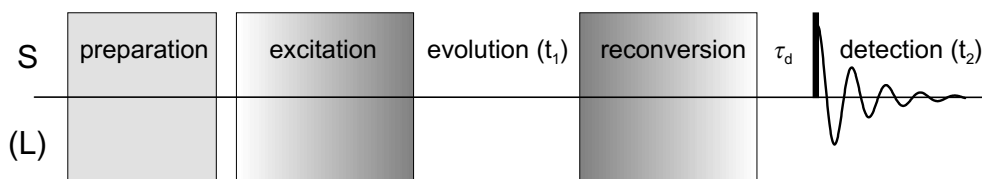


Figure 2.4: Basic structure of a multiple-quantum experiment.

means that the principles of coherence-order selection in MQ spectroscopy [Ernst 87] can be relaxed, giving way to more flexible methods, and, in particular, simpler phase cycles.

In fact, the phase cycle for the internal difference REDOR experiment can be regarded as a *multiple-quantum filter*. In order to appreciate that interpretation, we shall first review basic structure of a multiple-quantum experiment. In Fig. 2.4, the five stages of such an experiment are identified, with the possibility of including a second spin species already indicated. During the preparation period, the spin system is brought into the desired initial state. In many cases (for instance in ^1H MQ spectroscopy), this period could just correspond to doing nothing, i.e. starting with the \hat{S}_z -magnetization from thermal equilibrium. Alternatively, it could involve a CP step, if the S-spins have an inherently low polarization or some sort of presaturation. During the excitation period, a suitable pulse sequence for the excitation of MQ coherences is applied. Usually, an average Hamiltonian, \hat{H}_{exc} , can be used to describe the whole period. The resulting MQ coherence may then evolve during the t_1 -period of this inherently two-dimensional experiment. The MQ coherence is finally reconverted into longitudinal magnetization, and, after a possible z-filter of duration τ_d , a 90° read pulse is used to create detectable magnetization. The evolution of the MQ coherence is thus monitored as amplitude modulation of the final signal as a function of t_1 .

In order to obtain static MQ spectra with absorptive signals in t_1 , it was shown that the reconversion Hamiltonian has to be time-reversed with respect to the excitation, i.e. $\hat{H}_{rec} = -\hat{H}_{exc} \frac{\tau_{exc}}{\tau_{rec}}$ [Yen 83]. This can be achieved by applying the excitation pulse sequence a second time, but shifting its phase according to the quantum order to be selected (vide infra). Under MAS, such a time-reversal is automatically realized by the periodicity of the MAS Hamiltonian (“self time-reversal”, [Meier 86]), such that pure-phase reconversion is possible without altering the excitation sequence. The selection rules for the desired quantum order are based on Eq. (1.55). An MQ coherence of order m , involving L spins of spin $\frac{1}{2}$, can always be

written as a single tensor operator of rank L and order m , which transforms as

$$\hat{T}_{L\pm m} \xrightarrow{\phi_z} \hat{T}_{L\pm m} e^{\mp im\phi} \quad (2.12)$$

under a z-rotation. Such rotations can be realized by phase changes of the reconversion Hamiltonian relative to the excitation Hamiltonian. Thus, in order to achieve a sign change in the detected signal (phase change of 180°), the phases of all pulses in the reconversion (or excitation) sequence have to be shifted by $180^\circ/m$, if m is the desired quantum order. If pure $+m$ -quantum coherences are to be selected, with all lower quantum orders suppressed, a $2m$ -step phase cycle is needed, with the reconversion phase changing in steps of $180^\circ/m$, and an inverted receiver for every other scan. This MQ-filter procedure will also select some higher coherences of order $3m, 5m, 7m, \dots$. The proof is based on the Nyquist aliasing theorem from the theory of discrete Fourier transformations and can be found in the literature [Ernst 87, Munowitz 87a].

The above-mentioned ideas apply for any MQ experiment, homo- or heteronuclear. As long as a pulse sequence with a suitable Hamiltonian, \hat{H}_{exc} , is used, the phase-cycling rules apply. In the spirit of MQ spectroscopy, as presented above, we can identify the first half of the internal difference REDOR experiment (ending in the middle of the divided 180° -pulse, the first half of which we will henceforth call “conversion pulse”) as an MQ excitation period, and the second half (starting with a 90° “reconversion pulse” and ending with a “storage pulse”) with the reconversion period.¹ HMQ coherences may now be selected according to the above rules.

In the heteronuclear case, however, the situation is much more flexible since MQ selection can be performed *independently* for the different spin species. The phase cycle for the internal difference REDOR experiment is probably the simplest example: The inversion of the second “half” of the central π -pulse, along with an inversion of the receiver, is nothing but a *single-quantum* selection on the L-spins. Since S-spins are detected, these L-spin SQ contributions must have been part of an HMQ coherence. Selection of a specific quantum order on the S-spins is not necessary if the excitation Hamiltonian is not capable of exciting higher S-spin MQ coherences (which is true for the case of REDOR). It would not even be

¹The terminology is taken from solution-state HMQ spectroscopy, and will be explained more fully in Chapter 3.

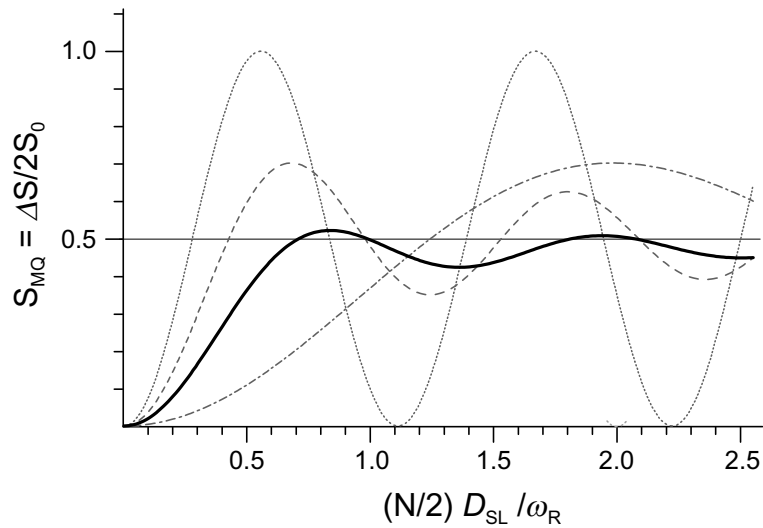


Figure 2.5: Powder-averaged REDOR-HMQ build-up master curve (thick line). The dashed and dot-dashed lines are γ -averages for single azimuthal angles $\beta = 45^\circ$ and 10° , respectively, and for the dotted line, a single orientation $\beta = 45^\circ$ with a single initial rotor phase, $\gamma = 90^\circ$, was used.

advisable to select pure HDQ (or HZQ) L-spin coherences, since in terms of the information they provide they are both equivalent, and the signal for each of these is only *half* of the full HMQ signal. In Chapter 4, it will be shown how even higher quantum orders on the L-spins, ^1H in particular, can be excited, selected, and detected on ^{13}C .

Finally, one can ask the question of how *efficiently* HMQ coherences can be excited. This has been of concern in the case of homonuclear MQ spectroscopy, where the build-up behavior can be very different for different excitation schemes [Graf 98a]. Continuing the product-operator treatment of Eqs. (2.10) and (2.11) and retaining only the MQ coherences (the \hat{S}_y -term is filtered out), we get

$$2\hat{S}_x\hat{L}_y \sin \frac{N}{2}\bar{\Phi} \xrightarrow{-\frac{\pi}{2}\hat{L}_x} -2\hat{S}_x\hat{L}_z \sin \frac{N}{2}\bar{\Phi} \quad (2.13)$$

$$\xrightarrow{-\frac{N}{2}\bar{\Phi} 2\hat{S}_z\hat{L}_z} -2\hat{S}_x\hat{L}_z \sin \frac{N}{2}\bar{\Phi} \cos \frac{N}{2}\bar{\Phi} + \hat{S}_y \sin \frac{N}{2}\bar{\Phi} \sin \frac{N}{2}\bar{\Phi}. \quad (2.14)$$

Note that the sign of the second dipolar evolution (Eq. (2.10) vs (2.14)) is inverted as a consequence of the fact that the average REDOR Hamiltonian assumes a π -pulse at the end

of the evolution over each rotor cycle, which is, however, not part of the pulse sequence for every last cycle in a π -pulse train. Only the last term represents observable signal:

$$S_{MQ} = \left\langle \sin \frac{N}{2} \bar{\Phi} \sin \frac{N}{2} \bar{\Phi} \right\rangle \quad (2.15)$$

$$= \frac{1}{2} - \frac{1}{2} \left\langle \cos N \bar{\Phi} \right\rangle \quad (2.16)$$

We see that this result differs from the conventional REDOR difference signal (Eq. (2.9)) by a factor of $\frac{1}{2}$. The representation of the MQ signal in terms of the product of two sine functions (Eq. (2.15)) is useful in that the arguments of the sines can be associated with the excitation and reconversion periods (each of duration $(N/2)\tau_R$) of a generalized MQ experiment, i.e., when a t_1 evolution period is inserted in the middle of the sequence. Then, the phases Φ need not be equal any more (see Section 2.2.2).

In Fig. 2.5, a powder-averaged build-up master curve is once again shown, along with two partial powder averages of Eq. (2.15), where a single internuclear orientation in the rotor frame, β , was used. These curves could in principle be measured for a single crystal rotating about the magic angle. The dotted curve, where the γ -average over the initial rotor phase was also skipped, shows that, in principle, a full MQ conversion could be achieved, and that the asymptotic value of $\frac{1}{2}$ is a mere consequence of destructive interference of contributions from different crystallites. The measurement of the latter curve would only be possible, however, if the rotor was triggered at the exact same rotor phase prior to each scan. Due to the loss of synchronization during long recycle delays, a γ -average is usually inherent to the experiment, and conversions exceeding 50% will not be observed. In contrast, in solution-state NMR, where free evolution under the isotropic J-coupling is used as a means to correlate different nuclei, transfer efficiencies of close to 100% are commonly realized.

We conclude by pointing out that the common normalization of REDOR data, i.e. $(S_N - S_0)/S_0$, is misleading, because the number of experiments conducted for $\Delta S = S_N - S_0$ is *twice* as large as for S_0 only. Displaying $(S_N - S_0)/2S_0$ is therefore a more sensible choice if the ordinate values are to be interpreted as MQ intensities.

2.2.1 Similarities between REDOR and Back-to-Back

The functional dependence of the MQ build-up signal for the REDOR experiment (Eqs. (2.6) and (2.15)) on N (with $\frac{N}{2}$ excitation and $\frac{N}{2}$ reconversion rotor cycles) is the same as for the homonuclear Back-to-Back (BABA) pulse sequence [Feike 96], with the exception of the familiar factor of $\frac{3}{2}$ distinguishing between homo- and heteronuclear dipolar couplings. In this section, it will be shown that BABA is indeed based on the same principles.

In Fig. 2.6, the two pulse sequences can be compared. The timing is the same in both cases, and the notable difference is that each π -pulse, responsible for the time-reversal of the heteronuclear dipolar evolution during the second half of each rotor period (cf. Eqs. (2.1)–(2.4)), is replaced in the homonuclear case by a pair of $\pi/2$ -pulses with orthogonal phases. The BABA sequence presented here consists of repeating the basic segment $(90_x - \tau_R/2 - 90_{-x}90_y - \tau_R/2 - 90_{-y})$. As in REDOR, it is possible to construct cycles of $2\tau_R$ or $4\tau_R$ length, which are partially compensated for effects of offsets and CSA. Since full CSA compensation would require refocusing over full rotor periods of evolution, BABA cannot completely compensate for CSA. The remainder of this discussion will be restricted to the uncompensated, $1\tau_R$ BABA cycle.

The hatched areas in Fig. 2.6 correspond to the interval over which the average dipolar Hamiltonian (acting on transverse magnetization) for a full rotor cycle is calculated. For BABA, the product operator treatment for this period reads:

$$\hat{I}_y^{(i)} + \hat{I}_y^{(j)} \xrightarrow{\frac{3}{2}\Phi \sqrt{\frac{2}{3}}\hat{I}_{20}} (\hat{I}_y^{(i)} + \hat{I}_y^{(j)}) \cos \frac{3}{2}\Phi - (2\hat{I}_x^{(i)}\hat{I}_z^{(j)} + 2\hat{I}_x^{(j)}\hat{I}_z^{(i)}) \sin \frac{3}{2}\Phi \quad (2.17)$$

$$\xrightarrow{-\frac{\pi}{2}\hat{I}_x + \frac{\pi}{2}\hat{I}_y} -(\hat{I}_x^{(i)} + \hat{I}_x^{(j)}) \cos \frac{3}{2}\Phi + (2\hat{I}_z^{(i)}\hat{I}_y^{(j)} + 2\hat{I}_z^{(j)}\hat{I}_y^{(i)}) \sin \frac{3}{2}\Phi \quad (2.18)$$

$$\xrightarrow{\frac{3}{2}\Phi' \sqrt{\frac{2}{3}}\hat{I}_{20}} -(\hat{I}_x^{(i)} + \hat{I}_x^{(j)}) (\cos \frac{3}{2}\Phi \cos \frac{3}{2}\Phi' + \sin \frac{3}{2}\Phi \sin \frac{3}{2}\Phi') \\ + (2\hat{I}_z^{(i)}\hat{I}_y^{(j)} + 2\hat{I}_z^{(j)}\hat{I}_y^{(i)}) (\sin \frac{3}{2}\Phi \cos \frac{3}{2}\Phi' - \cos \frac{3}{2}\Phi \sin \frac{3}{2}\Phi') \\ \stackrel{(\Phi' = -\Phi)}{=} -(\hat{I}_x^{(i)} + \hat{I}_x^{(j)}) \cos 3\Phi + (2\hat{I}_z^{(i)}\hat{I}_y^{(j)} + 2\hat{I}_z^{(j)}\hat{I}_y^{(i)}) \sin 3\Phi \quad (2.19)$$

$$\xrightarrow{-\frac{\pi}{2}\hat{I}_y + \frac{\pi}{2}\hat{I}_x} (\hat{I}_y^{(i)} + \hat{I}_y^{(j)}) \cos 3\Phi - (2\hat{I}_x^{(i)}\hat{I}_z^{(j)} + 2\hat{I}_x^{(j)}\hat{I}_z^{(i)}) \sin 3\Phi \quad (2.20)$$

This result can be compared to the corresponding calculation for REDOR, Eqs. (2.1)–(2.4), where Φ and Φ' have been defined. Obviously, the combination of the 90° -pulse pairs with

the inversion of the dipolar coupling due to the MAS during the second half rotor period of dipolar evolution also leads to an “effective” dipolar evolution, with an integrated phase of $2\frac{3}{2}\Phi$, thus demonstrating the similarities of both approaches. Yet, an important difference is that we cannot straightforwardly write down an average BABA Hamiltonian from the above equations, because the phases of the individual pulses do matter in this case. Using average Hamiltonian theory, the effective dipolar Hamiltonian corresponding to the hatched area in Fig. 2.6 can, however, straightforwardly be derived:

$$\begin{aligned}
 e^{-i\bar{H}_{II}\tau_R} &= \overbrace{e^{-i\frac{\pi}{2}\hat{I}_x} e^{+i\frac{\pi}{2}\hat{I}_y} e^{+i\frac{3}{2}\Phi\sqrt{\frac{2}{3}}\hat{T}_{20}} e^{-\frac{\pi}{2}\hat{I}_y} e^{+i\frac{\pi}{2}\hat{I}_x}} e^{-i\frac{3}{2}\Phi\sqrt{\frac{2}{3}}\hat{T}_{20}} \\
 \Rightarrow \bar{H}_{II} &= -\frac{3}{2}\bar{\Phi}(\hat{I}_z^{(i)}\hat{I}_z^{(j)} - \hat{I}_x^{(i)}\hat{I}_x^{(j)})\frac{1}{\tau_R}
 \end{aligned} \tag{2.21}$$

The braces indicate the two toggling frame transformations involved in the derivation. The effective dipolar Hamiltonian does not exhibit rotation symmetry around z (as opposed to the average dipolar REDOR Hamiltonian, Eq. (2.5)). Usually, the average Hamiltonian for BABA is calculated as the effective Hamiltonian acting on z-magnetization, i.e. including bracketing 90_x - and 90_{-x} -pulses. The very last bracketing pulse is not really a part of the pulse sequence. In Fig. 2.6 it is shown how this last bracketing pulse cancels with the last 90_x -pulse, which was used in the derivation of the effective dipolar Hamiltonian, to give the correct last BABA cycle, which ends with a 90_{-y} -pulse. For N rotor cycles, we obtain

$$\begin{aligned}
 e^{-i\bar{H}_{BABA}N\tau_R} &= e^{-i\frac{\pi}{2}\hat{I}_x} e^{-i\bar{H}_{II}N\tau_R} e^{+i\frac{\pi}{2}\hat{I}_x} \\
 \Rightarrow \bar{H}_{BABA} &= \frac{3}{2}\bar{\Phi}(\hat{T}_{22}^{(ij)} + \hat{T}_{2-2}^{(ij)})\frac{1}{\tau_R}
 \end{aligned} \tag{2.22}$$

The actions of this Hamiltonian on initial \hat{I}_z -magnetization can be derived from the commutator (1.55). The involved rotations occur within the subspace $(\hat{I}_z, -i(\hat{T}_{22}^{(ij)} - \hat{T}_{2-2}^{(ij)}), \hat{T}_{22}^{(ij)} + \hat{T}_{2-2}^{(ij)})$, which means that in a two-spin system, pure double-quantum coherence is created by the BABA sequence. In multi-spin systems, the above Hamiltonian also creates higher even quantum orders.²

²The Hamiltonian given here differs from one given in the literature [Graf 96] (which is incorrect) by a 90° -phase shift of the $(\omega_R t + \gamma)$ -dependence. The error might trace back to [Gottwald 95], where in Eq. (9) the evaluation of the integral over $\tau_R/2$ is not correct. The correct \bar{H}_{BABA} was given in [Sommer 95, Feike 96, Schnell 99], and in the paper of Feike et al. it is correctly noted that the average Hamiltonians of DRAMA and BABA are equal *except* for a 90° -phase shift in the γ -dependence.

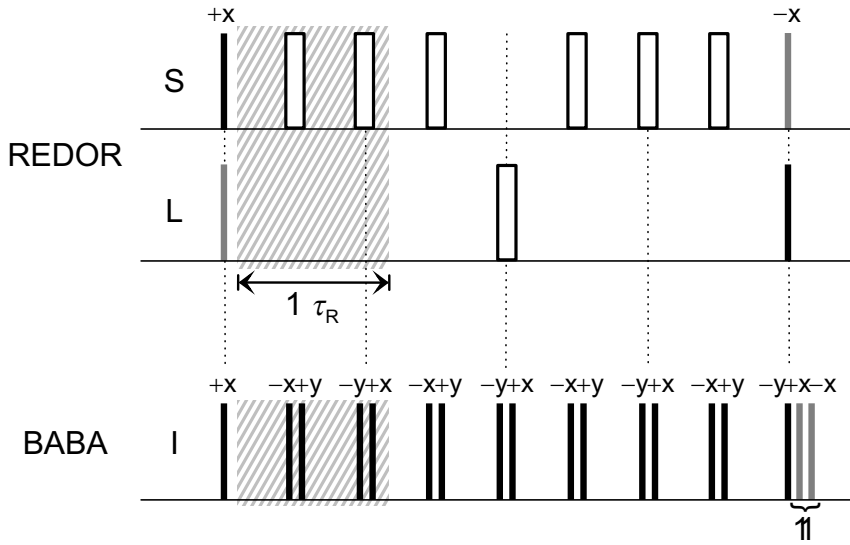


Figure 2.6: Comparison of the REDOR and BABA pulse sequences.

For REDOR, the average Hamiltonian for the bracketed dipolar evolution reads

$$\bar{H}_{REDOR,MQ} = \bar{\Phi} 2\hat{S}_y\hat{L}_y\frac{1}{\tau_R}, \quad (2.23)$$

where, for the sake of comparison, bracketing pulses were applied for both spin species. The evolution of initial \hat{S}_z -magnetization under this Hamiltonian occurs in the subspace $(\hat{S}_z, 2\hat{S}_x\hat{L}_y, 2\hat{S}_y\hat{L}_y)$, which shows once again that a mixture of HDQ and HZQ coherences $(2\hat{S}_x\hat{L}_y)$ is created, a result which has already been derived for the first “half” of the internal difference REDOR experiment (Eq. (2.11)). This result, even though it seems somewhat contradictory to the stated equivalence of the two experiments, is not surprising, since, as shown above, HDQ and HZQ are in some sense equivalent. Yet, it may be regarded as another corroboration of the increased flexibility of the heteronuclear approach. As is indicated in the top half of Fig. 2.6, two of the four bracketing pulses (the first L- and last S-pulse, marked grey) are immaterial for the creation of the MQ coherence from an initial state \hat{S}_z and can consequently be left out in the experiment. In the next chapter, it will be shown how this asymmetric building block can be used in both the “excitation” and “reconversion” parts of an experiment to transfer initial \hat{S}_z -magnetization to the other spin species.

Finally, it should be mentioned that heteronuclear MQ coherences can also be excited by synchronous application of the two-pulse segment [Saalwächter 99a] or of the BABA se-

quence [Sommer 95] on both channels, with MQ filtering based on the phase cycling principles outlined above. The two-pulse segment $90_x - \tau_R/2 - 90_{-x}$ can be used to create and reconvert MQ coherences in strongly coupled spin systems, where the restriction of the excitation time to the “quasi-static” limit of $\tau_R/2$ is still long enough to generate an appreciable amount of MQ coherence. Drawbacks are the lack of CSA compensation in the case of BABA, which hampered the observation of any HDQ signal in solids naturally abundant in ^{13}C for recoupling times $> 2\tau_R$, and the additional dephasing and loss of signal due to unavoidable recoupling of homonuclear MQ coherences in the same experiment. Also, half the the spectral intensity was lost, since HDQ as opposed to HMQ coherences have traditionally been selected. In [Saalwächter 99a], we have already pointed out that the synchronously applied two-pulse segment creates a variety of types of HMQ coherence stemming from initial magnetization of both channels, which in turn can be detected on either channel.

2.2.2 Rotor Encoding and Multiple-Quantum Spinning-Sideband Patterns

Up to this point, the demonstration of the existence of MQ coherences in the “middle” of the central π -pulse is completely academic. Nevertheless, following the basic idea of MQ spectroscopy, as depicted in Fig. 2.4, this aspect will become useful when a second indirect spectroscopic dimension, during which the evolution of these coherences may be probed, is introduced right after the end of the excitation period. Apart from the evolution of the MQ coherences with respect to chemical shifts and couplings to other spins, there is one more important aspect of MQ spectroscopy under MAS conditions, which is the appearance of unusual spinning-sideband patterns in the MQ dimension. These spinning-sideband patterns can cover a very large spectral width, and a characteristic feature of the patterns is the absence of sidebands of certain orders. Such patterns were first observed in homonuclear ^1H - ^1H DQ spectroscopy using the DRAMA (*dipolar recovery at the magic angle*) sequence [Geen 94], which was introduced by Tycko and coworkers [Tycko 90, Tycko 91] and is closely related to BABA [Graf 96].

The primary origin of these MQ spinning-sideband patterns was later found to be the way the t_1 dependence enters the reconversion Hamiltonian [Gottwald 95]. The experimental proof was based on the two-pulse segment for MQ excitation, but the principle applies equally well to the DRAMA [Geen 95] and BABA sequences since these are mere extensions of the

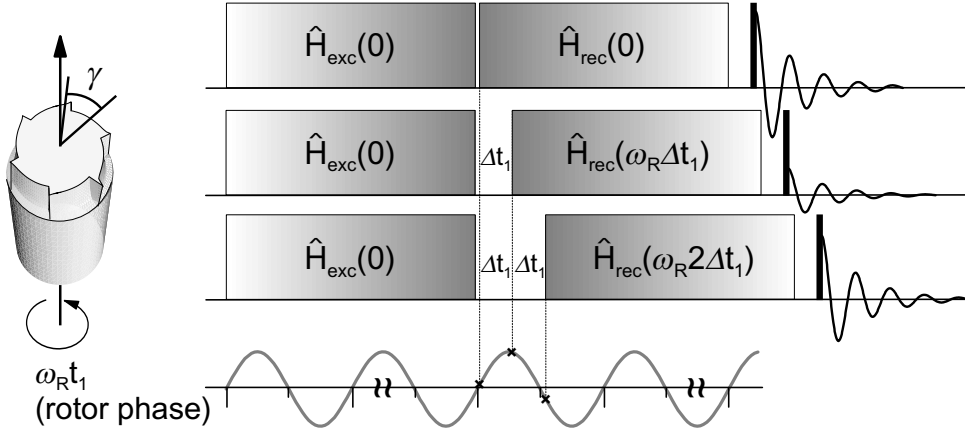


Figure 2.7: The principle of reconversion rotor encoding (RRE) in MQ MAS spectroscopy.

quasi-static excitation scheme and are based on the symmetry of the rotor modulation under MAS [Schnell 99]. Certainly, due to the equivalence pointed out in the last section, these ideas also pertain to REDOR-based heteronuclear MQ spectroscopy.

Neglecting any “real” evolution during t_1 , as is the case for on-resonance excitation (no chemical shift evolution and neglecting CSA) when the MQ coherence is a total spin coherence (TSC), i.e. the MQ coherence comprises all spins in a coupled subsystem, the t_1 -dependent signal for an SL-pair is given by Eq. (2.15),

$$S_{MQ}(t_1) = \langle \sin N_{exc} \bar{\Phi}_0 \sin N_{rec} \bar{\Phi}_{t_1} \rangle, \quad (2.24)$$

where the explicit t_1 -dependence of the average reconversion Hamiltonian, i.e. the limits for the integrated phase, must now be considered. We have introduced the possibility of choosing a different number recoupling rotor cycles for the excitation and reconversion periods, termed N_{exc} and N_{rec} ($= N/2$), respectively. Following the definition in Eq. (1.82), we obtain

$$\bar{\Phi}_{t_1} = 2\Phi_{DSL}(t_1; \tau_R/2 + t_1) = \frac{-D_{SL}}{\omega_R} 2\sqrt{2} \sin 2\beta \sin(\omega_R t_1 + \gamma). \quad (2.25)$$

Here, we see the intimate connection between the initial rotor phase, γ , and the change of phase effected by the sample rotation, $\omega_R t_1$. The reconversion Hamiltonian is therefore *encoded* by the rotation, and the t_1 -dependence thus introduced leads to an amplitude modulation of the

acquired signal. Upon Fourier transformation of the t_1 signal, spinning sidebands appear at integer multiples of the rotor frequency. This mechanism has been termed *reconversion rotor encoding* (RRE) [Friedrich 98a] and should be distinguished from modulations of MQ-coherences due to interactions with other spins in the system, when the MQ-coherence is not the TSC or when CSA-effects are non-negligible. This so-called *evolution rotor modulation* (ERM) leads to spinning sidebands as well, and is the more conventional sideband-generating mechanism, especially when the evolution of SQ-coherences is considered. ERM will also be a topic of discussion in the following chapters.

By inserting Eq. (2.25) into Eq. (2.24), and using the relation [Abramowitz 72]

$$\sin(x \sin(\omega_R t_1 + \gamma)) = 2 \sum_{n=0}^{\infty} J_{2n+1}(x) \sin((2n+1)\omega_R t_1 + (2n+1)\gamma), \quad (2.26)$$

it can be seen that the spinning-sideband patterns for an isolated SL-pair are symmetric and consist of *odd*-order sidebands only, due to the $(2n+1)$ -prefactor of $\omega_R t_1$. In the course of an explicit calculation, the powder-average over the γ -angle can be performed analytically [De Paul 00], and one is left with sideband intensities

$$I_{2n+1} = \frac{1}{2} \int_{\beta=0}^{\pi} J_{2n+1}(N_{exc} \frac{D_{SL}}{\omega_R} 2\sqrt{2} \sin 2\beta) J_{2n+1}(N_{rec} \frac{D_{SL}}{\omega_R} 2\sqrt{2} \sin 2\beta) \sin \beta d\beta. \quad (2.27)$$

This integral over a product of Bessel functions, $J_n(x)$, can be evaluated on a computer. For $N_{exc} = N_{rec}$ (equal arguments of the two Bessel functions), all sidebands are immediately proven to be positive.

In Fig. 2.8, spinning-sideband patterns are shown for various ratios $N_{rcpl} D_{SL} / \omega_R$. The higher-order ($n \geq 3$) sidebands start appearing only after the maximum of the build-up curve has been reached. Clearly, the sidebands do not map out the anisotropy of the dipolar interaction, as is common in SQ MAS spectra but can be “pumped” to cover arbitrary frequency ranges by increasing the excitation and reconversion times (henceforth also termed the recoupling time, for cases where $N_{exc} = N_{rec} (= N_{rcpl})$). Even though the dipolar coupling constant can be determined more accurately when more sidebands are present, the number of recoupling rotor cycles, N_{rcpl} , is limited because of increasing effects of T_2 relaxation and the

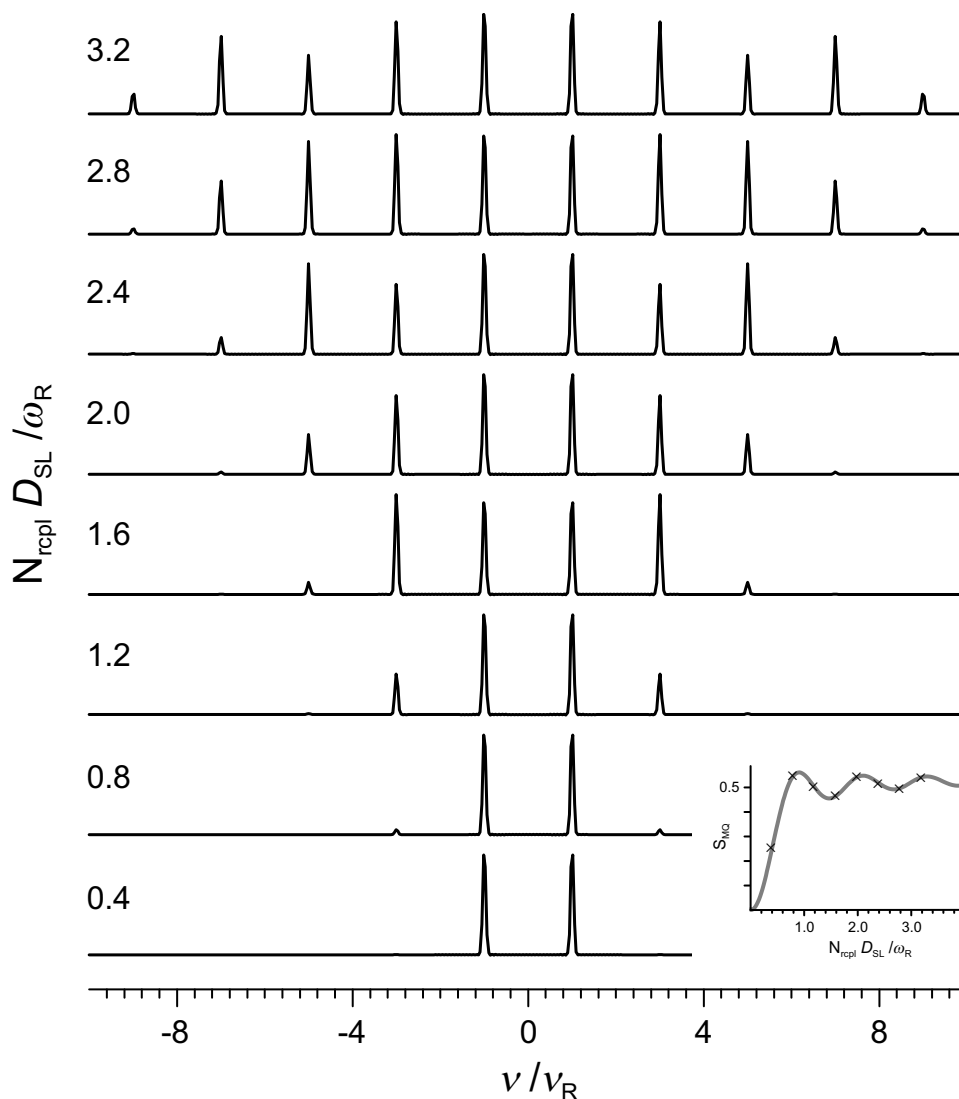


Figure 2.8: HMQ spinning sideband patterns, as obtained by Fourier transformation of the powder-averaged t_1 time-domain signal (Eq. (2.24)), as a function of the dimensionless parameter ND_{SL}/ω_R . The position of the specific values on the HMQ build-up master curve is indicated in the inset.

distribution of the same spectral intensity over more and more sidebands, which affects the signal-to-noise (S/N) ratio.

The explicit $(\gamma + \omega_R t_1)$ -dependence of the average MQ Hamiltonian, as obvious from the above equations, is the necessary prerequisite for the appearance of such spinning-sideband patterns. There are, however, classes of homonuclear MQ pulse sequences, commonly referred to as rotating-frame sequences, which do *not* exhibit this dependence and hence can-

not be used for spinning-sideband analysis. Examples of these are HORROR [Nielsen 94], MELODRAMA [Sun 95], and C7 [Lee 95], along with the higher-order compensated derivatives POST-C7 [Hohwy 98], CMRC7 [Rienstra 98], and SPC-5 [Hohwy 99].

The following two chapters are devoted to the application of REDOR-related recoupling in MQ spectroscopy of ^{13}C - ^1H systems, where the ^1H - ^1H dipolar coupling is the strongest interaction. It is shown that the application of simple REDOR recoupling is feasible if the perturbing homonuclear coupling can be significantly reduced by ultra-fast MAS. Multiple-quantum spinning-sideband patterns will be extensively used throughout this thesis, whenever dipolar couplings are to be determined. Moreover, it will become obvious that the rotor-encoding mechanism does not have anything inherently multiple-quantum about it; rotor encoding will prove to be a general principle applicable to all kinds of coherences.

Chapter 3

Recoupled Polarization-Transfer Methods

In this chapter, the application of the HMQ-REDOR concept to ^{13}C - ^1H correlation spectroscopy will be presented. Such heteronuclear correlation (HETCOR) techniques are of particular importance for the structure elucidation of organic compounds, and the accessing of proton chemical shift and dipolar coupling information is certainly one of the most important current challenges in solid-state NMR. The techniques presented here represent the natural extensions of the homonuclear ^1H MQ methodology, which has recently been developed and applied in our group.

Solid-state HETCOR experiments for high-resolution ^{13}C - ^1H correlation have been developed by various groups, the most recent of which [Rossum 97, Lesage 98a] are based on frequency-switched Lee-Goldburg (FSLG) homonuclear decoupling [Lee 65, Bielecki 89] in the ^1H or HMQ dimensions of MAS experiments at high spinning frequencies (up to 15 kHz). Earlier work was restricted to slower MAS (around 5 kHz), where multiple-pulse line narrowing techniques can be applied [Bielecki 91]. Even though multiple-pulse sequences can be used with faster spinning [Hafner 96, Schnell 98], these techniques are very demanding as to the technical equipment, and require elaborate spectrometer set-up procedures.

Recently, it has been shown that the development of MAS probeheads with spinning frequencies up to 35 kHz leads to a sufficient resolution enhancement in ^1H spectra without further line-narrowing necessary, and the relatively simple homonuclear BABA sequence proved easily applicable at such high spinning speeds. The theoretical foundations of fast MAS were already alluded to in Chapter 1, and repeating just the essential conclusion, strongly coupled

spin networks proved to be tractable within the *spin-pair approximation*. The heteronuclear applications presented here follow the same principles, i.e. analysis of the results in terms of isolated ^{13}C - ^1H pair couplings, and the application of relatively *simple* pulse sequences.

3.1 The REPT-HMQC Experiment

The pulse sequence presented in Fig. 3.1 is a straightforward extension of the building block in Fig. 2.6, used within the general framework of a multiple-quantum experiment. The sequence makes use of the improved flexibility of heteronuclear as compared to homonuclear MQ spectroscopy, in particular of the fact that the excitation and reconversion of HMQ coherence may be independent and that time-reversal is not a necessary prerequisite. It is *asymmetric* in that it uses initial proton magnetization for the generation of HMQ coherence, which is later transferred to the carbon channel. This important aspect is reflected in the name of this sequence and the whole class of experiments which stem from the basic idea, namely, *recoupled polarization-transfer* (REPT) methods, and here REPT-HMQC (*heteronuclear multiple-quantum correlation*) [Saalwächter 99b].

The obvious advantage is that no initial CP step is involved, which is usually not very efficient at ultra-fast MAS conditions. Even though this advantage is in part balanced by transverse (T_2) relaxation of ^1H during the excitation period, the experiment always proved more efficient than the symmetric variants with CP, which will be discussed in the next chapter. In order to avoid interference from directly excited ^{13}C signals, a saturation pulse train is applied to the S spin channel prior to the experiment. The scheme depicted here incorporates fully offset- and ^{13}C chemical shift anisotropy (CSA) compensated REDOR recoupling periods, the principles of which have been explained in the preceding chapter.

The sequence bears similarities to several known experiments, the “new” aspect only being its application to solid ^1H - ^{13}C systems. Similar, though symmetric, REDOR-based sequences were used by Hong and Griffin for investigations of (dilute and pairwise labeled) ^{13}C - ^{15}N systems [Hong 97, Hong 98]. It should be noted that the framework of the sequence, i.e. pulses 1–5 in Fig. 3.1, is one of the earliest *solution-state* HMQC experiments [Müller 79]. In this case, the HMQ coherence is created by evolution under the isotropic J-coupling, allowing for very high transfer efficiencies, with the REDOR π -pulse trains being simply replaced

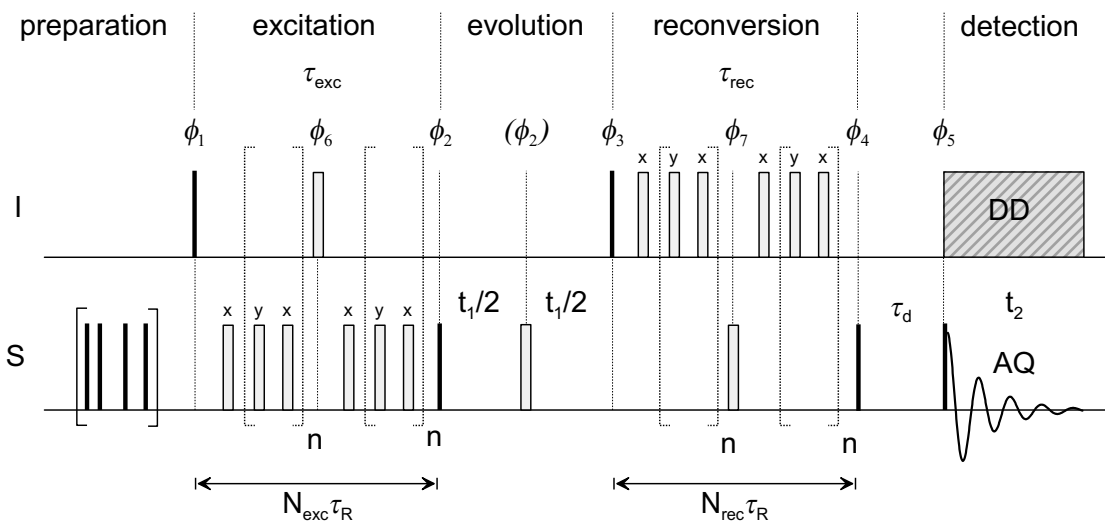


Figure 3.1: Pulse sequence for the two-dimensional REPT-HMQC experiment. The relative phases of the π -pulses in the trains are chosen according to the $(xy-4)$ scheme [Gullion 90] and are kept constant during the experiment. All other phases, ϕ_i , along with the experimental details, are listed in Appendix E.2. Setting $n = 0$ corresponds to a recoupling time of $2 \tau_R$. For just one rotor period of recoupling, the first π -pulse of each train and the corresponding delays are also omitted.

by free evolution intervals, the length of which are determined by J_{IS} . A recently published symmetric ^{13}C - ^1H HMQC experiment for solids under MAS [Lesage 98a] also utilizes the heteronuclear J-coupling, which is made observable by application of FSLG homodecoupling to the protons during the excitation and reconversion periods. The experiment was termed MAS-J-HMQC.

After the build-up of antiphase coherence, $2\hat{I}_x\hat{S}_z$, during a refocused excitation period in the solution-state case, or during a REDOR recoupling period in solids (in analogy to Eq. (2.10)), this coherence is converted into HMQ coherence, $2\hat{I}_x\hat{S}_x$, by a *conversion* pulse (ϕ_2). By virtue of the π -pulse in the middle of t_1 , the spectroscopic information is restricted to the chemical shift evolution of the I-spins. This is the point where the advantage of HMQ as opposed the homonuclear DQ or ZQ comes into play: The S-spin chemical shift can *independently* be refocused, and, consequently, there is no need to select either HDQ or HZQ. The *reconversion* pulse (ϕ_3) again creates antiphase coherence, but with switched identities of the constituent spins, $2\hat{I}_z\hat{S}_x$, which evolves back into observable SQ coherence, \hat{S}_y . The storage pulse, ϕ_4 , and the read-pulse, ϕ_5 , after the z-filter of duration τ_d , are not part of the solution-state experiment and may be left out, but usually, cleaner spectra are obtained when this part

of the pulse sequence is included.

By virtue of very-fast MAS, the dipolar interactions even in strongly coupled proton networks in solids, become localized and behave as an ensemble of pairwise coupled spins, such that these solution-state concepts are applicable. The key difference between the two approaches, however, is the rotor encoding due to the MAS. This concept was introduced in the last chapter for a modified REDOR pulse sequence (which corresponds to a symmetric HMQC experiment), and Eq. (2.24) can be used to describe the REPT-HMQC experiment also. For a single IS-pair, the theoretical treatment of the symmetric and asymmetric HMQC experiments is largely identical. For the time being, only the isotropic chemical shift evolution of the I-spins is additionally considered by introducing cosine and sine phase factors which are functions of $\omega_{CS,I}t_1$ and modulate the x- and y-components of the signal, respectively. Proton CSA is usually small and will be neglected throughout this thesis. The two components of the S-detected signal for an isolated IS-pair thus read [Saalwächter 99b]

$$S_x(t_1) = \langle \sin N_{exc} \bar{\Phi}_0 \sin N_{rec} \bar{\Phi}_{t_1} \cos \omega_{CS,I} t_1 \rangle, \quad (3.1)$$

$$S_y(t_1) = \langle \sin N_{exc} \bar{\Phi}_0 \sin N_{rec} \bar{\Phi}_{t_1} \sin \omega_{CS,I} t_1 \rangle, \quad (3.2)$$

where the possibility of choosing different recoupling times for the excitation and reconversion periods ($N_{exc} \neq N_{rec}$) has been included. These equations form the basis of a two-dimensional experiment, which can be performed in two ways: (i) Since the integrated dipolar phase $\bar{\Phi}_{t_1}$ (Eq. (2.25)) is periodic with respect to one rotor period, $\tau_R = 2\pi/\omega_R$, it is obvious from the above equations that incrementing t_1 in steps of full rotor cycles (“rotor-synchronized” experiment) leaves only the modulation of the t_1 signal with respect to the isotropic chemical shift $\omega_{CS,I}$ of the I spins. Thus a HETCOR spectrum is recorded, in which the intensity of the cross peaks is determined by the heteronuclear dipolar coupling and the number of recoupling cycles N_{rcpl} . The first slice of the 2D data set after one Fourier transformation for $t_1 = 0$ represents an HMQ-filtered S-spin spectrum. (ii) Incrementing t_1 in smaller steps gives a full MQ spinning sideband pattern in the t_1 dimension, as discussed in Section 2.2.2. From these spinning sidebands, the dipolar coupling constant can be derived. In the case of very weak couplings and low values of N , only first order sidebands are visible, and the build-up of MQ intensity can be studied by increasing the recoupling time.

The capabilities of the technique should first be demonstrated by showing measurements of crystalline L-tyrosine hydrochloride salt on different spectrometers with proton resonance

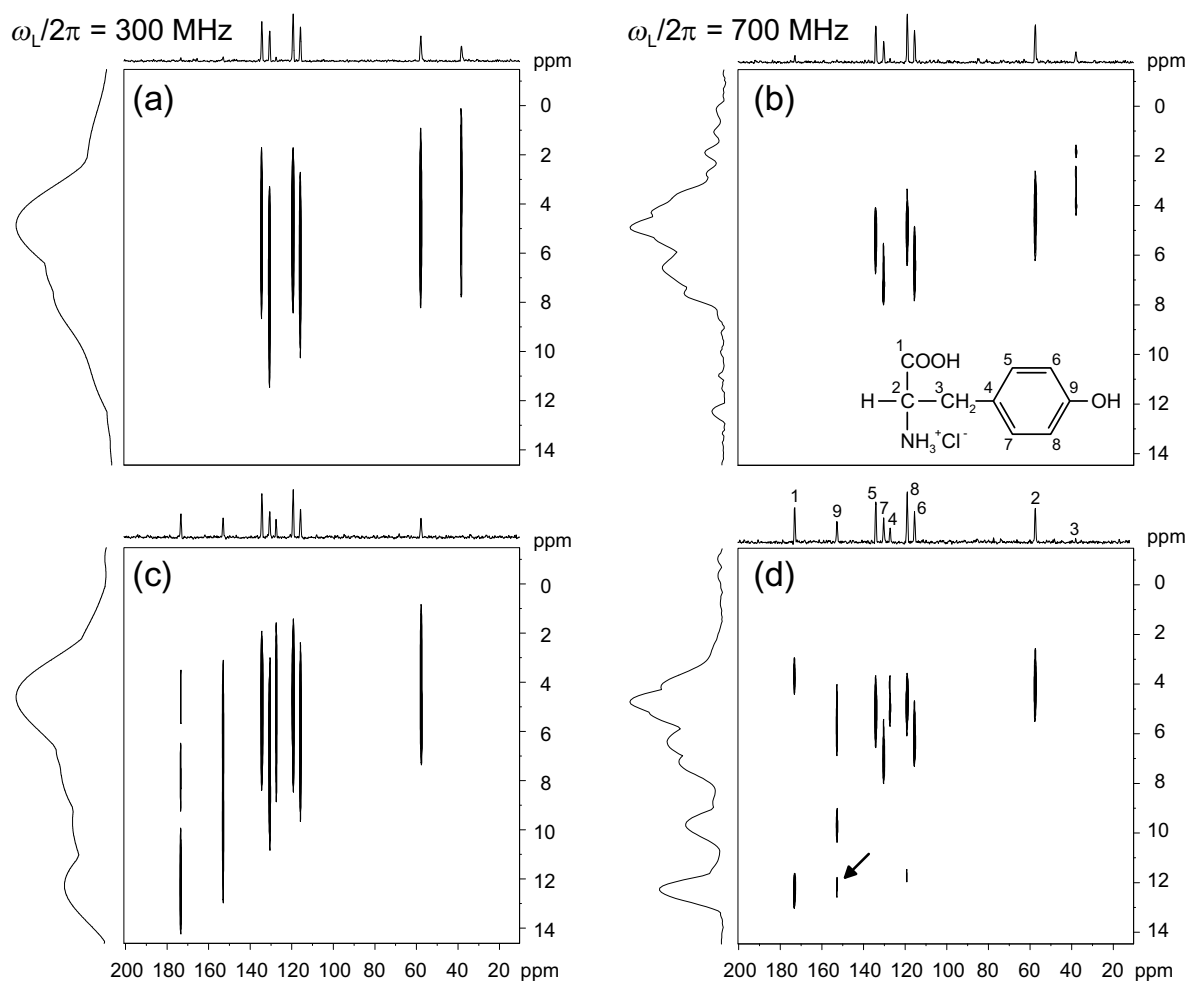


Figure 3.2: REPT-HMQC spectra of natural-abundance L-tyrosine·HCl at 30 kHz MAS and magnetic field strengths corresponding to proton Larmor frequencies of 300 MHz (a,c) and 700 MHz (b,d), rotor-synchronized in t_1 . The MQ recoupling times were $1 \tau_R$ for spectra (a) and (b), and $2 \tau_R$ for spectra (c) and (d). For each spectrum, skyline projections along both the MQ (1H) and the ^{13}C dimensions are shown. The ^{13}C spectral assignments, denoted in (d), are according to Lesage et al. [Lesage 98a]. The acquisition time for 32 slices in t_1 with 512 transients each was approx. 5 hours.

frequencies of 300 and 700 MHz. In Fig. 3.2, spectra recorded with $\tau_{rcpl} = 1 \tau_R$ and $\tau_{rcpl} = 2 \tau_R$ at 30 kHz MAS are compared for the two different magnetic field strengths. Clearly, the resolution in the proton (MQ) dimension is significantly increased at the higher magnetic field. The effect of higher magnetic fields on the proton resolution has been observed before in CP/WISE heteronuclear correlation spectra of L-tyrosine·HCl [Rossum 96] and has been explained by both the larger chemical shift frequency dispersion of protons in higher field, as well as the more effective truncation of the strong dipolar couplings among the protons by the increased Zeeman interaction. Proton linewidths on the order of 1 ppm for abundant ^1H systems have only been observed before at high spinning frequencies (about 15 kHz) in the HETCOR experiments mentioned above, which use elaborate line narrowing techniques in the proton dimension. It should be emphasized that all these techniques are very sensitive to effects of B_1 inhomogeneity and are strongly dependent on very precise settings of pulse durations and phases, and on an exact rotor synchronization. The REPT-HMQC sequence in turn is rather robust, requiring no elaborate setup of the spectrometer or exact matching conditions, and only the approximate pulse lengths on both channels have to be determined.

The assignment of proton and carbon signals in L-tyrosine·HCl has also been discussed before in great detail [Rossum 97, Lesage 98a]. The correlations visible for $1 \tau_R$ recoupling time (Fig. 3.2b)) are one-bond correlations only, the information content compares well to that obtained from MAS-J-HMQC spectra. For $2 \tau_R$ recoupling time, couplings of protons to quaternary carbons become visible. This is similar to the situation in the FSLG-decoupled CP/WISE spectra, where even at short CP contact times of 100 μs these correlations are already visible. Here, visible correlations correspond to localized 2-spin modes, with perturbing effects like spin diffusion being excluded. Hence, each cross peak corresponds to a well-defined dipolar-coupled ^1H - ^{13}C pair. As in the CP/WISE correlation spectra, even intermolecular couplings (e.g. the one of C_9 to the COOH-proton, located at 2.52 Å away, see arrow in spectrum (d)) can be identified. An alternative explanation of these long-range cross peaks in terms of relayed coherence transfer is unlikely for a sample at natural abundance and, in particular, when the substantial reduction of the homonuclear dipolar couplings by the very fast MAS is considered. Homonuclear spin flip-flops among the protons would be the only processes which could hold responsible for such a relayed transfer in the experiment considered here. These issues will be addressed in more detail in the next chapter, where symmetric variants of the experiment are presented.

A very interesting feature visible in such highly resolved HETCOR spectra of L-tyrosine has not yet been discussed: The chemical shifts of the protons associated with C₅ and C₇ (and with C₆ and C₈ alike) differ by about 2 ppm, although as to their magnetic properties both positions should be equivalent on a molecular level, which is indeed confirmed by solution-state NMR. Clearly, a packing effect is observed here. We attribute the significant up-field shift on the proton at C₅ (and C₈) to the influence of the phenyl ring current in adjacent molecules in the crystal. A pictorial representation of the relative position of the molecules is presented in Appendix D.2. Just recently in our group, similar effects have been observed in substituted hexabenzocoronene samples, disc-shaped molecules which are known to form columnar stacks in the solid phase [Brown 99]. To our knowledge, such effects have not been reported before to be present in solid-state ¹H NMR spectra. In the solution state, however, such effects have long been known; they were for instance observed in cyclophanes, which have aliphatic chains fixed above the aromatic plane of benzene rings.

A limitation of the technique is obvious from the disappearance of the methylene (C₃) signal at longer recoupling times (Fig. 3.2, spectra (c) and (d)). This is the consequence of an effect common to all MQ methods, namely the relaxation (i.e. dephasing) of the MQ coherences during the excitation and reconversion intervals. It is here due to the influence of the other proton of the CH₂-group on the CH 2-spin coherence. These effects will be discussed in Section 3.3.

Fig. 3.3 shows REPT-HMQC spectra, recorded on the DSX 300 spectrometer, also using naturally abundant L-tyrosine·HCl; the basic difference to the spectra (a) and (c) in Fig. 3.2 only being that the t₁ increment is not set to a full rotor period but rather to a small value, such that the full spinning sideband patterns are recorded. Spectrum (a), which was acquired with 1 τ_R recoupling time, is dominated by first-order spinning sidebands, the most intense signals being those due to the carbons directly bound to protons. In (b), the extracted MQ spinning sideband pattern for the methylene group is shown. Here, strong centerband and even order sideband intensity is observed, which cannot be explained from theory considering only a simple spin pair (Eqs. (3.1) and (3.2)). As alluded to above, the methylene group is in some way a "pathological" case, in the sense that the strong perturbations (homo- and heteronuclear) imposed by the second proton lead to a considerable dephasing of the heteronuclear 2-spin mode during excitation and reconversion after only 2 τ_R. This is clearly demonstrated by the numerical simulations of the methylene group signals for 1 and 2 τ_R, thus explaining the

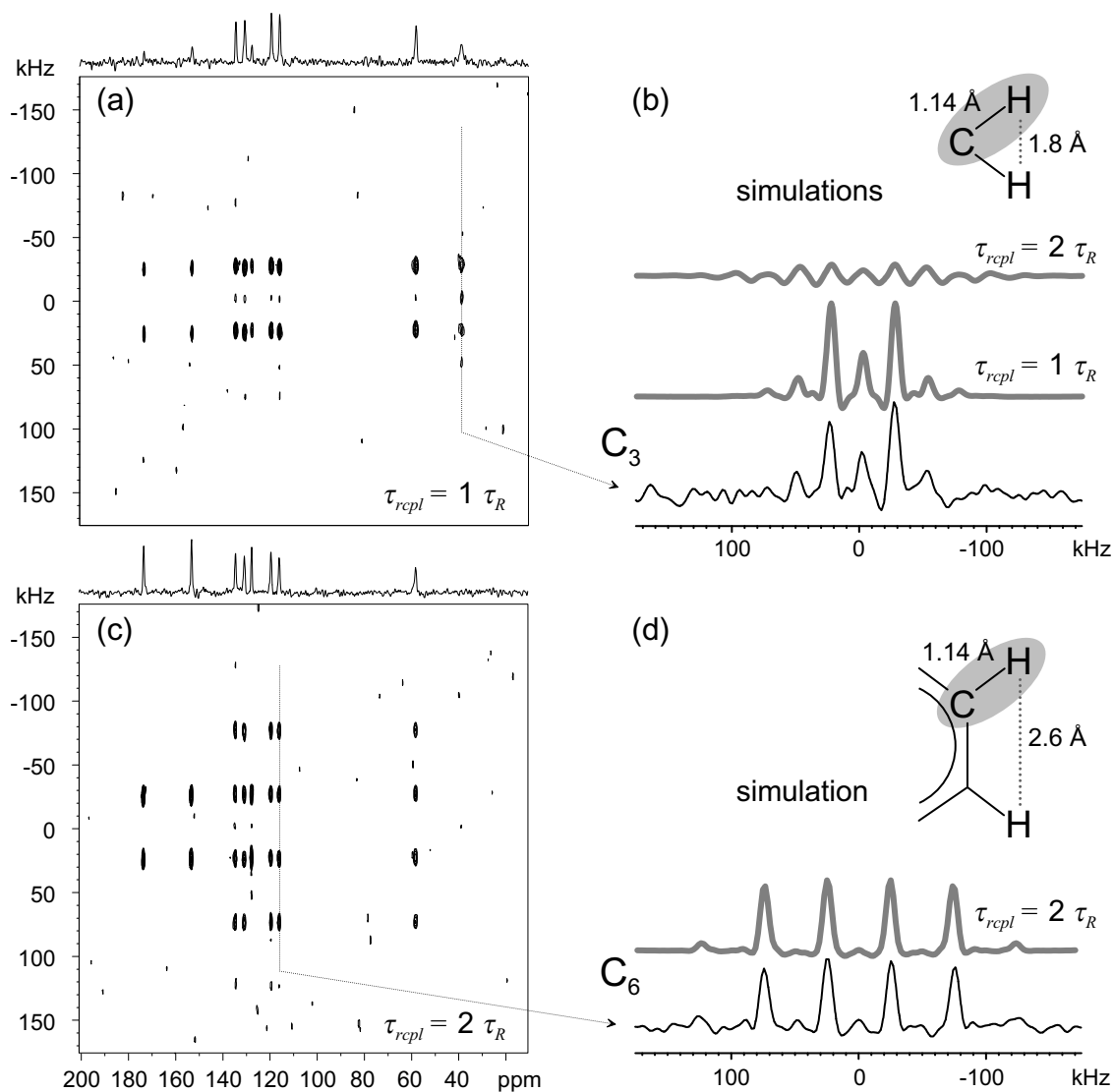


Figure 3.3: REPT-HMQC spectra of L-tyrosine-HCl at 25 kHz MAS and a proton frequency of 300 MHz. MQ recoupling times were $1 \tau_R$ for spectrum (a) and $2 \tau_R$ for spectrum (c), the t_1 increment was $1 \mu\text{s}$. The projections shown on top are HMQ-filtered spectra. The spectra shown in (b) and (d) represent sum projections along the direct dimensions of the methylene and the aromatic C_6 carbon signals, respectively, along with numerical density matrix simulations (grey traces) for the depicted three-spin subsystems, which take finite pulse length effects into account. These are merely responsible for the weak phase errors in the sideband spectra.

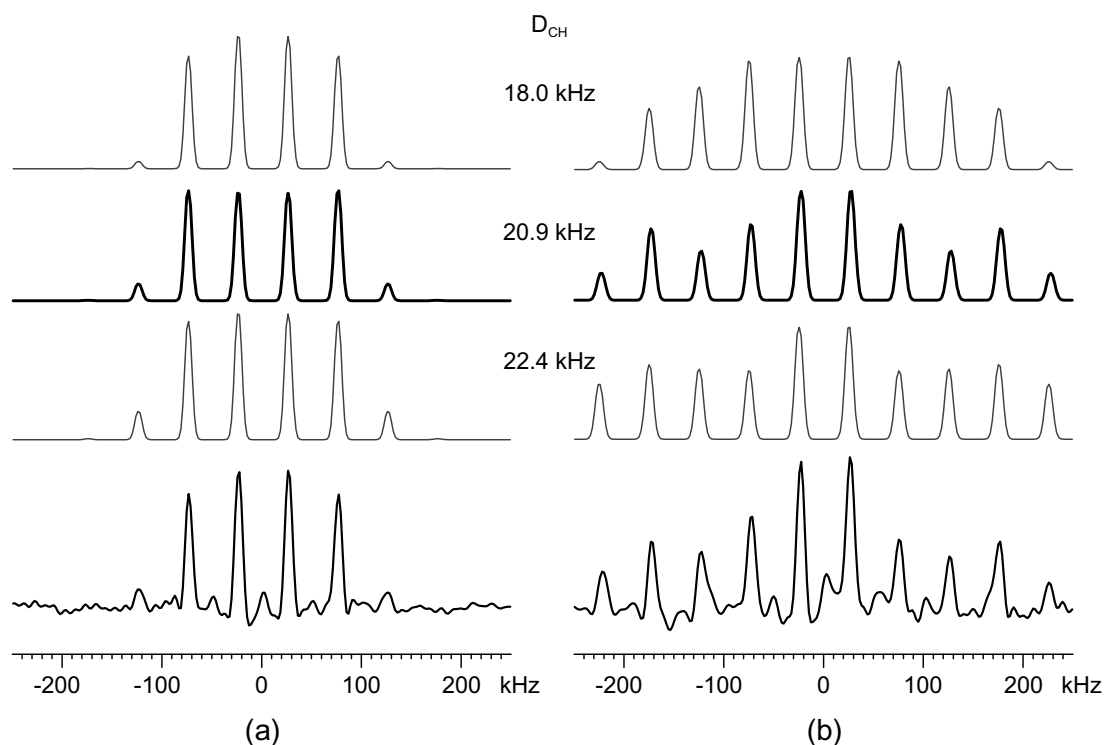


Figure 3.4: REPT-HMQ spinning sideband patterns for the aromatic CH groups in L-tyrosine·HCl, measured at 25 kHz MAS with recoupling times $2\tau_R$ (a) and $4\tau_R$ (b). The experimental spectra (lower traces) are summed over the sideband patterns of the 4 individual C-H groups, and are compared with the best-fit analytical spectra ($D_{CH} = 20.9$ kHz) as well as simulations for $D_{CH} = 18.0$ kHz and 22.4 kHz.

disappearance of the methylene signal in spectrum (c). This effect can, however, be put to good use for spectral editing applications (see Section 3.3.1).

As can be inferred from the contour plot in Fig. 3.3c, the spinning-sideband patterns of the CH moieties in the molecule look alike, because the CH bond lengths are similar for all CH groups. As an example, spectrum (d) in Fig. 3.3 shows the pattern for the aromatic C_6 carbon, along with a numerical simulation taking the closest remote proton into account. The origin of the weak centerband and even order sidebands will be discussed later (Sections 3.2.1 and 3.3). It should be noted that the intensities of the odd order sidebands are reliable, such that an interpretation of the pattern using the expressions for a spin pair is possible. Slight phase distortions in the spectra are in part due to finite pulse lengths, which have been taken into account in the simulations.

A solution of the powder-averages in Eqs. (3.1) and (3.2), with subsequent Fourier transformation, can be implemented in a C++-program using the Levenberg-Marquart algorithm from *Numerical Recipes* [Press 91] to fit the experimental spinning-sideband patterns in order to obtain the dipolar coupling constant, D_{IS} . For improved S/N, the signals from all 4 aromatic CH moieties have been summed for the experimental spectra in Fig. 3.4, where data from the spectrum in Fig. 3.3c and from another experiment with $\tau_{rcpl} = 4 \tau_R$ is shown. The best-fit spectra (thick traces) have been obtained by *excluding* the first-order sidebands from the fit. As will be shown in Section 3.3, their intensities tend to be slightly increased due to contributions of couplings to remote protons.

The best-fit dipolar coupling constants, $D_{IS} = 20.8$ kHz ($2 \tau_R$ experiment) and 20.9 kHz ($4 \tau_R$ experiment), correspond to a CH bond length of the aromatic carbon of 1.14 Å, which compares well with the value $r_{CH} = 1.09$ Å from neutron diffraction studies [Frey 73]. The difference of about 5% between distances from NMR measurements and distances from diffraction data has been observed before and can be explained by different averaging of fast vibrational motions [Henry 85, Nakai 89].

The other traces in Fig. 3.4 are solutions for higher and lower coupling constants of 18.0 and 22.4 kHz, corresponding to internuclear distances of 1.09 Å and 1.18 Å, respectively. Clearly, these patterns could still be distinguished from the best-fit spectra at a much poorer S/N level. For measurements in ^{13}C naturally abundant samples, differences in distances of ± 0.03 Å, or, equivalently, librations of $\pm 2^\circ$, should easily be discriminated in a single experiment.

3.1.1 Influence of Remote Protons

In order to experimentally justify the approach of analyzing HMQ sideband-patterns in terms of spin-pairs, ammonium formate was chosen as a model system for a relatively isolated ^{13}C - ^1H pair, with the added benefit of a possible “tuning” of remote proton influences by deuteration of the NH_4^+ -groups [Saalwächter 99a]. The sample is described in detail in Appendix D.3, where also the structures and preparation procedures for all other model substances used in this thesis are compiled.

In Fig. 3.5, spectra measured for different spinning frequencies and recoupling times

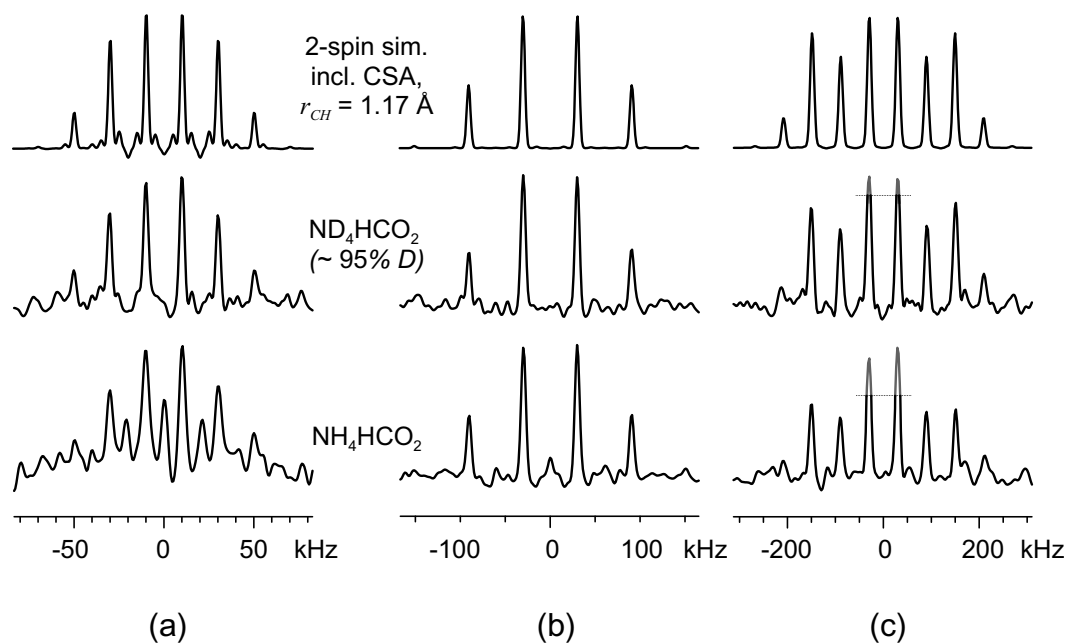


Figure 3.5: REPT-HMQ sideband spectra of ammonium formate, measured as bought, i.e. fully protonated (lower traces), and deuterated in the ammonium groups (middle), along with simulated spectra, where the best-fit CH-distance and the influence of the chemical shift anisotropy were taken into account. Spinning frequencies and recoupling times were 10 kHz, $1 \tau_R$ (a), 30 kHz, $2 \tau_R$, (b), and 30 kHz, $4 \tau_R$ (c).

using the non-deuterated and deuterated formates are compared. At 10 kHz MAS, a relatively clean sideband pattern is obtained for the deuterated compound. As is apparent from the corresponding simulation, the baseline distortions can be explained by the influence of the chemical shift anisotropy, which arises as a consequence of the incomplete refocusing of the CSA during the non-rotor-synchronized t_1 evolution period (see Section 3.2.1). At faster spinning, this contribution becomes negligible. In contrast, the pattern for the protonated sample has a considerably lower S/N, broader peaks, and exhibits appreciable even order sideband and centerband intensity. In pure NH_4HCO_2 , the closest formate proton-remote proton distance is 2.8 Å, which gives a dipolar proton-proton interaction more than five times smaller than the C-H interaction, not even considering the motional averaging due to rapid tumbling of the NH_4^+ ions. Nevertheless, the large number of perturbing homonuclear couplings from the numerous surrounding ammonium protons, along with an insufficient suppression of the homonuclear perturbation by the MAS, renders the method unsuitable at such “low” spinning frequencies.

The situation changes markedly for a spinning rate of 30 kHz, where the sideband patterns for both compounds are almost the same, except for some residual even-order sideband and centerband contributions for the NH_4HCO_2 . Especially for the longer recoupling time, though, deviations from the ideal behavior are observed in the first-order sidebands, which are higher than expected. This can straightforwardly be explained by contributions from recoupled interactions between the carbon and protons from neighboring ions, and these are consequently larger for the protonated compound. As already mentioned in the last section, excluding the first order sidebands from the fit of the $4 \tau_R$ patterns gives reliable results for both substances. Thus, these experimental results represent encouraging support for the validity of the spin-pair approach. A quantitative treatment of remote spin effects, with the proper distinction of homo- and heteronuclear influences, will be given in Section 3.3.

3.1.2 Sensitivity to Experimental Imperfections

To show the robustness of the technique, measurements on partially deuterated methylmalonic acid were performed. The acid protons, and, owing to its CH-acidic character, also the CH protons, can easily be exchanged by deuterium, yielding a substance with fairly isolated CH_3 -groups. The signal from the resulting CD-group (with about 12% residual CH, the signal of which is largely dephased for long recoupling times) with an apparent dipolar coupling constant to each of the CH_3 protons of about 2 kHz, can thus be used to study weak ^{13}C - ^1H couplings. The deuteration procedure and the characterization of the sample are described in Appendix D.4. A more detailed description of the dipolar coupling measurements for this sample will be given later (Section 3.3); here, only the possible application of rather long recoupling times is utilized.

In Fig. 3.6, experimental REPT-HMQ-filtered intensities for the CD-group are plotted as a function of varying several experimental parameters. The spinning speed (30 kHz) and the recoupling time ($16 \tau_R = 0.533$ ms) are kept constant. In the left diagram, the sensitivity on the effective flip angle of the π -pulse trains can be seen. Roughly, deviations of more than 20° from the ideal inversion can be tolerated, with the intensity still at about 80% of the maximum. This broadband nature is mainly due to the (xy-4) phase cycling: If the pulses are applied with constant phase, not more than about 20% of the maximum intensity could be measured, and slight deviations from the ideal pulse length lead to almost complete loss of

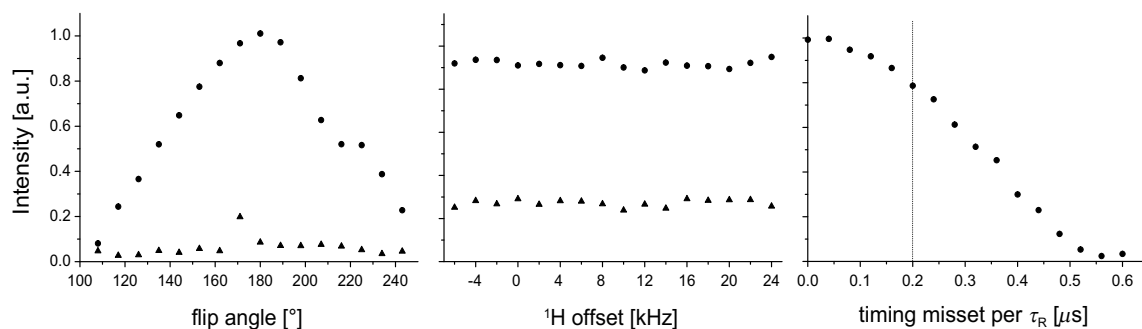


Figure 3.6: Integral REPT-HMQ-filtered intensities (arbitrary units) for the CD group (dipolar coupled to the methyl protons) in partially deuterated methylmalonic acid, measured with $\tau_{rcpl} = 16 \tau_R$ at 30 kHz MAS, as a function of the effective flip angle of the recoupling π -pulses (left), the ^1H offset frequency (middle), and rotor-synchronization timing imperfections (right), where the vertical line indicates a timing misset corresponding to a spinning speed deviation of ± 180 Hz. Triangles indicate measurements, where no (xy-4) phase cycling was employed.

the spectral intensity.

The middle diagram indicates that a dependence of the transferred HMQ intensity on the ^1H offset is not measurable. Similar results were also obtained upon changing the ^{13}C offset frequency. Contrary to common REDOR experiments, where only transverse magnetization of the observed nucleus is involved in the course of the pulse sequence, evolution of transverse magnetization of both the I and S-spins is involved in the REPT experiment during excitation and reconversion, respectively, which is the reason for the application of the excitation π -pulses on the S-spins, and vice versa for the reconversion pulses. This minimizes offset dependencies in the desired fashion, and again, (xy-4) phase cycling proves necessary for a good overall performance.

It has been noted, that proper stabilization of the spinning speed is essential for REDOR [Garbow 92]. At very-fast MAS, this could be expected to be of even higher importance. To test this assumption, measurements were performed, where the inter-pulse spacing was deliberately misset from the ideal $\frac{1}{2} \tau_R$. This should model variations of the spinning speed during the experiment. According to the results in the right diagram, deviations as large as ± 200 Hz (at 30 kHz MAS) can still be tolerated. Using commercial BRUKER equipment, the spinning speed is automatically stabilized at ± 10 Hz, such that problems arising from rotor synchronization should be negligible.

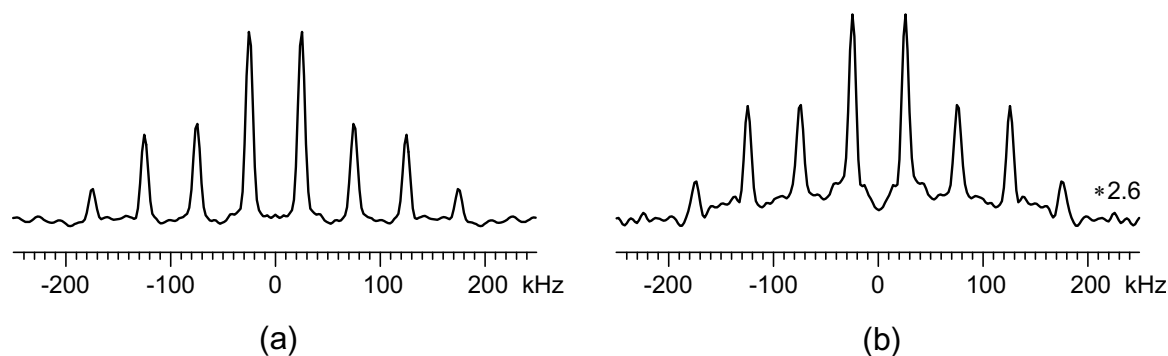


Figure 3.7: Spinning sideband patterns of the CH_3 -group in partially deuterated methylmalonic acid, measured with $\tau_{\text{rcpl}} = 10 \tau_R$ at 25 kHz MAS, (a) under ideal set-up conditions, and (b) using an effective 150° inversion pulse, 20 and 30 kHz offset on the ^{13}C and ^1H channels, respectively, and a rotor missynchronization of 100 Hz.

Finally, in Fig. 3.7, spinning sideband patterns are compared for an “ideal” set-up, and for deliberately mistuned experimental conditions. Even though the spectral intensity is reduced by a factor of 2.6, the mechanism of sideband generation, and its dependence on the experimental parameters discussed in this section, is apparently hardly influenced, and the sideband analysis is proven to be a feasible way to evaluate dipolar couplings even when the experiment is performed in a “quick and dirty” fashion. The distorted baseline in Fig. 3.7b is due to the severe rotor missynchronization, which made a strong first-order phase correction necessary. The patterns shown here were acquired with an optimized variant of the REPT-HMQC, namely the REPT-HDOR technique, with which the shown spectra could be acquired in much less time as compared to REPT-HMQC. The introduction of this (and other) variants of the experiment is the subject of the following section.

3.2 Generalized REPT Techniques

In Fig. 3.5, distortions of the HMQ sideband patterns due to the incomplete refocusing of the CSA interaction by the central π -pulse during t_1 became apparent. The inclusion of this π -pulse has a further disadvantage from an experimental point of view: its finite length leads to synchronization problems, because, for $t_1 = 0$, both the conversion and the reconversion pulses (with phases ϕ_2 and ϕ_3 in Fig. 3.1) should ideally be applied simultaneously on top of a rotor echo. Thus, introducing the π -pulse leads to a timing problem with respect to the t_1

dimension, and hence to phase errors in the spectra, as well as signal loss. Improvements to the technique are straightforward and can be rationalized by looking at the density matrix at the end of the excitation period (before the application of the S-spin 90° -pulse, as indicated by the “-” subscript).¹ For a single IS spin pair, we obtain

$$\hat{\rho}(N_{exc}\tau_R)_- = -\hat{I}_y \cos N_{exc} \bar{\Phi}_0 + 2\hat{I}_x \hat{S}_z \sin N_{exc} \bar{\Phi}_0. \quad (3.3)$$

The creation of HMQ coherence would now involve the application of a 90° y-pulse on the S-spins ($\rightarrow 2\hat{I}_x \hat{S}_x$). Another possibility is, however, to apply an I-spin 90° y-pulse first (the remaining \hat{I}_y transverse coherence and the phase factor are omitted for clarity):

$$\hat{\rho}(N_{exc}\tau_R)_- \xrightarrow{\frac{\pi}{2}\hat{I}_y} -2\hat{I}_z \hat{S}_z \quad (3.4)$$

Subsequent application of an S-spin 90° -pulse converts the resulting coherence into S-spin antiphase coherence,

$$-2\hat{I}_z \hat{S}_z \xrightarrow{\frac{\pi}{2}\hat{S}_y} -2\hat{I}_z \hat{S}_x, \quad (3.5)$$

which evolves back into observable magnetization during the reconversion period. Thus, by manipulation of a 2-spin coherence by 90° pulses on either channel, four different types of coherences are accessible: two different antiphase coherences (Eqs. (3.3) and (3.5)), the HMQ coherence, and a dipolar-ordered state given by Eq. (3.4). For the design of a 2D experiment, the experimentalist is free to choose which of these coherences are to be probed during t_1 . In all cases, the reconversion process, in particular the encoding of the reconversion Hamiltonian by the time-shifted rotor phase, occurs in the same way, which means that spinning-sideband patterns are generated, no matter which coherence is present during t_1 . This manifests that reconversion rotor encoding is not specifically a multiple-quantum mechanism, but reflects the rotor encoding of the interaction Hamiltonian.

Pulse sequences designed to probe three of the four mentioned types of coherences during t_1 are depicted in Fig. 3.8. They differ only in the placement of the t_1 period, and all pulse

¹All product operator calculations in this and the following sections follow the phases of the pulses given in Table E.1, Appendix E.2.

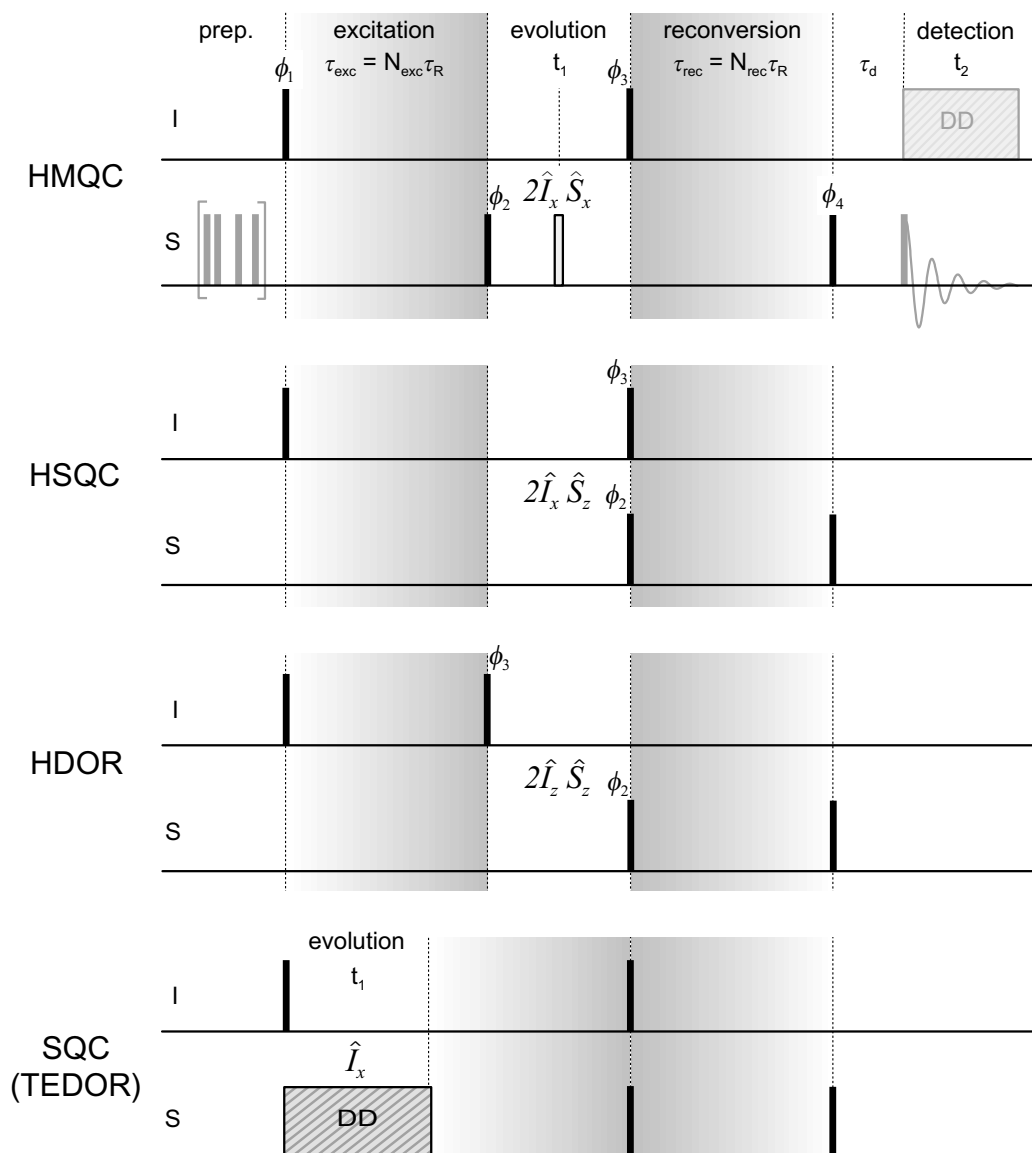


Figure 3.8: Variants of the REPT-HMQC experiment. The pulse sequences differ in the placement of the conversion and reconversion pulses (ϕ_2 ($= \phi_4 \pm 90^\circ$) and ϕ_3 ($= \phi_1 \pm 90^\circ$) in Fig. 3.1) with respect to the t_1 period. The recoupling π -pulse trains (in the grey shaded areas) are omitted for clarity, and the pulse phases are given in Appendix E.2.

phases are the same as for the REPT-HMQC experiment (see Appendix E.2). The experiment on top is the familiar REPT-HMQC, where the evolution of an HMQ coherence during t_1 necessitates the application of a refocusing π -pulse in the middle of t_1 , the disadvantages of which have already been mentioned.

If the proton antiphase coherence given in Eq. (3.3) is the spin state present during t_1 (second pulse sequence in Fig. 3.8), there is no need for refocusing any S-spin chemical shift interaction, since its free time evolution (without recoupling) is governed solely by the I-spin chemical shift. The indirect probing of the time evolution of such an antiphase magnetization has been introduced by Bodenhausen and Ruben [Bodenhausen 80] for solution-state ^1H - ^{15}N spectroscopy, and is referred to as heteronuclear *single*-quantum correlation (HSQC). After t_1 , the polarization-transfer $2\hat{I}_x\hat{S}_z \rightarrow -2\hat{I}_z\hat{S}_x$ is performed by applying the I- and S-spin 90° -pulses simultaneously. In the approximation of neglecting the dipolar evolution of the antiphase coherence (in contrast to the HMQ coherence, the antiphase coherence does evolve under the unrecoupled IS dipolar coupling during t_1), the time-domain signal for REPT-HSQC is identical to that of the REPT-HMQC experiment, given by Eqs. (3.1) and (3.2).

The effect of the pulse pair (pulses 2 and 3 in Fig. 3.8) responsible for the polarization transfer is a very famous concept in solution-state NMR, where, owing to the use of J-couplings, transfer efficiencies of 100% are theoretically possible. It was published by Morris and Freeman [Morris 79] under the acronym INEPT (*insensitive nuclei enhanced by polarization transfer*), and is one of the most abundant building blocks found in modern solution-state NMR pulse sequences.

The third pulse sequence in Fig. 3.8 involves the presence of a 2-spin dipolar-ordered state (Eq. (3.4)) during t_1 . This state is also termed *longitudinal dipolar order*, and has its homonuclear equivalent in the \hat{T}_{20} operator, which, in quadrupolar systems, is also referred to as a spin-alignment state. Its important property is that (neglecting homonuclear spin flip-flops with additional spins and relaxation) it does not undergo any time-evolution whatsoever, and is only subject to T_1 relaxation of the involved nuclei. The introduction of a t_1 interval, however, still leads to reconversion rotor encoding, such that a symmetric sideband pattern, centered around zero frequency, is obtained, the time-domain signal of which follows Eq. (2.24). This approach helps in saving considerable experiment time, and will be discussed in Section 3.2.2. It will be referred to as *heteronuclear dipolar order rotor encoding* (HDOR).

The carbon antiphase coherence resulting from the INEPT transfer (Eq. (3.5)), which represents the fourth of the possible coherences, is not an interesting candidate for another 2D correlation experiment, since its time-evolution is governed by the ^{13}C chemical shift, which is also probed in the direct dimension of the experiment. On the other hand, the more interesting ^1H chemical shift information can also be probed by inserting a t_1 dimension at the beginning of the pulse sequence (bottom experiment in Fig. 3.8). The polarization transfer then follows as a single block consisting of excitation, INEPT transfer, and reconversion. Consequently, rotor encoding does not occur, and the experiment is suitable for recording shift correlation spectra only. This experiment is known in solid-state NMR under the name TEDOR (*transferred-echo, double-resonance*). Its one-dimensional version (i.e. without a t_1 dimension) has been shown to be useful for the determination of weak heteronuclear dipolar couplings in selectively pairwise labeled systems, where the change in the spectral intensity as a function of N_{rec} , keeping the number of excitation rotor periods, N_{exc} , constant, is studied [Hing 92, Hing 93]. When a second I-spin chemical shift dimension is introduced, the S-spins have to be dipolar decoupled. The pulse sequence gives essentially the same result as a rotor-synchronized REPT-HSQC experiment, but since the emphasis of this work is on spinning-sideband analysis, this scheme will not be discussed further.

The one-dimensional versions (i.e. $t_1 = 0$) of all of the abovementioned REPT variants are identical and can be used to study the build-up of the heteronuclear coherences as a function of the recoupling time. Only the REPT-HMQC experiment differs by the appearance of the refocusing π -pulse, which is immaterial for $t_1 = 0$. The build-up behavior for any of the specific coherences probed during a possible t_1 dimension (HMQ, proton antiphase coherence, and heteronuclear dipolar order) is identical. The 1D version will henceforth always be referred to as REPT-HMQ-filtered experiment, since this terminology gives the best account of the fact that *heteronuclear multiple-quantum modes* are excited in all cases.

3.2.1 CSA and Dipolar Correction Terms

Although, to a first approximation, the time evolution during the t_1 dimension of the REPT-HMQ and REPT-HSQC correlation techniques can be described by the same formula (assuming spin pairs), both experiments differ in their dependence upon contributions from the ^{13}C CSA and the heteronuclear dipolar interaction. While — within the spin-pair approximation —

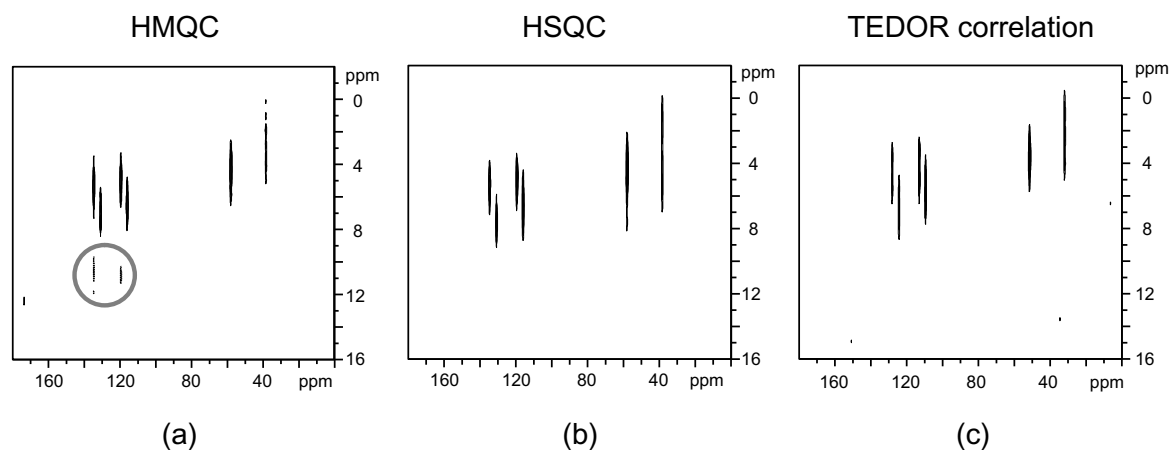


Figure 3.9: Comparison of the three HETCOR experiments shown in Fig. 3.8, using L-tyrosine·HCl as sample. All three spectra were measured in a 700 MHz magnet under the same experimental conditions (30 kHz MAS, $N_{rcpl} = 1 \tau_R$), rotor-synchronized in t_1 .

the REPT-HDOR experiment gives artifact-free sideband spectra, and the TEDOR approach ensures the same for ^{13}C - ^1H shift correlation spectra, correction terms can straightforwardly be calculated for the other two variants.

In Fig. 3.9, three ^{13}C - ^1H correlation spectra are compared. In the REPT-HMQC spectrum, weak negative intensities (marked with a grey circle), mirrored at the spectral center of the t_1 dimension, can be identified for the aromatic protons. These artifacts correspond to the ones in the sideband spectra of ammonium formate, Fig. 3.5, and are due to the incomplete refocusing of the CSA interaction by the central π -pulse, if $t_1/2 \neq 1 \tau_R$. In product operator notation, the HMQ coherence evolves during t_1 as

$$2\hat{I}_x\hat{S}_x \xrightarrow{\Phi_{CS,S}(0;t_1/2)\hat{S}_z} 2\hat{I}_x\hat{S}_x \cos \Phi_{CS,S}(0;t_1/2) + 2\hat{I}_x\hat{S}_y \sin \Phi_{CS,S}(0;t_1/2) \quad (3.6)$$

$$\xrightarrow{\pi\hat{S}_y} -2\hat{I}_x\hat{S}_x \cos \Phi_{CS,S}(0;t_1/2) + 2\hat{I}_x\hat{S}_y \sin \Phi_{CS,S}(0;t_1/2) \quad (3.7)$$

$$\xrightarrow{\Phi_{CS,S}(t_1/2;t_1)\hat{S}_z} -2\hat{I}_x\hat{S}_x [\cos \Phi_{CS,S}(0;t_1/2) \cos \Phi_{CS,S}(t_1/2;t_1) + \sin \Phi_{CS,S}(0;t_1/2) \sin \Phi_{CS,S}(t_1/2;t_1)] + \dots, \quad (3.8)$$

where the $2\hat{I}_x\hat{S}_y$ component is neglected in the last step, because it is purged by the final z-filter. $\Phi_{CS,S}(t;t')$ is the integral phase acquired upon CSA evolution under MAS, as given by Eqs. (1.74) and (1.82). The ^1H shift evolution can be evaluated independently, and the term in

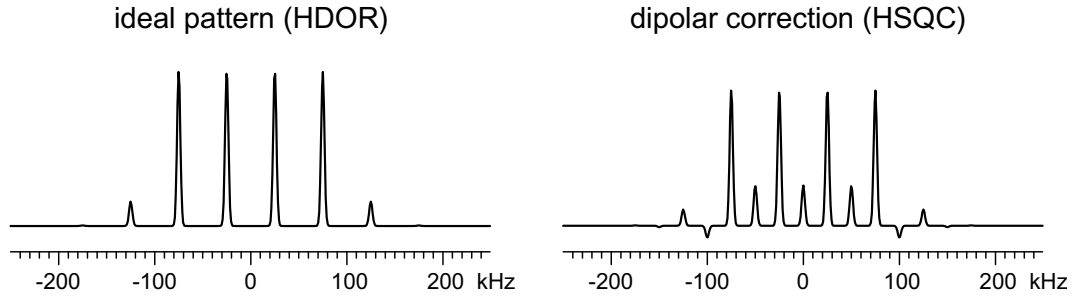


Figure 3.10: Effect of the dipolar correction term on REPT-HSQC sideband patterns for an IS-pair. The patterns are calculated for $D_{IS} = 21$ kHz, $\nu_{MAS} = 25$ kHz, and $\tau_{rcpl} = 2 \tau_R$.

brackets represents a multiplicative correction term for the t_1 time domain signal. Clearly, the full rotor echo ($\cos^2 a + \sin^2 a = 1$) is obtained if $t_1 = 2 \tau_R$. The spectra in the top line of Fig. 3.5 were calculated using this correction, and its influence was seen to be negligible for very fast spinning. The appearance of the artifact can be avoided completely if t_1 is incremented in steps of $2 \tau_R$, since $\Phi_{CS,S}(0; \tau_R) = 0$. It is then advisable to use the States method for sign-sensitive detection in t_1 since the possible spectral width is twice as high as for TPPI, making up for the increased increment.

For the REPT-HSQC experiment, the antiphase magnetization (and also the in-phase transverse magnetization) is subject to evolution due to residual (uncoupled) heteronuclear dipolar interaction during t_1 :²

$$-\hat{I}_y \cos N_{exc} \bar{\Phi}_0 + 2\hat{I}_x \hat{S}_z \sin N_{exc} \bar{\Phi}_0 \xrightarrow{-\Phi_{D_{IS}}(t_1) 2\hat{I}_z \hat{S}_z} -2\hat{I}_x \hat{S}_z \left[\cos N_{exc} \bar{\Phi}_0 \sin \Phi_{D_{IS}}(t_1) - \sin N_{exc} \bar{\Phi}_0 \cos \Phi_{D_{IS}}(t_1) \right] + \dots \quad (3.9)$$

The I-spin chemical shift evolution of $2\hat{I}_x \hat{S}_z$ during t_1 is evaluated independently, leading to expressions analogous to Eqs. (3.1) and (3.2) for the final time-domain signal, where $\sin N_{exc} \bar{\Phi}_0$ is to be replaced by the term in brackets in the above equation. This correction term reduces again to $\sin N_{exc} \bar{\Phi}_0$ in the case of rotor-synchronized shift correlation spectra, since $\Phi_{D_{IS}}(t_1)$ vanishes for $t_1 = N \tau_R$. Thus, for the HETCOR application, the TEDOR correlation and REPT-HSQC give identical spectra when only a heteronuclear spin pair is considered.

The above mixture of sines and cosines, with arguments depending on t_1 , in the time-domain signal, may serve as a qualitative argument for the appearance of a centerband and

²The sign of the dipolar evolution is again inverted due the reasons given on page 50.

even-order sidebands in REPT-HSQ spin-pair sideband patterns, as shown in Fig. 3.10. The influence of the additional dipolar evolution is strongest for a directly bound ^{13}C - ^1H pair, but quickly becomes negligible for weaker couplings (the perturbing interaction is not recoupled!). It is in any event advisable from an experimental point of view to record REPT heteronuclear sideband patterns with the HDOR technique rather than having any chemical-shift information in t_1 .

3.2.2 Rotor Encoding of Heteronuclear Dipolar Order

The REPT-HDOR experiment takes advantage of the fact that longitudinal dipolar order does not undergo time evolution during t_1 . The amplitude modulation measured as a function of t_1 is thus solely due to the rotor encoding of the reconversion Hamiltonian, which was shown to result in *symmetric* spinning-sideband patterns. Since these patterns are centered around the zero offset frequency in the indirect dimension, there is no need for a sign-sensitive detection in t_1 , which is needed for all other variants of the REPT technique in order to account for isotropic chemical shift contributions of the protons. The acquisition of a cosine dataset in t_1 thus reduces the experiment time by a factor of two. The spectral intensity in the sine dataset is zero, thus its presence would only add noise to the final intensity after the two-dimensional Fourier transformation.

Secondly, as can be inferred from Eq. (2.24), the signal is *periodic* with respect to the rotor period, and — apart from an increased probability for the occurrence of spin-diffusion effects, which are weak at very-fast MAS and will be neglected — the measured modulation pattern decays as a function of the T_1 relaxation times of the nuclei, which are much longer than the timescale of the MAS. Experimentally (Fig. 3.11a), no appreciable decay of the t_1 signal could be identified in any of the presented measurements. This opens up a number of approaches for the processing of this time-domain signal. Some results of approaches discussed below are presented in Fig. 3.11b.

The Fourier transform of the whole $3.2 \tau_R$ long FID is shown in slice (i) of 3.11b. The applied line-broadening (10 kHz) had to be chosen quite large, in order to avoid truncation effects, i.e. cut-off sinc wiggles. Narrower sideband linewidths can be obtained by catenating together integer rotor-period fractions of the FID, which allows for an arbitrarily small artifi-

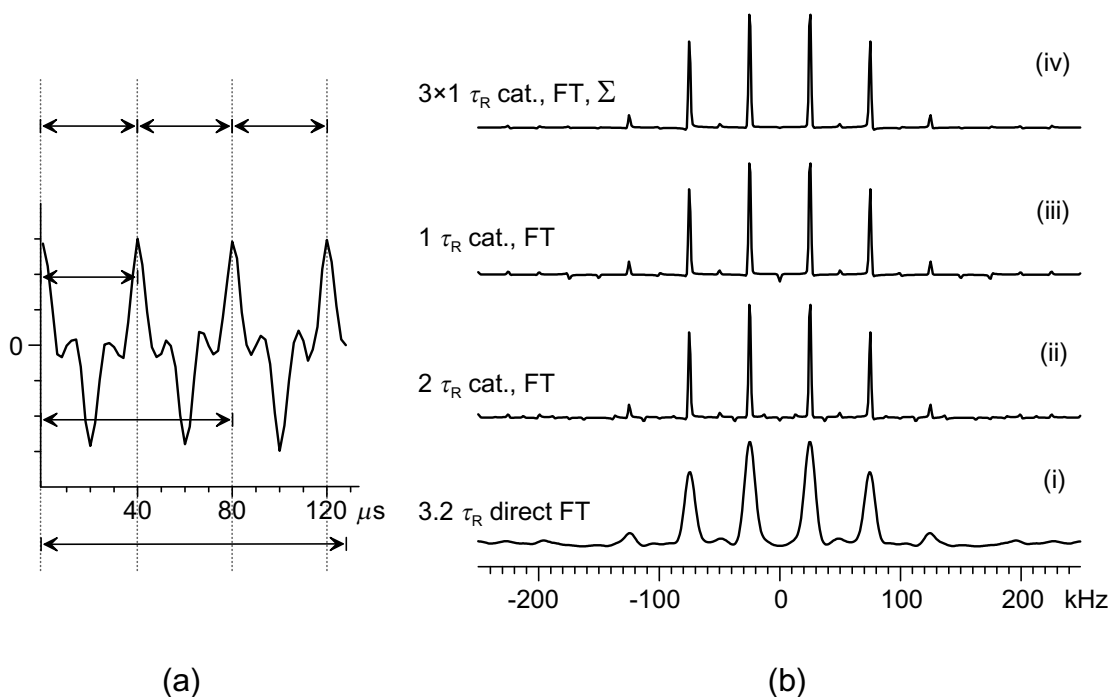


Figure 3.11: Processing of the t_1 time-domain signal as obtained from the HDOR experiment. The FID shown in (a), which is measured for the CH_3 -signal of partially deuterated methylmalonic acid at $\nu_{\text{MAS}} = 25$ kHz, with $\tau_{\text{rcpl}} = 6 \tau_R$ and $\Delta t_1 = 2 \mu\text{s}$, consists of 64 points, covering 3.2 rotor periods of encoding with 20 points each. In (b), Fourier transforms of the indicated parts of the FID are displayed, as discussed in the text.

cial line-narrowing, depending on the number of repetitions chosen. On the timescale of the experiment, no correction is necessary to account for signal decay during t_1 .

In principle, it should be sufficient to record just one rotor period of the FID, as can be seen in slice (iii). However, the catenation results in the appearance of *correlated noise*, i.e. random intensity variations of the NMR signal appear only in the sidebands (up to very high order), as a consequence of the interplay of the time-translational symmetry of the artificial “FID” and the Fourier transformation. If *two* rotor periods of experimental data are used, noise also appears at *half* rotor period intervals (slice (ii)). Such signals cannot be due to any physical effect, and thus allow a better estimation of the contribution of noise to the sideband intensities. Moreover, noise is seen to be significantly reduced by transforming the three subsequent rotor periods of the time-domain signal individually and adding the sideband spectra (slice (iv)). This approach is useful for the suppression of spectrometer drift effects,

when the acquisition time of a single slice is rather long.

In conclusion, the REPT-HDOR technique allows for a substantial decrease in experiment time. The time-domain data in Fig. 3.11 were obtained in only 3 hours (700 MHz spectrometer, ^{13}C in natural abundance), with the potential of analyzing just the first of three rotor periods of signal, measured in one hour. For less suited samples than the one used (short recycle delay of 1 s, good signal due to well-isolated CH_3 -groups), measurement times were less than 12 hours in most of the cases.

3.3 Multi-Spin Systems

Historically, heteronuclear recoupling methods such as REDOR were established as methods for the investigation of well-isolated spin-pairs. In the solid state, this is usually achieved by using selectively labeled compounds, with a considerable isotopic dilution, whereas in the liquid state, the use of J-couplings restricts the interactions to be considered to the nearest neighbors.

The emphasis of this work, however, is on ^{13}C - ^1H correlation, where the presence of a tightly coupled proton spin network cannot be neglected. The implications are twofold: Couplings between the protons are strong, and the influence of homonuclear coupling among these has to be investigated carefully. The results in Section 3.1.1 already justified the neglecting of the proton homonuclear coupling at very high spinning speeds, which is largely averaged out by MAS (as opposed to the heteronuclear dipolar interaction, which is recoupled). In the end of this section, results will be presented, which should contribute to a more complete picture of how homonuclear couplings influence the REPT spectra.

Secondly, couplings of the ^{13}C atoms to more than one proton have to be considered. This is of special importance for organic substances, where a theoretical understanding of spectra of the common structural units, CH , CH_2 , and CH_3 , is indispensable. The theoretical treatment of the couplings of an S-spin to multiple I-spins for the REDOR experiment is straightforward and has already been published [Goetz 97]. In short, since the heteronuclear dipolar coupling Hamiltonians all commute with each other, $[\hat{H}_D^{SI_i}, \hat{H}_D^{SI_j}] = 0$, the dipolar evolution for all individual SI_i -pairs can be evaluated *independently*, and product operator theory can be used to calculate the signals. In the following, the analytical calculation of the

t_1 time-domain signal for the REPT techniques will be described. Homonuclear couplings will be neglected, which is a well-justified approximation, as will be proven theoretically and experimentally. Since, due to the non-commutativity of homo- and heteronuclear couplings, $[\hat{H}_D^{SI_i}, \hat{H}_D^{ij}] \neq 0$, a first-order analytical treatment of such effects is not appropriate; numerical simulations of the time-evolution of the density matrix will be employed when homonuclear couplings are to be considered (see Appendix C).

The REPT technique, with its property of free I-spin evolution during the excitation period, is particularly easy to describe: since the S-spins are naturally abundant, only *one* coupling partner atom needs to be considered for each proton, i.e., the treatment is restricted to one S-spin and multiple I-spins. This experimental situation is commonly referred to as “proton-detected local field”. The product operator treatment for the excitation period and the INEPT transfer reads

$$-\sum_i \hat{I}_y^{(i)} \xrightarrow{N_{exc} \sum_i \bar{\Phi}_0^{(i)} 2\hat{S}_z \hat{I}_z^{(i)}} -\sum_i \left(\hat{I}_y^{(i)} \cos N_{exc} \bar{\Phi}_0^{(i)} - 2\hat{I}_x^{(i)} \hat{S}_z \sin N_{exc} \bar{\Phi}_0^{(i)} \right) \quad (3.10)$$

$$\xrightarrow{\frac{\pi}{2} \hat{S}_y} \xrightarrow{\frac{\pi}{2} \hat{I}_y} \dots -\sum_i 2\hat{I}_z^{(i)} \hat{S}_x \sin N_{exc} \bar{\Phi}_0^{(i)}. \quad (3.11)$$

During reconversion, S-spin antiphase magnetization, $2\hat{I}_z^{(i)} \hat{S}_x$, evolves in the local field of the surrounding protons (“separated local field” situation,³ SLF), and is reconverted to observable S-spin magnetization upon coupling to the i th I-spin. Couplings to all the other I-spins add cosine factors to this term, whereas higher antiphase coherences like $4\hat{I}_z^{(i)} \hat{I}_z^{(j)} \hat{S}_y$ (which acquire additional sine phases), are *not* reconverted to observable magnetization.

$$-\sum_i 2\hat{I}_z^{(i)} \hat{S}_x \sin N_{exc} \bar{\Phi}_0^{(i)} \xrightarrow{-N_{rec} \sum_i \bar{\Phi}_{t_1}^{(i)} 2\hat{S}_z \hat{I}_z^{(i)}} \sum_i \hat{S}_y \sin N_{exc} \bar{\Phi}_0^{(i)} \sin N_{rec} \bar{\Phi}_{t_1}^{(i)} \prod_{j \neq i} \cos N_{rec} \bar{\Phi}_{t_1}^{(j)} \\ -2\hat{I}_z^{(i)} \hat{S}_x \sin \dots + 4\hat{I}_z^{(i)} \hat{I}_z^{(j)} \hat{S}_y \sin \dots \quad (3.12)$$

The magnetization corresponding to the \hat{S}_y operator is stored along z during the final dephasing delay, and the powder average of its amplitude forms the time-domain signal of the HDOR

³“Local field” refers to the sum of all heteronuclear correlations experienced by a single spin. Historically, ^{13}C - ^1H SLF spectra were obtained under ^1H homodecoupling using multiple-pulse sequences [Hester 76]. Homonuclear decoupling is here achieved by the very-fast MAS.

experiment,

$$S_{REPT}(t_1) = \left\langle \sin N_{exc} \bar{\Phi}_0^{(i)} \sin N_{rec} \bar{\Phi}_{t_1}^{(i)} \prod_{j \neq i} \cos N_{rec} \bar{\Phi}_{t_1}^{(j)} \right\rangle. \quad (3.13)$$

If chemical shift evolution of the i th I-spin is to be included, x- and y-components of the signal can be written in exact analogy to Eqs. (3.1) and (3.2) for each of the I-spins. The CSA-correction for REPT-HMQC (Eq. (3.8)) can be appended as an additional factor, and for the dipolar correction (HSQC), $\sin N_{exc} \bar{\Phi}_0^{(i)}$ has to be replaced by the bracketed expression in Eq. (3.9).

Moreover, in the case of HMQ evolution during t_1 , the HMQ coherence picks up phases due to couplings to additional I-spins, which are not part of the coherence itself. The correction factor can be calculated in analogy to the treatment of t_1 evolution under CSA (Eqs. (3.6)–(3.8)):

$$\prod_{j \neq i} \left[\cos \Phi_{DIS}^{(j)}(0; t_1/2) \cos \Phi_{DIS}^{(j)}(t_1/2; t_1) + \sin \Phi_{DIS}^{(j)}(0; t_1/2) \sin \Phi_{DIS}^{(j)}(t_1/2; t_1) \right]. \quad (3.14)$$

This correction describes the heteronuclear contribution to evolution rotor modulation (ERM). Its effects will be discussed in Section 3.3.3. Note that this term is not periodic with respect to t_1 -increments of $1 \tau_R$, such that, in order to prevent artifacts in rotor-synchronized shift correlation spectra (see Fig. 3.9), t_1 has to be incremented in steps of $2 \tau_R$, which limits the accessible spectral width.

In the case of **methylene groups**, just one cosine factor appears in Eq. 3.13. For the time-domain signal of **methyl groups**, the equation can be simplified to obtain a more descriptive form. In essence, methyl groups undergo fast three-site jumps at ambient temperature, possibly with some orientational distribution around the three sites [Schmidt 85]. Therefore, the three heteronuclear couplings have an identical dependence on position, and the average REDOR phases $\bar{\Phi}^{(i)}$, $i = 1 \dots 3$, for the three protons are equal. The spatial part of the dipolar coupling is described by a symmetric second-rank tensor. The average of such second-rank tensors undergoing fast symmetric jumps with three or more positions around a specified axis is again represented by a uniaxial tensor with its symmetry axis along the rotation axis [Schmidt-Rohr 94]. Therefore, the acquired dipolar phase for a single IS-pair, with S located

on the rotation axis, can again be calculated using Eq. (2.5), but with a modified dipolar coupling constant [Terao 86],

$$D_{IS}^{app} = D_{IS} \frac{1}{2} (3 \cos^2 \theta - 1), \quad (3.15)$$

where θ is the angle between the IS-internuclear vector and the methyl rotation axis. For S-spins located off the rotation axis, the individual $\bar{\Phi}_I^{(i)}$ are still equal, but the averaged dipolar tensor (simply calculated as the average of the three different $\mathbf{A}_2^{D_{IS}}$) will be asymmetric. Consequently, it will explicitly depend on the position of the three individual I-sites relative to the S-spin, yielding a more complicated formula for D_{IS}^{app} . In the off-axis case, only when $r_{IS} \gg r_{II}$ and for small displacements of the S-spin from the rotation axis, i.e. very small asymmetry parameters, does Eq. (3.15) represent a good approximation.

Using a single $\bar{\Phi}$ for the three methyl protons, with $\cos^2 a = 1 - \sin^2 a$, we obtain from Eq. (3.13)

$$\begin{aligned} S_{REPT}^{CH_3}(t_1) &= \langle 3 \sin N_{exc} \bar{\Phi}_0 (\sin N_{rec} \bar{\Phi}_{t_1} - \sin^3 N_{rec} \bar{\Phi}_{t_1}) \rangle \\ &= \frac{3}{4} \langle \sin N_{exc} \bar{\Phi}_0 \sin N_{rec} \bar{\Phi}_{t_1} \rangle + \frac{3}{4} \langle \sin N_{exc} \bar{\Phi}_0 \sin 3N_{rec} \bar{\Phi}_{t_1} \rangle, \end{aligned} \quad (3.16)$$

where for the last line an addition theorem was used. The result has an interesting connotation in that it is the sum of two parts, where the first part is the time-domain signal for a single spin pair (with an apparent coupling constant), and in the second part the apparent coupling constant during reconversion is *three times* the coupling constant during excitation. Since powder averages of the type⁴ $\langle \sin Na \sin Nb \rangle$ approach the value of $\frac{1}{2}$ for $N \rightarrow \infty$ and $a = b$, and decay to zero for $a \neq b$, only the first term in Eq. (3.16) contributes in this limit, and the maximum polarization transfer for a methyl group is $\frac{3}{8} = 37.5\%$.

In order to study the applicability of the above formulae, i.e. in the approximation of neglected homonuclear couplings, methylmalonic acid was chosen as a model compound. In the easily obtained deuterated form (referred to as “partially deuterated”, with about 90% D in the CD and COOD groups; see Appendix D.4 for details), the methyl groups are fairly isolated, with next CH₃ proton neighbors about 4.3 Å away from the methyl carbon.

⁴Note the formal equivalence of this term to a correlation function.

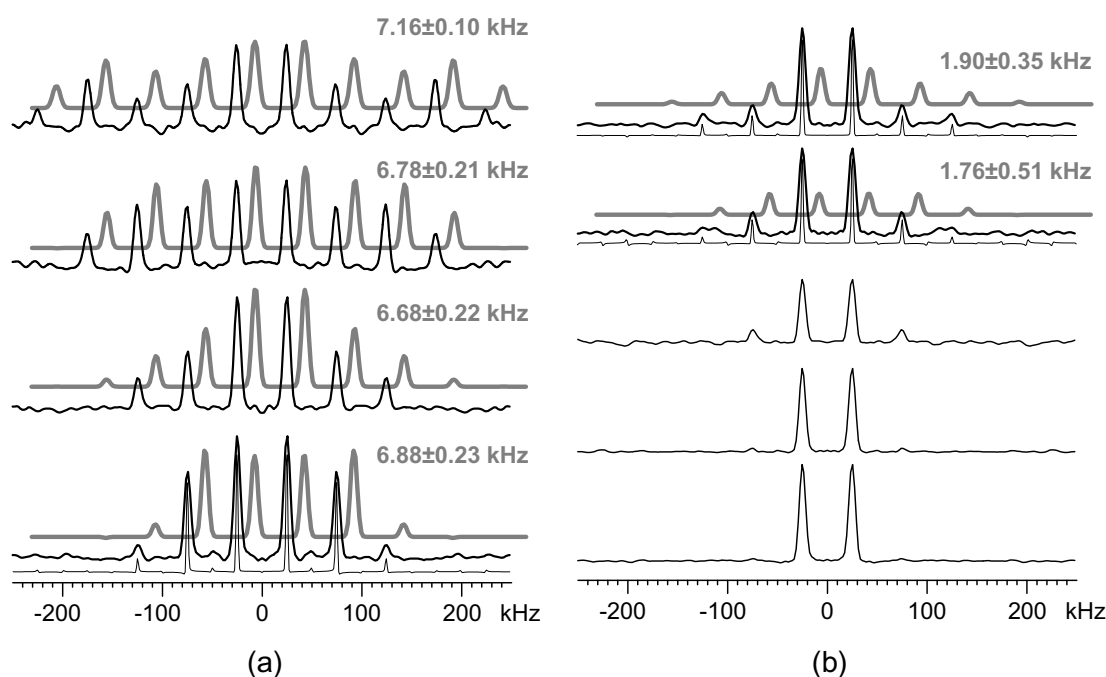


Figure 3.12: REPT-HDOR sideband patterns, recorded for a sample of partially deuterated methylmalonic acid at 25 kHz MAS and a total t_1 of $3.2 \tau_R$. (a) Data for the CH_3 carbon, with recoupling times 6, 8, 10, 12 τ_R , increasing from bottom to top. (b) Data for the CD carbon, with $\tau_{\text{repl}} = 6, 8, 18, 24, 28 \tau_R$. The grey background traces are the best-fit patterns (with the corresponding results for $|D_{IS}^{\text{app}}|$ indicated). The very thin lines are the experimental spectral obtained with the improved processing method; they are the sums of 3 individual rotor periods of t_1 signal, catenated before Fourier transformation to obtain narrow lines (cf. Fig. 3.11b, top), while the other spectra were obtained by direct FT of the complete FIDs.

Fig. 3.12 shows experimental REPT-HDOR sideband patterns for the CH_3 and the CD carbon, where the latter experiences mainly the rather small heteronuclear couplings from the methyl protons. Under the given experimental conditions, weak contributions from residual methyne protons to the sideband patterns of this carbon atom are distributed over many sideband orders, and should thus hardly interfere with the analysis of the lower order sidebands. Both carbon atoms lie on the methyl rotation axis, and Eq. 3.16 can be expected to hold for the description of the patterns. In all spectra, the familiar effect of higher than expected first-order sidebands, due to contributions from coherences involving remote CH_3 -groups, is again apparent. However, a fitting procedure, where the first-order sidebands were excluded, yielded dipolar couplings in good agreement with the crystal structure data (Ta-

Table 3.1: Experimentally observed and expected apparent ^{13}C - ^1H dipolar couplings and bond lengths for the methyl protons in partially deuterated methylmalonic acid.

sidebands	fits of NMR data			from crystal structure ^a	
	$ D_{IS}^{app} /2\pi$ [kHz]	$\Rightarrow r_{IS}$ [Å]	$D_{IS}^{app}/2\pi$ [kHz] ^b	r_{IS} [Å]	
CH ₃	6.88±0.21	1.14±0.01 ^c	-7.77	1.09	
CD	1.83±0.43	2.22±0.2 ^d	-1.97	2.165	
build-up	T_2^{app} [ms]				
CH ₃	0.93	–	–	-7.77	1.09
CD	0.63	1.33	2.47	-1.97	2.165
CO	0.52	0.78	–	-1.02/-0.96 ^e	–

^abased on X-ray data [Derissen 70], including an idealized model for the methyl group

^bcalculated from the average dipolar tensor of the three proton positions

^ccalculated from Eqs. (1.51) and (3.15), assuming $\theta = 109.5^\circ$

^dcalculated from Eqs. (1.51) and (3.15), assuming $\theta = 28.4^\circ$

^etwo inequivalent positions in the crystal

ble 3.1). The available crystal structure of methylmalonic acid (X-ray data, [Derissen 70]) is somewhat poor in that the protons are not properly located, such that for the comparison here, couplings calculated from an idealized, tetrahedral methyl group (based on a neutron structure of L-alanine [Lehmann 72], with $r_{CH} = 1.09$ Å), with the molecular carbon skeleton from the methylmalonic acid structure, was used. This topic is explained in more detail in Chapter 6, where a more sensitive method for the investigation of the methyl group will be presented.

It was even possible to obtain sideband patterns for the CD carbon, which could also be fitted under exclusion of the first-order sidebands, which completely dominate the spectra. Only at very high recoupling times was the 5th order sideband intensity sufficiently high to allow a reasonable fit. Even though the agreement with the expected values is still good, the performance of the method has certainly reached its limit for this measured apparent coupling of 1.8 kHz. Homonuclear effects and perturbations arising from the incomplete isolation of the 4 involved spins are expected to hamper a sideband analysis beyond this point. Moreover, the total measured intensity only reached about 20% of the intensity of the spectra with $\tau_{rcpl} = 6 \tau_R$, resulting in very long experiment times for a S/N sufficient for a reliable fit of the

relatively weak third and higher-order sidebands.

The data obtained from REPT-HMQ-filtered measurements for the same sample are summarized in Fig. 3.13. As opposed to REDOR data, the REPT build-up data cannot be normalized with a reference experiment to yield absolute values for the heteronuclear coherence transfer. As is expected, the intensity decreases as a function of the recoupling time after a first maximum is reached. This may tentatively be explained by T_2 relaxation during the recoupling periods. For the methyl carbon, only the point for $\tau_{rcpl} = 1 \tau_R$ coincides with the initial rise of the theoretical curve, Fig. 3.13a.

The time-resolution of the data for the CD and CO carbon was, however, good enough for a fit to a master curve based on Eq. (3.16), including an exponential damping function with an apparent transverse relaxation time (T_2^{app}). The results are given in Table 3.1. Such a fit is only possible if the observed maximum really coincides with the first maximum of the master curve. For cases where relaxation effects are very strong, this cannot be expected, and methods with the option of correcting for such effects have to be chosen. In the present situation, the fits gave reasonable results, which are, however, systematically too low, as a result of the exponential damping. The fit curve for the methyl carbon is based on the average coupling constant from the sideband analyses, and only T_2^{app} has been determined with the fit.

Sideband analysis is thus clearly the method of choice to evaluate the dipolar couplings from REPT experiments. Nevertheless, it is interesting to note that the data in Fig. 3.13a can be modeled by using Eq. (3.13), including the 24 protons of the 8 next-neighbor CH_3 units, with dipolar coupling tensors based on the crystal structure (Fig. 3.13b/c). The methyl rotation was accounted for in these calculations by averaging the dipolar tensors from the proton triplets. Even though the scaling of the y-axis was adjusted to fit the data, both the position of the maxima and the decay of the signal at longer recoupling times is reproduced in these simulated curves. The observed “apparent” T_2 is thus mainly due to heteronuclear couplings to remote protons, and can only weakly depend on the real T_2 values for ^{13}C and ^1H in this system. This notion is supported by the T_2^{app} values in Table 3.1, which indicate stronger “relaxation” for the carbon atoms which are farther away from the methyl protons. Clearly, the influence of the remote methyl groups increases with an increasing ratio of the remote heteronuclear coupling to the primary intramolecular coupling.

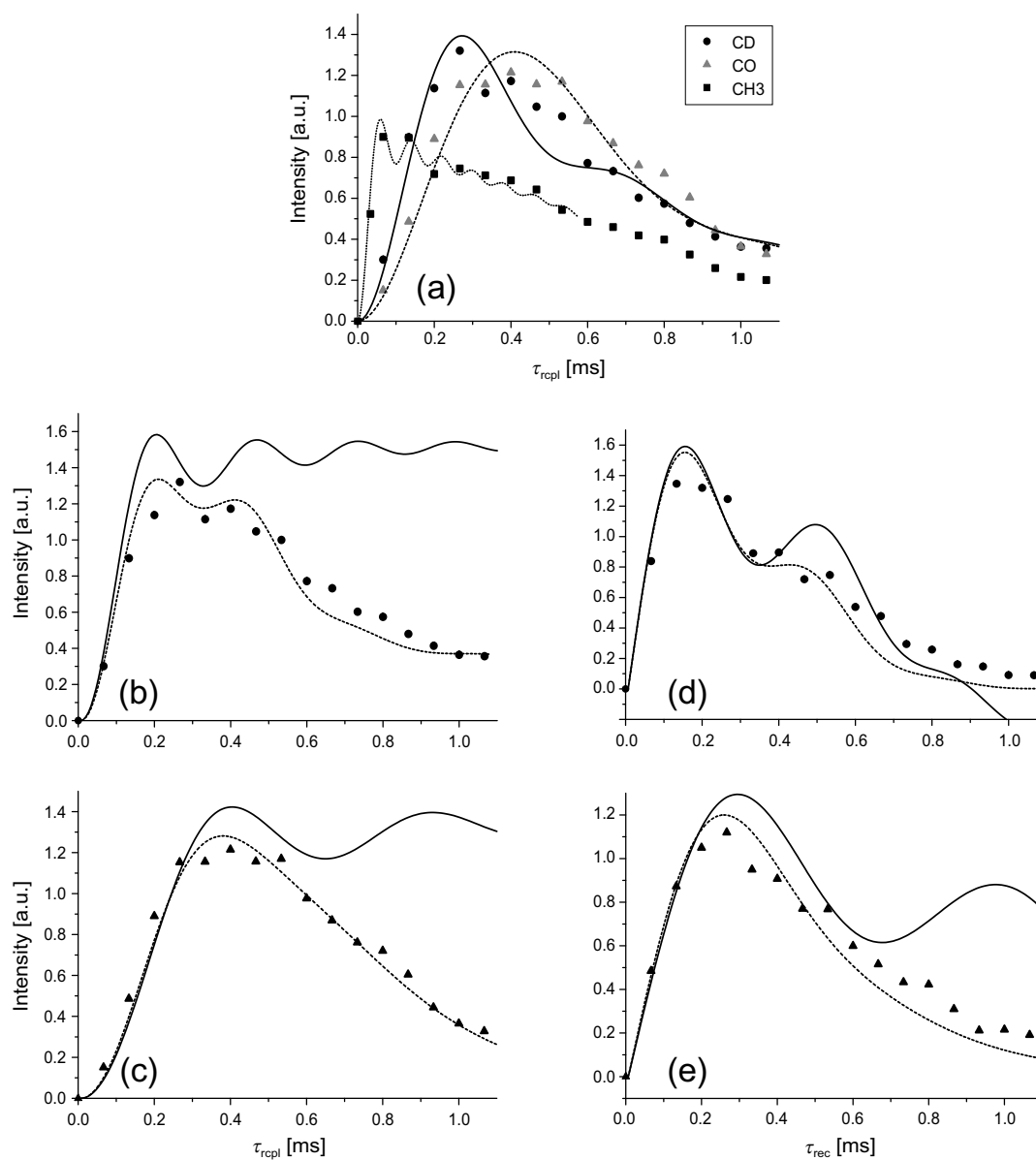


Figure 3.13: REPT-HMQ build-up measurements for partially deuterated methylmalonic acid, performed at 30 kHz MAS. (a) Data for all three carbon positions, along with best-fit curves. (b),(c) Separately plotted data for the CD and CO carbons. The curves were calculated from the crystal structure, including only the three protons from the same molecule (solid lines), or 24 further protons from the 8 next-neighbour CH₃-units (dashed lines). (d),(e) TEDOR data, with a constant excitation time of $8 \tau_R$.

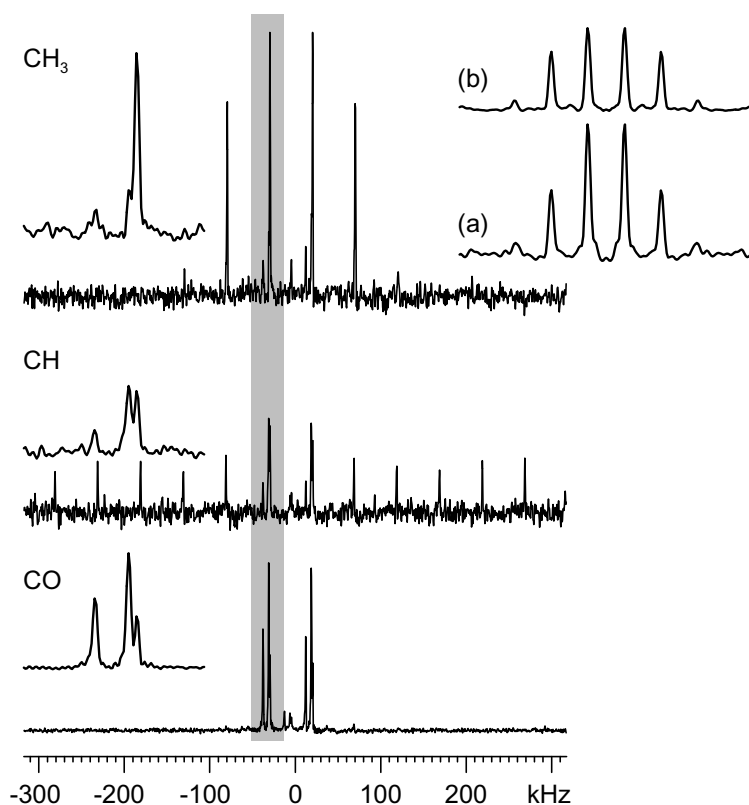


Figure 3.14: REPT-HSQ sideband patterns of methylmalonic acid, recorded at 25 kHz MAS and $\tau_{rcpl} = 6 \tau_R$. The regions of the first-order sidebands (grey shaded area) have been expanded. Inset (a) is the REPT-HDOR sideband pattern of the CH_3 signal, recorded under the same conditions, which can be compared with the REPT-HDOR pattern of partially deuterated methylmalonic acid, inset (b).

In Fig. 3.13d/e, TEDOR data are displayed. In these experiments, the excitation time is held constant, which in part alleviates the problems with transverse relaxation, because upon increasing τ_{rcpl} , only T_2 of ^{13}C should additionally contribute to the decay [Hing 93]. A disadvantage, however, is that a fit to a master curve is not possible, since the TEDOR curve explicitly depends on the fixed product $N_{exc} \tau_R D_{IS}$, thus Eq. (3.13) cannot be applied in a scaled form. The coupling constant is extracted by studying the oscillation in the decaying part of the curve behind the first maximum. A comparison of the experimental data with the analytical curves for 3 and 27 protons shows again that the data can be modeled using multiple heteronuclear couplings only. Nevertheless, the TEDOR approach is, in analogy to the study of the regular build-up behavior, not a feasible way to extract the strongest coupling constant in a multi-spin system, and spinning sideband analysis remains the method of choice.

An experimental proof of the assumption regarding the origin of the increased first-order sideband is presented in Fig. 3.14. The ^1H chemical-shift information, which is present in the t_1 dimension of the REPT-HSQC experiment, can be probed *simultaneously* with the spinning sideband information, if the resolution in this dimension is large enough, i.e. for a sufficient number of acquired slices. The data in Fig. 3.14 is based on a total number of 1024 slices in t_1 , with a total acquisition time of about 2 days. Undeuterated methylmalonic acid was used, and the correlations of the respective carbon atoms with the remote protons can be identified in the first-order sidebands. Consequently, these contributions add up in the REPT-HDOR sideband patterns, where the chemical-shift information in t_1 is lost, to give increased first-order sideband intensities, as can be seen in insets (a) and (b). There, REPT-HDOR sidebands of the CH_3 signal are compared for the undeuterated and the partially deuterated form (on which all other measurements in this section were performed). The first-order sidebands measured on the latter sample are still higher than expected; this fact can straightforwardly be attributed to intermolecular remote couplings to other methyl groups.

An important fact yet to be mentioned is that analytical simulations based on Eq. (3.13), using an idealized tetrahedral methyl group, gave *negative* cross-peaks for the coupling between the methyl carbon and the CH proton, a fact, which has not been observed experimentally. Preliminary studies show that the signs and the magnitudes of the *remote* cross-signals depend not only on the relative distances, but also on the geometry of the spin system, in particular on the relative orientation of the average tensor for the intra- CH_3 coupling and the methyl-C-remote-H tensor. This puts restrictions on the calculation of distance constraints from peak intensities in correlation spectra, the derivation of which is thus a non-trivial procedure. On the other hand, applications to the determination of torsion angles could be envisaged, where a method without the need of selective labeling would greatly enhance the current methodology.

3.3.1 Spectral Editing Applications

The analytical treatment in the last section suggests the investigation of the build-up behavior of the spectral intensity of CH, CH_2 , and CH_3 -groups, as measured in 1D HMQ-filtered spectra, as a method to differentiate between these characteristic building blocks. Fig. 3.15a shows results of analytical simulations for these moieties, assuming CH distances of 1.14 Å

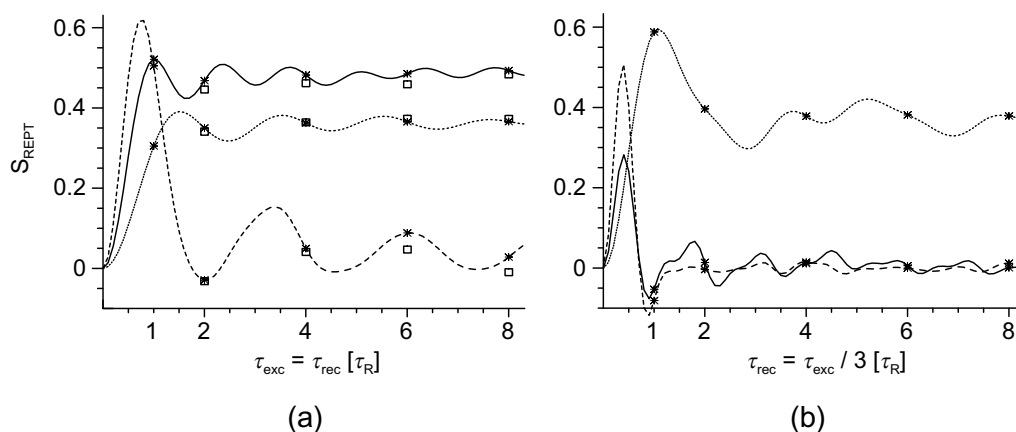


Figure 3.15: Build-up master curves for CH- (solid), CH₂- (dashed), and CH₃-groups (dotted lines), calculated using Eqs. (3.13) and (3.16), under standard conditions, i.e. $\tau_{exc} = \tau_{rec}$ (a), and for $\tau_{exc} = 3 \tau_{rec}$ (b). The experimentally accessible points for rigid moieties at 25 kHz and reconversion times of 1, 2, 4, 6, and 8 τ_R are indicated by asterisks. The squares in (a) are results from density matrix simulations additionally including homonuclear couplings and finite π -pulses of 4 μ s length.

and perfectly tetrahedral (sp^3 -hybridized) carbon atoms. Even at spinning speeds of 25 kHz, the rising part of the curves cannot be probed, as indicated by the asterisks. The methylene curve exhibits the striking feature of rapidly decaying to intensities close to zero for recoupling times larger than 1 τ_R . This has already been described in relation to the L-tyrosine measurements in Section 3.1, and is here shown to be explicable in terms of the simple theory based on heteronuclear couplings only.

As became obvious in Eq. (3.16), the rapid 3-site jumps of methyl groups result in three identical dipolar coupling tensors, and thus lead to contributions to the HMQ-filtered signal proportional to $\langle \sin N_{exc} \bar{\Phi}_0 \sin N_{rec} \bar{\Phi}_0 \rangle$ and $\langle \sin N_{exc} \bar{\Phi}_0 \sin 3N_{rec} \bar{\Phi}_0 \rangle$, where the former term explains the plateau value for the intensity at 37.5%. The latter term suggests that an experiment conducted with $\tau_{exc} = 3 \tau_{rec}$ should also lead to the observation of a plateau intensity, whereas the methyne and methylene signals should go to nearly zero at $\tau_{rec} > 1 \tau_R$. This is shown in Fig. 3.15b.

These results suggest that only a few 1D experiments, with excitation and reconversion times as discussed, should be sufficient for the differentiation of the four basic structural units in organic molecules, methyl, methylene, methyne, and quaternary carbons. A test of this spectral editing approach was performed on the amino acid L-isoleucine, which contains all

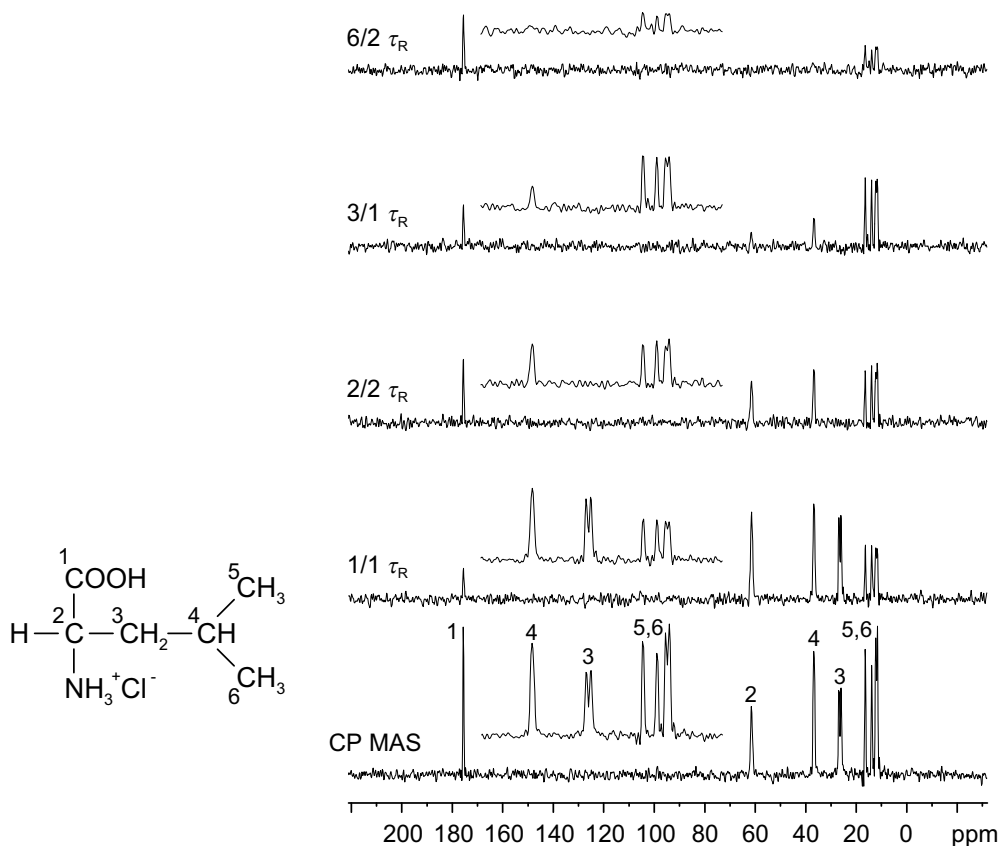


Figure 3.16: REPT-HMQ-filtered spectra of L-isoleucine, measured at 25 kHz MAS, with excitation and reconversion times as indicated. The assignments in the CP-MAS spectrum (bottom trace) are according to [Lesage 98b]. The multiple methylene and methyl lines are due to different crystallographic sites.

four kinds of carbon atoms, the results being shown in Fig. 3.16.

Methylene signals are most easily identified. Upon changing τ_{exc} and τ_{rec} from $1 \tau_R$ to $2 \tau_R$, they vanish completely. The transition to the spectra acquired under the asymmetric condition should, according to Fig. 3.15b, lead to the disappearance of the CH signals, which is experimentally observed for $6/2 \tau_R$. The (though weak) presence of these signals in the $3/1 \tau_R$ spectrum might be due to contributions of remote spins, and indicates deviations from the simple theory. As expected, the methyl intensities decrease with increasing recoupling times in the asymmetric spectra, whereas the quaternary carbon signal increases. Since the signal of quaternary carbons is more sensitive to local dipolar couplings to remote spins, this cannot be taken as a rule, even though experiments on other samples indicated the same

behavior.

In summary, methyne and methylene signals can unambiguously be identified with these 1D spectra, whereas some uncertainty remains for the quaternary and methylene signals. Nevertheless, the acquisition of a REPT-HDOR sideband pattern with $\tau_{rcpl} = 6 \tau_R$ at 25 kHz MAS is a possible way for an *unambiguous* assignment. Such a spectrum will yield the familiar pattern for a methyl group (see Figs. 3.11 or 3.14), and a spectrum dominated by first-order sidebands for quaternary carbons. CH-groups in turn show a multitude of spinning sidebands up to 13th order.

Considerable research efforts have been devoted to the development of spectral editing techniques in the solid state. Among the first approaches were separated local field methods [Sethi 91], CP-based methods [Wu 93, Wu 94, Sangill 94] using the concepts of polarization inversion or depolarization, and finally even methods utilizing ^{13}C - ^1H J-couplings [Lesage 98b]. Clearly, the latter approach is the only which is not critically influenced by molecular motion. Common to the mentioned dipolar-based methods are pulse sequences which require very careful set-up, and that they involve critical relative weighting of intensities of different spectra. The concepts presented here are, by comparison, based on a very simple pulse sequence, and CH- and CH_2 -groups can easily be identified by comparison of the 4 spectra, with some ambiguity only remaining for methyl and quaternary carbons.

3.3.2 Labeling Effects in HETCOR Spectra

A striking feature of some dipolar ^{13}C - ^1H HETCOR spectra is that samples in natural abundance exhibit more remote cross-signals than spectra taken of the same type of sample with global ^{13}C labeling. This has been observed for CP/WISE correlation spectra using FSLG homodecoupling for high proton resolution [Rossum 97], and is illustrated here for measurements on L-alanine (Fig. 3.17).

In the natural-abundance spectrum, the coupling of the CH proton to both the methyl and CO carbons can be identified. These peaks are missing in the spectrum of the globally labeled sample. To show the extent of such effects, proton slices of the CO carbon signal of the alanine samples are compared in Fig. 3.18 for increasing recoupling times. While in naturally abundant alanine all expected correlations can be identified, for the globally labeled

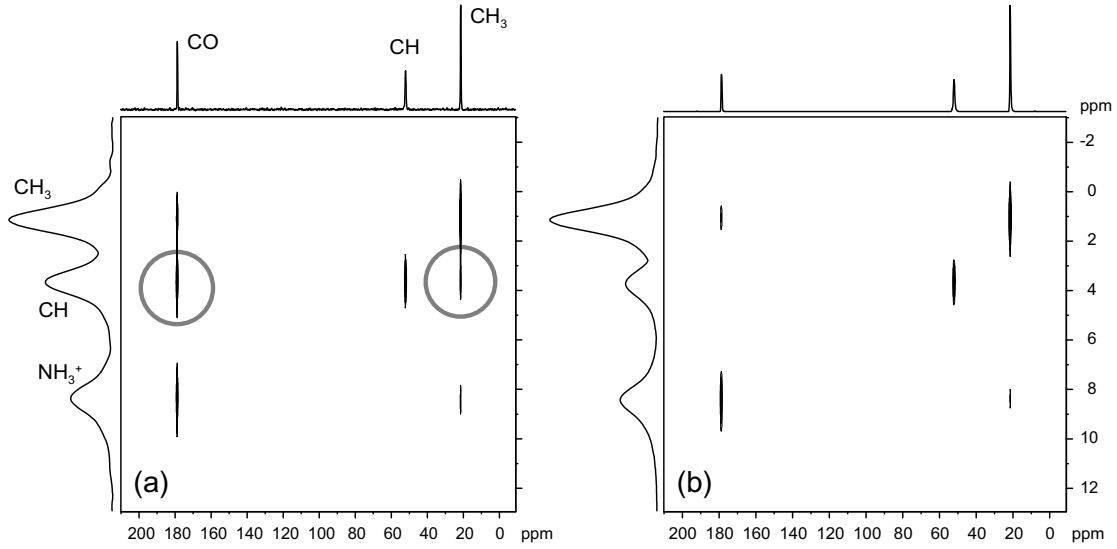


Figure 3.17: REPT-HSQ shift correlation spectra of L-alanine at 30 kHz MAS, with $\tau_{rept} = 4 \tau_R$, (a) with ^{13}C in natural abundance, and (b) with 100% labelling.

sample the cross peaks to the methyl protons, and even to a larger extent, cross peaks to the CH proton are suppressed, whereas the correlations to the COOH proton seem unaffected. The observed damping is a direct consequence of the fact that remote protons (as seen from the CO carbon) are directly bound to ^{13}C in the globally labeled sample. Pictorially, these carbons can be held responsible for dephasing the magnetization of the close protons before long-range correlations can build up [de Groot 99]. This kind of argument applies for the technique presented here, as well as to CP correlation techniques, since in both approaches transverse proton magnetization is involved as the initial state for the coherence transfer, and the strongest coupling dominates the spin dynamics in both cases.

In the case of REPT, the effect can even be described analytically. Considering one proton ($\hat{\mathbf{I}}$), one strongly coupled carbon ($\hat{\mathbf{S}}^s$) and the weakly coupled remote carbon ($\hat{\mathbf{S}}^w$), the spin dynamics of the excitation period reads

$$-\hat{I}_y \xrightarrow{N_{exc} \bar{\Phi}_0^s 2\hat{I}_z \hat{S}_z^s} -\hat{I}_y \cos N_{exc} \bar{\Phi}_0^s + 2\hat{I}_x \hat{S}_z^s \sin N_{exc} \bar{\Phi}_0^s \quad (3.17)$$

$$\xrightarrow{N_{exc} \bar{\Phi}_0^w 2\hat{I}_z \hat{S}_z^w} 2\hat{I}_x \hat{S}_z^w \cos N_{exc} \bar{\Phi}_0^s \sin N_{exc} \bar{\Phi}_0^w + 2\hat{I}_x \hat{S}_z^s \sin N_{exc} \bar{\Phi}_0^s \cos N_{exc} \bar{\Phi}_0^w + \dots \quad (3.18)$$

The remaining proton transverse magnetization term and the multi-spin term $\sim 4\hat{I}_y \hat{S}_z^s \hat{S}_z^w$ have been skipped in the last line, because they are filtered out in the course of the pulse sequence.

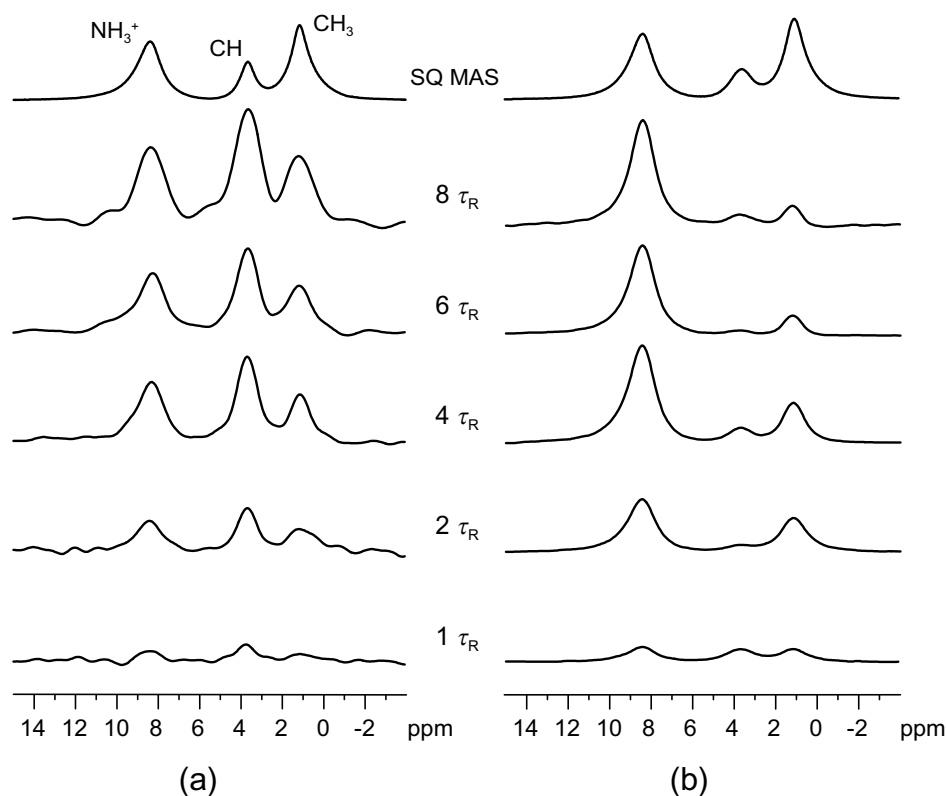


Figure 3.18: Sum slices (^1H spectra) of the CO signals in REPT-HSQC shift correlation spectra of L-alanine (30 kHz MAS), with recoupling times as indicated, (a) with ^{13}C in natural abundance, and (b) with 100% labelling.

The remaining two coherences are reconverted to give the cross signal of the proton with its directly attached carbon ($2\hat{I}_x\hat{S}_z^w$), and the remote cross signal ($2\hat{I}_x\hat{S}_z^w$). The signal resulting from the latter coherence will be proportional to $\langle \cos N_{exc} \bar{\Phi}_0^s \sin N_{exc} \bar{\Phi}_0^w \sin N_{rec} \bar{\Phi}_{t_1}^w \rangle$. It is the cosine with the acquired phase corresponding to the *strong* coupling which describes the mentioned dephasing, and is thus responsible for the damping of the intensity of such cross peaks. Clearly, these restrictions do not strictly apply for randomly enriched samples, as long as the degree of labeling is low enough to ensure the existence of a considerable fraction of protons bound to NMR-inactive ^{12}C .

3.3.3 Influence of Homonuclear Couplings

So far, the homonuclear couplings among the protons were neglected in the theoretical treatment, and the successful description of most of the spectral features justifies this approximation. Nevertheless, it cannot be expected that an influence of homonuclear couplings is completely absent, and in this section, results from simulations and measurements will be presented, which give some evidence for homonuclear effects.

A theoretical treatment of a system evolving under a combined homo- and heteronuclear dipolar coupling Hamiltonian is complex, and instead, numerical density matrix simulations will be used. This approach has the additional advantage that other adverse effects in real experiments, e.g. timing imperfections and finite pulses, can easily be incorporated.

In Fig. 3.19a/b, REPT-HDOR sideband patterns are compared for two arrangements of a second proton approaching a primary CH-pair. Note that ^1H - ^1H distances as indicated are unphysical ($r_{HH} = 1.24 \text{ \AA}$ corresponds to $D_{HH} = 61 \text{ kHz}$); the closest proton-proton distance usually found is 1.8 \AA , and occurs within methyl or methylene groups. These parameters were chosen because a pronounced effect only sets in at such unphysically high homonuclear couplings. The background traces are calculated from the analytical formulae, which take only heteronuclear couplings into account. The similarity of these patterns indicates that the carbon-remote proton distances are still too large to exert appreciable heteronuclear perturbations in all cases. The total intensity is seen to decrease upon the approach of the remote proton, and the odd-order sideband intensities become increasingly distorted. Additionally, even-order sidebands and, in the non-linear case, a centerband appears. The latter effect is *solely* due to the finite recoupling pulses, if δ -pulses are used, only a strong decrease in intensity, mainly of the first-order sidebands, is observed for both the perpendicular and the linear case. Again it should be emphasized that for reasonable inter-proton distances, almost no influence of homonuclear couplings is visible in the patterns.

These conclusions seem contradictory to previous studies [Saalwächter 99a], and to the experimental results on ammonium formate (Fig. 3.5). At a second glance, however, this is not surprising, since here, REPT-HDOR patterns are discussed, whereas the mentioned results refer to experiments with actual HMQ *evolution* during t_1 . For comparison, REPT-HMQ sideband patterns are also shown in Fig. 3.19, and are seen to exhibit higher even-order sidebands. This result therefore again stresses the advantage of the HDOR approach,

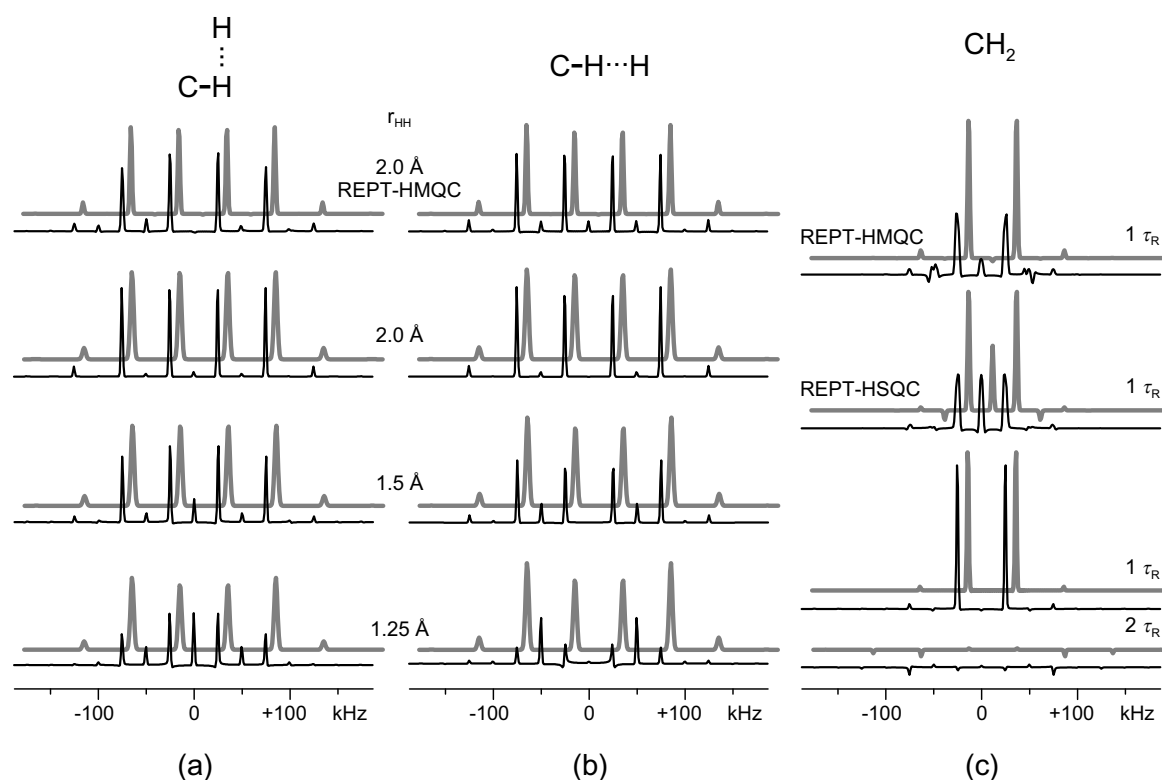


Figure 3.19: REPT-HDOR sideband patterns from numerical density matrix simulations for three different arrangements of a CH-pair ($r_{CH} = 1.14 \text{ \AA}$, $D_{CH} = 20.4 \text{ kHz}$) and an additional proton for 25 kHz MAS and $\tau_{rcpl} = 2 \tau_R$, assuming finite π -pulses of $4 \mu\text{s}$ length. For the methylene group in (c), an HCH-angle of 109.5° was used, and the recoupling times are as indicated. The grey background traces are analytical results based on Eq. (3.13). REPT-HMQ and REPT-HSQ patterns are also shown for comparison.

where the only possible evolution during t_1 are homonuclear spin flip-flops, the influence of which is obviously negligible. The REPT-HDOR experiment is thus well-suited to study the effect of reconversion rotor encoding (RRE) in a well-isolated fashion. By comparing the numerical and analytical HMQ patterns it can be concluded that the homonuclear contribution to evolution rotor modulation (ERM) is apparently stronger than the heteronuclear one.

In earlier studies on homonuclear dipolar and also “homonuclear” quadrupolar systems (which served as a model system for the dipolar case) [Friedrich 98a], it was not possible to experimentally distinguish between RRE and ERM, the latter of which also leads to spinning sidebands in the t_1 dimension. ERM was shown to lead to additional odd-order spinning sidebands and centerbands in MQ spectra. This is here illustrated by the simulated spectra

for a methylene group (Fig. 3.19c). In this case, the perturbing heteronuclear coupling to the second proton is strong enough to lead to an almost complete loss of intensity for $\tau_{rcpl} = 2 \tau_R$. The experimental HMQ patterns for $1 \tau_R$ recoupling (measurements on L-tyrosine, Fig. 3.3b) exhibit the mentioned deviations from the expected pair pattern.

The simulations for REPT-HSQ and -HMQ sideband patterns in Fig. 3.19c were calculated using the same artificial line broadening (2.5 kHz) as for the HDOR patterns. Therefore, the observed larger relative line broadenings (thus lower absolute intensities) are due to homonuclear couplings during t_1 , while the high centerband intensity for the HSQ spectrum is in part to be attributed to the dipolar correction to the time-evolution formula (Eq. (3.9)). The additional dipolar evolution of the spin-pair state under investigation during t_1 as described by this term does not occur when the evolution of an HMQ coherence is monitored. Thus, the comparison of *REPT-HDOR* with *REPT-HMQ* sideband patterns gives direct evidence for evolution rotor modulation. In particular, the influence of couplings to remote spins can be quantified.

In the first publication of the REPT-HMQC technique [Saalwächter 99b], most π -pulses during excitation were applied on the proton channel, which proved disadvantageous, and lead to signal loss at longer recoupling times. It is advisable to apply REDOR π -pulses on the channel, where only longitudinal magnetization is to be inverted. In order to explore the nature of this signal loss, HMQ build-up curves, measured for the CD carbon of partially deuterated methylmalonic acid, are compared for the two possibilities in Fig. 3.20a. The experiment with the pulse train on the protons (the central π -pulse is always applied on the other channel to ensure refocusing of the chemical shift interaction) gives roughly only *half* the maximum signal, indicating a strong interplay of the π -pulses and the ^1H homonuclear coupling. Four-spin simulations (three methyl protons and the CD carbon) proved that the decrease in intensity is indeed caused by *finite* pulses (open symbols). The simulations can, however, not account for the damping of the intensity at longer recoupling times, which has been shown in the previous section to be due to heteronuclear couplings to numerous remote methyl groups (dotted line). Density matrix simulations with such large numbers of spins are not feasible, and thus it was not attempted to model the data with the many π -pulse on ^1H .

In Fig. 3.20b, the influence of finite π -pulses of varying length, applied on ^{13}C and ^1H during excitation, is explored. No difference is discernible when π -pulses of 4 or 8 μs length are used when the train is applied on the carbon channel, and the simulations confirm this

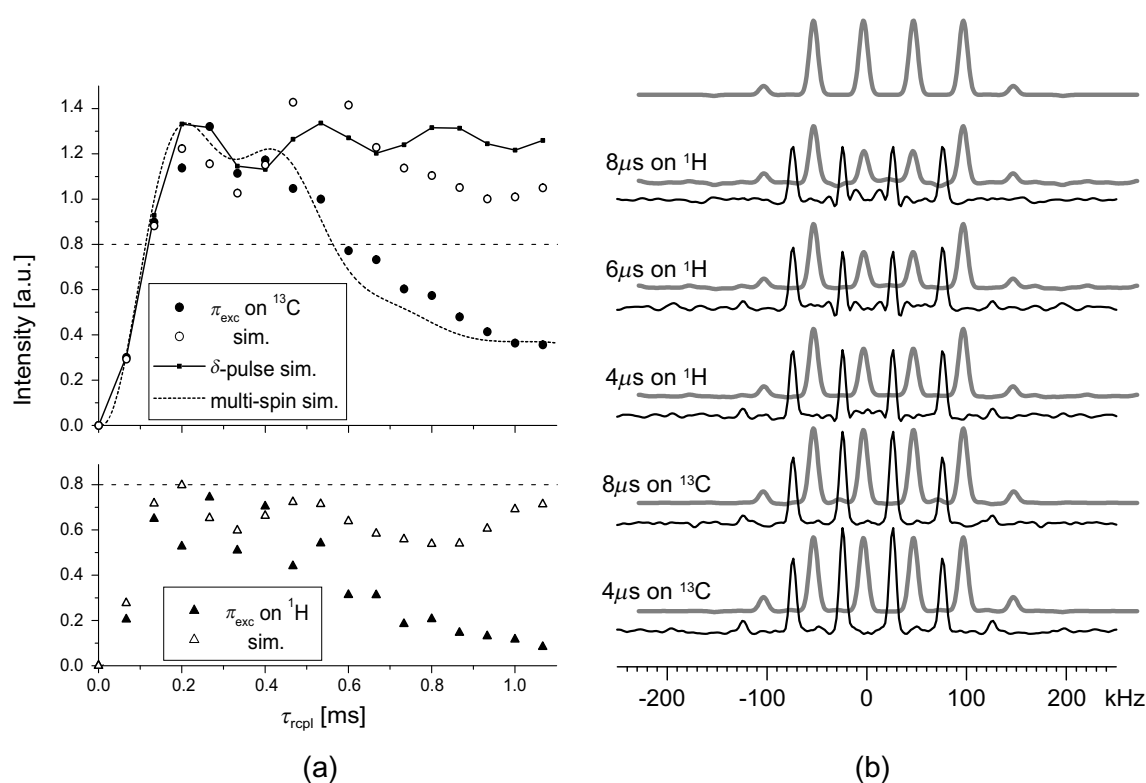


Figure 3.20: Build-up data and spectra from experiments on partially deuterated methylmalonic acid, showing the influence of homonuclear couplings on the REPT-HMQ intensity build-up for the CH carbon (a), and on REPT-HDOR sideband patterns of the methyl signal (b). The points in the two diagrams in (a) are plotted on the same vertical scale (with the dashed horizontal lines at $I = 0.8$ for comparison), and the dotted curve in the upper diagram is the same theoretical curve as in Fig. 3.13b. The π -pulse trains during the excitation period were applied on the carbon and on the proton channel, and the length of the pulses, thus the B_1 -field strength, was varied in (b), where the grey background traces are simulations using the experimental parameters. For the upper trace, δ -pulses were assumed.

result (again, experimental first-order sidebands are higher than expected). By comparison, the first-order sidebands suffer an intensity loss upon application of the excitation train to the proton channel, and a further slight deterioration is observed for longer pulses, which is also reproduced by the simulations.

In summary, homonuclear effects cannot be neglected if the π -pulses during excitation are applied to the proton channel, and the interplay of proton transverse magnetization, homonuclear couplings, and finite π -pulses, leads to HMQ signal loss and distortions in the spinning sideband patterns. These effects are reminiscent of the results of Goetz and Schae-

fer [Goetz 97], who observed deviations from the ideal REDOR dephasing in CF_2 -groups, where the different chemical shift of the fluorine atoms within these groups, together with the rather strong fluorine homonuclear coupling, was identified as the source of error. In a paper of Gullion and Vega [Gullion 92], it was shown that the presence of an isotropic chemical shift difference leads to dephasing in homonuclear experiments, where π -pulses are applied once per τ_R . In both cases, the isotropic chemical shift difference is identified as a necessary prerequisite for the observation of distortions due to the homonuclear coupling.

The effect observed here is new in that not the isotropic chemical shift, but rather finite pulses introduce the homonuclear effects. Further theoretical work is necessary to explore the nature of this effect, especially since the effects of finite pulses on REDOR recoupling have not yet been investigated in detail. The results presented in the Section 3.2 and 3.3 are currently being prepared for publication [Saalwächter 00a].

3.4 Comparison of the REPT Variants

In this chapter, several implementations of the REPT technique were presented. The order in which the variants appeared, namely the introduction focusing on REPT-HMQC, and the subsequent description of REPT-HSQC and REPT-HDOR, followed the order in which these experiments were actually investigated, and does not reflect any emphasis on the utility of each of the techniques for specific applications.

In summary, the **REPT-HSQC** is the method of choice for **heteronuclear ^{13}C - ^1H shift correlation**, i.e. rotor-synchronized 2D spectra. Spinning-sidebands *can* be obtained using this sequence (as shown in Fig. 3.14), and these consequently contain chemical-shift information. This information is useful only when contributions of different protons to a spinning-sideband pattern of a specific carbon nucleus are to be separated. However, the high resolution in t_1 needed for this application, and thus the large number of slices to be acquired, limits the applicability of this approach.

Spinning-sideband patterns are most conveniently measured with the **REPT-HDOR** sequence, for the reasons given in Section 3.2.2. The loss of chemical-shift information in t_1 means that the ^1H nucleus involved in the coupling constant reflected in the pattern has to be known. This complementary information can be obtained by measuring a shift correlation

spectrum separately, if no reasonable assumption is available (which is usually the case). The pattern always reflects the strongest pair coupling in a CH_n system, and the contributions of weak secondary couplings are present only in the first-order sidebands, which can be excluded from the fit. Only if no dominant coupling is observed, the measurement of a chemical-shift resolved pattern (using REPT-HSQC) cannot be circumvented.

Finally, on account of the very-fast MAS frequencies used in these experiments, homonuclear ^1H - ^1H effects were found to be virtually absent in most realistic systems (with the exception of methylene groups, and when the excitation π -pulse train is applied to the protons). The modulation of the coherence evolving in t_1 by homonuclear, and, more importantly, by heteronuclear couplings to additional ^1H spins (i.e. ERM) was shown to be absent in REPT-HDOR spinning-sideband patterns. Only when the effects of **ERM** due to additional protons are to be investigated, does the comparison of HDOR with **HMQC** sideband patterns allow to quantify these effects. REPT-HSQC patterns are slightly distorted by the dipolar t_1 evolution of the spin-pair antiphase coherence itself (Eq. (3.9)), while the REPT-HMQC suffers complications due to the timing problem introduced by the central π -pulse, which leads to small phase errors in t_1 and a slightly reduced overall intensity.

Chapter 4

Symmetric Dipolar Heteronuclear Multiple-Spin Correlation

The experiments to be discussed below have a closer relationship to the original REDOR concept than the REPT techniques discussed in the last chapter. We will deal with *symmetric* pulse sequences, where initial S-spin (^{13}C) magnetization, as usually generated by an initial CP step, is employed, such that S-spin transverse coherence is involved during both the excitation and reconversion periods of the experiment (in contrast to the asymmetric REPT). Generally, this class of experiments will be referred to as DIP-HMSC, for *dipolar heteronuclear multiple-spin correlation*, on account of the possibility of exciting multi-spin coherences involving two or more nuclei with these techniques.

4.1 DIP-HMSC of IS-Pairs and RELM

Fig. 4.1 depicts several variants of spinning-sideband generating HMSC experiments, which were designed to probe different coherence states during t_1 . The theoretical concepts and formulae describing the spectra of single IS-pairs are identical to the ones for the asymmetric REPT techniques (Eqs. (3.1)–(3.9)), and the fundamentals for the description of the sideband-generating mechanism are the same as in Section 2.2.2. Therefore, all spin-pair related aspects will not be repeated here.

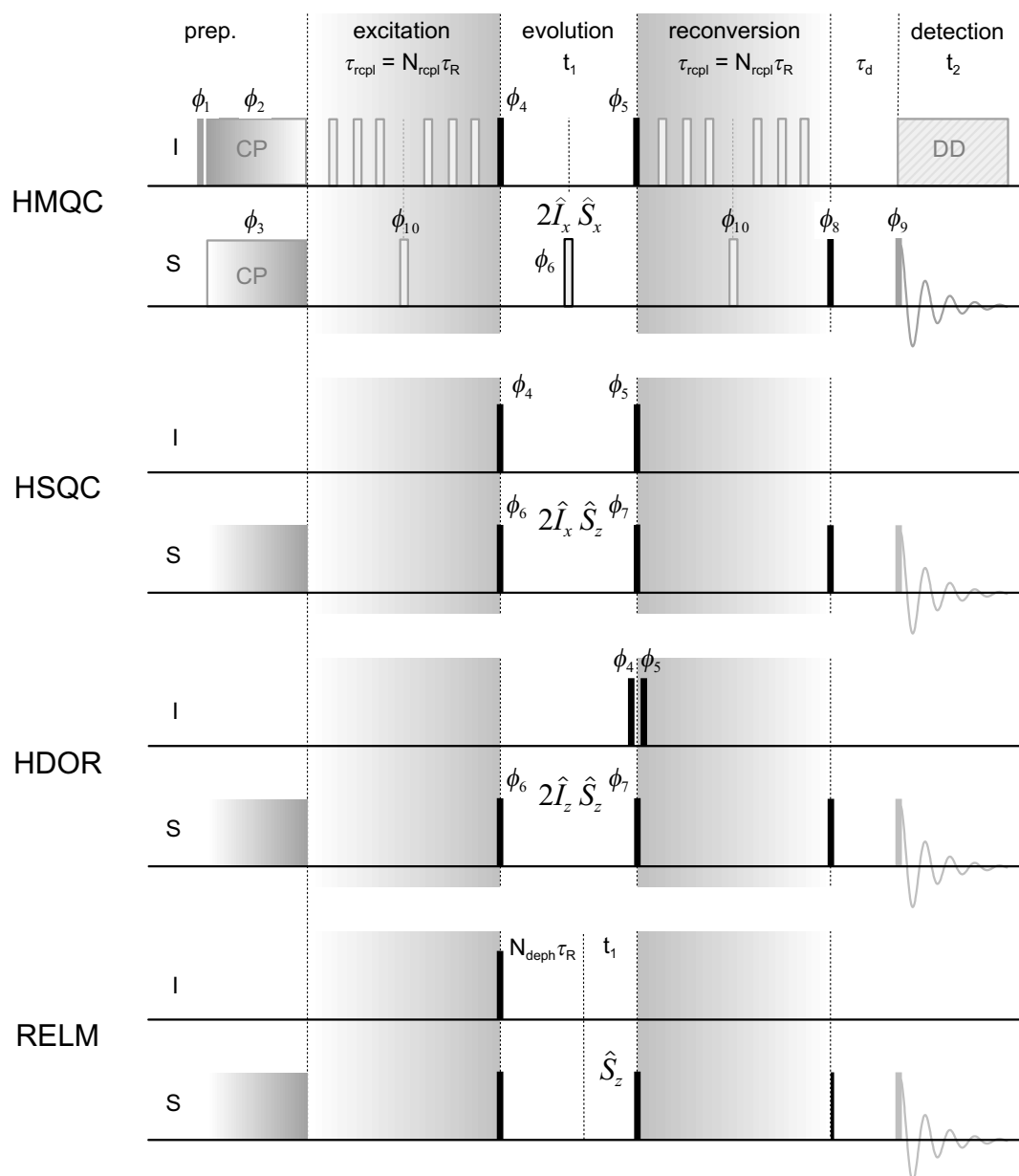


Figure 4.1: Different variants of symmetric dipolar HMS correlation experiments, and RELM. The upper three experiments are the analogs of the REPT sequences shown in Fig. 3.8, p. 75, while the bottom pulse sequence generates spinning-sideband patterns through rotor-encoding of longitudinal magnetization (RELM) [De Paul 00]. The phases for the upper three experiments are listed in Appendix E.3. Usually, the excitation and reconversion periods have equal length.

A few comments shall, however, be made on the possibility of choosing different excitation and reconversion times, $N_{exc} \tau_R$ and $N_{rec} \tau_R$, respectively. The effects of asymmetric recoupling periods on spinning-sideband patterns were investigated in detail for the RELM experiment (bottom of Fig. 4.1), where rotor-encoding of the single S-spin transverse coherence (stored as longitudinal magnetization during t_1) is monitored [De Paul 00]. As can be inferred from Eq. (2.11) and the definitions of the phases in Eq. (2.25), the t_1 time-domain signal is

$$S_{RELM} = \langle \cos N_{exc} \bar{\Phi}_0 \cos N_{rec} \bar{\Phi}_{t_1} \rangle, \quad (4.1)$$

which leads to spectra dominated by a centerband and *even*-order sidebands. The intensities of these sidebands are given by

$$I_{2n} = \frac{1}{2} \int_{\beta=0}^{\pi} J_{2n}(N_{exc} \frac{D_{SL}}{\omega_R} 2\sqrt{2} \sin 2\beta) J_{2n}(N_{rec} \frac{D_{SL}}{\omega_R} 2\sqrt{2} \sin 2\beta) \sin \beta d\beta. \quad (4.2)$$

This equation is completely analogous to Eq. (2.27), which was derived for the odd-order sidebands generated by the other three experiments in Fig. 4.1 (there, $S \sim \langle \sin \dots \sin \dots \rangle$). In [De Paul 00], it was found that, for certain ratios N_{exc}/N_{rec} at fixed ω_R , sideband intensities of specific (even) orders can be negative or even vanish. Such zero crossings are a sensitive measure of D_{SL} . Yet, such asymmetric excitation/reconversion leads to severe losses in intensity, since $\langle \cos N_{exc} \bar{\Phi}_0 \cos N_{rec} \bar{\Phi}_{t_1} \rangle \rightarrow 0$ for $N_{exc} \neq N_{rec} \rightarrow \infty$.¹ This has been exploited for the spectral editing applications in the last chapter, where, by virtue of the different coupling topologies during the excitation and reconversion periods in the REPT experiment for CH₃ groups, a factor of three appears in the argument of the sine-function, creating an asymmetric situation. In general, however, this loss in intensity leaves the experiments with $N_{repl} = N_{exc} = N_{rec}$ as the more feasible ones for the determination of dipolar couplings.

The details about the RELM experiment can be found in [De Paul 00]. The important and most interesting aspect of all of the symmetric methods is the entirely different behavior (as opposed to REPT) when multi-spin systems are considered. In particular, the focus will be on systems with isolated ¹³C spins, coupled to a number of protons. It will be shown that HMQ coherences, which comprise higher quantum orders in the I-spins, can be excited and detected.

¹Similarly, $\langle \sin N_{exc} \bar{\Phi}_0 \sin N_{rec} \bar{\Phi}_{t_1} \rangle \rightarrow 0$ for $N_{exc} \neq N_{rec} \rightarrow \infty$.

4.2 DIP-HMSC in Systems with Multiple I-Spins

For the theoretical considerations in this section, the evolution of a single S-spin, coupled to n I-spins, will be evaluated. Homonuclear couplings among the I-spins will be neglected. Experiments will be shown which demonstrate that this is an excellent approximation even when protons are the I-spins, provided that the experiments are conducted at spinning frequencies exceeding about 20 kHz. The excitation period of the symmetric HMSC experiments consists of free evolution of \hat{S}_x transverse coherence in the local field of the I-spins:

$$\hat{S}_x \xrightarrow{N_{exc} \sum_i \bar{\Phi}_0^{(i)} 2\hat{S}_z \hat{I}_z^{(i)}} \hat{S}_x \prod_i \cos N_{exc} \bar{\Phi}_0^{(i)} \quad (4.3)$$

$$+ \sum_j 2\hat{S}_y \hat{I}_z^{(j)} \sin N_{exc} \bar{\Phi}_0^{(j)} \prod_{i \neq j} \cos N_{exc} \bar{\Phi}_0^{(i)} \quad (4.4)$$

$$- \sum_{j < k} 4\hat{S}_x \hat{I}_z^{(j)} \hat{I}_z^{(k)} \sin N_{exc} \bar{\Phi}_0^{(j)} \sin N_{exc} \bar{\Phi}_0^{(k)} \prod_{i \neq j, k} \cos N_{exc} \bar{\Phi}_0^{(i)} \quad (4.5)$$

$$- \sum_{j < k < l} 8\hat{S}_y \hat{I}_z^{(j)} \hat{I}_z^{(k)} \hat{I}_z^{(l)} \sin N_{exc} \bar{\Phi}_0^{(j)} \sin N_{exc} \bar{\Phi}_0^{(k)} \sin N_{exc} \bar{\Phi}_0^{(l)} \\ \times \prod_{i \neq j, k, l} \cos N_{exc} \bar{\Phi}_0^{(i)} \quad (4.6)$$

⋮

$$= \hat{\rho}(N_{exc} \tau_R)_-,$$

We see that the density operator at the end of the excitation period, $\hat{\rho}(N_{exc} \tau_R)_-$, i.e. before further pulses are applied (as indicated by the “-” subscript), is composed of multi-spin antiphase coherences. For the dephased intensity in a REDOR experiment, S , a π -pulse is applied to the above coherences. Such a π -pulse inverts every other term because, for a pulse on spin S, every other $\hat{S}_{x/y}$ -phase in Eqs. (4.3)–(4.6) is shifted by 180° (sign inversion), or, for a pulse on I, products with even numbers of \hat{I}_z -operators are not inverted. This reflects the property of the analogous internal difference REDOR experiment (i.e. the sequences depicted in Fig. 4.1 with $t_1 = 0$, $\phi_4 = x$ and $\phi_5 = \pm x$ and constant and equal phases ϕ_6 and ϕ_7) of being an *odd-order selective multiple-quantum filter* (vide infra). During reconversion, all of the above coherences acquire respective sine and cosine phases (with the same argument when $t_1 = 0$, since $N_{rec} = N_{exc}$), and evolve back into observable \hat{S}_x -magnetization, with the signs

depending on the number of \hat{I}_z -multipliers. The signal for a single crystallite is thus

$$S_{\pm} = + \prod_i \cos^2 N_{rcpl} \bar{\Phi}_0^{(i)} \quad (4.7)$$

$$\mp \sum_j \sin^2 N_{rcpl} \bar{\Phi}_0^{(j)} \prod_{i \neq j} \cos^2 N_{rcpl} \bar{\Phi}_0^{(i)} \quad (4.8)$$

$$+ \sum_{j < k} \sin^2 N_{rcpl} \bar{\Phi}_0^{(j)} \sin^2 N_{rcpl} \bar{\Phi}_0^{(k)} \prod_{i \neq j, k} \cos^2 N_{rcpl} \bar{\Phi}_0^{(i)} \quad (4.9)$$

$$\mp \sum_{j < k < l} \sin^2 N_{rcpl} \bar{\Phi}_0^{(j)} \sin^2 N_{rcpl} \bar{\Phi}_0^{(k)} \sin^2 N_{rcpl} \bar{\Phi}_0^{(l)} \prod_{i \neq j, k, l} \cos^2 N_{rcpl} \bar{\Phi}_0^{(i)} \quad (4.10)$$

⋮

where the \pm -subscript indicates the sign of the second 90° -pulse in an internal difference REDOR experiment or, equivalently, the existence or omission of the central π -pulse. For the reference spectrum, the complete initial magnetization is regained ($S_0 = \langle S_- \rangle$), whereas the dephased signal, S , reduces to

$$S = \langle S_+ \rangle = \left\langle \prod_i \cos 2N_{rcpl} \bar{\Phi}_0^{(i)} \right\rangle. \quad (4.11)$$

This result can directly be obtained by calculating the full REDOR evolution for the integral excitation and reconversion time $2N_{rcpl}\tau_R$ [Goetz 97]. The multiple-quantum signal as created by the phase cycle is $S_{MQ} \sim (S - S_0) = \Delta S$. As opposed to REPT, it can be normalized (i.e., corrected for relaxation effects) by dividing by $2S_0$, which can be measured separately.

Using the pulse sequence depicted at the top of Fig. 4.1, the S-spin transverse and the multi-spin antiphase coherences in Eqs. (4.3)–(4.6) can be converted into various kinds of HMQ coherences, the evolution of which can be probed during t_1 . A 90° -pulse on the protons converts these coherences into

$$\begin{aligned} \hat{\rho}(N_{exc} \tau_R -) &\xrightarrow{\frac{\pi}{2} \hat{I}_y} \hat{S}_x c^n + \sum_j 2 \hat{S}_y \underbrace{\hat{I}_x^{(j)}}_{\text{SQ}} s c^{n-1} - \sum_{j < k} 4 \hat{S}_x \underbrace{\hat{I}_x^{(j)} \hat{I}_x^{(k)}}_{\text{DQ+ZQ}} s^2 c^{n-2} \\ &- \sum_{j < k < l} 8 \hat{S}_y \underbrace{\hat{I}_x^{(j)} \hat{I}_x^{(k)} \hat{I}_x^{(l)}}_{\text{SQ+TQ}} s^3 c^{n-3} + \dots, \end{aligned} \quad (4.12)$$

where a shorthand notation for the sine- and cosine phase factors has been used. As indicated, the product operators for the I-spins comprise mixtures of different multiple-quantum coherences, coupled to S-spin transverse coherence. As pointed out in Chapter 2, it is more convenient to treat the S-spin contribution separately, since it can be manipulated independently. For a coherence like $4\hat{S}_x\hat{I}_x^{(j)}\hat{I}_x^{(k)}$, the DQ coherence in the I-spin subspace can be selected by a phase cycle on the I-spins, and when the S-spin transverse coherence is included, it becomes a mixture of HSQ and HTQ coherences. There is no need to decide upon the selection of either \hat{S}_+ or \hat{S}_- , since S-spin chemical-shift evolution can be refocused.

The I-spin MQ contribution can also be probed in antiphase to the S-spin, if a 90° -store-pulse is applied to the S-spin prior to t_1 . This variant of the experiment is shown as second pulse sequence in Fig. 4.1. It is analogous to the HSQC experiment presented in Chapter 3, even though, strictly speaking, the coherences probed in the multi-I-spin case need not be heteronuclear *single*-quantum coherences. With this modification, the influence of the S-spin CSA (Eq. (3.8), p. 78) during t_1 and the heteronuclear contribution to ERM (Eq. (3.14), p. 84) are suppressed. The evolution of the $I_{MQ}S_{antiphase}$ -coherence under the IS-dipolar coupling must then be considered in analogy to Eq. (3.9), p. 79, with the difference that the situation here is a little simpler in that the MQ coherence picks up cosine factors of the form $\cos\Phi_{D_{IS}}^{(i)}(t_1)$ for all I-spins which are part of the coherence (see Fig. 4.11 for experimental evidence of this small effect). Rotor-synchronized HSQ shift correlation spectra can be recorded with twice the spectral width of the corresponding HMQC experiment, since the π -pulse in the middle of t_1 necessitates a t_1 increment of $2\tau_R$ for HMQC, if artifacts from incomplete CSA refocusing are to be avoided.

The reason for the versatility of the heteronuclear approach to MQ spectroscopy is the aforementioned possibility of selecting different coherence orders for each spin species. In our case, the phase cycle for the S-spin part consists of an SQ selection, along with 180° -pulse artifact suppression (EXORCYCLE) and quadrature artifact removal (CYCLOPS). As a *supercycle*, a multiple-quantum filter is implemented on the I-spins, the simplest example of which is the $\pm x$ phase inversion of the I-spin 90° -pulse after t_1 (ϕ_5 in Fig. 4.1) along with a receiver phase inversion. This 2-step cycle selects all odd-order coherences of the I-spins, i.e. $\dots -3 (-2) -1 (0) +1 (+2) +3\dots$. It will be henceforth referred to as the *HMQ* filter.

For the design of higher-order filters, one has to bear in mind that the S-spins act as single-channel “receiver”. No phase information can be transferred from one spin species to

the other as a result of the different rotating frames [Maudsley 77]. Therefore, the “filter-width”, i.e. the specificity of the desired quantum order, depends on the quantum order itself. Since an n -quantum coherence inverts its sign upon a relative phase change of $180^\circ/n$, only $2n$ -step-cycles are possible. This is the reason that, if I-spin SQ selection is wanted ($n=1$, i.e. the internal difference REDOR signal is selected), the phase-cycle has 2 steps, and I-spin TQ and higher odd order contributions cannot be suppressed.

It should again be emphasized that the DIP-HMQC experiments can be *referenced* by performing an experiment with $t_1 = 0$ and two effective π -pulses (one on each channel) in the middle of the sequences, which yields S_0 . The effective π -pulses correspond to no inversion of the dipolar evolution. This could also be achieved by applying *no* central pulses at all (which is done in the case of REDOR). Here, when a 2D-spectrum is to be referenced, the additional slight signal loss due to the ^{13}C conversion and reconversion pulses has to be accounted for in the reference. In conclusion, and in marked contrast to REPT, absolute MQ intensities are accessible with these methods, opening up the possibility of determining dipolar couplings from build-up data. This will be tested experimentally in Section 4.5.

As a more specific example of the principles outlined above, we will now sketch the derivation of formulae describing the HMQ build-up behavior and the t_1 time dependence for the signal of an isolated CH_3 -group. This is a particularly simple case since by virtue of the fast 3-site jumps, all three heteronuclear dipolar coupling tensors, and thus the integrated phases, $\bar{\Phi}^{Me}$, are equal. Furthermore, the isotropic chemical shifts of the protons are identical. The regular HMQ- (i.e. I-spin odd-order) filtered intensity is the sum of Eqs. (4.8) and (4.10) with $n = 3$:

$$S_{MQ}^{Me} = 3 \left\langle \sin^2 N_{rcpl} \bar{\Phi}_0^{Me} (\cos^2 N_{rcpl} \bar{\Phi}_0^{Me})^2 \right\rangle + \left\langle (\sin^2 N_{rcpl} \bar{\Phi}_0^{Me})^3 \right\rangle \quad (4.13)$$

The build-up of HMQ intensity is depicted in Fig. 4.2. It is noteworthy that although the 3I-spin contribution (second term in Eq. (4.13)) grows in more slowly upon increasing N_{rcpl} , it reaches higher intensities for longer recoupling times and thus contributes more strongly to the final HMQ-filtered signal. The indicated plateau values for the limits of $N_{rcpl} \rightarrow \infty$ can be derived by application of the familiar addition theorems for trigonometric functions to the products of sines and cosines of $\bar{\Phi}_0^{Me}$, e.g. for the 3I-spin term we obtain (with $a = N_{rcpl} \bar{\Phi}_0^{Me}$)

$$\left\langle \sin^6 a \right\rangle = \frac{1}{32} \left\langle 10 - 15 \cos 2a + 6 \cos 4a - \cos 6a \right\rangle \stackrel{N_{rcpl} \rightarrow \infty}{=} \frac{10}{32}. \quad (4.14)$$

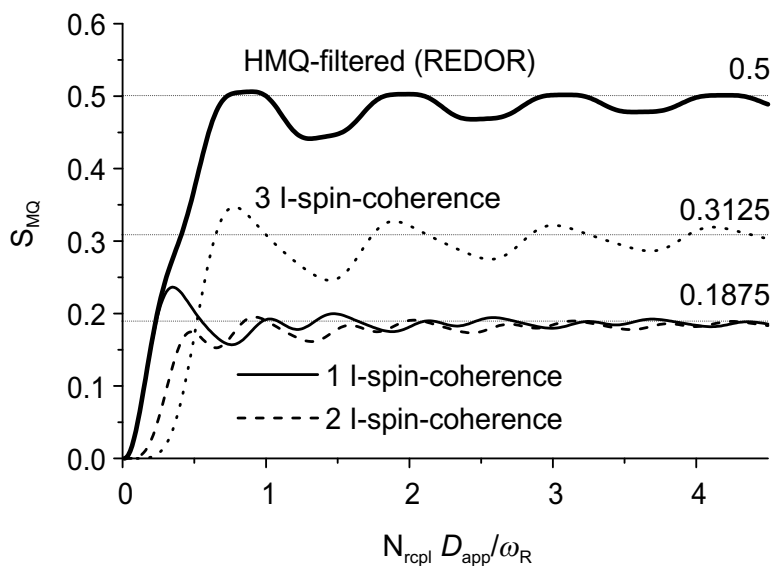


Figure 4.2: Dipolar DIP-HMQ build-up curves for three contributions to the signal of a rotating SI_3 -group (with an averaged apparent coupling constant, D_{app} , defined in Eq.(3.15)). The HMQ-filtered curve is the sum of the 1I-spin (Eq. (4.8)) and 3I-spin (Eq. (4.10)) contributions, and is equivalent to a REDOR curve, described by Eq. (4.11). The 2I-spin curve (Eq. (4.9)) represents the build-up of I-(DQ+ZQ) intensity (only half of this signal corresponds to the actual I-DQ-filtered intensity). The plateau values for $N_{rcpl} \rightarrow \infty$ are indicated by thin dotted lines.

By inserting the definition of the shift operators, Eq. (1.13), in the form $\hat{I}_x = \frac{1}{\sqrt{2}}(\hat{I}_+ + \hat{I}_-)$ into the different terms of Eq. (4.12), the fractions with which the different coherence orders in the I-spin subspace contribute to the individual n-spin coherences can easily be derived. Thus, the 2I-spin coherence consists of DQ and ZQ contributions in equal parts, while the 3I-spin coherence has 75% SQ and 25% TQ contributions.

The t_1 time dependence for the HMQ or HSQ experiments (including isotropic chemical shifts) is obtained by taking the t_1 -dependence of the dipolar phases, $\bar{\Phi}_{t_1}^{Me}$, during reconversion into account (for a definition see Eq. (2.25)). Thus each \sin^2 in Eq. (4.13) (or (4.7)–(4.10) in the general case) is replaced by a product of the form $\sin \bar{\Phi}_0^{Me} \sin \bar{\Phi}_{t_1}^{Me}$ (similarly for the \cos^2 terms). The transverse I-spin contributions pick up cosines and sines of the chemical-shift phases for each I-spin, and the x- the y-components of the t_1 -signal are given by

$$S_x^{Me} = \left\langle \cos \omega_{CS,t_1} \sin N_{rcpl} \bar{\Phi}_0^{Me} \sin N_{rcpl} \bar{\Phi}_{t_1}^{Me} (\cos N_{rcpl} \bar{\Phi}_0^{Me} \cos N_{rcpl} \bar{\Phi}_{t_1}^{Me})^2 \right\rangle + \left\langle \cos^3 \omega_{CS,t_1} (\sin N_{rcpl} \bar{\Phi}_0^{Me} \sin N_{rcpl} \bar{\Phi}_{t_1}^{Me})^3 \right\rangle, \quad (4.15)$$

$$\begin{aligned}
S_y^{Me} = & \left\langle \sin \omega_{CS,I} t_1 \sin N_{rcpl} \bar{\Phi}_0^{Me} \sin N_{rcpl} \bar{\Phi}_{t_1}^{Me} (\cos N_{rcpl} \bar{\Phi}_0^{Me} \cos N_{rcpl} \bar{\Phi}_{t_1}^{Me})^2 \right\rangle \\
& + \left\langle \sin^3 \omega_{CS,I} t_1 (\sin N_{rcpl} \bar{\Phi}_0^{Me} \sin N_{rcpl} \bar{\Phi}_{t_1}^{Me})^3 \right\rangle.
\end{aligned} \tag{4.16}$$

The $\cos^3 \omega_{CS,I} t_1$ and $\sin^3 \omega_{CS,I} t_1$ terms contain the effective evolution frequencies for the 3I-spin coherence, e.g.,

$$\sin^3 \omega_{CS,I} t_1 = \frac{3}{4} \sin \omega_{CS,I} t_1 - \frac{1}{4} \sin 3\omega_{CS,I} t_1. \tag{4.17}$$

This proves again the 25% contribution of I-spin TQ to this coherence, and shows that in the HMQ-filtered case, the TQ part evolves with $3\omega_{CS,I}$ but in the *opposite* direction to the SQ part (minus sign in Eq. (4.17)). If a pure I-TQ signal is selected, sign discrimination of the effective chemical-shift evolution in t_1 is achieved by time-proportional phase incrementation (TPPI, generalized for MQ experiments [Munowitz 87a]) of the second proton pulse (ϕ_5 in Fig. 4.1) by $90^\circ/n$, with $n = 3$ for TQ coherences. This procedure ensures that for an n -quantum coherence, a 90° phase-shifted component of the chemical-shift signal is detected on alternate scans, and it has the additional benefit that contributions from unwanted lower-order coherences (which may survive due to imperfections in the MQ-filter phase cycling) reside in regions of the spectrum where, due to the artificial offset introduced by the TPPI, no signal from the coherence of interest would reside. Unwanted higher-order coherences might be folded back into the spectrum, but these do not generally not pose a serious problem since their intensities are much lower than those of the desired coherence.

4.3 Heteronuclear Spin Counting

4.3.1 Principles of Spin Counting

The concept of spin counting was introduced by A. Pines and coworkers, who in the early 1980's pioneered the development of MQ spectroscopy in the solid-state [Baum 85]. Unlike in solution, where the localized J-coupling limits the number of coupled partners within a cluster of spins, it is possible to excite (homonuclear) MQ coherences comprising more than 100 spins by using the through-space dipolar coupling. Monitoring the build-up behavior of such high-order coherences gives valuable information about spin clustering in solids. Baum

et al. developed pulse sequences with suitable MQ Hamiltonians capable of exciting such coherences under static conditions. Spin counting involves carrying out an MQ experiment where a TPPI scheme is applied to either the excitation or reconversion pulse sequence in order to create an artificial offset which separates the different quantum orders excited by the sequence. This frequency offset is given by $\Delta\omega = \Delta\phi/\Delta t_1$, where $\Delta\phi$ is the phase increment. A coherence of order n is then offset from the spectral center by $n\Delta\omega$, resulting in a spectrum in which all excited coherence orders can be observed. Since with increasing order, coherences suffer increased line-broadening and sensitivity to B_0 inhomogeneity during t_1 , the sensitivity for the observation of higher-order coherences diminishes rapidly.

An improved experimental scheme was later been published [Shykind 88], in which t_1 is kept constant ($t_1 = 0$ is the most sensible choice) and only the phase is incremented in small steps. The phase is varied in $2n$ steps ranging from 0° to 360° in order to observe a maximum of n quantum orders. The signal in the indirect, phase-incremented dimension of such a 2D experiment is then catenated, and after a cosine Fourier transform, an MQ spectrum is obtained which consists of an array of up to n equally spaced peaks with an arbitrarily small linewidth and with intensities reflecting the contribution of the n^{th} quantum order to the integral intensity. This scheme was recently applied in an MAS experiment [Geen 99] using C7 [Lee 95] as the MQ excitation scheme. It was shown that the MQ build-up behavior, measured as a function of a scaled excitation time (which takes the different MQ excitation efficiencies of different sequences into account), is similar in the static and the MAS case, where spinning frequencies of 8 and 16 kHz were used.

As noted in the preceding section, the DIP-HMSC experiments are theoretically capable of exciting multiple higher-order coherences in the proton subspace of a I_nS -coherence, and I-spin counting should be possible. A phase-incrementation scheme can be implemented in such a sequence simply by incrementing the phase of to the second proton 90° -pulse (ϕ_5 in Fig. 4.1). If the DIP-HMQC sequence is used for this experiment, one has to make sure that the undephased *reference* intensity is measured for $\Delta\phi = 0$ (first slice), i.e., that no effective inversion of the dipolar coupling Hamiltonian occurs in the middle of the sequence, and that the full echo is measured. This is achieved by choosing equal initial phases for ϕ_4 and ϕ_5 .

Important differences are, however, to be expected in the behavior of the build-up of higher-order coherences in the homo- and the heteronuclear cases. In homonuclear spin-counting experiments, the growth of a spin cluster can be described by a statistical model

[Baum 85, Munowitz 87b]. The development of this model was inspired by the observation that in large and homogeneous coupling networks (e.g. adamantane), the intensity distribution among the coherence orders can be modeled with a Gaussian function, the variance of which increases with increasing excitation time. Such a behavior suggests that the build-up of homonuclear MQ modes occurs in a fashion similar to a *random walk* or a diffusion process. As more and more spins are correlated, the growth of the spin cluster proceeds from newly incorporated spins into all directions. The “diffusion” constant is dominated by the (rather strong) interaction of adjacent homonuclear spins. This notion is illustrated in the left side of Fig. 4.3. The different indicated pathways represent the non-localized nature of the growth process of the spin cluster which is characteristic for a random walk.

On the other hand, the multiple-quantum modes in the I-spin subspace of a heteronuclear experiment are excited as a consequence of the *heteronuclear* dipolar coupling of all of these spins to a single heteroatom. For this heteroatom, the multitude of surrounding I-spins creates a local field. This local field is probed by the spin counting process, and the number of proton spins that are incorporated into the heteronuclear MQ coherence grows as a function of their distance from the central heteroatom. This means that the higher the coherence order becomes, the more slowly its intensity builds up, as a consequence of the increasingly smaller coupling constants (Fig. 4.3, right).

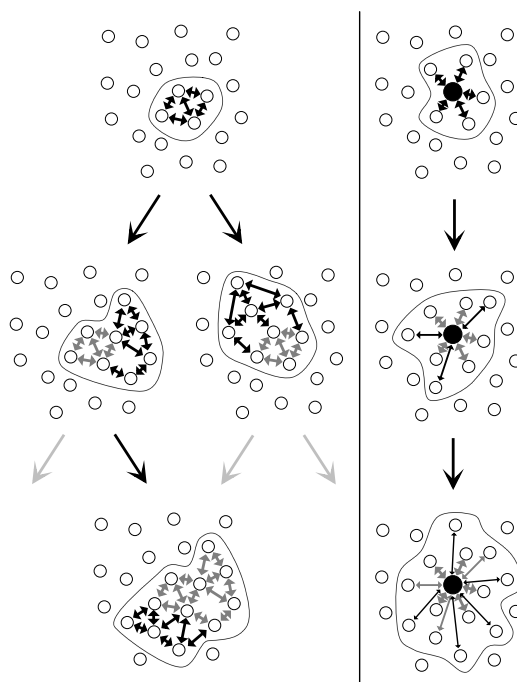


Figure 4.3: Growth of a spin cluster in homonuclear (left) and heteronuclear (right) MQ spectroscopy.

The differences are a direct consequence of the forms of the average Hamiltonians responsible for the excitation of the MQ modes and their action on the spin states they create. The *homonuclear situation* is characterized by the non-commutativity of the single MQ operators connecting individual pairs with the total excitation Hamiltonian, which is a sum over

all possible pairs, for instance:

$$H_{DQ} \sim \sum_{i < j} (\hat{T}_{22}^{(ij)} + \hat{T}_{2-2}^{(ij)}) \quad (4.18)$$

Usually, pulse sequences with an effective DQ Hamiltonian, which can excite only even orders have been used. The BABA-Hamiltonian, Eq. (2.22), is an example of such a Hamiltonian; however, spin counting using an odd-order selective Hamiltonian is also possible. The non-commutativity leads to the observed spreading of the correlated spin cluster over more and more spins. The process can be viewed as a random walk accessing *all possible product operator states* (where the possible states are, for instance, only product operators describing either even- or odd-order MQ coherences).

In the *heteronuclear case*, all individual dipolar coupling pair operators commute, and the experiment is conducted in such a way that multi-spin antiphase coherences are created, where the S-spin species is deliberately chosen as the transverse component of these coherences (Eqs. (4.3)–(4.6)). The spins are fixed in space relative to a given point represented by the S-spin. Coherence transfer, which could lead to a propagation of the build-up process through the combined I- and S-spin subspaces, does not occur unless the experimenter *chooses* to include an INEPT-type coherence-transfer step (which is the essential building block in the REPT sequences presented in the last chapter). Such steps would correspond to so-called “relay” building blocks, which are commonly used in solution-state NMR to establish correlations between spins which are separated by a well-defined number of chemical bonds. In the solution state, this is possible even for *homonuclear* J-coupled spins because of the very localized character of the J-coupling (where the coupling constant between protons separated by two bonds is usually about an order of magnitude larger than that of 3-bond separated protons) and thus the limited number of coupling partners. The “random walk” therefore occurs only along a chain (the carbon skeleton of the molecule) in this case, and its outermost point is determined by the number of relay steps in the pulse sequence.

4.3.2 Experimental Results

In order to demonstrate the existence of the various multi-spin antiphase coherences described by Eqs. (4.3)–(4.6), the possibility of converting them into heteronuclear MQ coherences, as

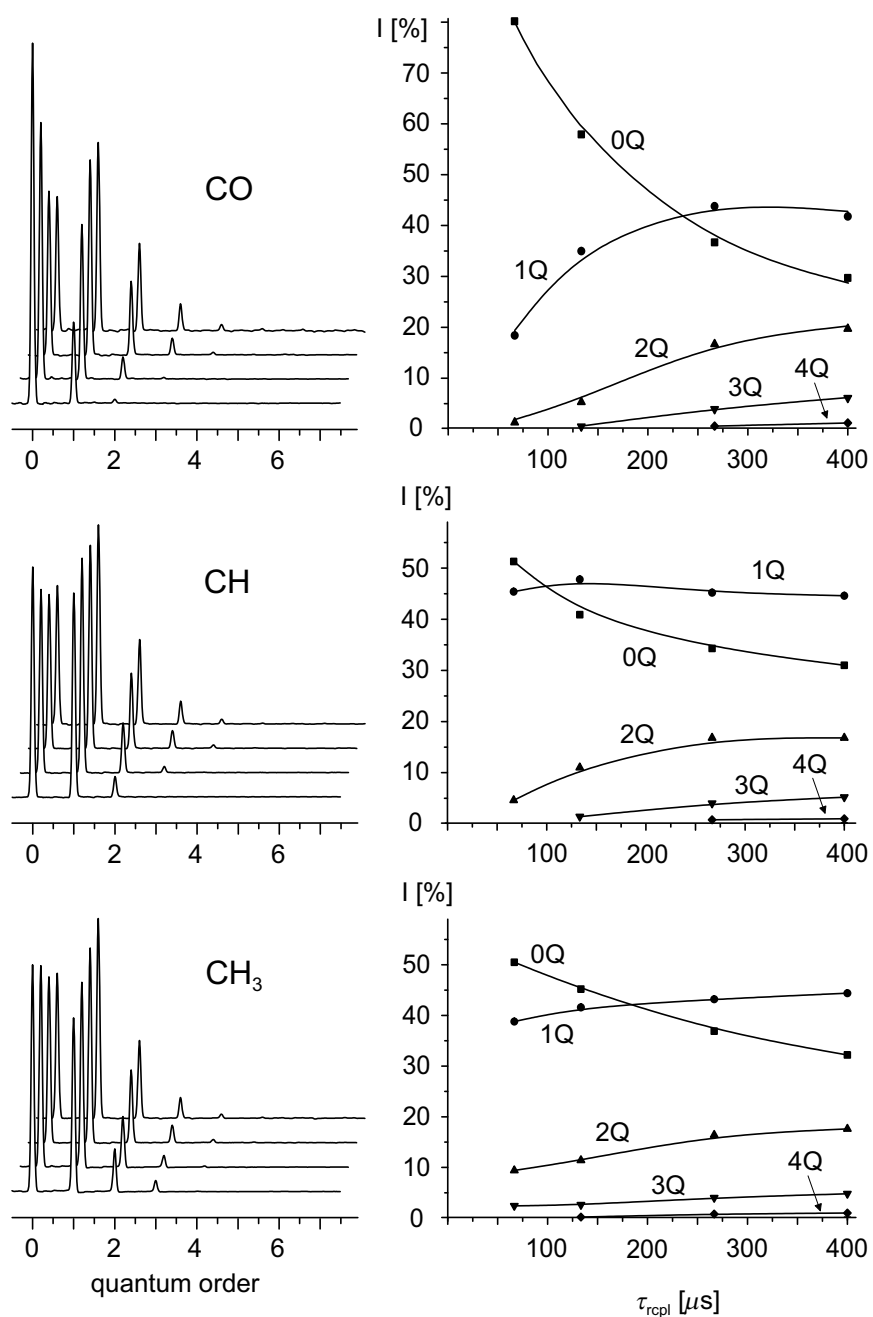


Figure 4.4: Spin counting experiments on $U\text{-}^{13}\text{C}$ L-alanine. The spectra on the left are slices from phase-incremented DIP-HMQC experiments at the indicated ^{13}C -positions obtained at 30 kHz MAS with $\tau_{rcpl} = 2, 4, 8, 12\tau_R$ (66.7, 133.3, 266.7, 400 μs). The individual peak intensities shown on the right are normalized with respect to the total integral intensity of the individual spectra. The lines are simply guides to the eye, and the labels indicate the quantum order in the ^1H subspace.

well as the possibility of separating coherence orders upon reconversion, phase-incremented 2D DIP-HMQC spectra were obtained for a sample of uniformly labeled L-alanine. The results of four experiments obtained with different recoupling times are summarized in Fig. 4.4.

The build-up of higher-order coherences is clearly shown by these spectra. The intensities are normalized with respect to the full spectral intensity of the signals at the individual carbon positions, which is equivalent to the intensity of the ^{13}C peaks in the first slice of the 2D dataset (the REDOR reference intensities). This normalization assumes that the (heteronuclear) dipolar evolution is completely reversed during the reconversion period. Processes such as different relaxation behavior of higher-order antiphase coherences and spin diffusion among the protons would interfere with this time reversal. However, the virtual absence of strong effects of ^1H homonuclear coupling in the REPT spectra shown in the last chapter and in the DIP-HMSC spectra to be presented in the following sections supports the validity of the assumption of negligible homonuclear couplings at very high spinning frequencies. Since only ^1H \hat{I}_z -operators are involved, different proton T_1 's could still lead to differences in the relaxation of the higher-order antiphase coherences, but these effects should also not play a significant role on the timescale of these experiments.

The normalization is more problematic in homonuclear systems, where, in principle, separate experiments to measure the influence of relaxation phenomena would be needed. In practice, one can resort to separately measuring spectra filtered for a specific quantum order (e.g., DQ) and using these to normalize the spin counting data [Geen 99]. The $n = 0$ peak is usually not used for a quantitative analysis, owing to the fact that a separation of ZQ coherences and residual longitudinal magnetization is not possible. In the homonuclear case, the T_2 relaxation times involved in the creation of these types of coherences can be expected to differ significantly. This problem does not arise in the heteronuclear case. Even though the $n = 0$ peak is composed of I-ZQ terms (e.g, half of the 2I-spin coherences, Eq. (4.5)) and pure, cosine-modulated ^{13}C *transverse* magnetization (Eq. (4.3)), the effects of ^{13}C relaxation on these contributions (mainly T_2) can be assumed to be equal.

As mentioned, the data in the diagrams on the left hand side of Fig. 4.4 cannot be interpreted in terms of a Gaussian growth process. Distinct differences are apparent in the distribution of the intensity among the different quantum orders for the three different ^{13}C atoms. While for the CO, the ^1H 1Q is less than 20% of the total signal for the shortest

recoupling time, it is more than twice as high for the protonated carbons. The CH_3 -group, in particular, has significant 2Q and 3Q contributions already at the same recoupling time of $66.7 \mu\text{s}$. Clearly, the different local fields of the individual ^{13}C atoms are responsible for these differences.

However, at $\tau_{rcpl} = 400 \mu\text{s}$, the contributions of the different orders to the signal is *very similar* for all three ^{13}C positions. This can be rationalized by looking at the theoretical build-up curves for the different higher-spin coherences in an I_3S -group (Fig. 4.2). Note that these curves *do not* represent the build-up of higher coherence *orders*, rather, the different higher-spin modes contain higher-order coherences in different ratios, as explained and calculated on p. 109f. Nevertheless, it becomes clear that for a specific number of spins in a subsystem, any type of higher-spin coherence or n -quantum order reaches a plateau value for its intensity. These values are different, however, when more and more spins (with increasingly weak heteronuclear coupling constants), e.g. from adjacent molecules, are included. If the local (strongly coupled) environment of a heteroatom is separated well enough from the surroundings (by the relative magnitude of the coupling constants), the distribution of intensity among the quantum orders should provide valuable information about this local environment.

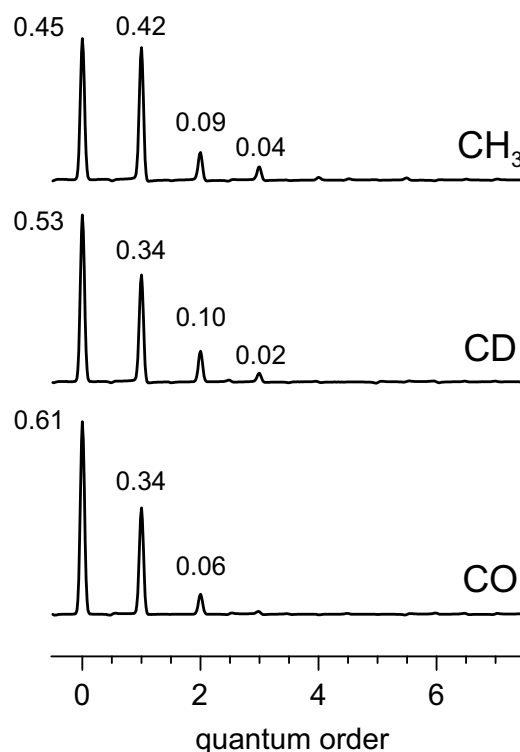


Figure 4.5: Slices from the phase-incremented spin-counting data at the different ^{13}C signal positions of partially deuterated methylmalonic acid, measured at 30 kHz MAS with $\tau_{rcpl} = 8 \tau_R = 266.7 \mu\text{s}$.

This idea is tested by a spin-counting experiment on a partially deuterated methylmalonic acid sample (see Appendix D.4 for details), where the CH_3 -groups are well-separated (Fig. 4.5). Assuming an apparent coupling constant of $D_{IS}^{app}/2\pi = 6.8 \text{ kHz}$ (see Tables 3.1 and 4.1) for the methyl carbon, we obtain $N_{rcpl} D_{IS}^{app}/\omega_R = 1.8$. From the data presented in Fig.

4.2, the intensities under the given experimental conditions are calculated to be 0.42, 0.42, 0.09 and 0.08 for the ^1H coherence orders 0, 1, 2, and 3, respectively. These values are in good agreement with the data in Fig. 4.5. For the CD carbon, with $D_{IS}^{app}/2\pi = 2$ kHz, the theoretical values are 0.49, 0.37, 0.08 and 0.06 and are also in reasonable agreement with the experiment. Deviations must be expected since the individual methyl groups are not completely isolated, and contributions from neighboring molecules change the measured ratios. Nevertheless, the experimental evidence indicates that heteronuclear spin counting, with its property of probing a selected local environment, represents an interesting new tool for the investigation of chemical structures.

4.4 ^{13}C - ^1H DIP-HMS Shift Correlation Spectra

Having demonstrated the possibility of exciting higher-quantum coherences among the I-spins with the DIP-HMSC sequences, we will now monitor the evolution of these coherences in 2D correlation experiments, where the different coherence orders are selected by a phase cycle. The DIP-HSQC pulse sequence (Fig. 4.1) is most suitable for rotor-synchronized applications since t_1 can be incremented in steps of one rotor cycle without artifacts arising from a refocusing π -pulse present in the HMQC variant. The States-TPPI method was used to achieve sign-sensitive detection in t_1 . Details about the phase cycles can be found in Appendix E.3.

Fig. 4.6 shows results of HMQ-filtered (i.e., regular I-spin odd-order selective filtered) spectra. These were measured using a 100% labeled ^{13}C L-alanine and should be compared to the REPT-HSQC spectra in Figs. 3.17 and 3.18 on pages 95 and 96, respectively. The disappearance of specific peaks, as observed in the REPT-HSQC spectra of fully labeled compounds, does *not* occur in the DIP-HSQC spectra. Rather, the spectra in Fig. 4.6b are very similar to the REPT-HSQC spectra measured on a naturally abundant sample. From the theory presented in Section 4.2, it is apparent that the dephasing of remote cross-signals due to neighboring, passive ^{13}C spins, cannot be expected to be present in DIP-HMQC spectra since no ^1H transverse coherences subject to heteronuclear dephasing are present during excitation and reconversion. However, the REPT always exhibited a higher S/N than the corresponding DIP-HMSC spectra, since losses due to inefficient CP at fast spinning frequencies can hardly be avoided.

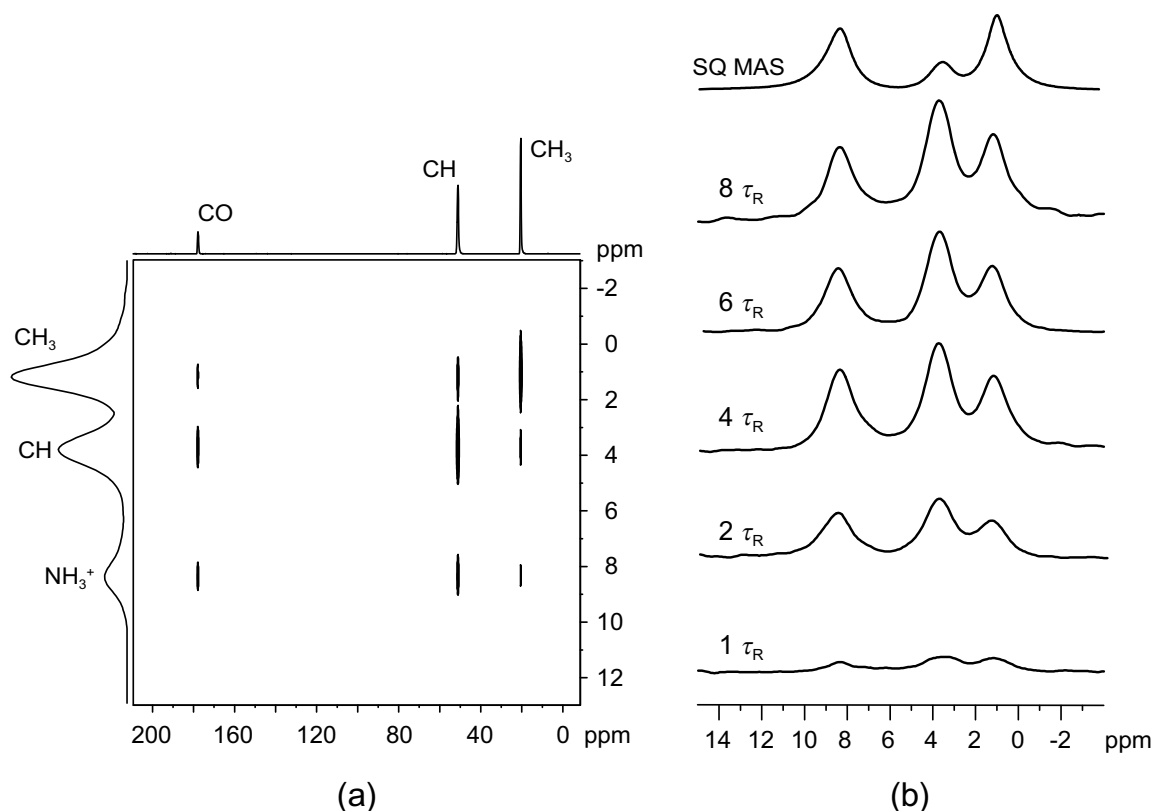


Figure 4.6: ^{13}C - ^1H (1Q) DIP-HSQ shift correlation spectra of U - ^{13}C L-alanine, measured at 30 kHz MAS with the second pulse sequence in Fig. 4.1. The recoupling time for the full 2D spectrum (a) was $4 \tau_R$. The spectra in (b) are slices from the CO signals in 2D spectra, obtained at the indicated recoupling times.

The spectra in Fig. 4.7 were acquired with the same DIP-HSQC pulse sequence, but with DQ and TQ filtering schemes and a corresponding adjustment of the TPPI scheme for sign-sensitive detection in t_1 . These spectra are somewhat unusual since a ^{13}C SQ dimension is correlated with either a ^1H -DQ or a ^1H -TQ dimension, where the chemical-shift information is the sum of two- or three-spin ^1H correlations, respectively. The information content in these spectra is entirely different from that of the more familiar homonuclear ^1H DQ and TQ correlation spectra [Schnell 99]. While in the homonuclear case a peak in the DQ or TQ dimension indicates a correlation of two or three spatially close I-spins, a peak in the heteronuclear spectrum means that two or three constituent I-spins, respectively, are close to an S -spin, the one at which the coherence is detected in the t_2 dimension (the HMQ coherence is created solely by the action of *heteronuclear* dipolar couplings). These protons can be

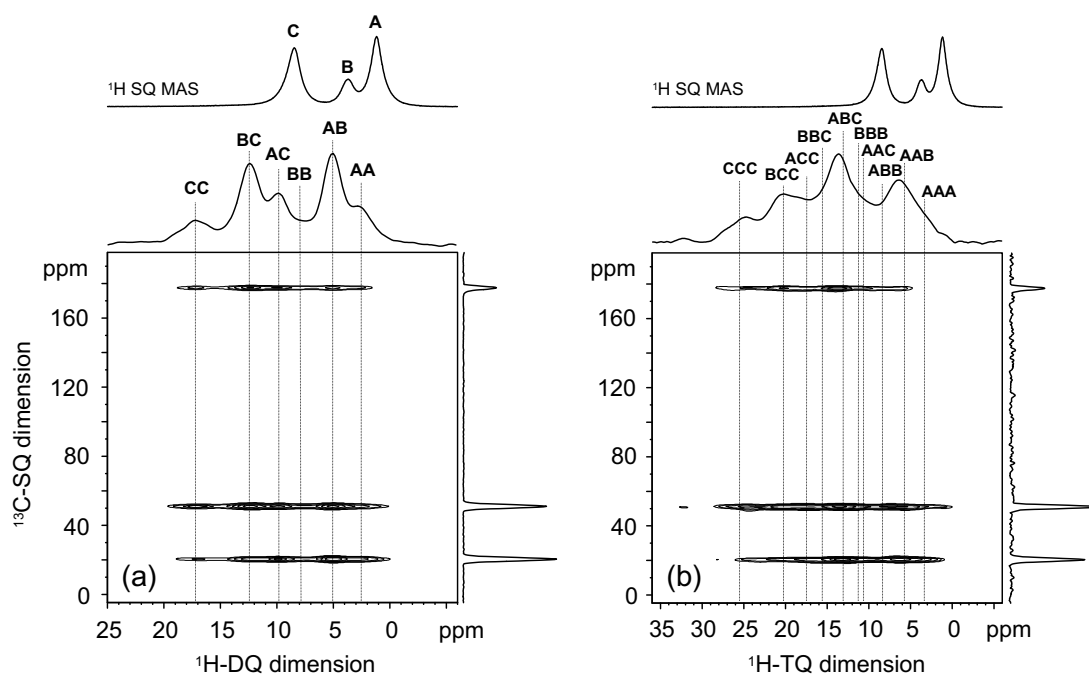


Figure 4.7: ^{13}C - $^1\text{H}(\text{DQ})$ (a) and ^{13}C - $^1\text{H}(\text{TQ})$ (b) DIP-HSQ shift correlation spectra of U - ^{13}C L-alanine, measured at 30 kHz MAS using the second pulse sequence in Fig. 4.1 and a recoupling time of $8\tau_R$. Additional line-broadening was applied in the ^{13}C dimensions to produce more visible contour lines. The projections are skyline projections, and on top of the ^1H dimensions, ^1H SQ MAS spectra are shown on the same chemical-shift scale for comparison. The assignments of the protons are **A**: CH_3 , **B**: CH , and **C**: NH_3^+ .

located on either side of the carbon atom, and the distance between them can thus be rather long.

Details can be seen in Fig. 4.8, where projections over individual carbon positions are shown. Data in the ^{13}C - $^1\text{H}(\text{DQ})$ spectrum measured with a relatively short recoupling time (Fig. 4.8a) can be expected to be governed by intramolecular correlations. The grey background traces are calculated spectra based on intensities given by Eq. (4.9), with the chemical shifts taken from an SQ MAS spectrum. The tensor parameters used for the calculation of the phase factors, $N_{rcpl}\bar{\Phi}_0^{(i)}$, are based on crystal structure data from a neutron diffraction study [Lehmann 72]. The calculated spectra (considering heteronuclear couplings only!) indeed yield a good prediction of the experimental intensities. The deviation of the **AA** and **AB** signals from the simulations in the CH_3 -slice may be due to the very large and possibly different linewidths of these signals. For a more quantitative analysis, a proper deconvolution would be

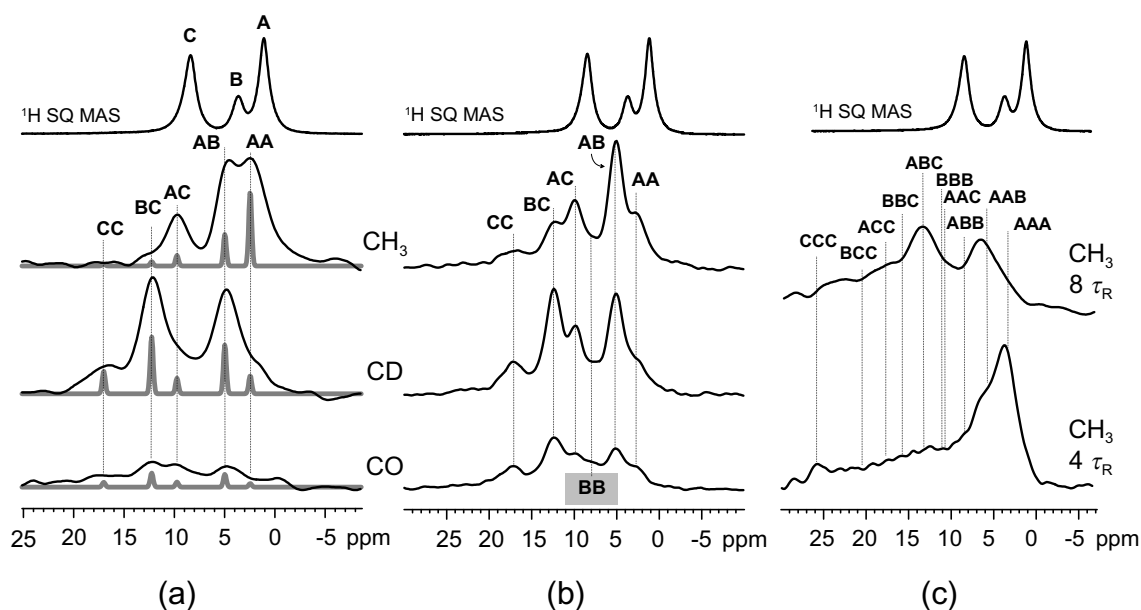


Figure 4.8: Slices from ^{13}C - ^1H (DQ) (a,b) and ^{13}C - ^1H (TQ) (c) DIP-HSQ shift correlation spectra of U - ^{13}C L-alanine, measured at 30 kHz MAS. In (a) and (b), the signals from the three carbon positions are shown for recoupling times of 4 and $8 \tau_R$, respectively. The relative intensities are to scale. In (c), the slices at the CH_3 position in ^1H -TQ spectra at $\tau_{\text{recpl}} = 4$ and $8 \tau_R$ are compared. For the assignments see Fig. 4.7. The grey traces in (a) are from simulations, as explained in the text.

necessary. It should again be emphasized that the information in these spectra is quantitative since a reference intensity can be measured for each 2D spectrum. The individual ^{13}C peaks in the first slice of the 2D spectrum can be normalized with respect to a separately measured REDOR reference spectrum, and the information in the indirect spectral dimension can then be used to calculate the distribution of this normalized intensity among the signals in the I-spin MQ dimension.

At longer recoupling times (Fig. 4.8b), the appearance of the spectra changes because protons in adjacent molecules are now included in the MQ modes. This is most obvious for the **BB** signal, which is clearly present in the CO slice (marked with a grey box). Since each alanine molecule has only one CH-group, this is necessarily a correlation extending over two molecules. This peak is a good example of the valuable information inherent in such spectra. From the crystal structure (see Appendix D.1 for a pictorial representation), we derive an intramolecular CO- H_B distance of 2.14 Å and an intermolecular distance of 2.67 Å. Even though the two correlated protons are 3.55 Å apart, which gives a homonuclear coupling

constant which is of comparable magnitude as the involved heteronuclear couplings, it should again be emphasized that this homonuclear coupling is not involved in the generation of the probed heteronuclear 3-spin coherence. Rather, it is averaged out by the MAS ($\omega_R/D_H \approx 10$) while the heteronuclear couplings are selectively recoupled. The carbon atom acts as a well-defined point of reference, from which the local environment is probed in a very selective fashion, through the chemical-shift information in the ^1H -DQ dimension. The mere existence of such peaks has important structural implications. Thus, this type of experiment represents a valuable addition to our toolbox of correlation techniques for structural studies.

Similar information is accessible using homonuclear 2D ^1H TQ MAS spectroscopy, which can be performed using a modified BABA sequence [Schnell 98]. Spectra obtained for L-alanine at 35 kHz MAS and an excitation time of $2 \tau_R$ exhibited a strong signal from the **BBC** proton triad, detectable at both NH_3^+ and CH SQ ^1H signal positions in the direct dimension. The type of connectivity derived from such spectra is, however, less specific than a 3-spin heteronuclear connectivity, since in the heteronuclear case, it is clear that only 2 heteronuclear couplings contribute to the build-up of a ^{13}C - ^1H (DQ) coherence, while in the homonuclear case, 3 homonuclear couplings can be involved. Moreover, selective isotopic labeling with ^{13}C building blocks can be used to introduce “spin probes”, for instance in specific residues of larger molecules such as proteins, in order to detect specific conformations locally.

The ^{13}C - ^1H (TQ) spectra have a much lower S/N, which is to be expected from the relative distribution of spectral intensity among the quantum orders. In addition, the intensity is spread out over an even larger spectral width since more cross signals are possible (10 as opposed to 6 in the DQ spectrum). Moreover, the linewidth of MQ signals increases with increasing quantum order [Schnell 99] as a consequence of the fact that more spins represent more points of attack for perturbing couplings to other spins, which leads to dephasing (i.e. T_2 relaxation). As a consequence, the circumstances are not too favorable for the exploitation of such higher-order coherences. One interesting observation can be made by reference to Fig. 4.8c. While, as expected, the intra-methyl ^{13}C - ^1H (TQ) signal (**AAA**) dominates the spectrum completely for $\tau_{rcpl} = 4 \tau_R$, it is merely a shoulder of the **AAB** cross signal at $8 \tau_R$. This indicates the complications in interpreting long-recoupling time dipolar correlation spectra in general. For short recoupling times, information about the strongest couplings dominate, permitting at least semi-quantitative interpretation of the spectra. However, the intensities always depend on the

relative orientations of the involved dipolar coupling tensors, and a careful consideration of the effects of relative orientations and coupling strengths is necessary to ensure the validity of the results obtained at longer recoupling times.

4.5 ^{13}C - ^1H Dipolar Couplings from Build-up Curves and Sideband Patterns

After having illustrated the use of HSQ shift correlation spectra as a method for obtaining qualitative distance constraints for structural investigations, we will now turn to means of obtaining quantitative dipolar coupling information. As mentioned in the preceding sections, one advantage of DIP-HMQC over REPT is the possibility of normalizing the build-up data. In the simplest case, this would just require ^{13}C - ^1H REDOR, which is indeed feasible at very fast spinning frequencies. Such measurements were performed on the partially deuterated methylmalonic acid sample described in Appendix D.4, the model substance for weak ^{13}C - ^1H couplings.

The experimental data are summarized in Fig. 4.9. The signals from all three carbon atoms approach the theoretically predicted plateau of 0.5. For $\tau_{rcpl} > 800 \mu\text{s}$, the measured values become unreliable on account of the increasingly weak signal at longer recoupling times, leading to a low S/N. Fits of the apparent dipolar coupling constants, D_{IS}^{app} (for a definition see Eq. (3.15)), were obtained by adjusting the x-scaling of a master curve calculated using Eq. (4.13) or (4.11). These are indicated as solid lines. The fit for the CH_3 -group is somewhat critical, since the time-resolution, even at 30 kHz MAS, is too crude to obtain more points in the initial-rise region of the curve. The scaled master curves model the experimental data reasonably well, but deviations are in some cases bigger than the experimental errors, which were estimated from the noise level. However, within the limits of uncertainty estimated from the fit, the coupling constants are close to the expected values (see Table 4.1), and the ^{13}C - ^1H distances are well reproduced. In particular, the results are more reliable than the ones obtained from REPT measurements (Table 3.1), where the apparent relaxation (i.e. dephasing) of the MQ signal at longer recoupling times posed a serious problem for the analysis of the build-up behavior.

The observed discrepancies are attributed to two main factors. Firstly, multi-spin effects,

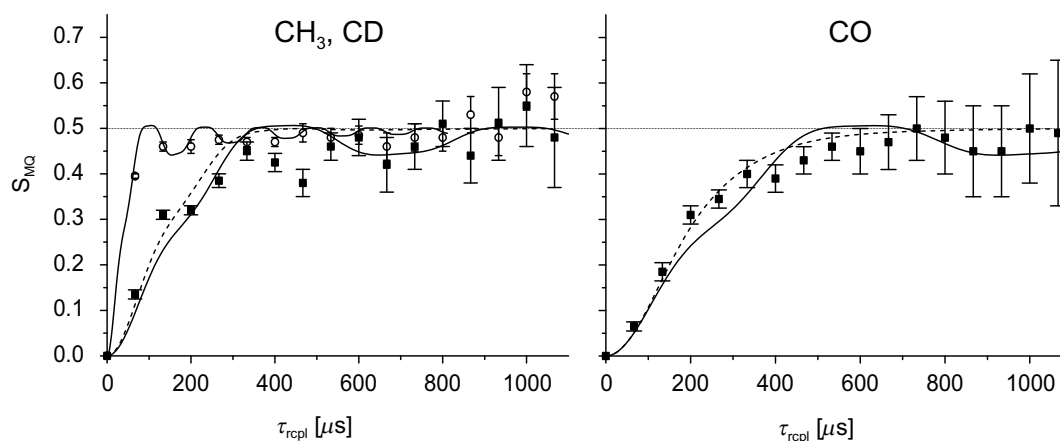


Figure 4.9: Normalized ^{13}C - ^1H DIP-HMQ-filtered (i.e. REDOR) intensities measured on partially deuterated methylmalonic acid at 30 kHz MAS. Open circles in the left diagram represent data for the CH_3 -carbon. The solid lines are REDOR master curves for a rapidly rotating I_3S -unit (see Fig. 4.2), with the x-axis scaling adjusted to obtain a fit for the apparent dipolar coupling constants given in Table 4.1. The normalized MQ intensities are on an absolute scale. Dashed lines are from analytical simulations for the CD and CO carbons, based on crystal structure data and taking into account the nine closest CH_3 moieties.

i.e., couplings to remote methyl groups, contribute to the build-up, and as a consequence, larger than expected coupling constants are obtained. This is most pronounced in the data for the CO carbon, which is located quite far away from the intramolecular methyl group. In Fig. 4.9, theoretical curves which were calculated from Eq. (4.11) using the tensor parameters of the nine closest methyl proton triplets (based on the crystal structure [Derissen 70]) are included as dashed lines. These curves match the experimental data slightly better, but they still underestimate the experimentally observed coupling. Homonuclear couplings among the protons might be another reason for the observed lower than expected MQ intensities at intermediate recoupling times. Homonuclear spin flip-flops would lead to an incomplete re-conversion of the excited MQ coherences, and these contributions would be lost in the integral signal. However, these effects are still rather small and do not hamper such a simplified data analysis as much as they do in REDOR experiments with quadrupolar nuclei as passive spins, where finite pulses can excite MQ transitions in these nuclei in a non-reversible fashion (see Chapter 5).

HMQ spinning-sideband patterns were also obtained, using the DIP-HDOR sequence

Table 4.1: Experimentally observed and expected apparent ^{13}C - ^1H dipolar couplings and bond lengths for the methyl protons in partially deuterated methylmalonic acid, for the case of the DIP-HMSC sequences. This data can be compared with measurements using the REPT-techniques on the same sample, Table 3.1, p. 87.

build-up	fits of NMR data		from crystal structure ^a	
	$ D_{IS}^{app} /2\pi$ [kHz]	$\Rightarrow r_{IS}$ [Å]	$D_{IS}^{app}/2\pi$ [kHz] ^b	r_{IS} [Å]
CH ₃	8.0±0.8	1.08±0.04 ^c	-7.77	1.09
CD	2.0±0.2	2.15±0.07 ^d	-1.97	2.165
CO	1.4±0.2	–	-1.02/-0.96 ^e	–
sidebands				
CH ₃	6.69±0.07	1.145±0.004	-7.77	1.09
CD	2.15±0.04	2.10±0.01	-1.97	2.165
CO	1.94±0.07	–	-1.02/-0.96 ^e	–

^abased on the idealized model for the methyl group, see Section 6.4.2

^bcalculated from the average dipolar tensor of the three proton positions

^ccalculated from Eqs. (1.51) and (3.15), assuming $\theta = 109.5^\circ$

^dcalculated from Eqs. (1.51) and (3.15), assuming $\theta = 28.4^\circ$

^etwo inequivalent positions in the crystal

(see Fig. 4.1). The advantages of the HDOR approach were discussed in detail for the REPT version in Section 3.2.2. The sequence used here is derived from the DIP-HSQC experiment by simply keeping the two proton 90° -pulses together for all values of t_1 , thus using them as an HMQ filter. To avoid spectrometer timing problems, it is useful to acquire the first slice on top of the first rotor echo, with $t_1 = 1 \tau_R$. The resulting patterns are virtually free of first-order phase errors.

The results are depicted in Fig. 4.10. It was even possible to obtain patterns at $\tau_{rcpl} = 16 \tau_R = 533 \mu\text{s}$. All patterns exhibiting more than just the first-order sidebands could be fitted to the analytical solution for a methyl group, Eq. (4.15) with $\omega_{CS,I} = 0$. The results are also listed in Table 4.1. Surprisingly, even the first-order sideband intensities were reliable (as opposed to the REPT patterns). This is the reason why even the weak couplings from the CD and CO carbons to the methyl protons could be fit. The measurement time for these patterns

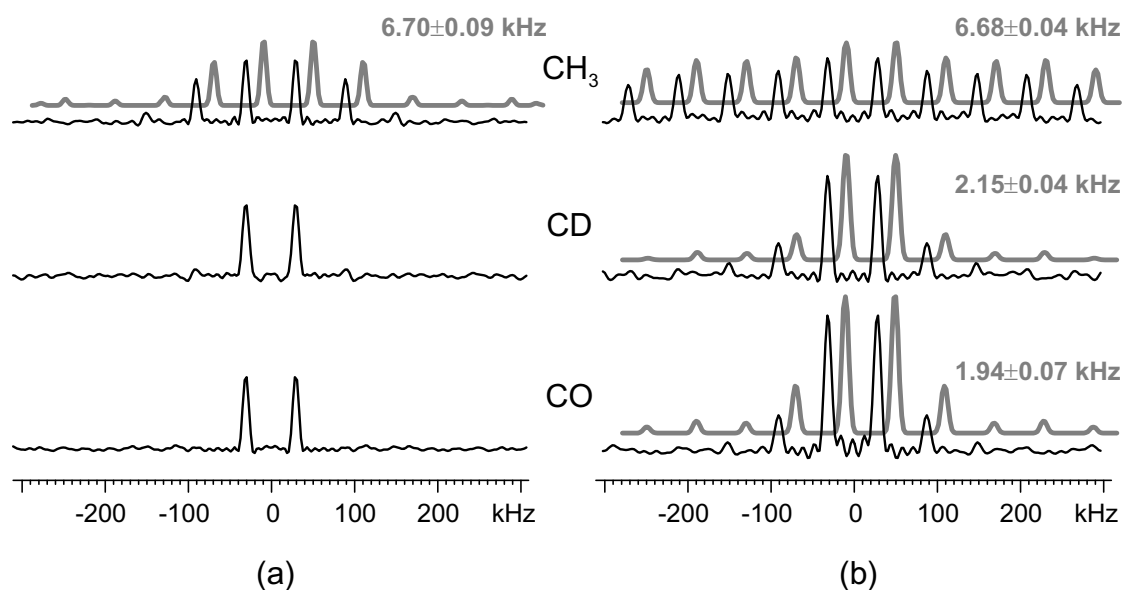


Figure 4.10: DIP-HDOR spinning sideband patterns of partially deuterated methylmalonic acid, measured at 30 kHz MAS with $\tau_{rcpl} = 6 \tau_R$ (a) and $16 \tau_R$ (b), along with best-fit patterns (grey background traces). The $D_{IS}^{app}/2\pi$ obtained from the fits are indicated.

was about twelve hours, using a ^{13}C naturally abundant sample. The results are more reliable than the ones from REPT patterns at long recoupling times (Fig. 3.12). Even though the DIP-HMQ techniques are less sensitive, the reliability of the first-order sideband intensities represents a major advantage since the losses due to the CP are more than compensated by the possibility of choosing a shorter recoupling time, thus having fewer losses due to relaxation. Note that recoupling times of 24 and 26 τ_R were necessary for the REPT experiments, to have appreciable intensity in the 5th-order sidebands.

Again, the coupling constants for the CD, and in particular for the CO-group, deviate towards higher values because of remote couplings. This was proven by performing two different analytical simulations of DIP-HDOR patterns for the CD carbon on the basis of the crystal structure of methylmalonic acid: one considering only the methyl group attached to the CD-group and one including eight additional methyl groups from adjacent molecules. These patterns were then fitted using the analytical formula for an ideal tetrahedral methyl group pattern. While for the single- CH_3 pattern the apparent coupling constant of 2 kHz could be verified (see Table 4.1), the multi- CH_3 pattern gave a best-fit value increased by 120 Hz, supporting the notion that in multi-spin systems, the DIP-HDOR patterns are governed

by “effective” coupling constants, not only the strongest one. In the REPT techniques, contributions from remote spins were found to reside in the first-order sidebands, leaving the rest of the pattern virtually unchanged, while stronger perturbing couplings lead to a loss of spectral intensity. It remains to be investigated whether these observations can be explained in terms of the simple theory based on heteronuclear couplings only.

4.6 DIP-HMS Spinning-Sideband Spectra

As a last topic, the specific properties of spinning-sideband patterns in the DIP-HMSC experiments will be explored. For this purpose, chemical-shift resolved sideband patterns were measured on uniformly labeled L-alanine in order to have reasonable measuring times for 2D spectra where up to 768 slices in t_1 were needed for high resolution spectra.

In Fig. 4.11, measurements from all three sideband-generating variants of the experiment are compared. For a specific carbon, the overall patterns are very similar for the three variants. The HDOR patterns were fitted to obtain coupling constants which were in good agreement with values expected for isolated CH and CH₃-groups. In the DIP-HSQC patterns, the even-order sidebands and weak centerbands that are introduced by dipolar evolution of the antiphase coherence during t_1 (see also Fig. 3.10) become apparent. Distortions of the DIP-HMQC patterns due to CSA and ERM are not apparent above the noise level.

From Eqs. (4.15) and (4.16) it can be seen that a ¹H-TQ contribution should be visible in DIP-HMQ spectra with the usual (odd-order selective) HMQ filter on the protons. This contribution is expected to be weak, and the sidebands are also spread over a larger spectral range than the primary ¹H-SQ pattern. In the CH₃ spectra, weak negative artifacts of unknown origin are stronger than the TQ contributions, which are not visible in the spectra presented here.

The most surprising observation can be taken from the enlarged insets, where correlations with protons that are *remote* to the respective ¹³C atoms are seen to appear in *all sideband orders*. This is contrary to similar patterns measured with the REPT sequences (Fig. 3.14), where such weak correlations were restricted to the lower-order sidebands. Even though surprising and somewhat counter-intuitive, this observation can be accounted for using the theoretical treatment presented in Section 4.2.

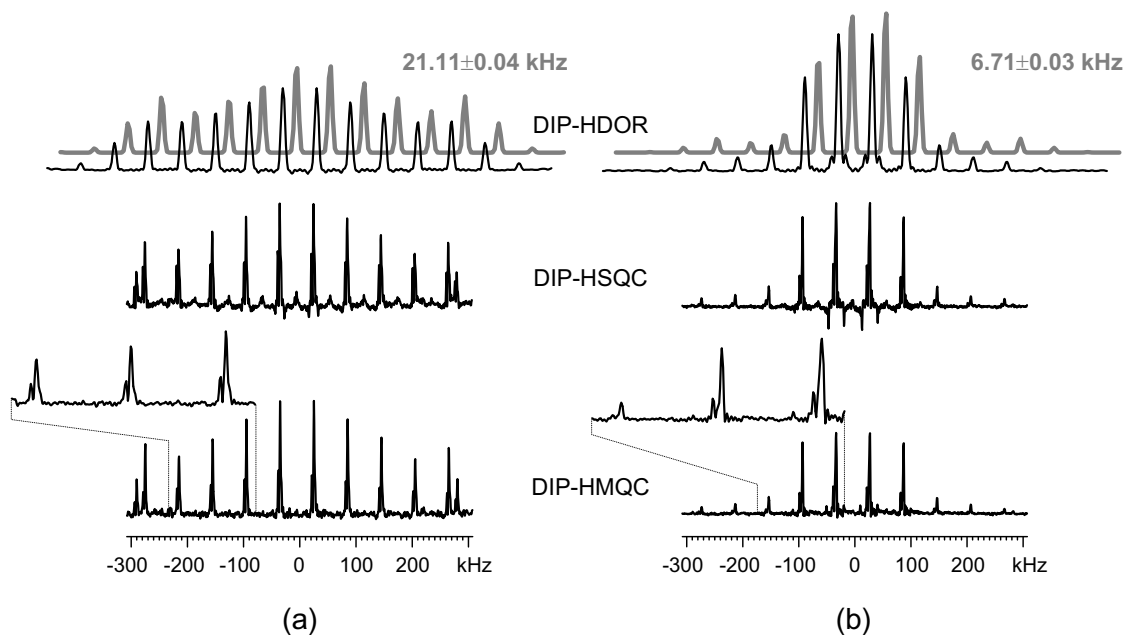


Figure 4.11: Sideband patterns from symmetric dipolar HMQ experiments, measured on $U\text{-}^{13}\text{C}$ L-alanine at 30 kHz MAS and $\tau_{rcpl} = 6 \tau_R$, with a ^1H offset of about 6 kHz from the CH signal in the ^1H SQ MAS spectrum. In (a) and (b), patterns from the CH and the CH_3 carbons, respectively, are shown. The DIP-HSQC and -HMQC patterns exhibit folded-back sidebands, due to a smaller spectral width chosen in order to save experiment time. The grey background traces are best-fit patterns, with the coupling constants indicated. For the pulse sequences see Fig. 4.1.

We will discuss the phenomenon in terms of a simple three-spin system, as indicated in Fig. 4.12. The time-evolution formula can be derived from Eq. (4.8) with $i = 1$. It consist of two contributions,

$$\begin{aligned}
 S \sim & \langle \sin N_{rcpl} \bar{\Phi}_0^s \sin N_{rcpl} \bar{\Phi}_{t_1}^s \cos N_{rcpl} \bar{\Phi}_0^w \cos N_{rcpl} \bar{\Phi}_{t_1}^w \rangle \\
 & + \langle \sin N_{rcpl} \bar{\Phi}_0^w \sin N_{rcpl} \bar{\Phi}_{t_1}^w \cos N_{rcpl} \bar{\Phi}_0^s \cos N_{rcpl} \bar{\Phi}_{t_1}^s \rangle,
 \end{aligned} \tag{4.19}$$

which correspond to the primary pattern, cosine modulated by the weak (w) coupling to $^1\text{H}^{(2)}$, and the secondary pattern, which is cosine modulated by the strong (s) coupling. For simplicity, the prefactors for the chemical shift evolution are omitted. Assuming two different shifts for the two protons, a spectrum calculated using this formula is shown in Fig. 4.12a. The patterns from the two components are also shown separately. Even though the pattern for the $\text{CH}^{(2)}$ correlation (ii) has the small phase factor, $\bar{\Phi}^w$, as the argument of the sine-function,

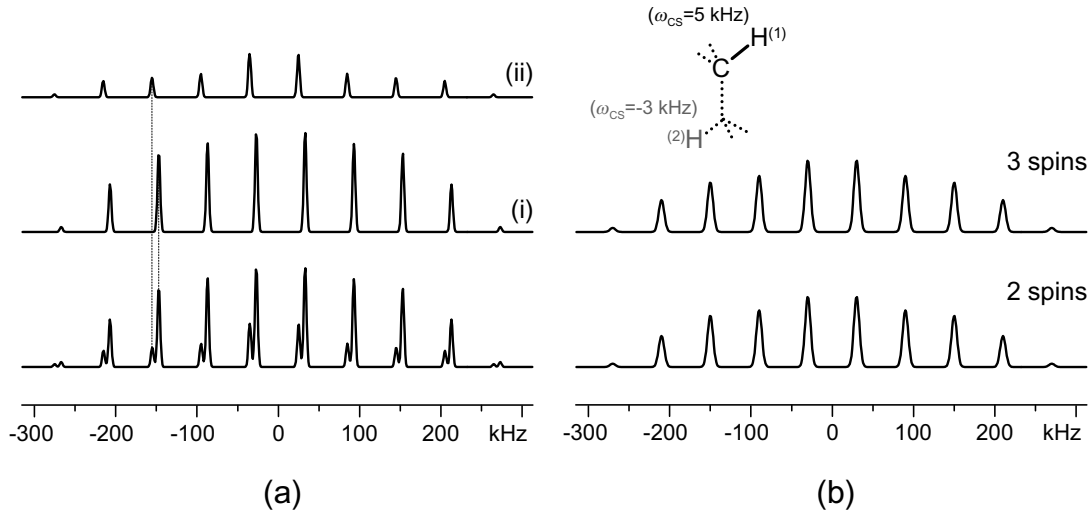


Figure 4.12: Sideband patterns calculated for an $H \cdots CH$ system with the indicated geometry, based on Eqs. (4.19). In (a), isotropic shifts were included as indicated, and the two constituent patterns corresponding to the $CH^{(1)}$ and $CH^{(2)}$ coherences are shown separately as (i) and (ii), respectively. The spectra in (b) are HDOR patterns for the primary $CH^{(1)}$ -pair (identical to (i)), and for the 3-spin case, which is sum of both contributions (i) and (ii) without a chemical-shift difference. The parameters used in the simulations were $D_{CH^{(1)}}/2\pi = 21.11 \text{ kHz}$, $D_{CH^{(2)}}/2\pi = 2.85 \text{ kHz}$, $\omega_R/2\pi = 30 \text{ kHz}$, and $\tau_{rcpl} = 4 \tau_R$.

the pattern extends over the same spectral range as the one for the primary pair. This can be rationalized by applying an addition theorem to the second line of Eq. (4.19):

$$\begin{aligned}
 & \langle \sin N_{rcpl} \bar{\Phi}_0^w \sin N_{rcpl} \bar{\Phi}_{t_1}^w \cos N_{rcpl} \bar{\Phi}_0^s \cos N_{rcpl} \bar{\Phi}_{t_1}^s \rangle \\
 &= \langle [\frac{1}{2} \sin N_{rcpl} (\bar{\Phi}_0^w + \bar{\Phi}_0^s) + \frac{1}{2} \sin N_{rcpl} (\bar{\Phi}_0^w - \bar{\Phi}_0^s)] \\
 & \quad \times [\frac{1}{2} \sin N_{rcpl} (\bar{\Phi}_{t_1}^w + \bar{\Phi}_{t_1}^s) + \frac{1}{2} \sin N_{rcpl} (\bar{\Phi}_{t_1}^w - \bar{\Phi}_{t_1}^s)] \rangle
 \end{aligned} \tag{4.20}$$

As a result, the patterns can be written in terms of pure sine-sine contributions, where the strong coupling, as represented by $\bar{\Phi}^s$, dominates the arguments of the sines. The argument does not hold for the REPT-sequences because of their *asymmetry*, i.e., a cosine modulation of the coherences due to remote spins occurs only in the reconversion period. An interesting limiting case is $\bar{\Phi}^s = \bar{\Phi}^w$, which would occur for a symmetric CH_2 system with identical, e.g. motionally averaged, coupling tensors. Then a pattern governed by twice the coupling constant would result. Results not presented here show that rigid methylene groups (where, of

course, $\bar{\Phi}^s \neq \bar{\Phi}^w$) exhibit sideband patterns which extend further out than CH sideband patterns under the same conditions, indicating an increased apparent coupling constant, while in the REPT case, *no* patterns with higher-order sidebands can be measured for rigid methylene groups.

The spectra in Fig. 4.12b are HDOR patterns (i.e., calculated without considering the chemical shifts) for the 3-spin system and for the primary pair only. Differences between these spectra are hardly visible, confirming that the perturbation exerted by $H^{(2)}$ is very weak and overwhelmed by the primary coupling of 21 kHz. Only the relative intensity of the two contributions in the chemical-shift resolved pattern carries information about the relative coupling strength. This information can, however, more efficiently be measured with a rotor-synchronized shift-correlation spectrum.

To conclude the section about the specific properties of DIP-HMQ sidebands, Fig. 4.13 shows DIP-HDOR sideband patterns of a methyl group, also measured on the fully labeled L-alanine sample. The spectra were acquired with different MQ filters on the protons. In this way, sideband patterns corresponding to different coherence orders could be measured separately.

Although the heteronuclear ^1H -SQF pattern has only odd-order sidebands, the heteronuclear ^1H -DQF pattern is described by a time-domain signal $\sim \langle \sin^2 \dots \sin^2 \dots \rangle$, which consists of a centerband and even-order sidebands. An analogous effect was investigated in homonuclear systems, where homonuclear DQ spinning-sideband patterns have only odd-order sidebands, while homonuclear TQ patterns in turn exhibit only even orders [Friedrich 98a]. The homo- and heteronuclear cases are analogous in that the rotor encoding of 2-spin coherences (now *including* the S-spin in the heteronuclear case) generally leads to odd-order sidebands, while for 3-spin coherences, even-order sidebands and a centerband are observed.

It is thus not surprising that the heteronuclear ^1H -TQ pattern has again odd-order sidebands: it corresponds to a rotor-encoded 4-spin coherence. It was shown on p. 109f that the odd-order HMQ-filtered (here termed ^1H -SQF for comparison) signal of a methyl group is the sum of 1- and 3- ^1H contributions. The ^1H -TQF pattern is naturally a pure 3- ^1H pattern. It also has the same shape as the 3- ^1H SQ contribution to the SQF pattern, which has a weighting factor of 3/4 as opposed to 1/4 for the pure TQF signal. Note that in the experimental

HDOR spectra the SQF pattern is the sum of both contributions, since they are not separated by different chemical-shift evolution (Eq. (4.15), with $\omega_{CS,I} = 0$), as opposed to the spectra in Fig. 4.11b.

The 1I- and 3I-spin contributions to the SQF pattern can be simulated on the basis of the first and the second terms in Eq. (4.15), respectively. Simulations using the experimental parameters given in Fig. 4.13 (not shown) indicated that the sidebands of order five and higher are mainly due to the 1- ^1H contribution. In comparison, the 3- ^1H pattern exhibits stronger first and third-order sideband intensities, and is identical to the experimental TQF pattern. The isolated 1- ^1H contribution to the SQF pattern is not accessible experimentally.

The appearance of the higher-order sidebands, and thus larger apparent coupling constants, can be explained in a qualitative fashion. A factor of three appears in the argument of the trigonometric functions describing such patterns: $\sin^3 a = \frac{3}{4} \sin a - \frac{1}{4} \sin 3a$. This property of products of trigonometric functions was already taken advantage of in the spectral editing applications of REPT (Section 3.3.1). It also has a quantum-mechanical connotation: when ^{13}C separated local field spectra of CH_3 -groups are discussed in terms of perturbation theory [Terao 86], the spectra are calculated as consisting of two contributions. One associated with the local field exerted by the three protons in $|\uparrow\uparrow\downarrow\rangle$ or $|\uparrow\downarrow\downarrow\rangle$ configuration (and four further permutations thereof), and the other with the protons in the $|\uparrow\uparrow\uparrow\rangle$ and $|\downarrow\downarrow\downarrow\rangle$ configurations. The local field exerted by the latter configurations is three times as large, and these yield a 25% contribution to the overall spectral intensity (simply by counting of the possible spin states). This is reflected in

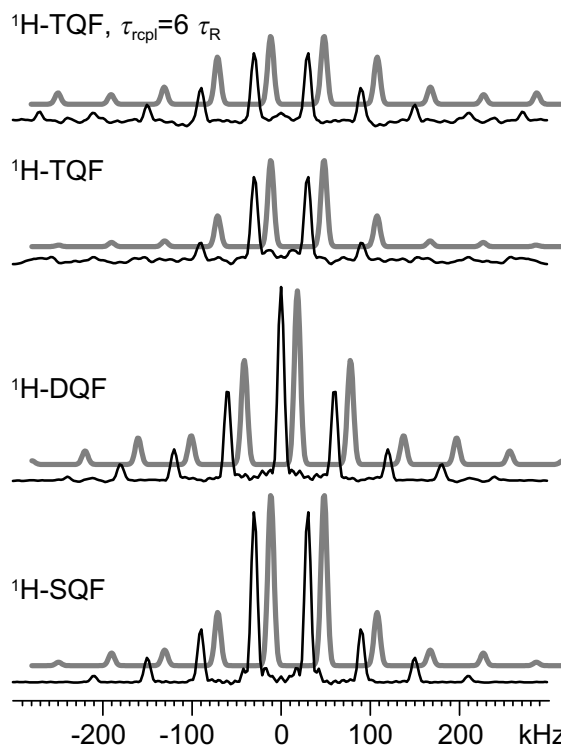


Figure 4.13: *HMQ-filtered DIP-HDOR sideband patterns of the CH_3 -signal of $U\text{-}^{13}\text{C}$ L-alanine at 30 kHz MAS and $\tau_{rcpl} = 4 \tau_R$. The grey traces are from analytical simulations based on the geometry of a single alanine molecule.*

the addition theorem used above for the result obtained from product operator theory.

4.7 Conclusions and Comparison with REPT

The class of experiments presented in this chapter was shown to exhibit features which are significantly different from the REPT techniques. Even though the two classes are based on the same principles, the fact that REPT has an I-spin evolution during excitation and an S-spin evolution during reconversion leads to spectra which are strictly dominated by individual heteronuclear spin pairs. The symmetric situation in the DIP-HMSC techniques allows an exploration of the whole product-operator subspace of MQ states encompassing a single S-spin and all the I-spins which are coupled to it. Spin counting is possible, and it was shown that the experimenter has considerable freedom in choosing not only odd-order coherences in the I-spin subspace, but also I-DQ and I-TQ coherences, which can be probed as heteronuclear multiple-quantum coherences ($\hat{S}_x \prod_i \hat{I}_x^{(i)}$), as antiphase terms ($\hat{S}_z \prod_i \hat{I}_x^{(i)}$), or as rotor-encoded heteronuclear dipolar order ($\hat{S}_z \prod_i \hat{I}_z^{(i)}$).

Many possible advantages of the spectroscopic investigation of HMQ coherences of the type $\hat{S}_\pm \prod_i \hat{I}_\pm^{(i)}$ in static samples have already been pointed out by Pines and coworkers [Weitekamp 82]. In this publication, several excitation schemes are discussed. They all have in common that initial *I-spin* magnetization is used, and that the I-spins are also the detected nuclei (due to sensitivity considerations). In the pulse sequences discussed by the authors, HMQ coherences are excited in two steps. During the first step, homonuclear couplings among the I-spins lead to I-spin homonuclear MQ modes, which are subsequently coupled to the S-heterospin to obtain the final HMQ coherence. The feasibility of the approach was demonstrated on singly ^{13}C -labeled benzene, oriented in a liquid crystal. However, most of the ingenious ideas mentioned in this paper were never pursued for actual applications, mainly because the strong homonuclear dipolar couplings in the static case interfere with a controlled manipulation of the spin system.

The simplicity and robustness of the purely heteronuclear approach to HMQ spectroscopy under very-fast MAS presented in this chapter might in turn open up a number of possible implementations. In particular, ^{13}C - ^1H (DQ) correlation spectra show promise for interesting applications in structural studies since the mere existence of a cross peak can have

considerable structural implications. The sensitivity of DIP-HMSC methods never reached the level of the REPT techniques. Nevertheless, measurements on low molecular weight compounds were shown to be possible with ^{13}C in natural abundance, the wealth of information in these spectra might merit the effort of isotopic labeling.

We expect fruitful applications of the experiments presented in this chapter to structural investigations of amorphous substances, small proteins in particular, where isotopic labeling has already entered a state of experimental routine. Moreover, the possibility of performing MQ experiments which are normalized in a manner analogous to REDOR is very promising for the study of confined molecular motion in polymers, where the increased chemical-shift resolution of ^{13}C might help to correlate order parameters (deduced from the motionally averaged dipolar coupling constants) with different chain configurations and conformations. We have obtained preliminary results on poly(styrene-*co*-butadiene) block copolymers, where the *cis* and *trans* monomer units in the butadiene block, which are difficult to resolve in homonuclear DQ NMR [Graf 98b], were indeed seen to have a different MQ build-up behavior, hinting at different residual dipolar couplings [Graf 00].

Chapter 5

HMQ Correlation Spectroscopy involving Quadrupolar Nuclei

The spectroscopic methods presented so far are very versatile in that they can easily be applied to various kinds of heteronuclear spin- $\frac{1}{2}$ pairs, where protons are simply used as a source of magnetization, by employing cross polarization to one of the two types of heterospins (for the principle, see Fig. 2.1). The theoretical treatment of the discussed methods proved quite straightforward, and the heteronuclear dipolar coupling was shown to be the dominating interaction, even in ^1H - ^{13}C systems, thus allowing a relatively simple analysis of the data. The recoupling π -pulse trains can be compensated for offset and chemical-shift anisotropy evolution using (xy-4) or higher phase cycling schemes.

Problems arise, however, when one of the involved heteronuclei (henceforth the L-spin) has a spin quantum number higher than $\frac{1}{2}$. Such spins possess quadrupole moments, whose coupling to the local electric field gradient tensor leads to quadrupolar-broadened spectra spread over hundreds of kHz or even MHz. As a result, the effect of the quadrupolar coupling on the evolution under a (finite) pulse will have a large influence on the measured signal. In this chapter, a few possibilities of how to perform REDOR and related HMQC experiments on quadrupolar nuclei with $L = 1$, ^2H in particular, will be discussed.

5.1 The Excitation Problem

The description of the action of rf-pulses applied to a certain spin species in terms of rotations in spin space (δ -pulse approximation) remains feasible only as long as the internal interactions are exceeded by the rf-frequency, $\omega_1 = -\gamma B_1$. With modern NMR probes, nutation frequencies of up to about 200 kHz can be typically realized, whereas static quadrupolar powder spectra of rigid ^2H , with splittings which are among the smallest of commonly measured quadrupolar nuclei, cover ranges of roughly ± 125 – 170 kHz. Both quantities are of the same order of magnitude, and the interplay of these interactions will be the main subject of the following sections.

In the ideal case, represented by a δ -pulse, an infinite range of frequencies is excited. The failure of a *finite* pulse to homogeneously excite spins with interactions covering large ranges of frequency can be described by its excitation profile, $E(\omega)$, which can be calculated as the Fourier transform of the rectangular pulse. This is an approximation, which is valid only in the linear-response regime [Schmidt-Rohr 94], i.e. for small flip angles, but the characteristics of $E(\omega)$ may serve as an illustrative example for the arising complications.

The excitation profile is calculated as

$$E(\omega) = \int_0^{t_p} e^{i\omega t} \omega_1 dt = \omega_1 \left(\frac{\sin(\omega t_p)}{\omega} + i \frac{\cos(\omega t_p) - 1}{\omega} \right), \quad (5.1)$$

the real part of which is a sinc-function, and solutions of the real part are shown in Fig. 5.1b. As background traces, simulated powder spectra of ^2H are shown, which are excited using a single pulse with the length corresponding to the pulses on the left. A homogeneous excitation of signals is possible only for frequencies located within the central maximum of the sinc-functions [Hentschel 79]. As is apparent from the bottom traces, an $8 \mu\text{s}$ 90° -pulse is by far insufficient to cover the spectral region of the Pake pattern, and even at higher B_1 -fields, distortions are severe. These are only in part due to the reduced excitation efficiency towards the wings of the quadrupolar spectrum; the depression of the central region and the broadening at the edges are caused by phase errors, as a result of evolution under the pulse.

Evolution under a pulse is correctly accounted for by a precession frequency around the effective field, $\omega_{eff} = -\gamma_L |\mathbf{B}_{eff}| = -\sqrt{\omega_1^2 + \omega^2}$, which has to be used to arrive at a correct

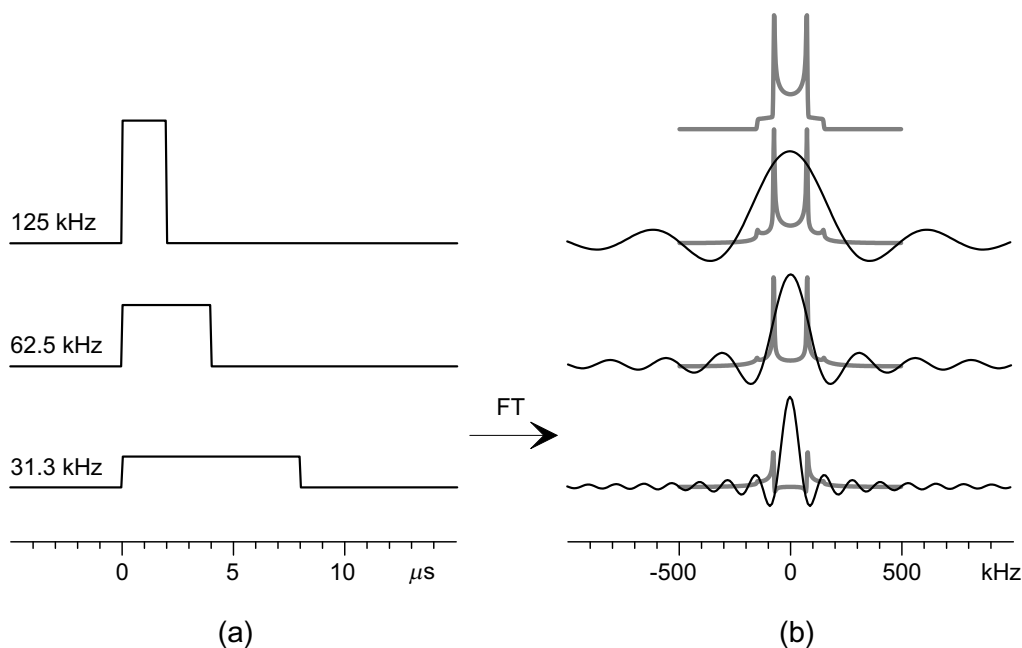


Figure 5.1: Rectangular pulses of constant flip-angle, $\phi = -\gamma_L B_1 t_p = \frac{\pi}{2}$, as represented by the area under the pulse (a), and the corresponding Fourier transforms (b). The grey background traces are simulated quadrupolar spectra ($\omega_Q/2\pi = 150$ kHz), as excited by the finite pulses. Corresponding B_1 -frequencies are indicated. On top, the spectrum excited with a δ -pulse is shown.

excitation profile, valid for arbitrary flip angles [Schmidt-Rohr 94]. A detailed analytical calculation of the effects of quadrupolar evolution during rf-irradiation was published for the special case of the solid-echo pulse sequence, which is commonly used to acquire ^2H spectra free of phase errors [Bloom 80]. Such a treatment correctly describes the phase distortions in spectra excited with a single pulse. Spectral distortions are only one manifestation of the problems introduced by finite pulses: Finite π -pulses can also not be expected to lead to a proper inversion of the magnetization, as required for REDOR and related methods. Moreover, multiple-quantum transitions are excited by finite pulses in quadrupolar nuclei [Vega 77]. An energy level diagram for $L = 1$ nuclei is shown in Fig. 5.2, where the DQ transition, $|-1\rangle \rightarrow |+1\rangle$ or $|1\rangle \rightarrow |3\rangle$, is indicated. In fact, transitions between all three states $|1 \dots 3\rangle$ (which are the eigenfunctions of the combined Zeeman and quadrupolar Hamiltonian), as induced by finite inversion pulses, contribute to the dephasing observed in a REDOR experiment.

A theoretical treatment of the spin dynamics is not straightforward, because the operators for the quadrupolar interaction, and those describing rf-pulses, do not commute:

$[\hat{T}_{20}^{L,Q}, \hat{L}_{x/y}] \neq 0$. Average Hamiltonian theory, with the cycle time defined by the rotation due to the pulse, has to be used to describe the time evolution, and higher orders become increasingly important for large quadrupolar couplings. Finally, the time-dependence of $A_{20}^{Q,LAB}(\omega_R t)$ due to the MAS requires further approximations and complex theories such as the FLOQUET approach [Levante 95]. Therefore, in Section 5.2.2, the time evolution of the density matrix will be explored with computer simulations, in order to arrive at a feasible REDOR recoupling scheme for quadrupolar nuclei.

Numerous applications of the REDOR experiment to quadrupolar systems have been published, and modifications have been devised to extend the applicability of the simple REDOR theory to quadrupolar systems. As remedies for the excitation problems of quadrupolar spins, composite pulses [Sack 99] or adiabatic passage pulses (REAPDOR, *rotational-echo, adiabatic-passage, double-resonance* [Gullion 95]) have been proposed.

The former approach relies strongly on the successful compensation of the imperfect inversion of the finite pulses, because the recoupling pulse train is applied to the L-spins, with only a central refocusing pulse left on the S-spins. This approach was chosen by the authors due to the poor B_1 -field strength on the S-spin channel of their triple-resonance probe, leading to excitation problems also for ^{13}C [Vega 99]. Even though their theoretical and experimental data proved a clear advantage of composite over conventional π -pulses, a large influence of the quadrupolar coupling remained, leading to a non-trivial dependence of the REDOR curve on the heteronuclear dipolar coupling.

A more promising approach is certainly to use the Garbow/Gullion version of the REDOR experiment [Garbow 91] shown in Fig. 2.1, p. 41, where the number of pulses on the L-spins is *minimized*. The one pulse left on the L-spins may then be a composite pulse, and this is the approach to be discussed in the following.

The REAPDOR technique, in turn, does use the Garbow/Gullion version of the REDOR

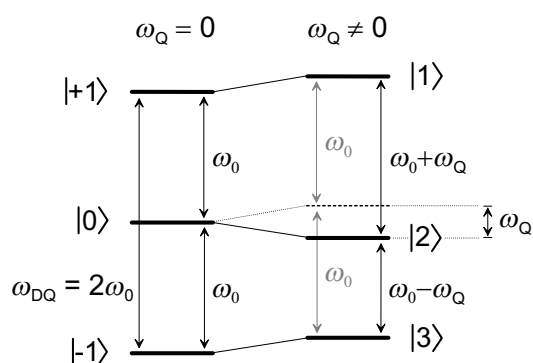


Figure 5.2: Energy level diagram for spin $L = 1$ quadrupolar nuclei.

experiment, but the pulse on the L-spin is deliberately applied using rather low rf-power, such that it can be described as *adiabatic*. The zero-crossings of the quadrupolar tensor brought about by the MAS, in combination with the rf-irradiation, lead to a transfer of populations between the eigenstates of the L-spin (in the adiabatic regime, the eigenstates avoid energy level crossings). This leads to the desired dipolar dephasing, which is yet very dependent on the quadrupolar tensor parameters, its relative orientation with respect to the heteronuclear dipolar tensor, and the applied rf-power. As a result, rather strong assumptions have to be made in order to analyze the experimental data.

5.2 ^2H - ^{13}C HMQC Spectroscopy

Before addressing the excitation problem and possible solutions in detail, we shall revisit the internal difference REDOR experiment presented in Chapter 2 (Fig. 2.3). The two-dimensional version of this ^{13}C - ^2H REDOR method has successfully been applied to separate ^2H quadrupolar powder spectra by ^{13}C isotropic chemical shifts [Sandström 99].

The pulse sequence meets the requirement of a minimum number of pulses on the L-spin channel, as is advisable for a $L = 1$ system. It has been shown in Section 2.2 that a simple phase cycle of the second L-spin $\pi/2$ -pulse leads to a selection of HMQ coherence, which is probed during the t_1 dimension of the experiment. The basic difference to the methods discussed so far is, however, that the full 2D experiment is here conducted in a constant-time fashion, i.e., while t_1 is incremented, the last and first rotor periods of the excitation and reconversion periods, respectively, are decremented by half the t_1 increment. Thus, t_1 is restricted to indirect acquisition times smaller than $1 \tau_R$. Moreover, the overall reconversion Hamiltonian is not modulated by t_1 (no reconversion rotor encoding), such that the central mechanism of MQ spinning-sideband generation as discussed in the preceding chapters is not active.

5.2.1 Theoretical Description

The theory for the experiment in Fig. 5.3 has been laid out in [Sandström 99], and is sketched here to highlight the basic differences to the REDOR and the related DIP-HMSC experiments

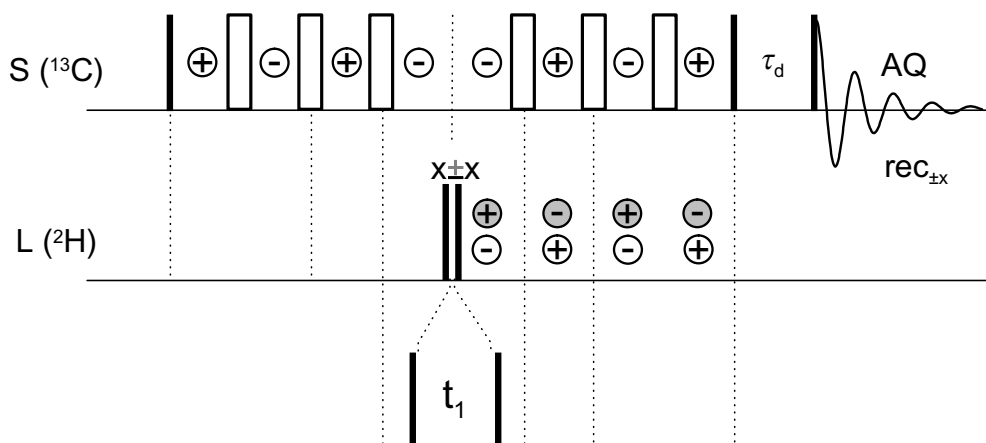


Figure 5.3: Pulse Sequence for ^2H - ^{13}C HMQC correlation spectroscopy under MAS. The experiment is performed within the general context of a CP pulse sequence, as shown in Fig. 2.1.

(Chapter 4), where protons were used as passive spin. We restrict the discussion to isolated ^{13}C - ^2H pairs.

The calculation of the S-spin evolution under SL-coupling is more involved if the L-spins are $L = 1$ nuclei. The \mathbf{S} operators have to be split into two components — one component associated with the $|0\rangle_L$ eigenstate of the L-spin, and the other with the $|+1\rangle_L$ and $| - 1\rangle_L$ states [Ernst 87],

$$\hat{\rho}(0) = \hat{S}_x = \hat{S}_x(\mathbb{1}_L - \hat{L}_z^2) + \hat{S}_x \hat{L}_z^2, \quad (5.2)$$

where the former component is invariant under the action of the heteronuclear dipolar Hamiltonian, and the latter evolves with *twice* the coupling constant into in- and anti-phase components according to

$$\hat{\rho}(\frac{1}{2}N\tau_R) = \hat{S}_x(\mathbb{1}_L - \hat{L}_z^2) + \hat{S}_x \hat{L}_z^2 \cos(\Phi') + \hat{S}_y \hat{L}_z \sin(\Phi'), \quad (5.3)$$

where the acquired dipolar phase is given by

$$\Phi' = 2(\frac{N}{2} - \frac{1}{2})\bar{\Phi} - 2\Phi_{DSL}(\tau_R/2; \tau_R - t_1/2). \quad (5.4)$$

$\Phi_{DSL}(t, t')$ and $\bar{\Phi}$ are defined in Eqs. (1.82) and (2.6). The second term accounts for phase acquired under the incomplete last half excitation rotor cycle, if $t_1 > 0$. Note that, owing to

the conventions of the authors, and as a reference to the original REDOR experiment, N is the total number of excitation plus reconversion recoupling rotor periods (in the preceding chapters, the excitation and reconversion periods were calculated separately with N_{rcpl} rotor periods each). During t_1 , the HMQ coherence $\hat{S}_x \hat{L}_y$ evolves under the S-spin CSA, L-spin chemical shifts and L-spin quadrupolar couplings. The S-spin CSA is refocussed, by virtue of the constant-time concept, and for the L-spins, the quadrupolar interaction is so large that any other interaction can safely be neglected. Only the cosine-part of the quadrupolar evolution (i.e., the x-component in t_1) is measured, which is sensible, because, for on-resonance excitation, the quadrupolar interaction leads to symmetric spectra. After the final z-filter, only observable magnetization $\sim \hat{S}_x$ is retained:

$$\begin{aligned} \hat{\rho}_{\pm}(N\tau_R + \tau_d) &= \hat{S}_x(\mathbb{1}_L - \hat{L}_z^2) + \hat{S}_x \hat{L}_z^2 (\cos \Phi' \cos \Phi'' \mp \sin \Phi' \sin \Phi'' \cos \Phi_Q(t_1)) \\ &= \frac{1}{3} \hat{S}_x + \frac{2}{3} \hat{S}_x (\cos \Phi' \cos \Phi'' \mp \sin \Phi' \sin \Phi'' \cos \Phi_Q(t_1)) \end{aligned} \quad (5.5)$$

The \pm -sign indicates the HMQ selection phase cycle of the second L-spin 90° -pulse along with a receiver phase inversion. The dipolar phase for the reconversion reads

$$\Phi'' = 2\Phi_{D_{SL}}(t_1/2; \tau_R/2) - 2\left(\frac{N}{2} - \frac{1}{2}\right)\bar{\Phi}, \quad (5.6)$$

and the quadrupolar evolution during t_1 leads to an integrated phase

$$\Phi_Q(t_1) = \frac{3}{2} \Phi_Q(-t_1/2, t_1/2) = \frac{3}{2} \frac{1}{t_1} \int_{-t_1/2}^{t_1/2} A_{20}^{Q,LAB} dt. \quad (5.7)$$

The definitions of the phases are all according to the formalism introduced on pp. 33f.

For $t_1 = 0$, Eq. (5.5) reduces to the corresponding density operator for a normal REDOR experiment, with a full stimulated echo (minus-sign) S_0 and a dephased signal (plus-sign) S . The normalized REDOR difference intensity is thus

$$\Delta S/S_0 = \frac{2}{3} (1 - \langle \cos 2N\bar{\Phi} \rangle) \quad (5.8)$$

A comparison with the equivalent expression for an SL-pair with $L = \frac{1}{2}$ (Eq. (2.9)) reveals that (i) a factor of 2 arises in the argument of the cosine due to the increased sensitivity of

an $L = 1$ nucleus to heteronuclear dipolar couplings, and (ii) the plateau value is decreased from 100% to $\frac{2}{3} = 66.7\%$ (or from 50% to 33.3% in terms of HMQ transfer) as a result of the invariant component during the dipolar evolution (first term in Eq. (5.5)).

In the full 2D-experiment, the spectrum in the indirect dimension is governed by the quadrupolar interaction (with some weak dipolar contribution due to the t_1 -dependence of Φ' and Φ''). The MAS is usually much slower than the width of the quadrupolar tensor, and since t_1 is restricted to one rotor period, the resulting resolution in t_1 is too low to observe spinning sidebands, such that the characteristic (though slightly distorted) Pake envelope is observed, where the quadrupolar splitting can be read off from the splitting between the singularities. The situation is reminiscent of the *wideline separation* (WISE) method [Schmidt-Rohr 92], where a ^1H wideline spectrum is detected in the first dimension of the 2D CP correlation experiment under MAS.¹ Therefore, the experiment discussed here will also be referred to as ^2H -WISE.

5.2.2 Evolution of $L = 1$ Spins Under Finite Pulses

Regarding the HMQ selection phase cycle, it is stated in the original paper [Sandström 99] that the $\pm x$ -phase inversion of the second 90° -pulse “corresponds to applying either a π -pulse or a zero degree pulse”. This was meant as argument for the reduced 1D version of the experiment to be analogous to REDOR. That this statement can only be true in a very approximate way, is proven by the fact that the method performs best if the two pulses are actually shorter than required for a 90° flip angle. This is common practice in ^2H spectroscopy [Hentschel 79, Spiess 80], and may provisionally be explained by an increased excitation efficiency for shorter finite pulses.

The aim of the work in this chapter is to show the inadequacy of the δ -pulse approximation employed for the theoretical treatment, and since the question of concern is the transformation behavior of the L -spins under the pulses, the dynamics of a single L -spin density matrix during the pulses will be explored using numerical simulations. The 3×3 -density matrix is depicted in Fig. 5.4, where the significance of its nine components as population

¹Inefficient cross-polarization to quadrupolar nuclei is the main reason for not applying the much simpler WISE experiment to the systems in question here.

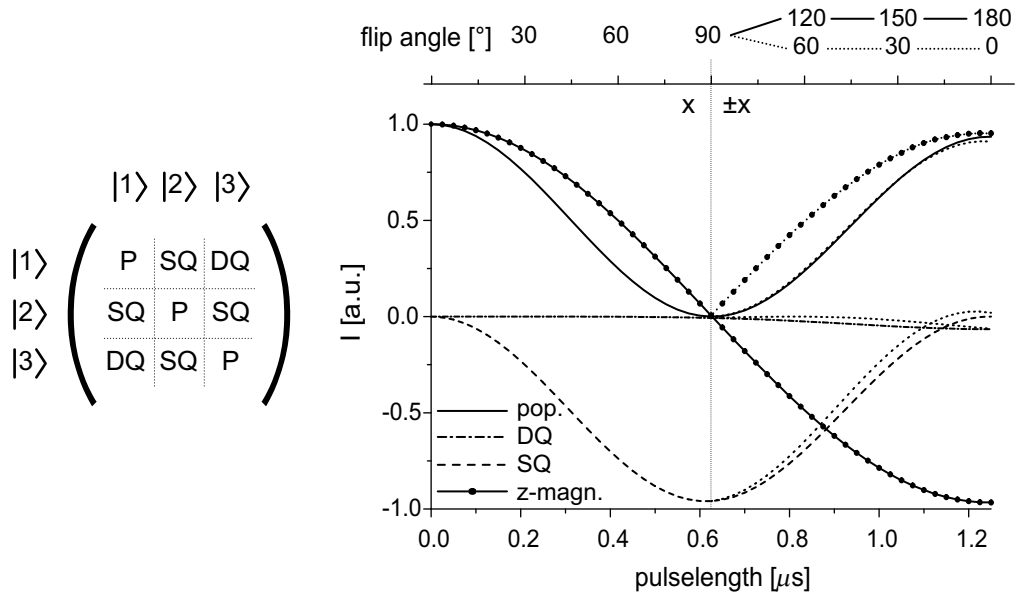


Figure 5.4: Simulated time dependence of the components of the density matrix of a $L = 1$ spin under the combined action of quadrupolar coupling ($\omega_Q/2\pi = 150$ kHz), rf-irradiation ($\omega_1/2\pi = 400$ kHz) and MAS ($\omega_R/2\pi = 5$ kHz), powder averaged. The z -magnetization is calculated as the expectation value of \hat{L}_z , and the norms of the different components have arbitrary signs for clarity. The dotted lines are continuations of the corresponding lines for the case of an inverted phase during the second pulse with effective flip angles as indicated on the axis on top.

states and SQ and DQ coherences is indicated. The transitions associated with the complex off-diagonal components can be identified in Fig. 5.2.

In Fig. 5.4, an unrealistically strong rf-field was used for the irradiation of the L-spin with $\omega_Q/2\pi = 150$ kHz, under MAS of $\omega_R/2\pi = 5$ kHz. The observed behavior is close to what would be expected for an ideal situation assuming no quadrupolar interaction (or δ -pulses): the z -magnetization is almost completely inverted for the $(90_x 90_x)$ sequence, and is restored to its initial value for the $(90_x 90_{-x})$ combination, supporting the argument of an effective cancellation of the two pulses for the case of opposite phases. The amplitudes of the different transitions and populations behave accordingly, the populations follow a \cos^2 -trend, i.e. going through a minimum for a flip angle of 90° , whereas the SQ intensities go through a maximum (\sin^2), with negligible build-up of DQ intensity, and almost no apparent difference for the two cases with different phases for the second pulse (differences would manifest in the phase and signs of the SQ coherences, which are lost upon calculating the norm).

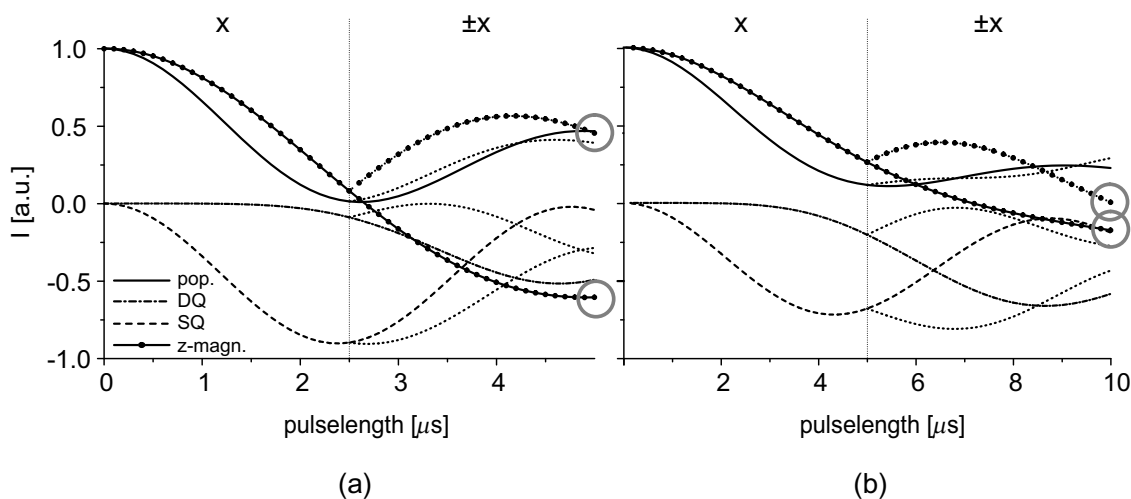


Figure 5.5: Time-dependence of density matrix components and z -magnetization, in analogy to Fig. 5.4, for a finite $90_x 90_{\pm x}$ -pulse using rf-field strengths corresponding to $\omega_1/2\pi = 100$ kHz (a) and 50 kHz (b).

The situation changes entirely if more realistic rf-fields (100 and 50 kHz) are considered. In Fig. 5.5, it is shown that an effective π -pulse fails to completely invert the magnetization, while the combination with different phases does not even produce a magnetization with the same sign as the initial one. Rather, the resulting magnetizations are similarly close to zero for $\omega_1/2\pi = 50$ kHz in both cases.

The consequence for an internal difference REDOR experiment is readily apparent: The $(90_x 90_{-x})$ pulses cannot lead to a complete stimulated echo, as required if the simple theory is to be applied, it rather leads to an appreciable dephasing as well, as a result of (pictorially speaking) the fraction of spins which have not been inverted. Also, the dephasing resulting from the application of the $(90_x 90_x)$ pulses is not at a maximum. Moreover, DQ transitions become increasingly important, and are responsible for a mixing between the $\hat{S}_x(\mathbb{1}_L - \hat{L}_z^2)$ and $\hat{S}_x \hat{L}_z^2$ components of \hat{S}_x transverse magnetization. Thus, the once invariant component, the existence of which leads to the REDOR difference plateau at 66.7%, contributes to the dephasing, such that, even for a single SL-pair, the dephasing will eventually reach 100%, if many pulses are applied. This is exactly what has been observed by Sack et al. [Sack 99], who compared the common REDOR experiment (with many π -pulses on ^2H), with composite pulse schemes. The accumulating effect of DQ transitions upon applying many π or composite pulses lead to complete dephasing in all their experiments.

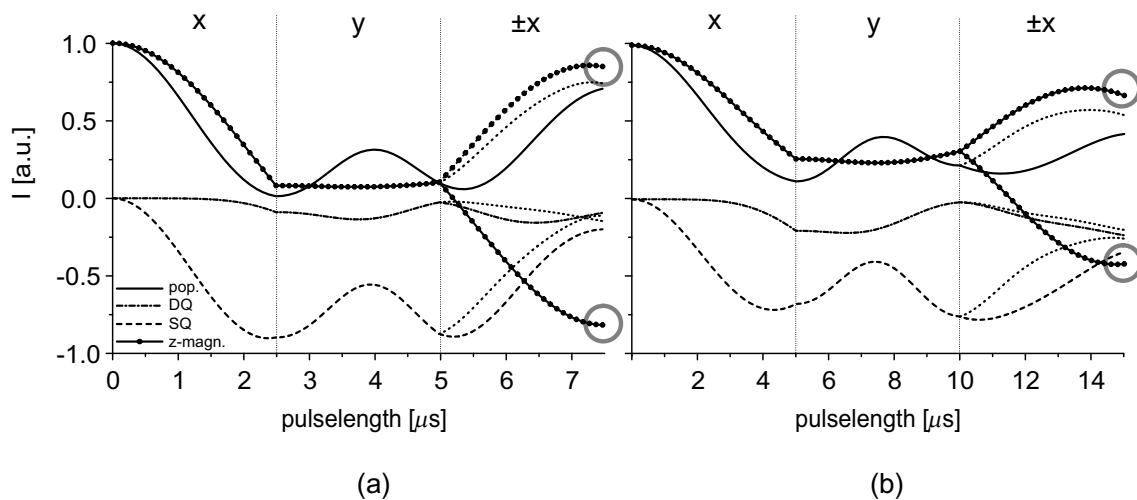


Figure 5.6: Time-dependence of density matrix components and z -magnetization, in analogy to Fig. 5.4, for a finite $90_x90_y90_{\pm x}$ -composite pulse using rf-field strengths corresponding to $\omega_1/2\pi = 100$ kHz (a) and 50 kHz (b).

The question remains, are the composite inversion pulse schemes still useful, if only one composite pulse is applied for the central inversion in the REDOR sequence? The composite pulses studied by Sack et al. were the $(90_x90_y90_x)$ and $(90_x180_y90_x)$ combinations, which have been thoroughly analyzed by Levitt and coworkers [Levitt 84] for static experiments, using average Hamiltonian theory and simulations. Longer and better-compensated sequences have also been proposed by the authors, but due to the time-dependence of the quadrupolar coupling, the compensation is expected to break down for these sequences when being applied under MAS. In fact, the simulations presented here indicated the best performance for the $(90_x90_y90_x)$ sequence, which is analyzed in Fig. 5.6. The rotor period at 5 kHz MAS is 200 μs long, which should be compared to the duration of 15 μs for the whole sequence at an rf-field as low as 50 kHz. The quasi-static treatment of the composite pulse would thus be well-justified.

The successful inversion by the $(90_x90_y90_x)$ composite pulse has a particularly straightforward interpretation, namely that the second pulse can be seen as forming a solid echo, the maximum of which would be effective at some time during the third pulse, thus in part compensating the action of the quadrupolar coupling during the whole period.

At $\omega_1/2\pi = 100$ kHz, the $(90_x90_y90_x)$ sequence is seen to successfully invert almost the complete initial z -magnetization, with only minor excitation of DQ coherences. Even at 50

kHz, there is still an appreciable inversion, as opposed to the conventional π -pulse, where the final z-magnetization is almost zero (Fig. 5.5b).

Therefore, a REDOR experiment performed with such a composite pulse should lead to a higher dephasing. Also, the internal difference (i.e. HMQ-filtered) intensity will be much bigger, which is most strikingly proved by comparison of the differences in z-magnetizations for the $(90_x 90_{-x})$ and $(90_x 90_y 90_{-x})$ combinations in Fig. 5.5b and 5.6b, respectively, from which it is clear that almost *no* signal would be observed for conventional $(90_x 90_{\pm x})$ pulses with $\omega_1/2\pi = 50$ kHz.

The placement of the phase inversion $(90_x 90_y 90_{\pm x})$ is somewhat arbitrary, in that an approach such as $90_x 90_{\pm y} 90_{\pm x}$ would work equally well for the internal difference REDOR experiment. For the ^2H -WISE experiment, it is still a matter of concern where to insert the t_1 evolution period. This information can be inferred from Fig. 5.6. For an HMQ evolution, a “clean” $(\hat{S}_x)\hat{L}_y$ state, with a maximum amplitude would be desired. Even though the presented diagrams lack phase information, it is still apparent that the maximum SQ intensity is present before or after the middle 90_y -pulse. In the experiment considered in the next two sections, the sequence used is thus $(90_x - t_1 - 90_y 90_{\pm x})$.

It should be noted that the conventional 1D REDOR experiment is still preferably performed in the usual way, i.e. by omitting the composite pulse completely for the acquisition of the reference intensity. On the one hand, this scheme is performed within only two thirds of the experiment time of the internal difference approach (half of the difference signal, $\Delta S = S_0 - S$, is due to the reference, which has to be measured separately with half the number of scans, in order to obtain the desired $\Delta S/S_0$), and on the other hand, the S/N ratio is bigger, because even for the composite pulse, the $(90_x 90_y 90_{-x})$ combination will always lead to some dephasing.

5.2.3 Simulated and Experimental Results

In Fig. 5.7a, a simulated quadrupolar powder pattern of ^2H is compared with the ^{13}C -detected ^2H -WISE spectrum, as obtained as t_1 -signal of the full HMQC experiment. δ -pulses were assumed for the simulations. The characteristic features of the quadrupolar evolution in the HMQC experiment (Eq. (5.5)) are seen to be the reduced intensity towards the wings of the

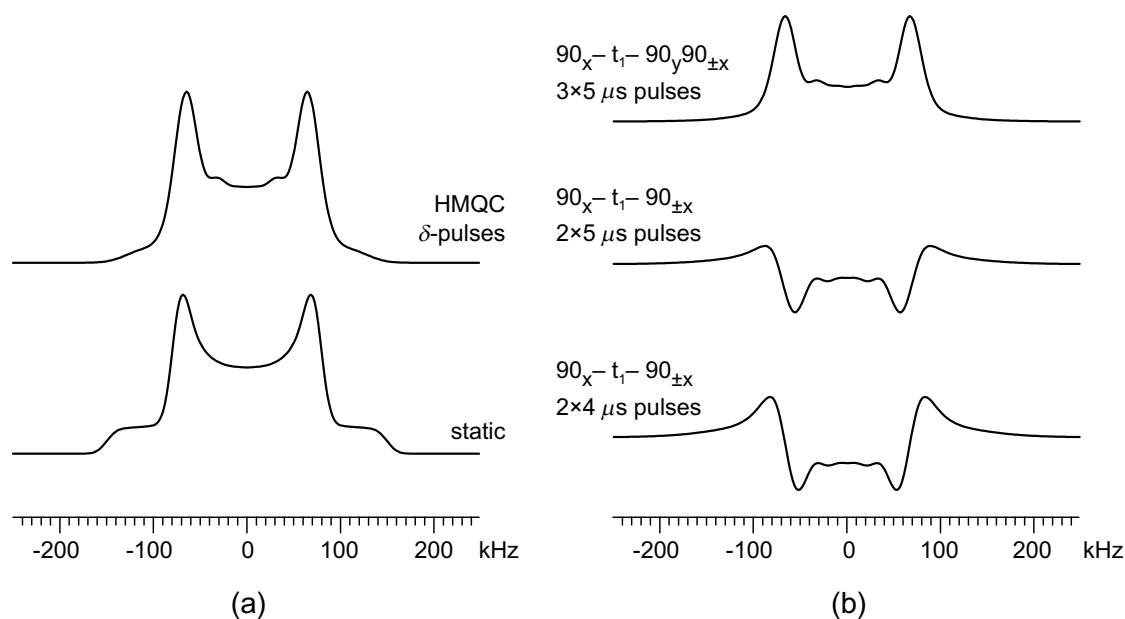


Figure 5.7: Simulated ^2H -WISE spectra for a ^{13}C - ^2H pair, assuming $D_{\text{SL}}/2\pi = 500$ Hz, $6\tau_{\text{R}} = 1.2$ ms total recoupling time at $\omega_{\text{R}}/2\pi = 5$ kHz, and $\omega_{\text{Q}}/2\pi = 150$ kHz. In (a), the δ -pulse HMQC spectrum is compared to the static quadrupolar spectrum. In (b), HMQC spectra using the conventional pulse sequence, calculated for two different pulse lengths, assuming an rf-field corresponding to $\omega_1/2\pi = 50$ kHz, are compared to the composite-pulse approach (top slice). All intensities are to scale.

spectrum, as well as distortions in the central part. The splitting read off from the ^2H -WISE slice is typically about 10% smaller than the real quadrupolar splitting.

The middle slice in Fig. 5.7b is the result of a density matrix simulation, taking into account the finite pulse lengths. This spectrum bears almost no resemblance to the δ -pulse spectrum, most notably, the middle region is depressed to a level below the baseline. This is a result of severe symmetric phase distortions, which arise due to the finite length of the pulses. Pictorially, the “real” $t_1 = 0$ slice cannot be detected because the pulse length is on the order of the typical t_1 -increment. The distortions are much too big to justify a simple first-order phase correction, such that a mathematical extrapolation of the time-domain data remains as the only feasible way to remove this strong artifact. If the splitting would be erroneously read off from the two maxima, a much too large value would result.

The problem is seen to be slightly alleviated by application of pulses with smaller flip angles (bottom slice). Shorter pulses excite the quadrupolar spin more efficiently, and the

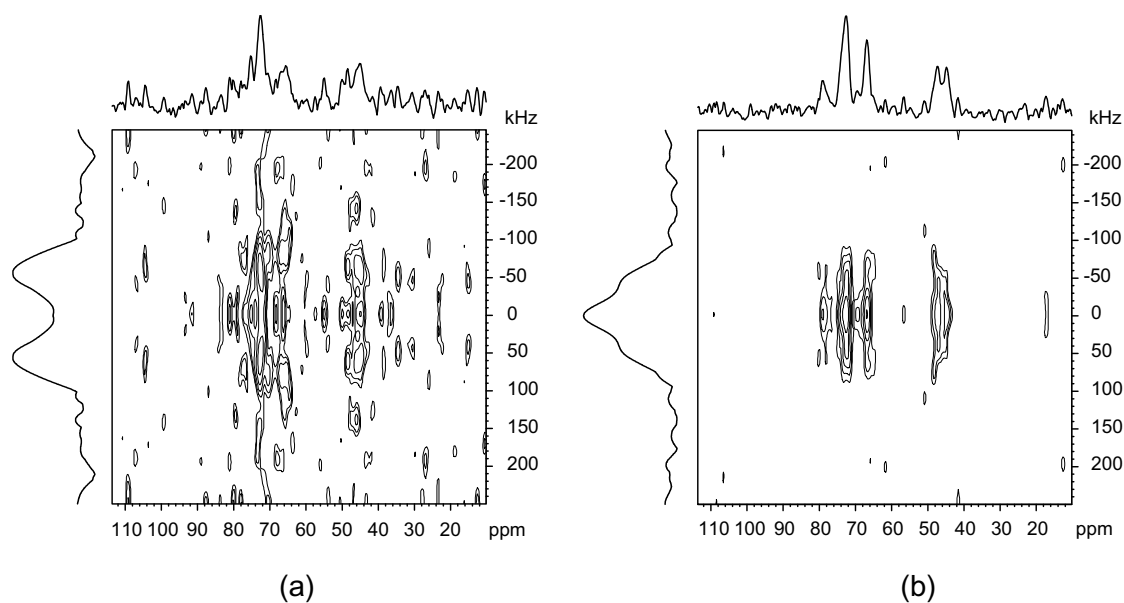


Figure 5.8: Experimental ^2H -WISE spectra of O^2H -poly(vinyl alcohol), acquired under the same conditions ($\omega_1^{\text{H}}/2\pi = 67$ kHz, corresponding to a 3.7 μs 90° -pulse, $\omega_R/2\pi = 5$ kHz, $8 \tau_R$ recoupling, 4096 scans, $T = 363$ K), using two conventional L-spin pulses of 2.5 μs length (a), and the composite-pulse scheme with three 3.7 μs pulses (b). The spectra on top and to the left are skyline projections.

intensity and the phasing is better in this case. A dramatic improvement is, however, achieved if the composite pulse scheme is used (top slice). Phase distortions are not visible any more, and the resulting lineshape is almost identical to the δ -pulse spectrum, with the same splitting between the horns. The only apparent effect of the finite composite pulse is that the intensity is decreased by a factor of about two as compared to the δ -pulse simulation. The simulation here is for $\omega_1/2\pi = 50$ kHz, where according to Fig. 5.6b the decrease in intensity is to be expected. The integral intensity for the middle slice is close to zero, which was concluded from Fig. 5.5b as a result of the lack of differences in the L-spin z-magnetizations for the two steps of the phase cycle. Therefore, in the latter case the spectral intensity resides almost completely in the imaginary parts of the signal.

Finally, an experimental proof of the feasibility of the concepts discussed in this chapter is presented in Fig. 5.8. Two 2D ^2H -WISE spectra are shown, both measured on OH-deuterated poly(vinyl alcohol) under nearly the same conditions. The ^{13}C signals are those from the crystalline regions of the polymer, where the dynamics of the hydrogen bonds was the subject of investigation. The details are presented in Section 7.2.

The marked difference between the spectra is that spectrum (a) was measured with the conventional $(90_x 90_{\pm x})$ scheme, where ^2H pulses with effective flip angles of 61° were used, whereas the spectrum in (b) was acquired with the $(90_x - t_1 - 90_y 90_{\pm x})$ composite pulses, using the correct flip angles. The S/N ratio is obviously about twice as good for the composite pulse spectrum. Most notably, as seen in the projections of the ^2H dimension, the quadrupolar lineshapes not only differ among themselves, but are also different from the typical rigid-limit lineshape. This gives valuable information about the dynamics in PVA at the given temperature, and also marks another important point: the projection in spectrum (a), where the central part is depressed as a consequence of the large phase distortions, nevertheless looks much like an expected rigid-limit lineshape. A failure of properly treating the expected phase distortions in a conventional ^2H -WISE spectrum might thus lead to serious misinterpretations of the dynamical information contained in such spectra.

As a concluding remark, the concept of REDOR-recoupled dipolar HMQC spectroscopy proved applicable under the more adverse experimental conditions posed by quadrupolar nuclei as L-spins, if their excitation behavior is accounted for by composite pulses. It should be noted, however, that the numerical simulations for the composite-pulse scheme indicated that an rf-field of 50 kHz and a quadrupolar coupling of 150 kHz mark the lower and upper limits, respectively, for the application of a simple \pm -phase cycle for the selection of HMQ coherence. As a consequence, the composite pulse approach to HMQ correlation involving quadrupolar nuclei presented in this chapter is limited to nuclei with comparably weak quadrupolar couplings, such as ^2H or ^7Li .

Chapter 6

Relaxation-Induced Dipolar Exchange with Recoupling

In most systems with spin $L > \frac{1}{2}$, the quadrupolar couplings are so large that their theoretical treatment as a first-order perturbation is no longer appropriate. The conditions under which the composite-pulse schemes discussed in the last chapter are still applicable within the δ -pulse approximation were shown to be limited to moderate quadrupolar couplings. Thus, for most quadrupolar nuclei the theoretical analysis of composite-pulse REDOR and REAP-DOR results is extremely involved since the amount of dipolar dephasing is dependent on the quadrupolar coupling constants, and a careful spectrometer setup and calibration are essential.

6.1 Circumventing the Excitation Problem

Fig. 6.1 raises the question of whether it might be possible to perform a REDOR experiment where the central inversion π -pulse is also applied on the S-spin, i.e. without irradiating the L-spin at all. This might seem counterintuitive at a first glance because, how could information about the coupling between two nuclei possibly be obtained without manipulating both coupling partners? A review of the theory of REDOR as presented in Section 2.1 reveals that the average dipolar REDOR Hamiltonian (Eq. (2.5)) was derived *without* any restriction on the placement of the inversion pulses. Therefore, the approach can, in principle, be expected to function even though, clearly, the selectivity with respect to the L-spin species would be

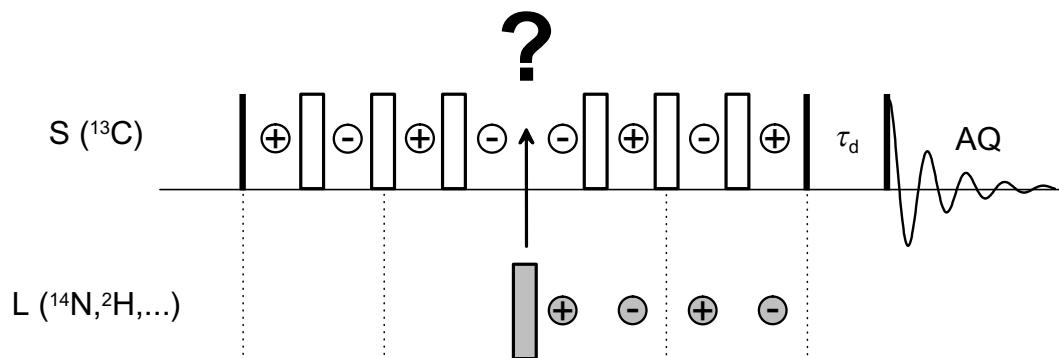


Figure 6.1: Independence of the principle of REDOR on the placement of the central π -pulse.

lost. Here, this is not considered a serious restriction since the number of NMR-active nuclei is limited in organic substances, and might be controlled by isotopic labeling.

However, the experiment proposed in Fig. 6.1 remains not feasible for another reason: the CSA time-evolution becomes non-trivial once an uninterrupted π -pulse train with $\frac{1}{2} \tau_R$ spacings is applied. The CSA is, in analogy to the heteronuclear dipolar coupling, *recoupled* by such a π -pulse train, and the average CSA phase acquired for one rotor period of evolution with π -pulses at the center and end can be defined in analogy to Eqs. (2.5) and (2.6):

$$\bar{\Phi}_{CS} = 2 \Phi_{CS}(0; \tau_R/2) = 4 \frac{S_1}{\omega_R} \cos \gamma - 4 \frac{C_1}{\omega_R} \sin \gamma \quad (6.1)$$

The coefficients S_1 and C_1 , as given by Eqs. (1.77) and (1.75), respectively, are proportional to the CSA anisotropy parameter, δ_{CS} , and also depend on the asymmetry of the tensor, η_{CS} . For $N/2$ rotor periods of the π -pulse train, the CSA evolutions of transverse \hat{S}_x -magnetization reads

$$\hat{S}_x \xrightarrow{\frac{N}{2} \bar{\Phi}_{CS} \hat{S}_z} \hat{S}_x \cos \frac{N}{2} \bar{\Phi}_{CS} + \hat{S}_y \sin \frac{N}{2} \bar{\Phi}_{CS}. \quad (6.2)$$

Even in proton systems, where the CSA is usually negligibly small, the amplification after an evolution time of $\frac{N}{2} \tau_R$ is large enough to substantially dephase of the \hat{S}_x component, as described by the powder average of $\langle \cos \frac{N}{2} \bar{\Phi}_{CS} \rangle$.

The recoupling of the CSA interaction can, however, be employed to probe slow reorientational dynamics in ^{13}C spin systems [deAzevedo 99]. The pulse sequence for the so-called

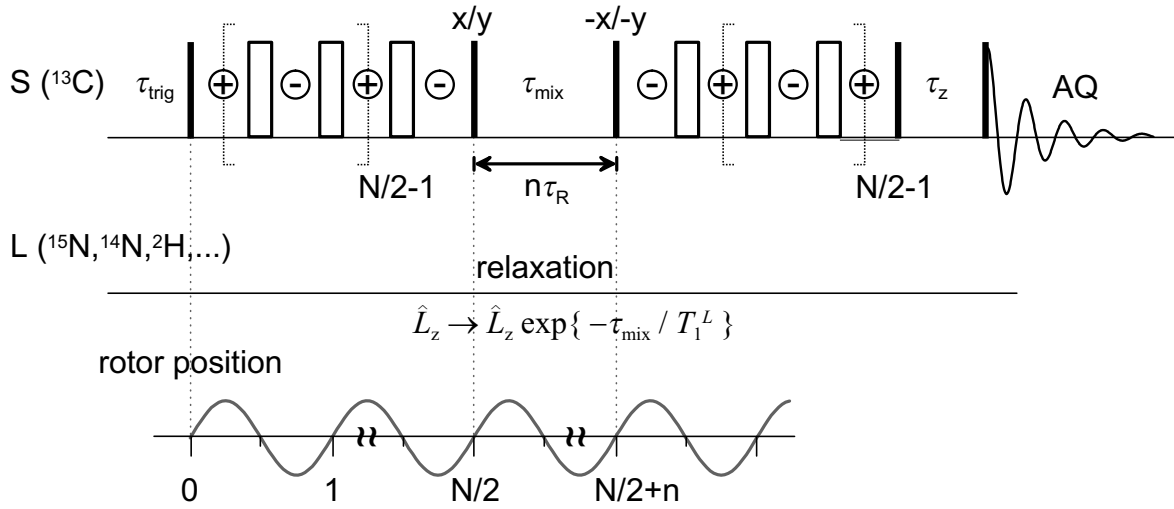


Figure 6.2: Pulse Sequence for the RIDER and CODEX experiments. The π -pulse trains (open bars) may be phase-cycled according to the $(xy-n)$ schemes [Gullion 90]. Note that ^1H dipolar decoupling is applied only during the recoupling and acquisition periods (see Fig. 2.1).

CODEX (centerband-only detection of exchange) experiment is shown in Fig. 6.2. The principle of the method is as follows: both components of the S-spin transverse magnetization in Eq. (6.2) are stored along z in different scans, as indicated by the two orthogonal phases of the storage pulse after the first recoupling period (of $N/2$ rotor periods length). After a mixing time, τ_{mix} , each of these components is returned to the transverse plane where it evolves during a second recoupling period (of again $N/2 \tau_R$ length), acquiring another cosine or sine phase, respectively. If reorientation occurs during τ_{mix} , the orientation of the CSA tensor during the second recoupling period differs from the first recoupling period, as indicated by the subscript of the integrated phase, $\bar{\Phi}_{CS,2}$. The final signal, as detected after a second z-filter, τ_z , is thus

$$S_{echo} = \left\langle \cos \frac{N}{2} \bar{\Phi}_{CS,1} \cos \frac{N}{2} \bar{\Phi}_{CS,2} + \sin \frac{N}{2} \bar{\Phi}_{CS,1} \sin \frac{N}{2} \bar{\Phi}_{CS,2} \right\rangle_{(\Phi_{CS,1} = \Phi_{CS,2})} 1, \quad (6.3)$$

where a full stimulated echo ($S_{echo} = 1$) is obtained only if no reorientation of the CSA tensor occurs during τ_{mix} ($\cos^2 a + \sin^2 a = 1$). A reorientation during τ_{mix} results in a dephasing of the stimulated echo, which depends both on τ_{mix} (i.e., on the correlation time of the dynamical process) and on the geometry of the motion. Details of the CODEX method are published in [deAzevedo 99, deAzevedo 00]. Note that the mixing time has to be an integer multiple of τ_R because $\bar{\Phi}_{CS}$ is also a function of the initial rotor phase. For $\tau_{mix} \gg \tau_R$, an external trigger must be used to ensure proper rotor synchronization.

The CODEX technique is described here, because it actually represents the solution to the CSA problem posed above for the single-channel REDOR concept: a REDOR heteronuclear recoupling π -pulse train can indeed be applied on a single channel, with retention of the full signal uninfluenced by CSA. However, the heteronuclear dipolar interaction should not have any influence on the intensity measured in a such an experiment from first principles, because the concept of the stimulated echo (Eq. (6.3)) applies equally well for recoupled dipolar phases. The influence of heteronuclear dipolar couplings enters in a more subtle way: the antiphase component of the dipolar evolution, stored as heteronuclear dipolar order, $\hat{S}_z\hat{L}_z$, during τ_{mix} , is subject to *L-spin relaxation*, as indicated in Fig. 6.2. Thus, heteronuclear dipolar couplings become observable.

In the following, the details of how weak dipolar coupling constants between naturally abundant ^{13}C and quadrupolar nuclei can be determined *without irradiating* the heterospin in question, will be described. Of course, the method also works for pairs of spin- $\frac{1}{2}$ heteronuclei. The experimental advantages are tremendous since only a double-resonance probe is needed and the difficulties of calibrating pulses on quadrupolar nuclei are avoided.

The basic effect was observed first by Frydman and coworkers [Sachleben 96] and is termed DEAR (*dipolar exchange-assisted recoupling*). However, DEAR is neither an MAS method nor does it explicitly use the concept of recoupling. The method is here generalized for application to any kind of heteronuclear spin system under MAS. The requirements are that T_1 relaxation times of the passive heteronucleus are on the order of 1 s or less, which is the case for most quadrupolar systems, and that slow dynamics and spin diffusion on the same timescale can be excluded. The mechanism of exchange by dipolar coupling to a relaxing heteronucleus is so different from the principles of CODEX that we suggest a different acronym for the application presented here: RIDER, for *relaxation-induced dipolar exchange with recoupling*. Another descriptive acronym would be HERESY, for *heteronuclear relaxation spectroscopy*, which was, however, not chosen for reasons of political correctness [Schmidt-Rohr 99]. The experiment will be shown to yield distance-dependent dephasing curves in close analogy to REDOR. The results presented in this chapter have been accepted for publication [Saalwächter 00b].

6.2 Experimental Procedure

The pulse sequence has been modified from the original CODEX experiment [deAzevedo 99] by insertion of another z-filter, τ_{trig} , after the CP contact pulse to provide trigger time for rotor synchronization.¹ In the original experiment, this was done before the CP such that the minimum mixing time was at least as long as the contact pulse. This sequence is now suitable for cases where long CP times are needed and fast relaxation processes are to be monitored, calling for very short mixing times.

In order to measure the dipolar dephasing as a function of τ_{mix} for a given recoupling time, two experiments are performed. The *dephased* echo (S) is measured by choosing a long mixing time, τ_{mix} , and a final z-filter time, τ_z , which is long enough for the dephasing of unwanted coherences. The *undephased* echo, S_0 , which serves as a reference, can be measured by choosing a very short mixing time, $\tau_{mix,0}$, which should be just one or a few rotation periods. The loss of S-spin magnetization due to relaxation is identical to the first experiment if the overall periods of transverse and of longitudinal relaxation are the same in both experiments. Therefore, the final z-filter time in the reference experiment, $\tau_{z,0}$, is set such that $\tau_{mix,0} + \tau_{z,0} = \tau_{mix} + \tau_z$. The reference S_0 is thus used to correct for S-spin T_1 and T_2 relaxation and is the equivalent of the reference spectrum in a REDOR experiment, where the dephasing π -pulse on the L-spin is skipped to measure the undephased spectrum. The normalized dephasing, calculated as $\frac{\Delta S}{S_0} = 1 - \frac{S}{S_0}$, is then *only* dependent on the total recoupling time $N \cdot \tau_R$, the dipolar coupling to the L-nuclei, and the relaxation times of the L-nuclei. In cases where the heteronuclei in question are not 100% abundant, the intensity, S_0 , has to be corrected accordingly.

6.3 Theoretical Description

The spin dynamics for the RIDER experiment will be described for SL_n -spin systems, with $S = \frac{1}{2}$, with $L = \frac{1}{2}$ or $L = 1$, and with T_1 relaxation of the L-spins in the mixing time. Analytical solutions are presented for the most important cases including isolated SL -spin pairs and

¹Fig. 6.2 shows only the essential parts of the full pulse sequence, to be put into the context of a CP-experiment, as shown in Fig. 2.1.

rapidly rotating SL_3 -moieties, as encountered in CD_3 -groups. Throughout this section, we will assume the heteronuclear dipolar interaction to be the dominant interaction for the spectra. The average dipolar REDOR Hamiltonian (Eq. (2.5)), with the definition of the acquired dipolar phase (Eq. (2.6)), can be used for the recoupling periods of the RIDER experiment. In reference to the underlying concept of REDOR, the number of recoupling rotor periods, N , is given as the sum of the first and second recoupling periods, each with $N/2$ rotor cycles (see Fig. 6.2).

As discussed above, due to the acquisition of the full stimulated echo any chemical shift evolution is compensated for by the pulse sequence, and chemical shifts will not be considered.

6.3.1 Coupling to $L = \frac{1}{2}$

To highlight the principles of the method, we shall first consider the simple case of an SL -pair with each of the nuclei being spin- $\frac{1}{2}$. The density matrix after the first recoupling period acting on transverse x-magnetization before the flip-back pulse reads

$$\hat{\rho}(\frac{1}{2}N\tau_R) = \hat{S}_x \cos(\frac{1}{2}N\bar{\Phi}) + 2\hat{S}_y\hat{L}_z \sin(\frac{1}{2}N\bar{\Phi}). \quad (6.4)$$

The transverse S-magnetization and the antiphase coherence are stored along z in alternate scans. Thus, during τ_{mix} only the effect of L-spin T_1 relaxation has to be taken into account, and explicit calculation of the storage pulses is not necessary. S-spin T_1^S or T_2^S relaxation need not be considered since the quantity $\frac{\Delta S}{S_0}$ will not depend on these.

The operator \hat{L}_z represents a non-equilibrium state and is thus subject to randomization by longitudinal relaxation according to $\hat{L}_z \rightarrow \hat{L}_z \exp\{-\tau_{mix}/T_1\} \xrightarrow{\tau_{mix} \rightarrow \infty} 0$. Throughout this chapter, we will neglect any anisotropy of the T_1 relaxation since the emphasis of this work is on the determination of dipolar coupling constants and internuclear distances. Nevertheless, in applications of RIDER to the study of relaxation processes of the heteronucleus, a better understanding of the influence of the T_1 anisotropy would be desirable. Apart from implications for the powder averaging, it may lead to the observation of non-exponential relaxation behaviour [Spiess 78, Torchia 82].

The treatment presented here is based on the assumption that the relaxation of the $\hat{S}_z\hat{L}_z$ state (which is present during τ_{mix}) can be treated as a product of independently relaxing, pure \hat{S}_z and \hat{L}_z states. This is true if the SL-dipolar coupling itself does not contribute to the relaxation to a large extent (due to its small size of 1 kHz and less, this can safely be assumed for the systems studied in this chapter). Moreover, in the description of dipolar-mediated cross-relaxation [Abragam 61] (i.e. NOE), the cross-relaxation rate of one spin is proportional to the expectation value of the z-magnetization of the other spin. In the RIDER experiment, the phase cycle is designed in such a way that both the cosine and sine components of S-magnetization are stored along z and -z in different scans during τ_{mix} . This should largely cancel contributions from SL-cross relaxation to the polarization of the L-spins.

The density matrix after the second recoupling period (where the sign of the dipolar Hamiltonian is effectively inverted) is thus given by

$$\begin{aligned} \hat{\rho}(N\tau_R) = & \hat{S}_x \cos^2(\tfrac{1}{2}N\bar{\Phi}) + 2\hat{S}_y\hat{L}_z \cos(\tfrac{1}{2}N\bar{\Phi}) \sin(\tfrac{1}{2}N\bar{\Phi}) \\ & + e^{-\tau_{mix}/T_1} (2\hat{S}_y\hat{L}_z \sin(\tfrac{1}{2}N\bar{\Phi}) \cos(\tfrac{1}{2}N\bar{\Phi}) + \hat{S}_x \sin^2(\tfrac{1}{2}N\bar{\Phi})) \end{aligned} \quad (6.5)$$

After the final z-filter, only the \hat{S}_x (i.e. in-phase) components of the transverse magnetization will be detected. Therefore, for vanishing mixing time the full initial S-spin signal is measured ($\cos^2 a + \sin^2 a = 1$). The powder-averaged normalized dipolar-dephased signal reads

$$\begin{aligned} \frac{\Delta S^{(L=\frac{1}{2})}}{S_0}(\tau_{mix}, N) &= 1 - \left\langle \cos^2(\tfrac{1}{2}N\bar{\Phi}) + e^{-\tau_{mix}/T_1} \sin^2(\tfrac{1}{2}N\bar{\Phi}) \right\rangle \\ &= 1 - \frac{1}{2} \left\langle \cos(N\bar{\Phi}) + 1 + e^{-\tau_{mix}/T_1} (1 - \cos(N\bar{\Phi})) \right\rangle \\ &\xrightarrow{\tau_{mix} \rightarrow \infty} \frac{1}{2} - \frac{1}{2} \langle \cos(N\bar{\Phi}) \rangle \xrightarrow{N \rightarrow \infty} \frac{1}{2}. \end{aligned} \quad (6.6)$$

For long mixing times, the \sin^2 -component will not contribute to the stimulated echo, and the result (last line) then represents a dephasing curve identical to the one measured in a REDOR experiment, but with the difference that the relative dephasing $\frac{\Delta S}{S_0}$ will not reach a final value of one, but will be scaled down to $\frac{1}{2}$.

6.3.2 Coupling to $L = 1$

The description of an $S = \frac{1}{2}$ coupled to an $L = 1$ nucleus has already been outlined in Section 5.2.1. Using the initial density matrix given by Eq. (5.2), we obtain for the evolution under the first recoupling period:

$$\hat{\rho}(\frac{1}{2}N\tau_R) = \hat{S}_x(\mathbb{1}_L - \hat{L}_z^2) + \hat{S}_x\hat{L}_z^2 \cos(N\bar{\Phi}) + \hat{S}_y\hat{L}_z \sin(N\bar{\Phi}) \quad (6.7)$$

Again, the storage pulses for the S-spins before and after the mixing time do not need to be considered explicitly. It seems tempting to conclude that for $L = 1$, with $\frac{1}{3}$ of the signal being invariantly coupled to $|0\rangle_L$ (first term in Eq. (6.7)), and $\frac{2}{3}$ of the magnetization being dephased according to the last two terms Eq. (6.7) (in analogy to the $L = \frac{1}{2}$ case, Eq. (6.6)), that the overall intensity of $\frac{\Delta S}{S_0}$ reaches only $1 - (\frac{1}{3} \cdot 1 + \frac{2}{3} \cdot \frac{1}{2}) = 33\%$. This is, however, not true since the randomization of the \hat{L}_z components during τ_{mix} also affects the $\hat{S}_x(\mathbb{1}_L - \hat{L}_z^2)$ component, which is invariant under dipolar coupling. In Appendix B, the relaxation behavior of the \hat{L}_z and \hat{L}_z^2 spin states is derived:

$$\hat{L}_z \longrightarrow \hat{L}_z e^{-\tau_{mix}/T_1^{app}} \xrightarrow{\tau_{mix} \rightarrow \infty} 0 \quad (6.8)$$

$$\hat{L}_z^2 \longrightarrow \frac{2}{3}\mathbb{1}_L - \left(\frac{2}{3}\mathbb{1}_L - \hat{L}_z^2\right) e^{-3\tau_{mix}/T_1^{SQ}} \xrightarrow{\tau_{mix} \rightarrow \infty} \frac{2}{3}\mathbb{1}_L \quad (6.9)$$

From this, it is possible to derive a correct qualitative description of the dephasing process for long recoupling and mixing times. It is clear that, after substituting Eqs. (6.8) and (6.9) into Eq. (6.7), one has to regroup some of the product operators before calculating the effect of the second recoupling period in analogy to Eq. (6.5). The \hat{S}_x component associated with $|0\rangle_L$, $\hat{S}_x(\mathbb{1}_L - \hat{L}_z^2)$, will thus relax to $\hat{S}_x\frac{1}{3}\mathbb{1}_L$ for long mixing times. This coherence splits into yet another triplet (randomization upon relaxation during the mixing time), of which only $\frac{1}{3}$ remains invariant during the second recoupling period, while the rest acquires a cosine modulation with an average of zero. Thus the invariant component contributes $\frac{1}{9} \cdot 1$ to the signal in the long-time limit. Of the $\frac{2}{3}$ of the components originally associated with $|+1\rangle_L$ and $|-1\rangle_L$, a further $\frac{2}{3}$ will acquire an overall phase factor $\cos^2(N\bar{\Phi})$, resulting in a signal contribution of $\frac{2}{3} \cdot \frac{2}{3} \cdot \frac{1}{2}$ in the long-time limit. The plateau value of $\Delta S/S_0$ for infinite τ_{mix} and infinite N is thus $1 - S_\infty/S_0 = 1 - (\frac{1}{3} \cdot \frac{1}{3} \cdot 1 + \frac{2}{3} \cdot \frac{2}{3} \cdot \frac{1}{2}) = 66\%$.

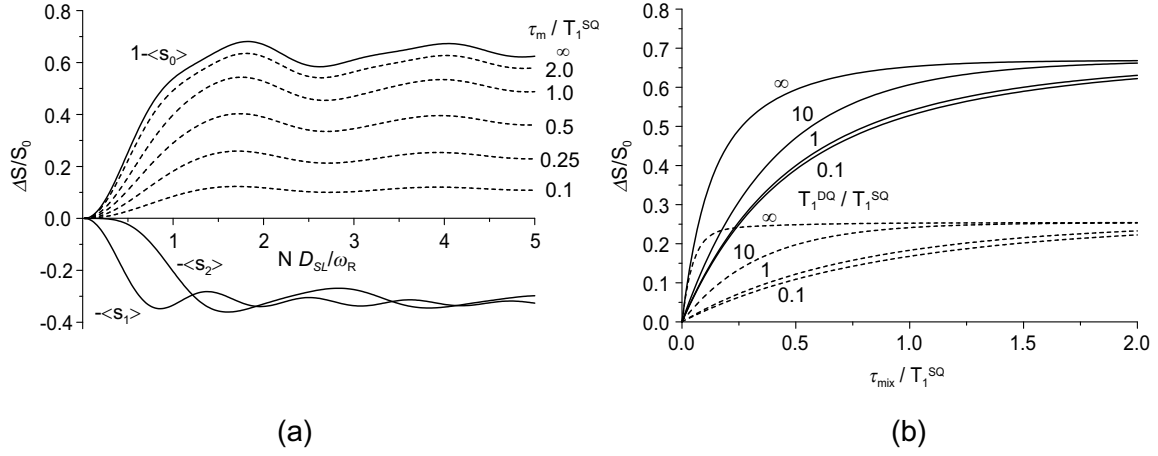


Figure 6.3: Theoretical RIDER build-up (a) and relaxation (b) curves for spin $L = 1$, as calculated from Eq. (6.10). The solid lines represent the powder-averaged coefficients $(1 - \langle s_0 \rangle)$, $-\langle s_1 \rangle$ and $-\langle s_2 \rangle$, whereas the dashed lines are linear combinations of these with respect to the indicated ratios τ_{mix}/T_1^{SQ} and $T_1^{DQ} \rightarrow \infty$. The curves in (b) are calculated for $ND_{SL}/\omega_R = 0.5$ (dashed lines) and $ND_{SL}/\omega_R = 2.0$ (solid lines) and ratios of T_1^{DQ}/T_1^{SQ} as indicated.

Following the procedure outlined in the preceding section, the full time dependence of the measured signal can be derived for all τ_{mix} and N . The powder-averaged τ_{mix} - and N -dependent dephasing for an S-spin coupled to one $L = 1$ spin is calculated to be

$$\frac{\Delta S^{(L=1)}}{S_0}(\tau_{mix}, N) = 1 - \left\langle s_0(N) + s_1(N)e^{-\tau_{mix}/T_1^{app}} + s_2(N)e^{-3\tau_{mix}/T_1^{SQ}} \right\rangle, \quad (6.10)$$

$$\text{where } s_0(N) = \frac{1}{9} (3 + 4 \cos(N\bar{\Phi}) + 2 \cos(2N\bar{\Phi})),$$

$$s_1(N) = \frac{1}{9} (3 - 3 \cos(2N\bar{\Phi})),$$

$$s_2(N) = \frac{1}{9} (3 - 4 \cos(N\bar{\Phi}) + \cos(2N\bar{\Phi})),$$

$$\text{and } T_1^{app} = T_1^{SQ} T_1^{DQ} / (T_1^{DQ} + 2T_1^{SQ}). \quad (6.11)$$

As required, for $\tau_{mix} = 0$ the three coefficients $s_i(N)$ add up to unity to give the full stimulated echo. For longer mixing times, dephasing curves are obtained, the plateau value of which for long recoupling times ($N \rightarrow \infty$) depend on the single- and double-quantum relaxation times of the L-nucleus.

In Fig. 6.3a, some build-up curves are depicted for different values of τ_{mix}/T_1 (for the case of $T_1^{DQ} \rightarrow \infty$). In the limit of $\tau_{mix} \rightarrow \infty$, the dephasing curve is $\langle 1 - s_0(N) \rangle$, with a plateau

value of $1 - \frac{3}{9} = 66\%$. It should be noted that the position of the first maximum of the build-up curves does not change considerably as a function of the two T_1 relaxation times if the mixing time is sufficiently long (at least $2 T_1^{SQ}$); thus the dipolar coupling constant can be determined quite accurately without exact knowledge of the ratio of T_1^{SQ} and T_1^{DQ} .

To further probe the effects of T_1^{SQ} and T_1^{DQ} on the dephasing curve, the relative dephasing for various ratios T_1^{DQ}/T_1^{SQ} is explored as a function of the mixing time in Fig. 6.3b. The relaxation-time dependences are weighted by the coefficients s_1 and s_2 , the ratio of which is different for the two recoupling times indicated (see Fig. 6.3a). Since the double-quantum relaxation time appears only in the exponential prefactor of the s_1 term, it is possible to extract both relaxation times from measurements of relaxation curves at suitably chosen recoupling times.

The structure of Eq. (6.10) suggests an efficient way for numerically fitting the experimental data. The dependence on the recoupling time, and thus on the dipolar coupling constant, resides in the three coefficients $s_i(N)$. Since all three scale with the ratio of ND_{SL}/ω_R (Eq. 2.6), powder-averaged master curves can be calculated for each coefficient as a function of this parameter. Derivatives of these master curves with respect to the dipolar coupling can be obtained by interpolation between discrete values of $s_i(ND_{SL}/\omega_R)$, and the derivatives with respect to the relaxation times can be calculated analytically. These derivatives are needed for gradient-based χ^2 -minimization algorithms such as the Levenberg-Marquart method, which was used here. Such a non-linear least-squares fitting procedure will yield the relaxation times and a stretching factor for the ratio ND_{SL}/ω_R , from which the dipolar coupling can be obtained.

6.3.3 Couplings to Multiple L-spins

Couplings of one S-spin to multiple L-spins for the REDOR experiment can straightforwardly be accounted for by writing the dephased signal as the *product* of individual pair contributions [Goetz 97]. The underlying principles have been explained in detail in Section 3.3, and hold equally well for the RIDER experiment. Homonuclear couplings among the L-spins are assumed not to contribute as a first approximation. In weakly coupled spin systems, this interaction should largely be averaged out by MAS. For RIDER, homonuclear coupling among the S-spins is also of no importance since the exclusion of spin diffusion restricts the application

of the method to the case of high isotopic dilution of the S-spins. The dephased signal is therefore calculated as

$$\frac{\Delta S}{S_0}(\tau_{mix}, N) = 1 - \left\langle \prod_{i=1}^{n_L} f_i \right\rangle, \quad (6.12)$$

where the individual pair contributions f_i are the terms subject to the powder average in Eqs. (6.6) and (6.10). It should be emphasized that the powder average has to be evaluated *after* the multiplication of the individual dephasing factors. Also, the dipolar phases, $\bar{\Phi}_i$, are now dependent on each other via the geometry of the spin system. Consequently, Eq. (2.6) cannot be applied any more since the individual SL-pair vectors cannot all be assumed to coincide with the z-axis of the crystal frame. Rather, another transformation of these individual pair vectors from their dipolar PAS to the crystal frame has to be introduced before powder-averaging the dephasing product over Ω_{CR} . A treatment of $\bar{\Phi}_i$ as a function of individual pair vector orientations has also been given by Goetz and Schaefer [Goetz 97]. If coordinates of the various nuclei rather than Euler angles are known, it is more convenient to calculate the spherical components of the dipolar tensors directly and use Eq. (1.71).

When couplings to a methyl- (or CD₃-) group are to be considered, Eq. (6.12) can be simplified even further. This has also been laid out in detail in Section 3.3. The identical trajectories of the three heteronuclear coupling tensors leads to

$$\frac{\Delta S^{Me}}{S_0}(\tau_{mix}, N) = 1 - \langle f_{Me}^3 \rangle. \quad (6.13)$$

When the S-spin is located on the methyl rotation axis, the dipolar phases acquired under the recoupling, $\bar{\Phi}$, depend on an apparent dipolar coupling constant, D_{SL}^{app} , as given by Eq. (3.15). In the off-axis case, the components of a now asymmetric dipolar tensor, \mathbf{A}_2^{Dis} , have to be used for the calculation of $\bar{\Phi}$, as explained on p. 85.

For the case of $\tau_{mix} \rightarrow \infty$, the N -dependent dephasing for the CD₃-group is calculated from Eqs. (6.10) and (6.13) to be

$$\begin{aligned} \frac{\Delta S^{CD_3}}{S_0}(N) &= 1 - \langle s_0^3(N) \rangle \\ &= \frac{1}{9^3} \left\langle 588 - 252 \cos(N\bar{\Phi}) - 180 \cos(2N\bar{\Phi}) - 100 \cos(3N\bar{\Phi}) \right. \\ &\quad \left. - 42 \cos(4N\bar{\Phi}) - 12 \cos(5N\bar{\Phi}) - 2 \cos(6N\bar{\Phi}) \right\rangle \end{aligned} \quad (6.14)$$

The dephased signal thus reaches a plateau of $\frac{588}{729} = 80.66\%$.

6.4 Experimental Demonstration

6.4.1 ^{13}C - ^{14}N Distances in L-Alanine

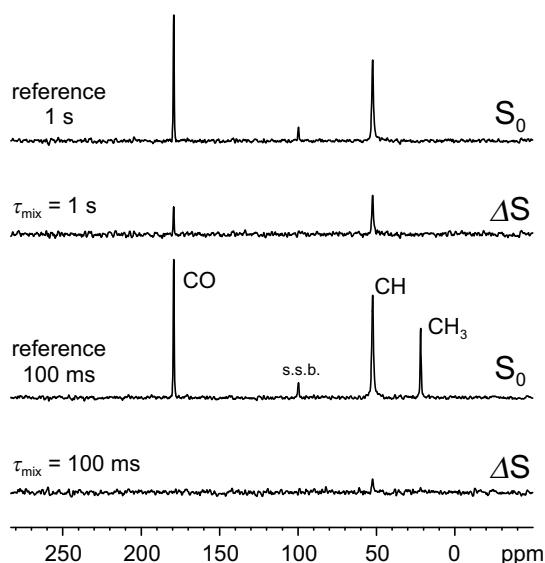


Figure 6.4: RIDER reference (S_0) and difference (ΔS) spectra of L-alanine for a total recoupling time of $26 \tau_R = 4.33$ ms, using two different mixing times. Spinning sidebands of the CO carbon are denoted by *s.s.b.*

In Fig. 6.4, RIDER difference spectra (ΔS) for a rather long recoupling time and two different mixing times, along with the corresponding reference spectra, are displayed for L-alanine. At short mixing times, the exchange due to ^{14}N relaxation is minor. Therefore, only the CH peak is visible, whereas at longer mixing times the carbonyl signal becomes observable as well. Moreover, the intensity of the CH signal (to be interpreted relative to the corresponding reference intensity, S_0) increases considerably. A basic limitation of the technique becomes obvious by comparing the two reference spectra. At mixing times as short as 1 s, the signal from the methyl carbon is already completely relaxed, which means that the distance information for this site cannot be determined with this method.

To obtain distance information between two types of nuclei, the relaxation time of the detected nucleus should be at least equal to the relaxation time of the passive spin.

The dipolar coupling constants can be determined most accurately by measuring the normalized dephasing, $\Delta S/S_0$, as a function of recoupling time and fitting the data according to Eq. (6.10), following the procedure outlined in the theory section. The build-up data for two different mixing times are presented in Fig. 6.5a. The data points were fit to Eq. (6.10), assuming that the contribution from ^{14}N DQ relaxation is insignificant (i.e. $T_1^{app} = T_1^{SQ}$),

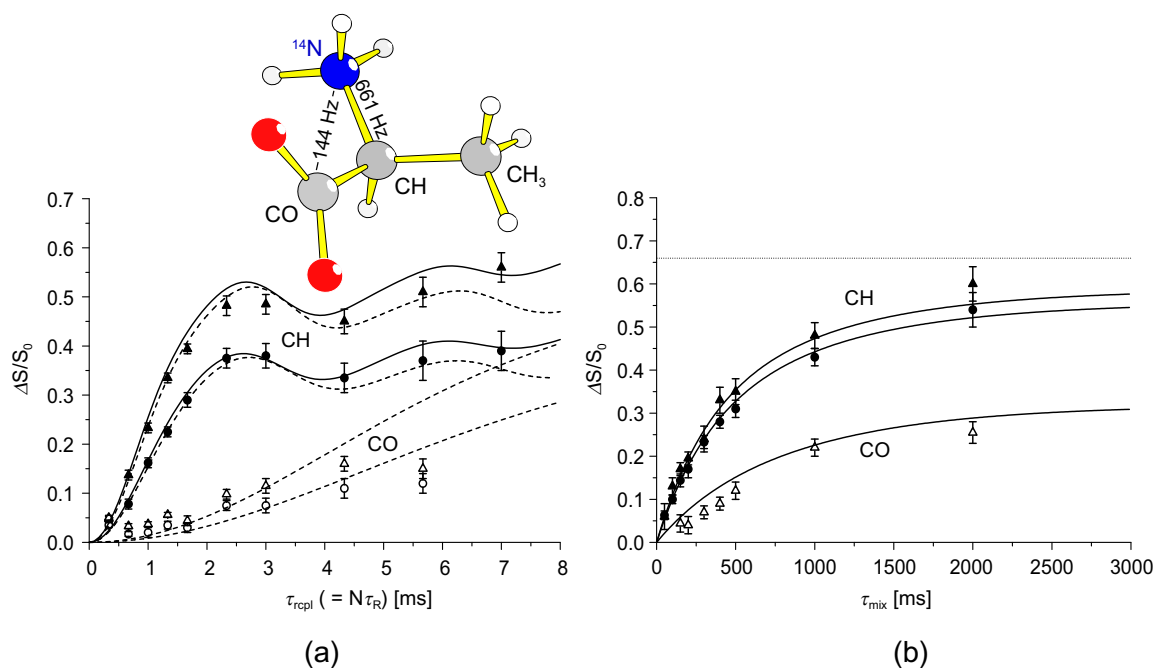


Figure 6.5: RIDER build-up (a) and relaxation (b) curves of L-alanine. Solid symbols denote data for the CH resonance, open symbols are from the CO signal. In (a), mixing times were 800 ms (triangles) and 400 ms (circles). The dashed lines are the best-fit spin pair curves using Eq. (6.10), solid lines represent simulations based on Eq. (6.12), considering the CH-N-pair and the 12 closest N atoms from neighboring molecules. The relaxation times for these simulations were taken from the data displayed in (b), acquired using recoupling times of $10 \tau_R = 1.67$ ms (triangles) and $26 \tau_R = 4.33$ ms (circles). The averaged best-fit curves (solid lines) using Eq. (6.10) with fixed coefficients $\langle s_i \rangle$ were calculated for $T_1^{SQ} = 0.903 \pm 0.033$ s and $T_1^{DQ} = \infty$.

which has previously been shown to be a valid assumption for L-alanine [Naito 84]. For the CH carbon, the agreement between the experimental data and the fit (dashed lines) is good. The dipolar coupling constant is determined to be 630 ± 40 Hz, which corresponds to a CH-N distance of 1.51 ± 0.03 Å.² This agrees well with previous NMR measurements [Sachleben 96]. The value should be compared with $r_{CN} = 1.489$ Å obtained from neutron and low-temperature X-ray diffraction data [Lehmann 72, Destro 88]. Small discrepancies between distances measured by NMR and scattering methods are commonly encountered and can be explained by different averaging of fast vibrational and librational motions [Henry 85].

²The given errors are based on a χ^2 -analysis which assumed also ratios of T_1^{DQ}/T_1^{SQ} different from ∞ .

Deviations from the theoretical behavior are observed for longer recoupling times. This can straightforwardly be explained by the fact that we did not dilute the spin pair in question. As a result, for large τ_{rcpl} couplings to remote spins contribute to the signal appreciably. The last one or two datapoints of each series were actually excluded from the fit in order to achieve a good agreement with the spin pair approximation. It is common practice in experiments like REDOR to analyze only the initial build-up behavior, which is largely independent of the remote couplings. If an estimate of the influence of remote couplings is not available, an isotopic dilution is necessary.

In the graph we also included simulated dephasing curves (solid lines) based on the crystal structure of L-alanine [Lehmann 72, Destro 88] (see Appendix D.1), which, apart from the primary CH-N-pair also take into account the 12 closest ^{14}N -spins from neighboring molecules. The reason for the shift of the maxima of these curves relative to the fits, and thus the difference in experimentally determined and expected dipolar couplings, has already been explained above. Apart from that, these simulations can indeed account for the higher dephasing measured at longer recoupling times. The plateau values given in the theory section are strictly valid only for the cases of completely isolated spin pairs or SL_3 -groups. In a real system, the normalized dephasing will always reach a value of 1 (complete dephasing) in the limit of infinite recoupling time. From the simulations, it is, however, obvious that satisfactory results *can* be obtained in systems without isotopic dilution, if one restricts the analysis to reasonably short recoupling times. As is obvious, the simulated curve and the fit assuming an isolated spin pair agree well even beyond the first maximum of the build-up curve.

As already mentioned, the signal from the methyl group could not be evaluated. Also, the agreement between the data for the carbonyl carbon and the theoretical curves is somewhat poor. We believe that this problem arises primarily because for the calculation of $\Delta S/S_0$, due to signal-to-noise considerations, only centerband intensities were used, whereas at a spinning speed of 6 kHz, owing to the rather large CSA of a carbonyl group, weak spinning sidebands were still visible. The intensity distribution between the centerband and first-order sidebands was different between the dephased and the reference spectra in some cases, which was possibly due to timing imperfections of the rotor trigger. In the light of this kind of problem, it is advisable to work at spinning frequencies which are large enough to completely average out the CSA, i.e., in a regime where no spinning sidebands appear. Alternatively, TOSS (*total suppression of spinning-sidebands*) detection can be implemented in CODEX/RIDER exper-

Table 6.1: Experimentally observed and expected dipolar couplings and bond lengths for L-alanine.

	NMR		from crystal structure ^a	
	$D_{CN}/2\pi$ [Hz]	r_{CN} [Å]	$D_{CN}/2\pi$ [Hz] ^b	r_{CN} [Å]
CH	630±40	1.51±0.03	661	1.489
CO	130±20	2.56±0.13	144	2.473

^a as determined by neutron scattering [Lehmann 72]

^b calculated from Eq. (1.51)

iments [deAzevedo 00]. Nevertheless, as shown in Table 6.1, the distance derived from the fit again agrees with the expected value.

The height of the first maxima and the plateau values of the best-fit curves in Fig. 6.5a depend on the two relaxation times T_1^{SQ} and T_1^{DQ} . Since a fit of build-up curves alone does not yield reliable results for these two times (as shown, the expected plateau is often increased due to the influence of remote spins), it is advisable to record relative dephasings for various recoupling times as a function of the mixing time and fit these to Eq. (6.10), but with fixed coefficients $\langle s_i \rangle$. The $\langle s_i \rangle$ can be calculated for any recoupling time once the dipolar coupling constant is known. It is of advantage to measure these relaxation curves at moderate recoupling times, in order to keep the perturbing influence of remote spins small. The experimental data along with the fits are displayed in Fig. 6.5b, where it is shown that a single-quantum relaxation time $T_1^{app} = T_1^{SQ} = 0.903 \pm 0.033$ s with $T_1^{DQ} = \infty$ agrees with the measurements. It was not possible to reliably fit the data with the two relaxation times as independent parameters; it can merely be stated that a χ^2 -analysis of the data indicated that T_1^{DQ} is at least five times larger than T_1^{SQ} . These results are in good agreement with the work of Naito et al. [Naito 84], where single-crystal static ¹³C 2D exchange measurements were analyzed. The value due to Frydman et al. of $T_1^{SQ} = 0.090 \pm 0.06$ s [Sachleben 96], as determined using the DEAR experiment, does, however, differ significantly.

In the analysis outlined above, an interdependence of the fits of the build-up and the relaxation data becomes apparent, which arises because in the fits of the build-up curves for the determination of the dipolar coupling, the dependence on the relaxation times could not be neglected, since the mixing times were only on the order of T_1^{SQ} . Thus, a χ^2 -analysis

was required to ensure the reliability of the results for the dipolar coupling and the relaxation times. It shall again be mentioned that the determination of the dipolar coupling constants is most accurate for long mixing times, i.e. $\tau_{mix} > 2 T_1^{SQ}$. Then, the dependence of the result on the relaxation times is negligible. If the sample is not isotopically diluted, the influence of remote spins can be minimized by restricting the analysis to the initial rise of the build-up data and the measurement of relaxation curves to moderate recoupling times.

6.4.2 ^{13}C - ^2H Distances in CD_3 -Methylmalonic Acid

Relatively well-isolated deuterated methyl groups represent a good system for testing the dephasing behavior in the RIDER experiment for the case of couplings to multiple spins. The data for the chosen model compound (which is, in a sense, the complementary compound to the partially deuterated methylmalonic acid used in Chapters 3 and 4), along with best-fit and simulated curves, are displayed in Fig. 6.6. A comparison between measured and expected values for the coupling constants is presented in Table 6.2. When simulating dephasing curves based on crystal structure data, the rapid 3-site jumps of methyl deuterons were generally accounted for by arithmetically averaging the 5 spherical components $A_{2,m}^C$ of the 3 different dipolar coupling tensors and assigning the average tensor to each of the CD dipolar pairs. Also, all dipolar coupling constants and recoupling times were scaled by factors of 0.25 and 4, respectively, in order to obtain more points for the curves.

For the measurements presented here, arcing in the probe limited the B_1 field strengths to about 55 kHz, corresponding to 4.5 μs pulses. For the same reason, the acquisition time was limited to about 10 ms, making quite large line broadening necessary. This explains the relatively poor signal to noise ratio and resulting large error bars in Fig. 6.6.

The fits (dashed lines) in Fig. 6.6a are based on Eq. (6.14), i.e. on the assumption of complete relaxation of the deuterons. Apart from deviations at long mixing times, the agreement with the experiment is good. In particular, the predicted plateau value of about 81% is confirmed. For a quantitative comparison with a simulation based on the crystal structure, neutron scattering results would be desirable, since they locate the protons reliably. Unfortunately, we had only data from X-ray scattering with which to compare the NMR results [Derissen 70]. The shortcomings of X-ray scattering for the exact localization of protons become obvious

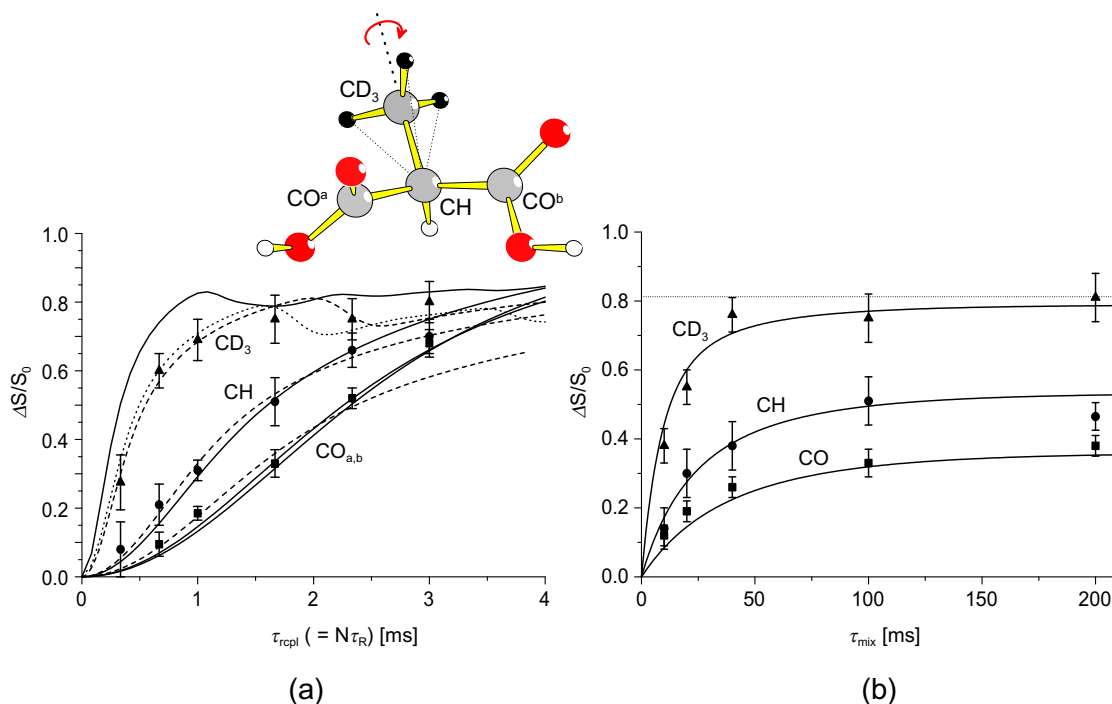


Figure 6.6: RIDER build-up (a) and relaxation (b) curves of CD_3 -methylmalonic acid. Triangles, circles, and squares represent the experimental results for the CD_3 , the CH, and the CO resonances, respectively. In (a), the mixing time used was 100 ms. The best-fit curves, based on Eq. (6.14) in the limit of long mixing times, are indicated by dashed lines. The solid lines are simulations based on the average dipolar coupling tensors of the 9 closest deuteron triplets and include a finite mixing time and the relaxation time determined by fitting the data in (b). The dotted line is a 4-spin simulation based on an idealized tetrahedral CD_3 -group, also based on the experimentally determined relaxation time, $T_1^{\text{app}} = T_1^{\text{SQ}}$. In (b), the recoupling time was $10 \tau_R = 1.67$ ms. The fits were performed using Eq. (6.13) under the assumption of negligible DQ relaxation. The result of the fits (solid lines) are plotted for the average $T_1^{\text{app}} = T_1^{\text{SQ}} = 56 \pm 14$ ms.

by comparing the experimental NMR data with the simulated dephasing curve for the CD_3 -signal (upper solid line). The curve rises considerably faster and reaches a first maximum which is higher than theoretically expected. As can be seen in Table 6.2, the average dipolar coupling tensor for the three deuteron sites in the X-ray structure has an asymmetry parameter of $\eta = 0.59$ and a rather large positive apparent dipolar coupling constant (from Eq. (3.15), with θ being close to the tetrahedral angle, a negative sign would be expected). This means that the three sites are not equivalent in the X-ray structure and the local C_3 -symmetry is apparently broken. One of the three distances is stated to be even shorter than 1 Å (see Table

Table 6.2: Experimentally observed and expected apparent dipolar couplings and bond lengths for CD₃-methylmalonic acid. Coupling constants are given in Hz.

	NMR		from crystal structure			idealized CD ₃ -group		
	$ D_{CD}^{app} /2\pi$	r_{CD} [Å]	$D_{CD}^{app}/2\pi^a$	η^c	r_{CD} [Å]	$D_{CD}^{app}/2\pi^c$	η^c	r_{CD} [Å]
CD ₃	966±198	1.17±0.08 ^b	1625	0.59	1.12	-1193	0.0	1.09
					0.93			
CH	348±38	2.06±0.08 ^c	-323	0.15	1.16	-302	0.0	2.165
					2.043			
CO	224±22	—	-162/-158 ^d	0.17/0.11	2.12	-156/-148	0.05/0.09	2.75/2.75
					3.2/2.8			2.7/2.7
					2.7/3.5			2.59/3.49

^a calculated from the average dipolar tensor of the 3 proton positions

^b calculated from Eqs. (1.51) and (3.15), assuming $\theta = 109.5^\circ$

^c calculated from Eqs. (1.51) and (3.15), assuming $\theta = 28.4^\circ$

^d two inequivalent positions in the crystal

6.2). Neutron scattering has shown that methyl groups in L-alanine and many other molecules possess a nearly tetrahedral symmetry, with a CH-distance of 1.09 Å [Terao 86]. Thus, dipolar coupling tensors calculated from such an arrangement of deuterons, with the carbon skeleton still taken from the X-ray data, represent a much better structural model. The dotted line in Fig. 6.6a is calculated from this model, the deviation now being within the expected range for differences between scattering and NMR distances.

The data for the CH and CO groups suggest higher coupling constants than calculated from the idealized spin pair model. This is again due to the influence of the deuteron triplets of neighboring molecules, 8 of which are accounted for in the simulated curves (solid lines) of Fig. 6.6a. For longer distances, the poor localization of the protons by X-ray scattering becomes less significant, and these curves are seen to fit the data very well. The CH–D distance as determined from the fit on the basis of the idealized model (assuming $\theta = 28.4^\circ$) is still within 5% of the expected value. Since the CO carbon is located off-axis from the methyl group, it is not possible to derive a unique distance from the apparent dipolar coupling constant (the motionally averaged dipolar tensor is now asymmetric). Also, the deviation of

the measured coupling constant from each of the two values for the idealized spin pair model (which takes into account the two inequivalent CO sites in the crystal) is quite large in that case, again as a consequence of couplings to neighboring molecules.

The mixing time dependent data in Fig. 6.6b have again been fitted under the assumption of negligible DQ relaxation. In this case, this was merely due to the signal-to-noise ratio, which did not permit a reliable fit of both times. Deviations are observed, and T_1^{DQ} might thus be important, but more accurate data would be needed for a closer investigation. The $T_1^{SQ} = 56 \pm 14$ ms was obtained by fitting the data according to Eqs. (6.10) and (6.13), i.e. considering the powder average of all mixed products $\langle s_i s_j s_k \rangle$ with the appropriate exponential factors. In all but one of these contributions, τ_{mix}/T_1^{SQ} occurs with a prefactor > 1 , which actually explains the good agreement of the build-up data (acquired with $\tau_{mix} \approx 2 T_1$) with the theoretical curves for the limit of long relaxation times. Deviations between the master curves for the two cases of $\tau_{mix} = 2 T_1$ and $\tau_{mix} = \infty$ are within 2%.

6.5 Concluding Discussion

The RIDER experiment represents a promising new tool for quantitative distance measurements between unlike spins in solids, where one of the two spins is not irradiated at all. Thus, for distance measurements between ^{13}C or ^{29}Si and other heteronuclei, only double-resonance equipment is needed. The unspecific nature of the experiment might at first seem to be a serious limitation; nevertheless, a wide applicability is expected, since, firstly, it is usually possible to chemically control the isotope composition of the investigated compound, and, secondly, the T_1 relaxation times of various NMR-active nuclei differ by orders of magnitude, e.g. in ^{29}Si containing systems, the ^{29}Si T_1 is usually so long that ^{29}Si is well-suited as the S-spin, but dipolar couplings to ^{29}Si as the L-spin cannot be detected within experimentally feasible mixing times.

Compared to REDOR or REAPDOR, the intrinsic loss of 50% of the signal due to the alternating acquisition of the x- and y-components in subsequent scans represents a serious drawback, which is, however, at least partially compensated by the considerably higher sensitivity of the double-resonance probe heads used for RIDER compared to the triple-resonance probes needed to conduct the corresponding REDOR or REAPDOR measurements.

Moreover, the theoretical framework used to describe and model the measured data is quite straightforward, and no empirical factors have to be included in order to account for instabilities of the spectrometer with respect to the excitation of quadrupolar nuclei. Such problems usually arise in REAPDOR experiments, where it is often unavoidable to do a calibration in order to extract the distance information [Gullion 95]. For the case of RIDER, it was shown that the data measured for the two compounds, L-alanine and CD₃-methylmalonic acid, can be described *quantitatively* by using the crystal structure of these compounds and the longitudinal relaxation times determined from the RIDER experiment itself. Even though the measurements presented here were not particularly suited for an in-depth exploration of relaxation processes in quadrupolar nuclei, RIDER shows promise for such applications, since, in particular, higher-quantum relaxation cannot be assessed using classical methods like inversion recovery.

Among the most basic limitations of the technique is that the T_1 relaxation time of the observed nucleus must be *at least* of the same order of magnitude as T_1 of the passive spin. This, however, is the case for almost all ¹³C- and ²⁹Si-containing systems.

Another serious restriction is the requirement that slow dynamics (and spin diffusion) have to be excluded, since the stimulated echo at the end of the second recoupling period is not only reduced by heteronuclear dipolar dephasing, as described here, but also by changes (or differences) in the orientation of the (neighboring) spins [deAzevedo 00]. By conducting experiments at different temperatures or B_0 field strengths, it should be possible to distinguish between dephasing due to reorientations, spin diffusion, and relaxation-induced dipolar exchange: in the slow-motion limit of relaxation, the T_1 relaxation times decrease with increasing temperature, while reorientation speeds up and spin diffusion remains mostly unchanged. The correlation time of reorientations is field-independent, and the time dependence of spin diffusion nearly so, while T_1 relaxation times change significantly with B_0 . Also, the dephasing due to CSA-related mechanisms (reorientations and spin diffusion) scales with B_0 as a function of the recoupling time, whereas for dipolar exchange the build-up curves are independent of B_0 in the limit of complete relaxation of the L-spin.

Chapter 7

Applications

In the previous chapters, experiments demonstrating the capabilities of a number of new heteronuclear recoupling methods were performed using model compounds of known molecular structure. In this chapter, some applications of this methodology on new systems will be presented, where yet uninvestigated structural and dynamical properties were of interest.

The first section is dedicated to structure and dynamics in discotic mesophases. Numerous derivatives of discotic mesogens with large aromatic planes, such as hexabenzocoronene or perylene, have been investigated in our group during the past five years, using a wide range of methodology such as ^2H NMR [Herwig 96], 2D exchange NMR [Kayser 99], and ^1H SQ and DQ MAS NMR. For example, using the BABA sequence in ^1H DQ experiments under ultra-fast MAS, it was possible to unravel details of the packing of the discotic layers of hexaalkyl-substituted hexabenzocoronone based on isotropic chemical shifts of protons in the solid state [Brown 99]. How the techniques discussed in Chapter 3 could extend our experimental capabilities will be illustrated for experiments on even more complex discotic molecules. The greater part of these results has already been published [Fechtenkötter 99].

The second part will show how the ^2H -REDOR and -WISE techniques discussed in Chapter 5 can be put to good use for the investigation of the H-bond structure and dynamics in the crystallites of poly(vinyl alcohol). These results are yet unpublished, and were obtained in collaboration with Prof. Klaus Schmidt-Rohr and Hironori Kaji, Univ. of Massachusetts, Amherst, USA.

7.1 Structure and Dynamics of Discotic Hexabenzocoronene Mesophases

Hexa-peri-hexabenzocoronenes (HBCs) with long chain alkyl substituents, e.g. $C_{12}H_{25}$ (HBC- C_{12}) or $C_{14}H_{29}$ (for structures, see Fig. 7.2), are of considerable interest on account of their unusually large liquid-crystalline (LC) phase widths and favorable physical, electronic, and opto-electronic properties, such as a very high one-dimensional charge carrier mobility [Craats 98, Craats 99]. In addition, HBC- C_{12} has the ability to form adsorbate layers on graphite, which have been investigated by scanning tunneling microscopy (STM) [Stabel 95].

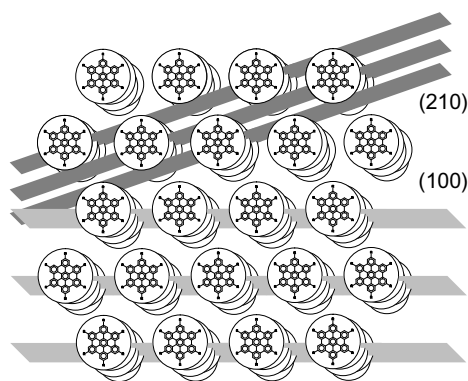


Figure 7.1: Structure of the discotic mesophases of HBC derivatives. Two typical diffraction planes of the hexagonal lattice are indicated.

At elevated temperatures, these substituted HBCs form columnar liquid crystals, in which the aromatic cores undergo rapid axial rotation on the μs timescale [Demus 98]. The rapid rotation of the disc-shaped molecules about the columnar axis has been confirmed by 2H NMR [Herwig 96], and more recently by 1H DQ MAS NMR [Brown 99]. This rotation leads to an averaging of the respective interaction tensors, i.e. the quadrupolar coupling tensor in the case of 2H NMR, and the homonuclear dipolar coupling tensor in the case of 1H DQ spectroscopy. Thus, fast motional processes can be quantified by measuring the reduction of the coupling constants upon transition from the solid phase (in which the cores are rigid) to the LC phase. If the symmetry axes of the tensors (the CH-bond vector and the H-H internuclear vector of the two core-CH protons) lie in a plane perpendicular to the rotational axis, the coupling constants are reduced by a factor of 0.5.¹ The measured reduction factor, $\omega_{LC}/\omega_{solid}$ can be used to calculate the order parameter, S , with $0 \leq S \leq 1$, as $S = 2\omega_{LC}/\omega_{solid}$. Instead, with the two methods, reduction factors of 0.40 and 0.42 have been observed, corresponding to order parameters for the discs of $S = 0.80$ and $S = 0.84$, respectively, indicating additional

¹The formula for the apparent dipolar coupling for a rapidly rotating methyl group, Eq. (3.15), with $\theta = 90^\circ$, applies in this case.

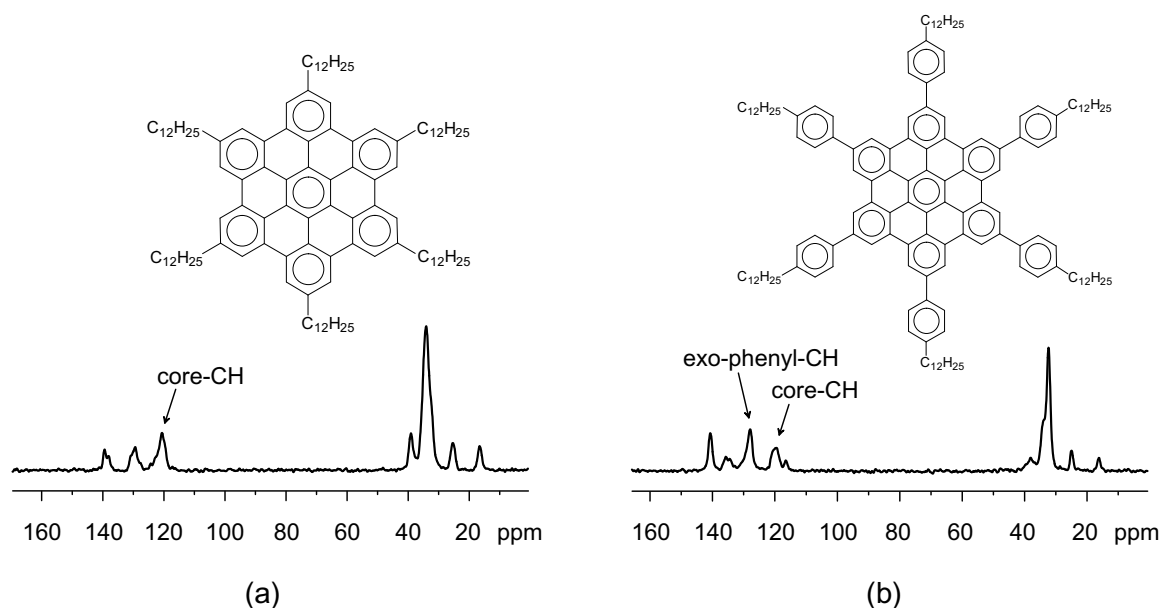


Figure 7.2: CP-MAS spectra ($\omega_R/2\pi = 15$ kHz, taken at room temperature) of HBC- C_{12} (a) and HBC- PhC_{12} (b), with the positions of the aromatic CH signals identified.

out-of-plane or librational motions. These order parameters are considerably lower than for other columnar discotics, e.g. triphenylenes [Vallerien 90, Leisen 92]. Since high mobility and low order limit the charge carrier mobility, a less mobile mesogen would be desirable, which at the same time should improve hexagonal columnar ordering.

A derivative which showed particular promise for an improved ordering is hexa(*para*-*n*-docecylphenyl)-substituted HBC (HBC- PhC_{12}). The 1H DQ MAS approach was, however, unsuitable in the case of HBC- PhC_{12} , since the core-CH and the *exo*-phenyl-CH 1H resonances cannot be differentiated. This limitation is overcome by the REPT-HMQC method, which benefits from the enhanced site-resolution of the detected ^{13}C spins. In Fig. 7.2, a CP MAS spectrum of HBC- PhC_{12} is shown, along with the analogous spectrum of HBC- C_{12} , with which the new compound will be compared. Clearly, the *exo*-phenyl-CH signal of HBC- PhC_{12} can be distinguished from the core-CH signal.

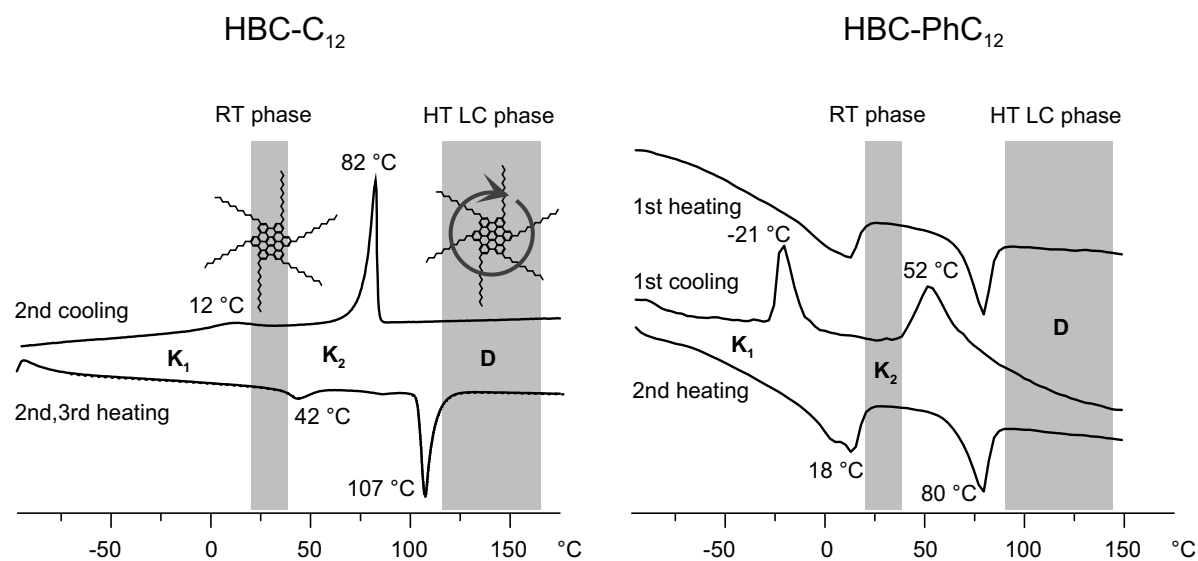


Figure 7.3: DSC traces of the two HBCs. The transition temperatures (peak maxima) are indicated at the corresponding peaks.

7.1.1 DSC and X-Ray Results

Both HBC-PhC₁₂ and HBC-C₁₂ form thermotropic columnar discotic (D) mesophases. The DSC curves (Fig. 7.3) show that the transition to the mesophase occurs at a significantly lower temperature for HBC-PhC₁₂ than for HBC-C₁₂, and in addition, the temperature range over which the phase transition occurs is slightly broader in HBC-PhC₁₂. Apart from the LC phase transition, another transition can be identified for both samples, which occurs at 18 °C and 42 °C for HBC-PhC₁₂ and HBC-C₁₂, respectively. Most notably, this transition is hardly visible for HBC-C₁₂, whereas for HBC-PhC₁₂, the enthalpy change upon this transition is comparable to the value for the LC phase transition. Thus, two low-temperature (LT) phases exist for both samples, henceforth referred to as “solid” phases, K₁ and K₂. Some confusion exists in the literature about the nomenclature of these phases. Sometimes, they are also called “crystalline”, which is not quite appropriate in the light of the fact that considerable sidechain mobility exists in these phases. The X-ray characterization of the structure of the K₁ and K₂ turned out to be problematic, but the results to be presented in Section 7.1.3 indicate that these transitions are coupled with changes in the dynamics of the sidechains of the HBC cores.

The D-phase of both samples could, however, be characterized using Wide-Angle X-

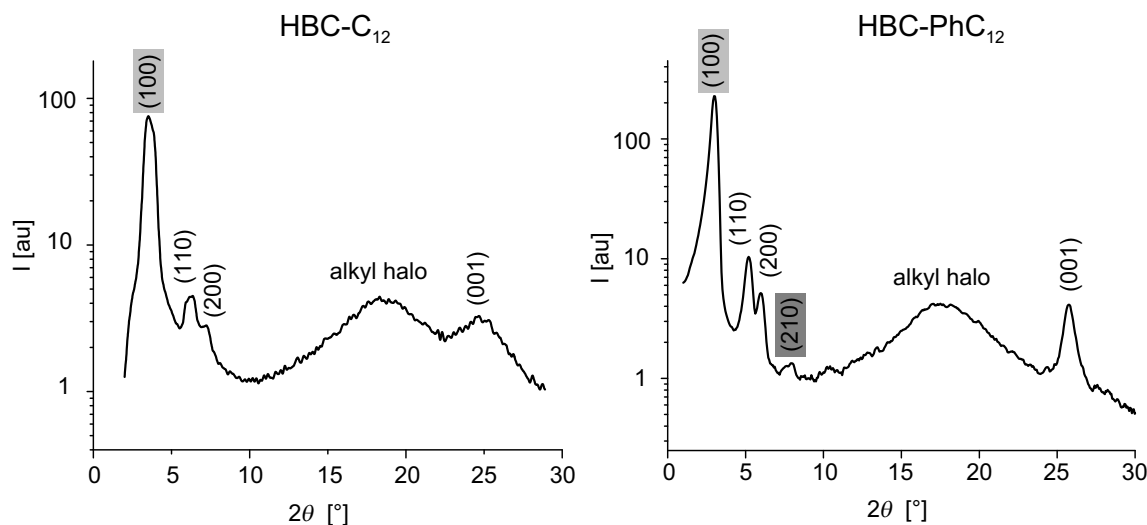


Figure 7.4: X-ray diffraction patterns of the LC mesophases of two HBC-C₁₂ and HBC-PhC₁₂, obtained with CuK_α radiation. The intensities (arbitrary units) are plotted on a logarithmic scale. The shaded areas denote peaks corresponding to the diffraction planes indicated in Fig. 7.1.

Ray Scattering (Fig. 7.4). The WAXS pattern demonstrates that the high temperature LC mesophases exist as ordered columnar hexagonal superstructures (Fig. 7.1). For a perfect hexagonal lattice, reflexions at small angles with relative spacings of $1 : \sqrt{3} : \sqrt{4} : \sqrt{7} : \sqrt{9}$ are expected, where the intensities depend on the perfection of the lattice and the order parameter. As shown in Fig. 7.4, for HBC-C₁₂ only the first three peaks, i.e. (100), (110), and (200), are observed, while for HBC-PhC₁₂ the fourth peak, (210), is apparent above the noise level, indicating improved long-range packing of the columns to form a hexagonal arrangement. In addition, the packing within the columns is improved, as indicated by the sharp (001) reflection at $2\theta \approx 25.6^\circ$. This corresponds to an intermolecular distance of 0.350 nm between the aromatic cores, which should be compared to a spacing of about 0.355 nm in the LC phase of HBC-C₁₂, where the (001) reflection is significantly broader.²

7.1.2 Core Dynamics in the HT Mesophases

Both the heteronuclear dipolar and the quadrupolar coupling tensor of a C-¹H and a C-²H group, respectively, exhibit the same symmetry, such that a determination of the reduction

²The measurements presented in this section were performed by Martha Harbison and Andreas Fechtenkötter, whose help is greatly appreciated.

factor of the CH heteronuclear dipolar coupling constant upon transition into the mesophases should lead to analogous results to those obtained by ^2H NMR, which is a well-established method for the investigation of liquid crystals [Schmidt 98].

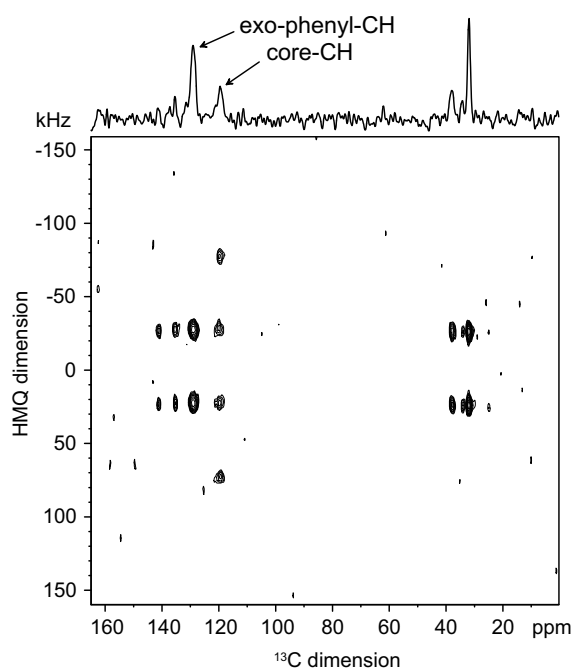


Figure 7.5: Full 2D ^{13}C - ^1H REPT-HMQ sideband spectrum of the HT mesophase of HBC-PhC₁₂, measured at 120°C with $\omega_R/2\pi = 25$ kHz and $\tau_{\text{rcpl}} = 4 \tau_R$.

In Fig. 7.5, a 2D HMQ sideband spectrum of the D-phase of HBC-PhC₁₂ is shown. Third-order spinning sidebands are seen to appear only for the core-CH signal. A sum-projection over the whole signal in the core-CH region of the ^{13}C dimension was used to obtain the spinning sideband patterns displayed in Fig. 7.6, where measurements at two different temperatures and recoupling times are compared. A sum-projection over the third-order sidebands in the HMQ dimension onto the ^{13}C dimension (not shown) is in turn useful to estimate the presence of contributions from quaternary carbons to the rather broad core-CH signal. Here, the ^{13}C lineshape of the third-order sideband projection matched the one from a projection over the first-order sidebands (where contributions from other ^{13}C atoms could be expected to be present), indicating clean sideband patterns.

The investigation of fast molecular dynamics is a potentially promising application of the REPT techniques. It was shown in Chapter Three (p. 68) that the spectrum of a rigid (aromatic) CH-group in a common organic molecule, with $D_{IS}/2\pi = 20.9$ kHz, can be determined to very high precision, using the simple theory for a spin pair for the analysis. Perturbing couplings hardly contribute to the spectra, and since fast molecular motion can be assumed to scale down all the couplings in the system (this might not be generally true, due to the orientational dependence), the spin pair approach should, therefore, be even better justified for a weaker, motionally reduced coupling of a CH-group as compared with a rigid system.

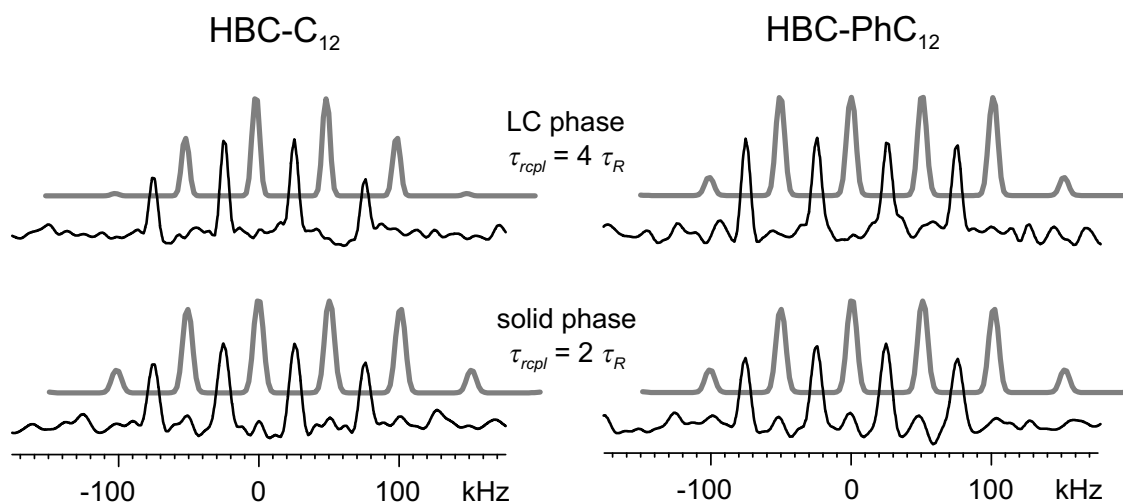


Figure 7.6: REPT-HMQ sideband patterns, obtained as the sum projection over the CH-signals in the 2D spectra (Fig. 7.5). The temperatures were 35°C and 120°C for the RT and HT phases, respectively. The background traces are the best-fit spectra.

The sideband patterns for the RT and HT LC phases of both materials (Fig. 7.6) are similar, but the recoupling times are $2 \tau_R$ and $4 \tau_R$ for the RT and LC phases, respectively. This means that the dipolar couplings are reduced by approximately 50%. A closer inspection reveals that the sideband pattern for the LC phase of HBC-C₁₂ exhibits less intense third-order sidebands, indicating a weaker coupling than in HBC-PhC₁₂. It may further be noted that the MQ measurements were carried out at 120°C, such that the motional processes in both HBC samples are assured to be fast on the NMR timescale, i.e. at least in the μs range. In this respect, from the decrease of ¹H MAS linewidths upon heating, it became clear that for HBC-PhC₁₂, despite its lower calorimetric phase transition temperature of 80°C, the degree of motional averaging still increases up to about 110°C. This may indicate a broad distribution of correlation times or, equivalently, activation barriers, which is characteristic for a cooperative process.

The dipolar coupling constants were evaluated quantitatively by numerically fitting the sideband patterns to the analytical solution for the case of a heteronuclear spin pair; such best-fit spectra are shown as grey background traces in Fig. 7.6. From various independent measurements, including the results obtained on L-tyrosine·HCl (Fig. 3.4), the average dipolar coupling constant for a rigid aromatic CH group — as found in the D-phases of both materials — was determined to be 20.9 ± 0.5 kHz, which corresponds to an internuclear distance of

114±1 pm, while the motionally reduced coupling constants for the LC phases were determined to be 8.2±0.9 kHz and 9.7±0.9 kHz for HBC-C₁₂ and HBC-PhC₁₂, respectively. Thus, one calculates reduction factors of 0.39±0.04 and 0.46±0.04 for the motional processes in the two materials, corresponding to order parameters of 0.78±0.09 and 0.93±0.09. Within the limits of experimental error, the value for HBC-C₁₂ agrees with the earlier findings.

For HBC-PhC₁₂ the order parameter for the discs has increased by 15%, which means that the rotational motion is better defined and that additional out-of-plane motions are suppressed more effectively. It should be emphasized that the increase in the order parameter is better defined than its absolute value, which is subject to systematic deviations, such as influences from remote protons to the first-order sidebands (Section 3.1.1).

These NMR findings strongly support the conclusion of high intracolumnar order drawn from the X-ray data, and thus we can state that order phenomena in the LC phase of HBC-PhC₁₂ not only extend to longer ranges — as detected by scattering experiments — but also manifest themselves in a well-defined packing of the rotating discs on a molecular level.

7.1.3 Sidechain Dynamics of HBC-PhC₁₂ in the LT Phases

In Fig. 7.3, a pronounced enthalpy change upon transition from the K₁ to the K₂-phases became apparent for HBC-PhC₁₂. REPT-HMQ spinning sideband patterns and 1D REPT-HMQ-filtered spectra were used for the investigation of the underlying molecular processes in this case.

At room temperature and below, sideband patterns could be obtained for the *exo*-phenyl-CH group in the HBC-PhC₁₂. These are compared with 3-spin simulations of such a moiety in Fig. 7.7. In the interval between -4°C and -42°C, the pattern changes from a spectrum dominated by first-order sidebands, with only weak third-order contributions, to a spectrum very close to the one for a rigid CH-group (with slightly increased first-order sidebands, possibly due to the familiar influence of other remote protons, or a fraction of rings still performing fast motions). As can be inferred from the simulations, the room temperature spectrum can be best explained in terms of phenyl groups undergoing fast 180°-flips. This is a very characteristic motional process for *para*-substituted phenyl rings, and is encountered in many low-molecular weight compounds and polymers. The 180°-flip gives the best agreement between the simula-

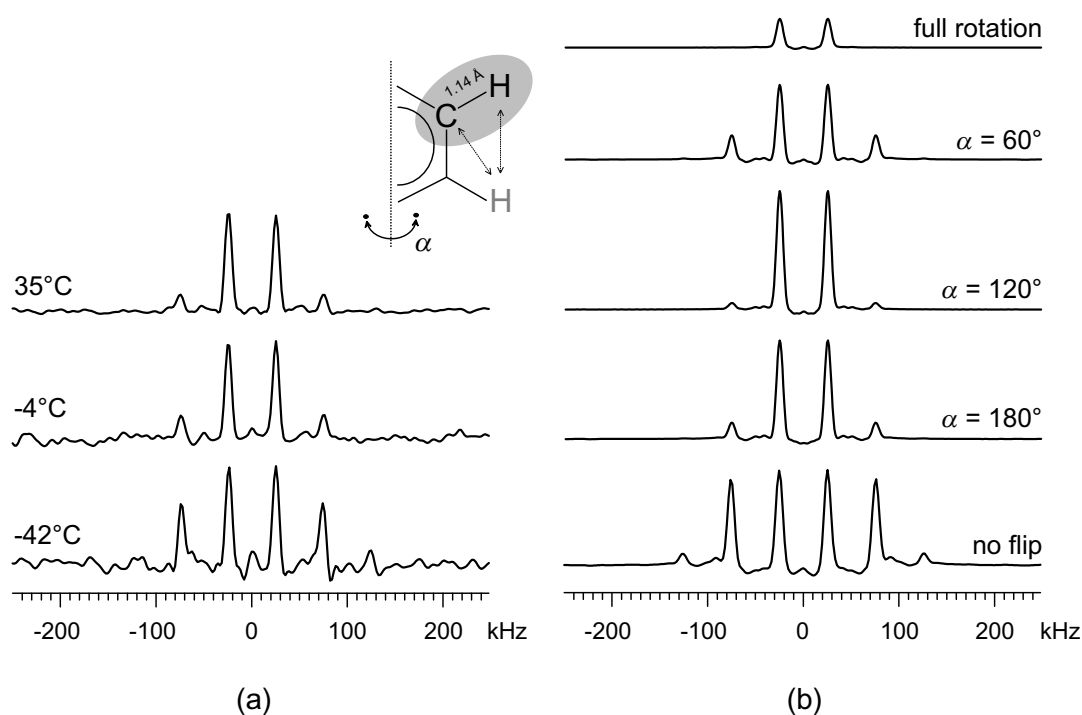


Figure 7.7: REPT-HMQ spinning sideband patterns for the exo-phenyl-CH signal of HBC-PhC₁₂, with $\omega_R/2\pi = 25 \text{ kHz}$ and $\tau_{rcpl} = 2 \tau_R$, measured at different temperatures (a). In (b), simulated spectra for a phenyl group, considering a primary CH-pair with $r_{CH} = 1.14 \text{ \AA}$ and the adjacent proton, are shown for the rigid case and for a ring performing fast flips between two sites separated by the indicated reorientation angle, α . The fast flip was accounted for by averaging the dipolar tensors calculated for the two ring positions.

tions and the measured spectra, but some ambiguity remains insofar as the 60° -flip spectrum would also fit the experimental pattern, if the first-order sidebands are still assumed to be increased at higher temperatures. An ultimate proof would require the application of methods probing other tensorial interactions, for instance the reorientation of the CSA tensors in the phenyl group. Nevertheless, fast torsional vibrations with $\alpha < 60^\circ$ would not lead to the observed reduction in the dipolar coupling, and with a free rotation, no third-order sidebands are observable. At -42°C , the flip motion is essentially frozen out.

Therefore, the fast phenyl flip is identified as one of the dynamical processes characteristic for the intermediate solid phase, K₂. Information on the mobility of the sidechains can be extracted from REPT-HMQ-filtered spectra, as presented in Fig. 7.8a. The interpretation of these spectra is based on the “anomalous” behavior of CH₂-groups, which show a charac-

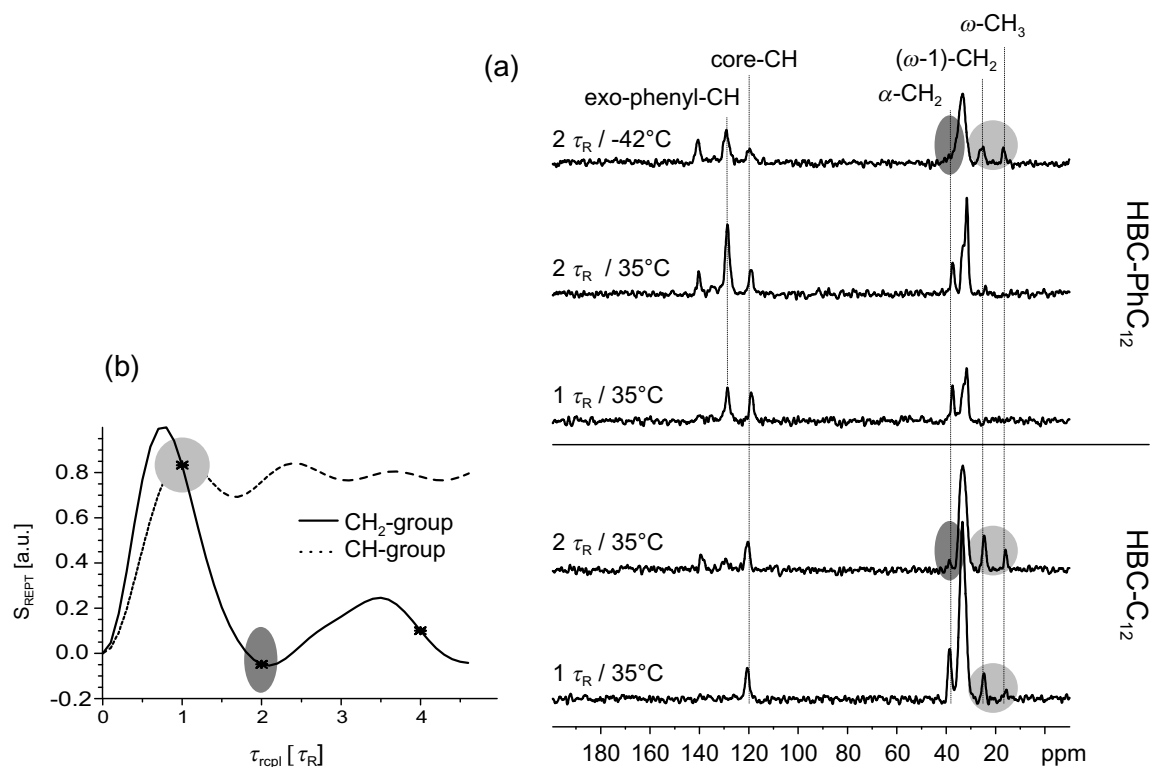


Figure 7.8: REPT-HMQ-filtered spectra of the two samples at different temperatures, acquired at $\omega_R/2\pi = 25$ kHz (a). The recoupling times and temperatures were as indicated on the spectra. The expected intensity profile for a CH₂-group, along with a curve for a CH spin pair for comparison, is depicted in (b). Experimentally accessible points are marked as asterisks.

teristic sharp maximum in the HMQ excitation curve (Fig. 7.8b). At 25 kHz MAS, the signal for a rigid CH₂-group is expected to vanish completely for a recoupling time of only $2 \tau_R$; this behavior can be used as a qualitative marker for the rigidity of a CH₂-group.

In the spectra, the α - (attached to the phenyl ring) and the $(\omega-1)$ -CH₂-group are clearly resolved. The assignment was confirmed by comparison with solution-state NMR spectra. At room temperature, no signal is observed for the $(\omega-1)$ position of HBC-PhC₁₂ at a recoupling time of $1 \tau_R$, as opposed to HBC-C₁₂, where the $(\omega-1)$ - and the terminal CH₃-signals are present. Thus, HBC-C₁₂ is less mobile at this temperature.

Even though the sample was not heated for the room temperature measurements, bearing air friction leads to an increase of the temperature inside the used rotors of 2.5 mm diameter (see Appendix E). The sample temperature of 35°C is close to the $K_1 \rightarrow K_2$ transition temper-

ature for HBC-C₁₂. The observations for this sample can thus not uniquely be attributed to one of these two phases. HBC-PhC₁₂, however, can safely be assumed to be in the K₂-phase under these conditions, and the results clearly show a largely increased sidechain mobility. Upon doubling the recoupling time, still no signal from the chain ends is visible, and only below the K₂→K₁ transition do these signals appear. In the top spectrum, the α-CH₂-group is seen to obey the rigid-limit behavior, i.e. it is not observable any more for $\tau_{rcpl} = 2 \tau_R$. The presence of signal from the chain ends and the disappearance of the α-CH₂ is exactly what is observed for HBC-C₁₂, though already at room temperature, and for both samples, a *mobility gradient* along the chain is thus proven. A detailed investigation of such phenomena has only been possible before by ²H NMR on compounds, where specific positions along the chain had to be labeled [Leisen 92]. This once more illustrates one of the advantages of the novel techniques used here.

7.1.4 Summary and Discussion of the Results

- DSC results showed that both HBC samples exhibit a similar phase behavior, with broader transitions, reduced transition temperatures, and a considerably larger enthalpy change for the K₁→K₂ transition for HBC-PhC₁₂.
- The inter-disc spacings in the hexagonal LC phases are comparable for both samples (0.35 nm); HBC-PhC₁₂ exhibits a better-defined long-range order.
- The reduction of the heteronuclear dipolar coupling constant of the core-CH group of HBC-C₁₂ upon transition into the discotic LC phase proved the fast rotation of the discs, and the so-obtained order parameter, $S = 0.78$, is supported by previous NMR measurements.
- The order parameter of HBC-PhC₁₂, $S = 0.93$, indicates less out-of-plane motions and improved order.
- HBC-PhC₁₂ exhibits a considerable sidechain mobility in the room temperature (K₂) phase; the K₂→K₁ transition is characterized by a pronounced loss in chain mobility, and a quenching of the exo-phenyl flip motion.

As to the structure of the room temperature phases, the cores of HBC-C₁₂ are known to exist in a staggered arrangement, which relative carbon positions in analogy to graphite, with optimized π - π interactions [Brown 99]. The proof was based on ¹H-¹H DQ correlation spectra, and utilized the fact that the chemical shifts within two of the three ‘bay’ proton pairs of the core-CH-groups are different, which can be explained by π - π interactions with adjacent molecules (“ring current effects”). Heteronuclear ¹³C-¹H shift correlation experiments for HBC-PhC₁₂ indicated that at room temperature, no equivalent packing arrangement is assumed by these molecules, probably due to steric hindrances caused by the exo-phenyl rings (for this sample, only one ¹H signal is found for the core-CH groups, but ring current effects are still present).

In a very recent publication [Craats 99], these conclusion are nicely supported by intracolumnar charge carrier mobility measurements on the two discussed samples. Firstly, in the K₁ and K₂-phases of HBC-C₁₂, the conductivities assume the highest values ever measured on low-molecular weight discotic compounds ($> 1 \text{ cm}^2\text{V}^{-1}\text{s}^{-1}$), already approaching the value for the intersheet mobility in graphite ($3 \text{ cm}^2\text{V}^{-1}\text{s}^{-1}$), which is in support of the well-defined π - π interactions. This value drops to about $0.3 \text{ cm}^2\text{V}^{-1}\text{s}^{-1}$ upon entering the LC phase. Secondly, *no* decrease is observed for HBC-PhC₁₂. Rather, the conductivity is almost constant over the whole temperature range, with a trend towards higher mobilities at higher temperatures and a mean value of again about $0.3 \text{ cm}^2\text{V}^{-1}\text{s}^{-1}$.

The conclusion is clear: The insertion of the phenyl rings undermines the possibility of an optimized π - π packing even in the low-temperature phases of HBC-PhC₁₂, leading to a lower conductivity, but a smooth profile over the whole temperature range. The thermally activated rotation of the cores in the LC-phase obviously does not interfere with the dynamics of the hopping process of charge transport, which takes place on a timescale of less than 1 ns. Moreover, the *lifetimes* of the charge carriers parallel the improved intra-columnar order in the mesophases: they are about 4 times longer in HBC-PhC₁₂. It is hypothesized in the cited paper that the improved order also increases the anisotropy of the one-dimensional conductivity.

One point yet to be discussed is that, in the same publication, the low-temperature phases of HBC-PhC₁₂ were concluded to be discotic mesophases as well, taking the monotonic behavior of the conductivity and the malleability of the compound as evidence. Moreover, the authors interpret the two observed phase transitions in terms of “conformational changes within the mesophase”. This is clearly shown to be incorrect by the NMR results presented

here, and shows that, if a proper X-ray characterization of such phases is not available, NMR can successfully contribute to the understanding of the characteristics of such phases. The rigidity of the *cores* in the LT phases of both substances was here used to define a “solid” phase, in contrast to a discotic LC phase, where the cores rotate rapidly.

The increased sidechain mobility in the LT phases of HBC-PhC₁₂ has another interesting implication: Since the charge carrier transport properties in such systems are limited by the degree of long-range order within the columns, the possibility of the system to undergo molecular reorientations due to this motional freedom, thus allowing for self-healing, is highly desirable. More detailed investigations of slow reorientation dynamics in the LT phases using CODEX and related techniques are under way.

In summary, the successful improvement of short- and long-range order in the mesophase of HBC-PhC₁₂ by insertion of phenyl rings into the sidechains, along with an altered solid-phase structure, lead to a substance with well-reproducible charge carrier mobilities over a wide range of temperatures. Together with the much higher solubility of HBC-PhC₁₂ in common organic solvents (e.g., greater than 10 gL⁻¹ in THF for HBC-PhC₁₂ versus less than 1 gL⁻¹ for HBC-C₁₂), the described combination of favorable properties makes this substance a promising candidate for the intended electro-optical and photonic applications.

7.2 Hydrogen Bonds in Poly(vinyl alcohol)

Poly(vinyl alcohol) (PVA) is a semicrystalline polymer with a range of interesting properties, such as water solubility, biocompatibility, and a favorable dynamic-mechanical behavior. PVA films exhibit an unusually high tenacity, and fibers have a tensile modulus higher than that of polyethylene. The investigation of whether inter- and intramolecular hydrogen bonds are the main reason for this high stability is of importance for a better understanding of the properties of PVA.

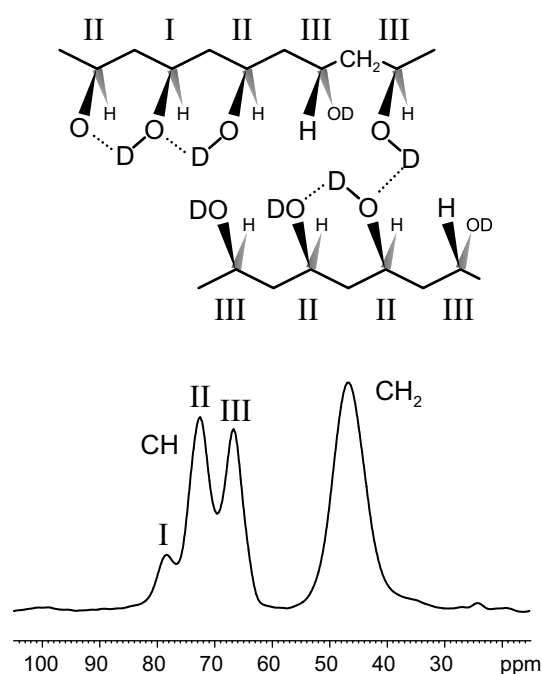


Figure 7.9: ^{13}C CP MAS spectrum of hydrated aPVA, along with a sketch of the crystal structure, with the supposed assignment of the individual signals.

enhance the chemical shift differences between the signals; these differences are unusually high in the case of PVA. Only CHOH-groups in a *meso* (mm) triad sequence are capable of forming two intramolecular hydrogen bonds. Since not all mm triads (with a frequency of occurrence of $\frac{1}{4}$ in a completely atactic polymer) can be expected to contain an OH-group forming two

The degree of crystallinity of PVA, even of the atactic form (aPVA), reaches very high values, comparable to those of common isotactic polymers. The exact crystal structure is still a matter of some debate, even though it is agreed upon that the chains exist in an all-trans conformation, with a disordered hydrogen bond structure between the chains [Bunn 48]. Much effort has been devoted to the investigation of PVA using NMR spectroscopy. The ^{13}C CP MAS spectrum of PVA exhibits an unusual fine structure, which is also not yet fully understood.

According to the most common interpretation [Terao 83, Horii 92], the three main contributions to the CH signal (denoted as I, II, and III) are attributed to CHOH-groups forming two, one, and no *intramolecular* hydrogen bonds, respectively (Fig. 7.9). The basic splitting pattern reflects the tacticity of the sample, while the intramolecular hydrogen bonds are believed to en-

H-bonds, the intensity of peak I is rather low.

The aim of this work is to further examine the validity of this assignment, and to provide experimental evidence for dynamical processes in the crystallites. Since PVA is soluble in water, a deuteration of the OH protons is easily achieved, and ^2H REDOR is used to examine whether possible structural implications of the model, i.e. closer ^{13}C - ^2H proximities for the signal associated with two intramolecular hydrogen bonds, are detectable. Moreover, changes in the ^2H quadrupolar lineshape at elevated temperature, as detected by ^2H - ^{13}C HMQ correlation spectroscopy, indicate yet unobserved dynamical processes in the hydrogen bond structure.

7.2.1 Selection of the Crystalline Components

The crystalline parts of aPVA are of primary interest in this study, and the question arises how to selectively observe these in an NMR experiment. Horii and coworkers [Horii 92] have successfully obtained spectra of the amorphous and crystalline components in aPVA films. The spectra from the different components turned out to be rather similar in appearance, the most prominent difference only being an improved splitting between the three CH components in the crystalline subspectra. The selection was based on different ^{13}C longitudinal relaxation times (T_1^C), as measured in a CP experiment. These times were 1.2 s, 14.6 s, and 65.0 s for the mobile amorphous, interface, and rigid crystalline parts of the polymer, respectively. In order to selectively measure the crystalline components, experiment times of more than 60 s for a single transient are thus mandatory. Since the above-mentioned ^{13}C - ^2H correlation methods have a notoriously poor S/N ratio, and require extensive signal averaging, a more efficient way for the selection has to be chosen.

The crystallites are thermodynamically very stable, such that excess water in the polymer resides in the amorphous parts, which are consequently mobilized to a large extent in a swollen sample. The preparation and characterization of the swollen PVA samples used for our experiments is summarized in Appendix D.5. Since ^1H T_1 (T_1^H) relaxation times do not differ largely between the domains of such a swollen polymer, and T_1^C times were still prohibitively high (an experiment time on the order of a few seconds would be desirable), T_2^C and $T_{1\rho}^H$ remained as potential candidates ($T_{1\rho}^C$ was not tested).

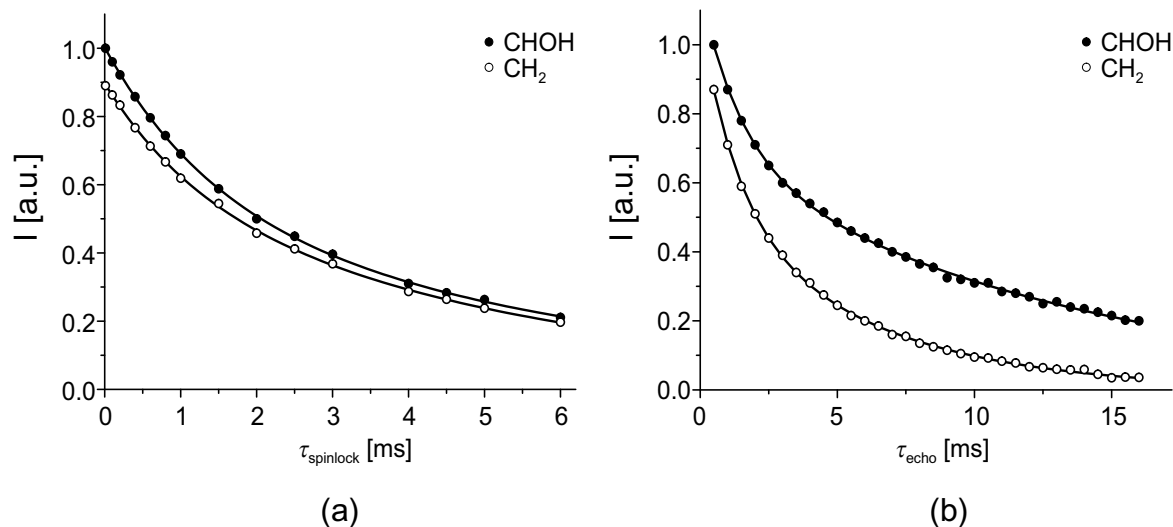


Figure 7.10: ^{13}C signal intensities of swollen aPVA, measured with a CP MAS sequence with an initial ^1H spin-lock and a Hahn echo prior to detection (4 kHz MAS, room temperature), as a function of the spin-lock time, τ_{spinlock} , and the total echo delay τ_{echo} . The solid lines are results from two-component fits of $T_{1\rho}^H$ (a) and T_2^C (b) for the crystalline and amorphous regions. For the results see Table 7.1.

Table 7.1: Results of the two-component exponential fits to the data in Fig. 7.10, and analogous measurements at 90°C .

τ_{spinlock} - dependence	fast — swollen amorphous		slow — crystalline	
	$T_{1\rho}^H$ [ms]	amplitude	$T_{1\rho}^H$ [ms]	amplitude
25°C CH	1.4 ± 0.1	0.44 ± 0.06	6.1 ± 0.7	0.55 ± 0.06
CH ₂	1.2 ± 0.2	0.34 ± 0.05	5.4 ± 0.5	0.66 ± 0.05
90°C CH	0.88 ± 0.11	0.32 ± 0.04	6.1 ± 0.4	0.68 ± 0.04
CH ₂	0.75 ± 0.09	0.29 ± 0.03	5.8 ± 0.3	0.71 ± 0.03
τ_{echo} - dependence	fast — swollen amorphous		slow — crystalline	
	T_2^C [ms]	amplitude	T_2^C [ms]	amplitude
25°C CH	1.46 ± 0.07	0.41 ± 0.01	12.7 ± 0.2	0.59 ± 0.01
CH ₂	1.33 ± 0.07	0.48 ± 0.01	5.75 ± 0.13	0.52 ± 0.02
90°C CH	1.61 ± 0.10	0.40 ± 0.01	16.4 ± 0.4	0.60 ± 0.01
CH ₂	1.52 ± 0.11	0.58 ± 0.03	6.04 ± 0.31	0.42 ± 0.04

Using a standard CP experiment, Horii et al. [Horii 92] found that, upon increasing the CP contact time, the data for aPVA could be well explained with a uniform $T_{1\rho}^H$ over the whole, dry sample. Equilibration of the ^1H magnetization between the domains as a result of spin diffusion was neglected in the treatment, such that the measured ^{13}C magnetization of the bulk sample could originate mainly from the crystalline regions. The approach presented here is based on an initial proton spin-lock, followed by a CP (500 μs contact time) and a Hahn spin echo prior to detection.

Separate curves of the spin-lock and echo-delay time dependencies were obtained for the CH and CH₂ signals of the hydrated aPVA sample. The room temperature measurements are depicted in Fig. 7.10, and the results for the relaxation times, obtained at 25°C and 90°C, are listed in Table 7.1. In all cases, the data could be fitted very well assuming a doubly exponential decay, and the resulting relaxation times for the fast and slow components are separated by a factor of at least four, sufficient for a good selection. The fraction of the slow component is consistently fitted to be about $60\pm 10\%$, which is a measure of the crystallinity of the sample. However, the cross polarization process is less efficient in the mobile swollen regions, such that the real degree of crystallinity is certainly lower than this value.

In most cases, only a negligible change in the relaxation times is observed when comparing the different temperatures and the two kinds of carbon atoms. There are, however, two notable exceptions. The crystalline T_2^C are less than half for the methylene as compared to the methyne carbons at both temperatures, while $T_{1\rho}^H$ of the swollen regions represents the only case where relaxation speeds up significantly upon increasing the temperature.

In Fig. 7.11, CP MAS spectra of the sample are depicted, which were acquired using either $T_{1\rho}^H$ or T_2^C for the selection of the crystalline regions. The temperature changes in the spectra without selection, i.e. the decrease of peak III, along with the appearance of a shoulder between peaks II and III, are seen to pertain to the amorphous regions of the polymer, where rapid averaging between different conformations or breaking of intermolecular hydrogen bonds can be envisaged to be the reason for such a behaviour. The filtered spectra are all very similar, with characteristically narrower, thus better resolved lines in the methyne regions.

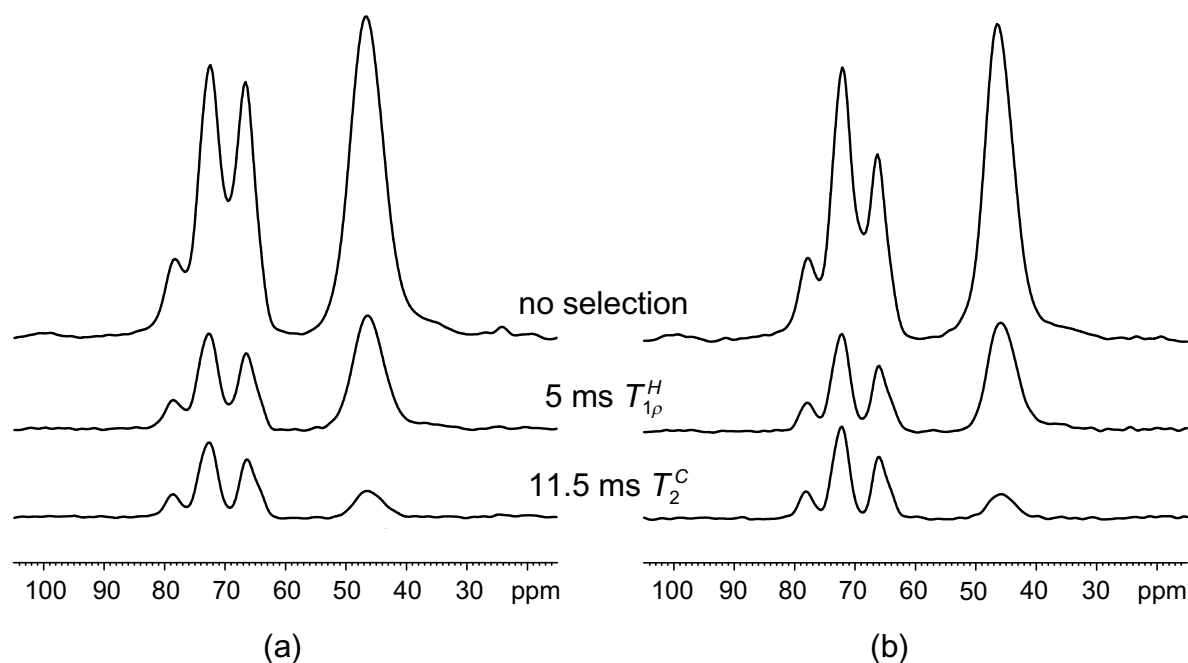


Figure 7.11: CP MAS spectra of swollen aPVA demonstrating the effect of filtering via T_{1p}^H by an initial 1H spin-lock (middle slice) and via T_2^C by a Hahn echo prior to detection (bottom slice), at 25°C (a) and 90°C (b). The recycle delays were 2 s and 1 s, respectively.

7.2.2 2H -REDOR Measurements

In the experiments presented in the following, deuterated aPVA, swollen with D_2O , was used. The relaxation behavior of this sample was not analyzed thoroughly, but the relaxation behaviour and filtering efficiency was seen to be comparable to the hydrated sample studied in the preceding section (e.g., the optimum recycle delays were also 2 s and 1 s for measurements at room temperature and at 90°C, respectively). In all experiments, an initial 1H spin-lock of 4–5 ms length was used. No special T_2^C filter was implemented in the pulse sequence, rather, the REDOR recoupling periods in these experiments served as an additional “internal” T_2^C filter, owing to the evolution of transverse ^{13}C magnetization during these periods.

Both conventional REDOR (with a minimized number of pulses on the 2H channel, and an inversion pulse with a flip-angle of less than 180°) and composite-pulse REDOR experiments were performed on the D_2O -swollen d_1 -aPVA. A representative spectrum is depicted in Fig. 7.12.

Structurally, the formation of two intramolecular hydrogen bonds should lead to closer ^2H proximities for component I of the CH-signal. This is based on the argument that the relative bond angles within the O-H \cdots OC arrangement of intra- and intermolecular H-bonds are on the order of 120° and 180° , respectively, where the former configuration should lead to a closer proximity of the H-bonded proton and the carbon attached to the acceptor-O. This should then manifest itself in a higher REDOR dephasing of peak I. The experimental problem associated with this is readily apparent from Fig. 7.12. The low intensity of peak I is coupled with a rather low S/N, such that the error in $\Delta S/S_0$ observed for this peak is larger than in the values for the other signals in the spectrum.

The data from the conventional ^2H REDOR measurements are presented in Fig. 7.13, where $\Delta S/S_0$ is plotted as a function of the recoupling time (build-up curve). As expected from the chemical structure, the dephasing of the methylene group is always less than of the methyne carbon. For the longest recoupling time (3.2 ms), the values of all signals in the spectrum surpass the theoretically predicted plateau of 66% considering a single ^{13}C - ^2H pair (Eq. (5.8)). This is not surprising, since the investigated sample was not isotopically diluted, such that the situation is governed by multiple ^{13}C - ^2H couplings. Higher than expected dephasings may also be due to the excitation of DQ transitions of the ^2H nuclei by finite pulses, as examined in detail in Chapter 5.

No attempt will therefore be made to model the REDOR data. Although, due to the S/N problem already mentioned, the $\Delta S/S_0$ values for peak I are not too significant within the experimental error, it is apparent that these values indeed exhibit a trend towards larger values as compared to peaks II and III. This trend is observed also for the room temperature (RT) composite-pulse data represented in Fig. 7.14a. These values are comparable to the ones measured with the conventional REDOR pulse sequence, indicating that the influence of ^2H

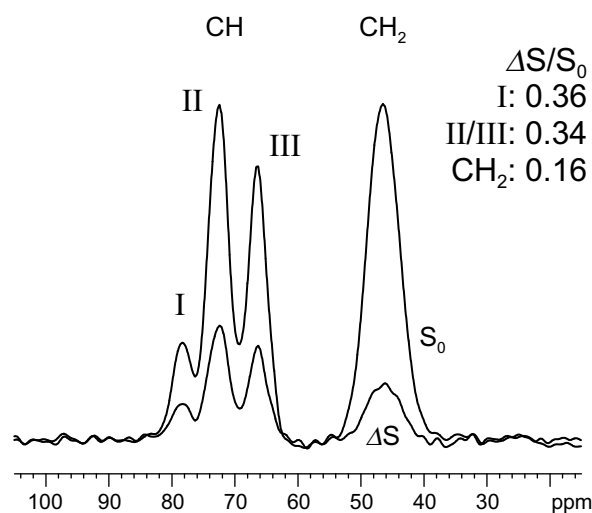


Figure 7.12: ^{13}C - ^2H composite-pulse REDOR reference and difference spectra of D_2O -swollen d_1 -aPVA (for experimental details see Fig. 7.14).

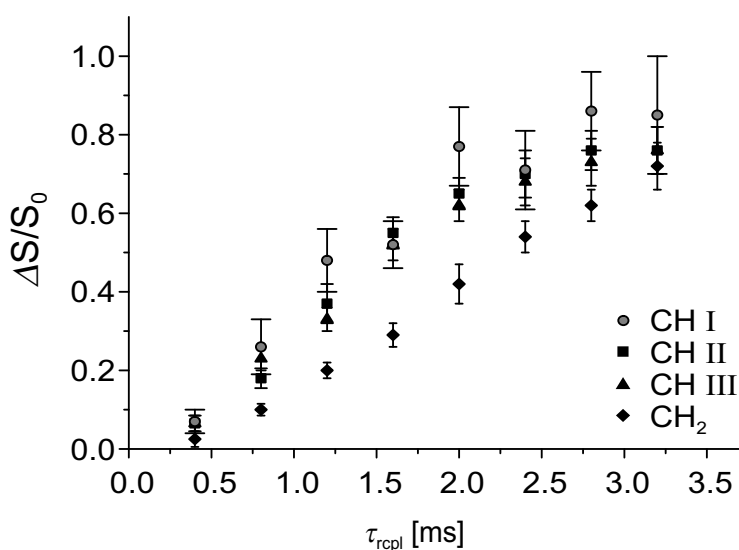


Figure 7.13: Normalized ^{13}C - ^2H REDOR difference intensities of D_2O -swollen d_1 -aPVA, measured at room temperature with a REDOR sequence analogous to the one shown in Fig. 2.1, i.e. with only one inversion pulse on ^2H ($4 \mu\text{s}$ length, $\omega_1^D/2\pi = 70 \text{ kHz}$), at 5 kHz MAS.

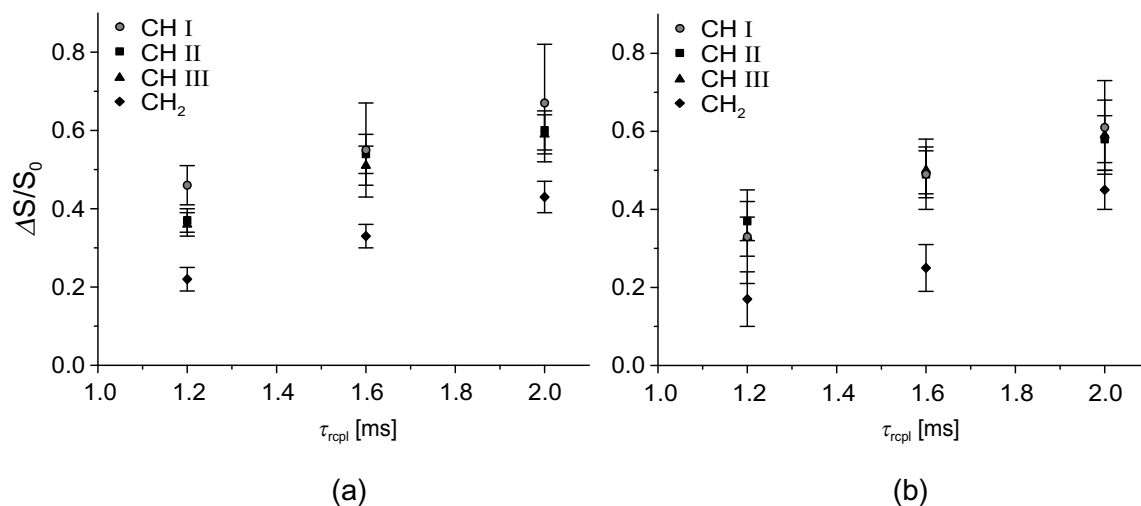


Figure 7.14: Normalized ^{13}C - ^2H composite-pulse REDOR difference intensities of D_2O -swollen d_1 -aPVA, acquired with a $90_x 90_y 90_x$ inversion sequence on ^2H ($3 \times 3.7 \mu\text{s}$ length, $\omega_1^D/2\pi = 68 \text{ kHz}$, $\omega_R/2\pi = 5 \text{ kHz}$). The data was obtained for three different recoupling times ($6, 8, 10 \tau_R$), at room temperature (a) and 90°C (b).

DQ transitions (which are excited more efficiently with a conventional inversion pulse) on the measured dephasing is small.

In Fig. 7.14b, data measured at 90°C are shown. These REDOR dephasings are not significantly different from the ones measured at room temperature. Therefore, the heteronuclear ^2H - ^{13}C dipolar couplings are not reduced to a large extent, as may be expected if substantial molecular motion occurred in the kHz range. Yet, the trend of peak I towards higher dephasings seems to be lost at the higher temperature. These observations will gain importance when conclusions from the measurements presented in the next section are discussed.

7.2.3 ^2H -WISE and Static ^2H Spectra

The study of static ^2H quadrupolar lineshape is a well known tool for the investigation of molecular motions which are on the timescale of the NMR experiment (i.e. on the order of tens of kHz) up to the fast-motion limit of about 200 kHz [Spiess 83]. The ^{13}C - ^2H dipolar HMQC experiment presented in Section 5.2, here referred to as ^2H -WISE, represents a means of separating quasi-static ^2H quadrupolar lineshapes by the ^{13}C chemical shift of nearby carbon atoms. The experiment is suitable for selective observation of the ^2H signals from the crystalline parts of aPVA, by taking advantage of the selection of ^{13}C signals from the crystalline parts via their relaxation properties, as discussed above.

Full 2D ^2H -WISE spectra are shown on page 147, where the advantage of the composite-pulse approach as compared to a conventional MQ-filter based on two 90°-pulses was proven. Fig. 7.15 shows sum projections over all ^{13}C signals in those spectra.

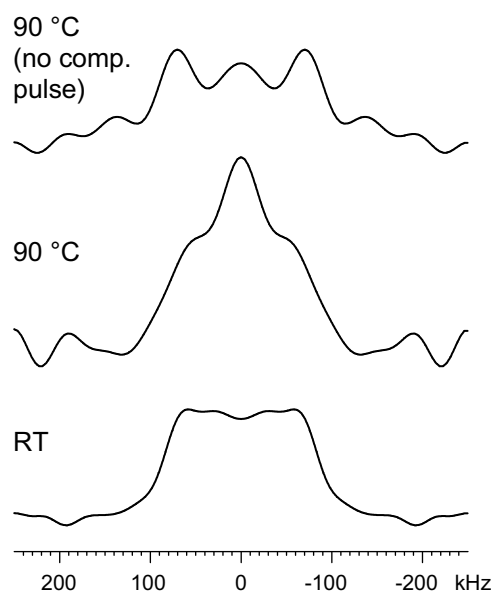


Figure 7.15: Sum projections over all ^{13}C signals in the ^2H -WISE spectra of Fig. 5.8, with the result from an additional room temperature spectrum (bottom slice).

As is readily apparent, the appearance of these spectra differs significantly as to whether the conventional or the composite-pulse approach is used (middle and top spectra). As was shown in Section 5.2.3, phase distortions in the spectra acquired with the composite-pulse scheme can be expected to be weak. Nevertheless, neither the RT nor the high temperature (HT) composite-pulse spectrum exhibits a conventional quadrupolar lineshape. Of course, this cannot be expected from first principles, owing to the fact that the ^2H -WISE is a MAS experiment. However, simulations showed that for a rigid quadrupolar tensor under the experimental conditions used here, such deviations should not be very significant (Fig 5.7 on p. 146). Therefore, the presence of molecular motion on the ms-timescale, or, more specifically, reorientations of the quadrupolar tensor of the deuterium atoms associated with the H-bonds in the crystalline parts of aPVA, are present at both temperatures.

Static ^2H spectra of the same sample were measured in order to prove this assumption. These spectra are depicted in Fig. 7.16a. Two components are observed at both room temperature and 90°C . The spectra are dominated by a narrow central peak, which corresponds to the signal from the swollen, thus very mobile regions. The splitting of the broad component, observed at room temperature, is 150 kHz, corresponding to a quadrupolar coupling constant (QCC) of 200 kHz, which is expected for rigid deuterons in H-bonds [Aliev 98]. The lineshape of the broad component changes upon heating, again indicating molecular reorientations.

The motional process in the crystalline regions thus detected has yet to be proven not to be due to the swelling of the sample. Therefore, the sample was dried at elevated temperature, and quadrupolar spectra of the dried sample are shown in Fig. 7.16b. The narrow central component has, as expected, completely disappeared and the lineshape changes in these spectra upon heating parallel those of the broad component in the swollen sample. The room-temperature spectrum of the dried sample, acquired with a better S/N, lacks the pronounced wings of a quadrupolar peak patterns, showing an influence of the motional process already at room temperature. It should be emphasized that the lineshapes for the bulk dried sample are superpositions of the amorphous and crystalline parts of the sample, where the glass transition temperature of the former is reported to be about 70°C – 85°C [Sakurada 85]. How the dynamics observed for both the crystalline and the amorphous parts is related to the glass transition process remains an open question.

Preliminary results on the T_1 and T_2 relaxation times of ^2H in the crystallites of the

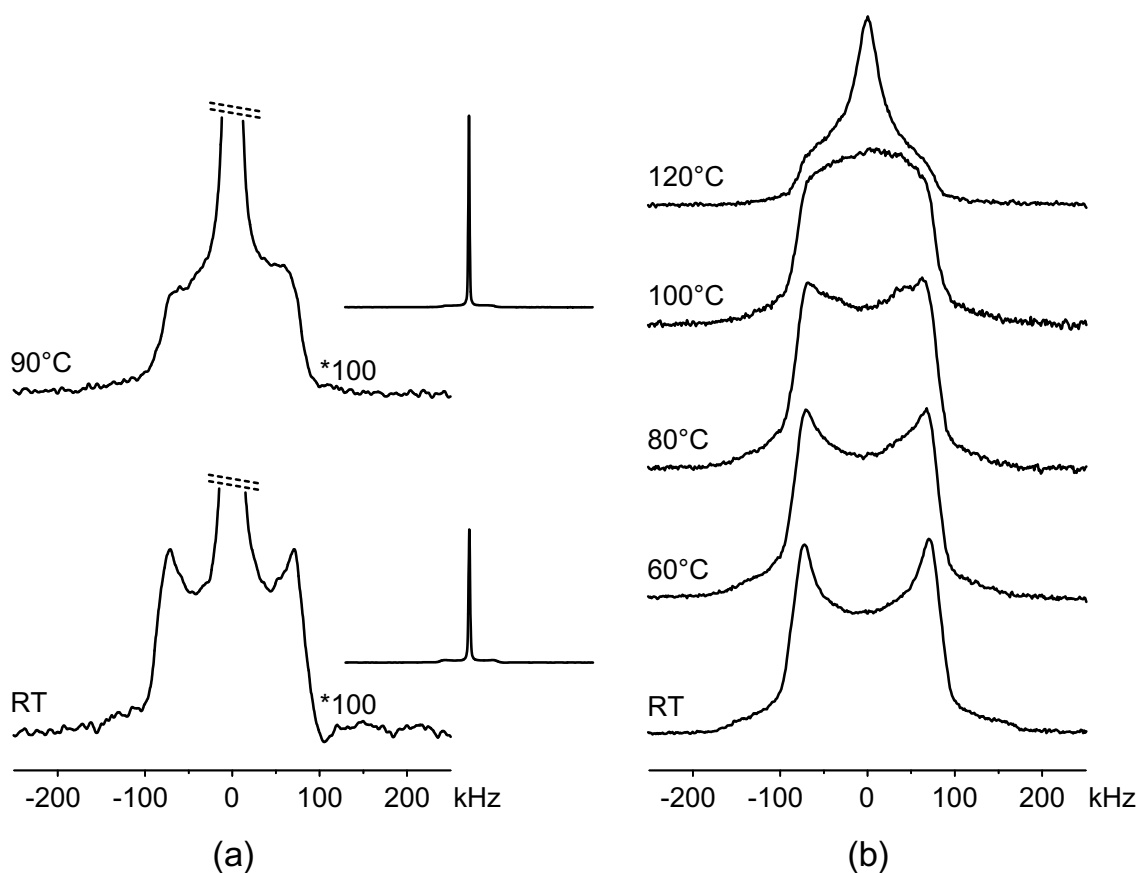


Figure 7.16: Static ^2H solid-echo spectra ($\tau_{\text{echo}} = 40 \mu\text{s}$, $\omega_1^D/2\pi = 70 \text{ kHz}$, 250 ms recycle delay) of the same d_1 -aPVA sample in the swollen state (a) and free of excess water (b). The spectra in (b) are shown with kind permission of H. Kaji.

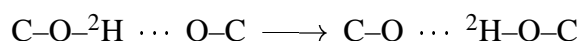
swollen samples indicate surprisingly small values, on the order of about 200 ms and 60 μs , respectively, which are also in accord with substantial dynamics of the quadrupolar tensor (which can be assumed to be the main contributor to the relaxation processes). More detailed studies of the relaxation processes in dried and swollen aPVA samples, deuterated either in the OH-groups or in the main chain, are under way, and a publication of these results and the ones presented in this section is in preparation.

7.2.4 Discussion of the Experimental Results

Summarizing the observations, it is clear that a motional process of the H-bonds in the crystalline regions of aPVA was found. From the similarity of the lineshapes of the broad compo-

ment in Figs. 7.16a and b, it can be concluded that this process occurs also in the amorphous regions of the polymer, and is *not* an effect specific for a swollen sample. The lineshapes of the ^2H -WISE spectra in Fig. 7.15 differ from those of the static spectra. Molecular motions influence ^2H -WISE spectra in a more complex way, since the signal in such a spectrum also depends on the relative orientation of the heteronuclear dipolar coupling tensor and the quadrupolar interaction tensor (see Eq. (5.5), p. 140). The different lineshapes are thus not surprising.

Yet, it is very surprising that, even with the reorientations of the quadrupolar tensor occurring on the timescale of the experiment, the build-up behavior of HQM intensity (as quantified by the REDOR data in Figs. 7.13 and 7.14) hardly changes in the same temperature interval. Dipolar recoupling in the intermediate motional regime has not yet been investigated in detail, but the loss of phase coherence during recoupling due to random reorientations of the dipolar coupling tensor can be expected to lead to a considerable loss in signal intensity, while in the fast-motion limit, the signal intensity depends on a weak residual coupling. From the experimental observations, we therefore conclude that the observed reorientation of the ^2H quadrupolar tensor is not coupled with large-scale reorientations of the ^2H - ^{13}C heteronuclear dipolar tensor. A tentative model for that process would be to assume deuteron exchange via the H-bonds:



Such a process does not involve large changes in the ^{13}C - ^2H distances. The quadrupolar tensor, however, which is influenced by the local electronic structure, can be expected to reorient considerably upon H-bond reorganization.

As mentioned, such a process has — to the best of our knowledge — not yet been described to be present in poly(vinyl alcohol), while in other mobile H-bonded systems, it is commonly observed (H^+ -transport in water is a prominent example). Moreover, using CODEX and related techniques, no (slow) main-chain dynamics (as probed by reorientations of the ^{13}C CSA tensor or isotropic shift exchange during a mixing time on the order of 1 ms–1 s) has been found in the crystallites of swollen aPVA in the range between 25°C and 100°C, proving the localized character of the presumed H-bond exchange.

If this process is occurring on a ms-timescale already at room temperature, and speeds up upon heating, an important implication is that the assignment of peaks I–III of the methine signal as representing CHOH-groups with two, one, or no intramolecular H-bonds is questionable. If fast hydrogen exchange occurred between COH-groups of different types I–III (i.e., between groups on the same chain), it would cause a broadening of the lines, ultimately leading to a coalescence of these peaks upon heating. This is not observed, rather, the crystalline subspectrum hardly changes (Fig. 7.11). Therefore, the splitting of the CH-signal is either solely due to conformational or configurational effects, or H-bond exchange occurs only between different chains, leaving the intra-chain H-bonds unaffected.

Data in support of the hypothesis of a conformational origin of the splittings has been published recently [Imashiro 95]. The authors performed ab-initio calculations of ^{13}C chemical shifts on 1,3-propanediols and 1,3,5-pentanetriols in all possible all-trans configurations as model compounds for the aPVA backbone. The results are such that the highest deshielding is indeed found for the mm-configuration of 1,3,5-pentanetriol, i.e. where all OH-groups lie on the same side of an all-trans carbon chain, and the central CHOH-moiety *would be* capable of forming two H-bonds (one as donor, one as acceptor). However, a deshielding effect of the same magnitude is also found for like configurations of 4-methylheptan, indicating a pure configurational origin of the shift. The potential H-bond formation merely has an impact on the energetic stabilization of different conformers.

In the crystallites of aPVA, the conformation is fixed to all-trans, leading to large possible configurationally induced deshielding effects. In hydrocarbon polymers, such effects are not observed simply because the atactic varieties hardly crystallize. Yet, the relative intensities of the components I–III of the CH-signal are not consistent with the configurational statistics [Terao 83]. At this point, a consistent model explaining all experimental observations cannot be given. Our results indicate, however, that if the observed dynamics in the H-bonds are to be taken seriously, the assignment of the CH-triplet has to be altered towards a more complex and flexible model. For the time being, it can not be excluded that the observed dynamics pertains only to a fraction of the CHOH-groups represented by one of the three contributions.

Summary

Recent improvements in high-resolution solid-state NMR technology, namely the availability of MAS equipment capable of spinning frequencies up to 35 kHz and high-field spectrometers with ^1H Larmor frequencies of 500 MHz and higher, lead to the possibility of performing relatively simple high-resolution ^1H SQ and DQ experiments. In such experiments the ^1H isotropic shift information can be combined with the measurement of spatial proximities and dipolar coupling constants, in order to obtain site-resolved structural and dynamical information in solids. The primary aim of this thesis was to extend the homonuclear ^1H DQ methodology established in our group to the heteronuclear case, in particular to ^{13}C - ^1H systems with ^{13}C in natural abundance.

At very-fast MAS conditions, a *recoupling* of the ^1H - ^1H and ^{13}C - ^1H dipolar interactions is necessary for an efficient excitation of the MQ modes subject to spectroscopic investigation. The REDOR technique, where π -pulses are applied every half rotor period, is an efficient and very robust approach to a selective recoupling of the *heteronuclear* dipolar interaction. It is shown that only minor modifications of the original REDOR pulse sequence are needed in order to arrive at an actual *heteronuclear multiple-quantum* (HMQ) experiment, which has features very similar to homonuclear DQ experiments based on the BABA sequence. Namely, the excitation dynamics of HMQ coherences can be monitored, their precessional properties can be probed in a two-dimensional experiment, and MQ spinning-sideband analysis for the determination of dipolar coupling constants is also possible in the heteronuclear case. A theoretical proof is presented showing that MQ experiments using the REDOR and BABA sequences are governed by essentially the same principles.

Heteronuclear MQ spectroscopy is flexible in that the HMQ coherences can be excited from initial magnetization of any of the spin species, and that they can in turn be reconverted

to observable magnetization on any of the two participating nuclei. Two ways of making use of this freedom of choice are explored in this thesis. Firstly, a new class of experiments termed recoupled polarization-transfer (REPT) techniques is presented. These pulse sequences take direct advantage of the high initial polarization of ^1H (without an initial CP step), and ^{13}C is the observed spin. High-resolution 2D ^1H - ^{13}C shift correlation spectra can be obtained with these sequences, and an HMQ spinning-sideband analysis to obtain the involved heteronuclear dipolar coupling constants is proven to be feasible even for weak ^{13}C - ^1H couplings.

Different variants of the original HMQ technique are discussed, which probe different coherence states during t_1 , and it turns out that the t_1 evolution of a heteronuclear antiphase coherence, $\hat{I}_x\hat{S}_z$, is best-suited for shift correlation, while spinning-sidebands are most conveniently obtained by monitoring heteronuclear dipolar order, $\hat{I}_z\hat{S}_z$. It becomes clear that re-conversion rotor encoding, the mechanism responsible for the generation of the characteristic spinning sideband patterns, is not a mechanism specific for HMQ coherences, but applies for any coherence state present during t_1 , and merely reflects the rotor encoding of the interaction Hamiltonian.

An important implication of the theoretical treatment of REPT is that the excited HMQ modes are strictly limited to heteronuclear spin-pair coherences. This has influences on the appearance of the spinning-sideband patterns, in which the first-order sidebands are not reliable due to contributions from weak remote ^{13}C - ^1H couplings, and on spectra of globally ^{13}C enriched samples, in which correlations to remote protons may be absent because of dephasing effects of adjacent ^{13}C nuclei. The REPT technique is shown to be useful for spectral editing applications.

The investigation of the build-up of HMQ intensity as a function of the recoupling time in the REPT experiment is not a reliable method for the determination of dipolar couplings, which is explained by the dephasing of the spin-pair HMQ modes by heteronuclear couplings to remote protons. The HMQ build-up can, however, be of use in symmetric heteronuclear multiple-spin correlation techniques (DIP-HMSC), where an initial CP step is used to create ^{13}C magnetization, which evolves as the transverse component of the multi-spin coherences during both the excitation and reconversion periods. These sequences bear a strong similarity to the original REDOR, and absolute HMQ intensities, corrected for relaxation effects and less seriously affected by multi-spin couplings, are accessible with these techniques by means of a reference spectrum. DIP-HMSC experiments are very similar to REPT in that analogous

shift correlation and spinning-sideband experiments can be performed.

However, the most interesting new aspect of this class of experiments is the possibility of exciting multi-spin HMQ modes of the type $\hat{S}_x \prod_i \hat{I}_x^{(i)}$, where in the I-spin subspaces different coherence orders can be selected by a phase cycle. Heteronuclear spin counting of the I-spins was performed, and its characteristics are discussed in relation to the more familiar homonuclear spin counting experiments. Shift correlation and the generation of spinning sideband patterns were also realized using specifically selected ^1H coherence orders in t_1 .

Summing up the results from the experiments on ^{13}C - ^1H systems, it is concluded that

- In all the experiments conducted at very fast MAS ($\nu_R > 20$ kHz), the only significant influence of homonuclear couplings among the protons on the spectra was the residual linewidth in the shift correlation spectra. All other spectral features like absolute HMQ intensities and the appearance of the spinning-sideband patterns can be explained well in terms of heteronuclear couplings only, with the result of a straightforward analytical treatment of most of the observed phenomena in terms of a sum of isolated pair interactions.
- All ^{13}C - ^1H experiments discussed in this thesis are based on well-known concepts from solution-state NMR. These become applicable on account of the well-localized character of the heteronuclear dipolar couplings as a result of the successful suppression of homonuclear couplings by very-fast MAS.
- The REPT techniques are most efficient for standard applications in ^{13}C - ^1H shift correlation and spinning-sideband analysis. The feasibility of this approach is demonstrated by the application of these techniques to the investigation of structure and dynamics in as-synthesized complex discotic mesophases with ^{13}C in natural abundance.
- The multi-spin character of the multitude of coherences excited in the DIP-HMSC experiments holds promise for interesting applications in structural studies, with particular emphasis on the possible correlation of three spins (one ^{13}C and two ^1H) in heteronuclear shift correlation spectra of ^{13}C with the sum of the shifts of two nearby ^1H nuclei, and on the interesting characteristics of heteronuclear spin counting.

The concept of REDOR-like recoupling can also be used to perform MAS experiments in which ^{13}C shifts and ^2H quadrupolar wide-line spectra are correlated. An existing experiment is improved by introduction of a composite pulse on ^2H , leading to spectra free of phase distortions and an improved S/N. The technique was successfully applied to identify a yet unreported dynamical process of the H-bonds in the crystallites of atactic poly(vinyl alcohol).

The limit of this method, namely the very large quadrupolar interaction of most other spin $I > \frac{1}{2}$ quadrupolar nuclei, is overcome by performing relaxation-induced dipolar exchange with recoupling (RIDER), another technique closely related to REDOR, with which the heteronuclear dipolar coupling between ^{13}C and a quadrupolar nucleus can be determined *without irradiating* the second heterospin. The method takes advantage of the T_1 relaxation of the quadrupolar nucleus, and it is shown that apart from the dipolar coupling constant, information about higher-quantum relaxation processes of the quadrupolar spin can be assessed with this method.

Future work will concentrate on the application of the ^{13}C - ^1H correlation techniques to the study of motional processes and order phenomena, i.e. the measurement of residual dipolar couplings, in polymers above T_g . The results will benefit from the increased ^{13}C site-resolution as compared to homonuclear ^1H experiments, yielding information about possible differences in mobility and order parameters for segments of the polymer chain with different conformations and configurations, which can be differentiated by their ^{13}C shifts. In addition, more theoretical and experimental work needs to be devoted to the interplay of the recoupling process and molecular motions on the same timescale (the intermediate motional regime). Preliminary results indicate changes in the appearance of the spinning-sideband patterns and a subsequent breakdown in MQ excitation efficiency upon entering this regime, and more detailed knowledge is needed to appreciate the possibility of using the presented techniques for the assessment of dynamical information on this timescale.

Appendix

A Tensor Algebra

In this section, some of the most important relations establishing the connection between tensors in the Cartesian and irreducible spherical tensor representations are summarized. The transformation properties of these tensors upon rotation are also described.

For a three-dimensional vector operator $\hat{\mathbf{V}}$ (i.e. a tensor operator of rank 1), the irreducible spherical components are

$$\hat{V}_0 = \hat{V}_z, \quad (\text{A.1})$$

$$\hat{V}_{\pm 1} = \mp \frac{1}{\sqrt{2}} (\hat{V}_x \pm i\hat{V}_y) = \mp \hat{V}_{\pm}. \quad (\text{A.2})$$

The shift operators are thus proportional to the spherical vector operators. The spherical tensor operators of rank 2, $\hat{\mathbf{T}}$, are composed of products of the components of the vector operators which are parts of the bilinear Hamiltonian $\hat{H} = \hat{\mathbf{V}} \mathbf{A} \hat{\mathbf{U}}$. The components of $\hat{\mathbf{T}}$ are \hat{T}_{Lm} , where L and m are the rank and the order of the tensor component, respectively.

$$\hat{T}_{00} = \hat{\mathbf{V}} \hat{\mathbf{U}} = \hat{V}_x \hat{U}_x + \hat{V}_y \hat{U}_y + \hat{V}_z \hat{U}_z, \quad (\text{A.3})$$

$$\hat{T}_{10} = \frac{i}{\sqrt{2}} (\hat{V}_x \hat{U}_y - \hat{V}_y \hat{U}_x), \quad (\text{A.4})$$

$$\hat{T}_{1\pm 1} = -\frac{1}{2} [\hat{V}_z \hat{U}_x - \hat{V}_x \hat{U}_z \pm i(\hat{V}_z \hat{U}_y - \hat{V}_y \hat{U}_z)], \quad (\text{A.5})$$

$$\hat{T}_{20} = \frac{1}{\sqrt{6}} (2\hat{V}_z \hat{U}_z - \hat{V}_x \hat{U}_x - \hat{V}_y \hat{U}_y), \quad (\text{A.6})$$

$$\hat{T}_{2\pm 1} = \mp \frac{1}{2} [\hat{V}_x \hat{U}_z + \hat{V}_z \hat{U}_x \pm i(\hat{V}_y \hat{U}_z + \hat{V}_z \hat{U}_y)], \quad (\text{A.7})$$

$$\hat{T}_{2\pm 2} = \frac{1}{2} [\hat{V}_x \hat{U}_x - \hat{V}_y \hat{U}_y \pm i(\hat{V}_x \hat{U}_y + \hat{V}_y \hat{U}_x)]. \quad (\text{A.8})$$

For the interaction matrix $\underline{\mathbf{A}}$, the spherical components are found by carrying out the matrix multiplication, $\hat{\mathbf{V}}\underline{\mathbf{A}}\hat{\mathbf{U}}$, and sorting the different contributions according to the form of the interaction in the spherical representation, $\sum_L \sum_{m=-L}^L (-1)^m A_{Lm} \hat{T}_{L-m}$:

$$A_{00} = \frac{1}{3} \text{Tr} \{ \mathbf{A} \} = \frac{1}{3} (A_{xx} + A_{yy} + A_{zz}), \quad (\text{A.9})$$

$$A_{10} = -\frac{i}{\sqrt{2}} (A_{xy} - A_{yx}) \left\{ \stackrel{\text{PAS}}{=} -i\sqrt{2}A_{xy} \right\}, \quad (\text{A.10})$$

$$A_{1\pm 1} = -\frac{1}{2} [A_{zx} - A_{xz} \pm i(A_{zy} - A_{yz})] \left\{ \stackrel{\text{PAS}}{=} A_{xz} \pm iA_{yz} \right\}, \quad (\text{A.11})$$

$$A_{20} = \frac{1}{\sqrt{6}} (2A_{zz} - A_{xx} - A_{yy}) \left\{ \stackrel{\text{PAS}}{=} \sqrt{\frac{3}{2}}\delta \right\}, \quad (\text{A.12})$$

$$A_{2\pm 1} = \mp \frac{1}{2} [A_{xz} + A_{zx} \pm i(A_{yz} + A_{zy})] \left\{ \stackrel{\text{PAS}}{=} 0 \right\}, \quad (\text{A.13})$$

$$A_{2\pm 2} = \frac{1}{2} [A_{xx} - A_{yy} \pm i(A_{xy} + A_{yx})] \left\{ \stackrel{\text{PAS}}{=} -\frac{1}{2}\delta\eta \right\}. \quad (\text{A.14})$$

The last terms in curly brackets are for the tensor components in the principal axes system (PAS), with the anisotropy parameter, δ , and the asymmetry parameter, η , as for instance defined in Eq. (1.45).

Rotations in Cartesian space are calculated using the unitary transformation matrix $\underline{\tilde{\mathbf{R}}} = (\underline{\tilde{\mathbf{R}}}^{-1})^T$:

$$\underline{\tilde{\mathbf{R}}}(\Omega) = \begin{pmatrix} c\alpha \cdot c\beta \cdot c\gamma - s\alpha \cdot s\beta & s\alpha \cdot c\beta \cdot c\gamma + c\alpha \cdot s\gamma & -s\beta \cdot c\gamma \\ -c\alpha \cdot c\beta \cdot s\gamma - s\alpha \cdot c\gamma & -s\alpha \cdot c\beta \cdot s\gamma + c\alpha \cdot c\gamma & s\beta \cdot s\gamma \\ c\alpha \cdot s\beta & s\alpha \cdot s\beta & c\beta \end{pmatrix} \quad (\text{A.15})$$

$\Omega = (\alpha, \beta, \gamma)$ is the set of Euler angles, according to the convention of Rose [Rose 59]. Sines (*s*) and cosines (*c*) are abbreviated for clarity. Rotations of vectors \mathbf{a} and matrices $\underline{\mathbf{A}}$ from reference frame *X* to reference frame *Y* are of the form

$$\mathbf{a}^Y = \underline{\tilde{\mathbf{R}}}\mathbf{a}^X, \quad (\text{A.16})$$

$$\underline{\mathbf{A}}^Y = \underline{\tilde{\mathbf{R}}}\underline{\mathbf{A}}^X\underline{\tilde{\mathbf{R}}}^{-1}, \quad (\text{A.17})$$

which deviates from the classical definition of a unitary transformation, $\mathbf{R}^{-1}\underline{\mathbf{A}}\mathbf{R}$, because $\underline{\tilde{\mathbf{R}}}$ is a ‘‘pseudo-active’’ transformation matrix, and Eqs. (A.16) and (A.17) describe passive

Table A.1: Reduced Wigner rotation matrix elements $d_{m'm}^{(1)}$

m		1	0	-1
m'				
1		$\frac{1}{2}(1 + \cos \beta)$	$-\frac{1}{\sqrt{2}} \sin \beta$	$\frac{1}{2}(1 - \cos \beta)$
0		$\frac{1}{\sqrt{2}} \sin \beta$	$\cos \beta$	$-\frac{1}{\sqrt{2}} \sin \beta$
-1		$\frac{1}{2}(1 - \cos \beta)$	$\frac{1}{\sqrt{2}} \sin \beta$	$\frac{1}{2}(1 + \cos \beta)$

Table A.2: Reduced Wigner rotation matrix elements $d_{m'm}^{(2)}$

m		2	1	0	-1	-2
m'						
2		$\frac{1}{4}(1 + \cos \beta)^2$	$-\frac{1}{2}(1 + \cos \beta) \sin \beta$	$\sqrt{\frac{3}{8}} \sin^2 \beta$	$-\frac{1}{2}(1 - \cos \beta) \sin \beta$	$\frac{1}{4}(1 - \cos \beta)^2$
1		$\frac{1}{2}(1 + \cos \beta) \sin \beta$	$\cos^2 \beta - \frac{1}{2}(1 - \cos \beta)$	$-\sqrt{\frac{3}{8}} \sin 2\beta$	$\frac{1}{2}(1 + \cos \beta) - \cos^2 \beta$	$-\frac{1}{2}(1 - \cos \beta) \sin \beta$
0		$\sqrt{\frac{3}{8}} \sin^2 \beta$	$\sqrt{\frac{3}{8}} \sin 2\beta$	$\frac{1}{2}(3 \cos^2 \beta - 1)$	$-\sqrt{\frac{3}{8}} \sin 2\beta$	$\sqrt{\frac{3}{8}} \sin^2 \beta$
-1		$\frac{1}{2}(1 - \cos \beta) \sin \beta$	$\frac{1}{2}(1 + \cos \beta) - \cos^2 \beta$	$\sqrt{\frac{3}{8}} \sin 2\beta$	$\cos^2 \beta - \frac{1}{2}(1 - \cos \beta)$	$-\frac{1}{2}(1 + \cos \beta) \sin \beta$
-2		$\frac{1}{4}(1 - \cos \beta)^2$	$-\frac{1}{2}(1 - \cos \beta) \sin \beta$	$\sqrt{\frac{3}{8}} \sin^2 \beta$	$\frac{1}{2}(1 + \cos \beta) \sin \beta$	$\frac{1}{4}(1 + \cos \beta)^2$

rotations, as required by the definitions of Euler angles. In passive rotations, the basis of the coordinate system is transformed rather than the individual vector or matrix.

In the irreducible spherical representation, the rotation of a tensor yields a linear combination of components with the same rank L :

$$A_{Lm}^Y = \sum_{m'=-L}^L A_{Lm'}^X \mathcal{D}_{m'm}^{(L)}(\Omega), \quad (\text{A.18})$$

where the $\mathcal{D}_{m'm}^{(L)}(\Omega)$ are elements of the Wigner rotation matrices

$$\mathcal{D}_{m'm}^{(L)}(\alpha, \beta, \gamma) = d_{m'm}^{(L)}(\beta) e^{-im'\alpha} e^{-im\gamma}, \quad (\text{A.19})$$

with $d_{m'm}^{(L)}(\beta)$ as the reduced matrix elements. These are given in Table A.1 and A.2.

B Phenomenological Description of T_1 Relaxation for Spin-1 Nuclei

In order to derive the relaxation behavior of the operators \hat{L}_z and \hat{L}_z^2 for the case of $L = 1$, a connection has to be established between the classical picture of relaxing expectation values of magnetization and the quantum statistical picture as represented by the product operators. To this purpose, we employ the concept of polarization operators [Ernst 87]. In the energy basis, the matrix representation of each of these operators has one non-zero entry, on the diagonal, representing the population of the associated spin state. These operators are the longitudinal equivalents of the single-transition shift operators \hat{L}^+ and \hat{L}^- , which each describe a single complex off-diagonal (transverse) mode of coherence. The complete set of these operators forms a basis set for the representation of the density operator $\hat{\rho}$. A transformation into this representation is well-suited to describe relaxation, because these processes can generally connect any two matrix elements of $\hat{\rho}$. Mathematically, the simplicity of this description is due to the fact that the matrix representation of the relaxation superoperator \hat{K} in this basis (the so-called Redfield Matrix \mathbf{R}) has a block diagonal structure.

For a spin-1 system, one defines

$$\hat{L}^{[+1]} = \frac{1}{2} (\hat{L}_z^2 + \hat{L}_z), \quad (\text{B.1})$$

$$\hat{L}^{[0]} = \mathbf{1} - \hat{L}_z^2, \quad (\text{B.2})$$

$$\hat{L}^{[-1]} = \frac{1}{2} (\hat{L}_z^2 - \hat{L}_z). \quad (\text{B.3})$$

The \hat{L}_z and \hat{L}_z^2 operators can thus be written as linear combinations

$$\hat{L}_z = \sum_{m=-1}^{+1} p_{\hat{L}_z}^{(m)}(0) \hat{L}^{[m]}, \quad (\text{B.4})$$

$$\hat{L}_z^2 = \sum_{m=-1}^{+1} p_{\hat{L}_z^2}^{(m)}(0) \hat{L}^{[m]}, \quad (\text{B.5})$$

where \mathbf{p} are vectors with components of individual populations. These can be visualized as representing classical magnetizations associated with the three spin states. In the single-transition operator basis, the time-dependence upon relaxation is, as required within the Schrodinger picture, contained solely in the coefficients $p^{(m)}(t)$. Using the definitions of

the polarization operators (Eqs. (B.1)–(B.3)), we arrive at the desired representation of the z-operators in terms of populations:

$$\mathbf{p}_{\hat{L}_z}(0) = (+1 \ 0 \ -1)^T \quad (\text{B.6})$$

$$\mathbf{p}_{\hat{L}_z^2}(0) = (+1 \ 0 \ +1)^T \quad (\text{B.7})$$

Longitudinal relaxation leads to the randomization of the components of these vectors. Employing a phenomenological approach to describe T_1 relaxation, the time dependence of $\mathbf{p}(t)$ during relaxation is described by $\dot{\mathbf{p}} = \underline{\mathbf{K}}\mathbf{p}$, where $\underline{\mathbf{K}}$ is the exchange matrix characterizing the relaxation process [Naito 84]. For spin-1 relaxation,

$$\underline{\mathbf{K}} = \begin{pmatrix} -a-b & a & b \\ a & -2a & a \\ b & a & -a-b \end{pmatrix}. \quad (\text{B.8})$$

The coefficients $a = 1/T_1^{SQ}$ and $b = 1/T_1^{DQ}$ represent the single- and double-quantum relaxation rates, respectively [Naito 84]. The solution,

$$\mathbf{p}(t) = e^{\underline{\mathbf{K}}t} \mathbf{p}(0), \quad (\text{B.9})$$

can be obtained by diagonalization of the $\underline{\mathbf{K}}$ -matrix. The matrix representation of $\exp\{\underline{\mathbf{K}}t\}$ is given in [Naito 84], and is reproduced here for convenience.

$$e^{\underline{\mathbf{K}}t} = \frac{1}{6} \begin{pmatrix} 2 + e^{-3at} + 3e^{-at-2bt} & 2 - 2e^{-3at} & 2 + e^{-3at} - 3e^{-at-2bt} \\ 2 - 2e^{-3at} & 2 + 4e^{-3at} & 2 - 2e^{-3at} \\ 2 + e^{-3at} - 3e^{-at-2bt} & 2 - 2e^{-3at} & 2 + e^{-3at} + 3e^{-at-2bt} \end{pmatrix} \quad (\text{B.10})$$

Evaluating the t -dependence of the polarization vectors, and using $\mathbf{p}_{\parallel} = (+1 \ +1 \ +1)^T$, the “time dependence” of the z-operators according to Eqs. (B.4) and (B.5) is calculated to be

$$\hat{L}_z \xrightarrow{\underline{\mathbf{K}}t} \hat{L}_z e^{-(a+2b)t}, \quad (\text{B.11})$$

$$\hat{L}_z^2 \xrightarrow{\underline{\mathbf{K}}t} \frac{2}{3} \mathbb{1} - \left(\frac{2}{3} \mathbb{1} - \hat{L}_z^2\right) e^{-3at}. \quad (\text{B.12})$$

These relations are to be understood in the same sense as in product operator theory, where the arrow is a shorthand notation to describe the time evolution in terms of the application of a unitary transformation superoperator as derived from the Liouville-von Neumann equation. Here, however, the time evolution under longitudinal relaxation is not described by a unitary transformation, as is clear from the non-conservation of the trace. Also, these relations only hold in the case of pure relaxation, with time evolution due to internal Hamiltonians of the system being excluded.

The treatment presented here can directly be extended to spins with $L > 1$, although the amount of algebra involved in solving $\exp\{\underline{\mathbf{K}}t\}$ may then call for some approximations, such as neglecting higher-quantum relaxation rates. It is interesting to note that the longitudinal relaxation time, measured as the decay time constant of z -magnetization (Eq. (B.11)), is equal to the single-quantum longitudinal relaxation time only in the case of insignificant double-quantum relaxation. Otherwise, an apparent $T_1^{app} = T_1^{SQ}T_1^{DQ}/(T_1^{DQ} + 2T_1^{SQ})$ is observed.

C Numerical Procedures

C.1 Powder Averaging

Two kinds of numerical methods were employed in this thesis. Firstly, powder-averages of the analytical solutions for the time-domain signals presented in the body of this work have to be performed:

$$\langle S(t) \rangle = \frac{1}{8\pi^2} \int_0^{2\pi} d\alpha \int_0^\pi \sin\beta d\beta \int_0^{2\pi} d\gamma S(t, \alpha, \beta, \gamma) \quad (\text{C.1})$$

The integrals can, in most cases, not be performed analytically, such that numerical solutions must be used. In the majority of the formulae, the information about the spin system enters in terms of *phases* acquired under the action of the respective coupling tensors, where the expressions for these depend explicitly on the experiment time, as a result of the MAS. Eqs. (1.74) and (1.80) are applicable as long as only a single interaction tensor is considered, or if different tensors share the same PAS. Then, the solution can be calculated by specifying different values for (α, β, γ) , which represent the common orientations of the tensors in the

powder sample. The γ angle is the initial rotor phase, and enters only for MAS experiments, whereas for static spectra, only averaging over (α, β) , which can be interpreted as polar coordinates, is needed. Note that the signals obtained from density matrix simulations are subject to powder averaging following the same principles.

Numerous approaches exist for carrying out the powder-averaging integral numerically, the most straightforward of which are certainly (i) to increment the three angles linearly in three nested loops or (ii) to use numerous random angles (Monte-Carlo integration). Convergence is, however, hard to achieve with these methods, and the most common improved algorithms for the calculation of (α, β) pairs are compared in a very instructive paper by Bak and Nielsen [Bak 96]. In the same publication, a novel method for the calculation of angles (REPULSION) is presented, which is based on the minimization of a hypothetical repulsive potential energy between a given number of points on a sphere, which are represented by their polar coordinates. The (α, β) -lists obtained with this method perform very well for MAS spectra, and this approach was used throughout this thesis. Each FID obtained for a single orientation is to be weighted by the relative area assigned to the point on the sphere, and for a well-converged list, this value should be close to 1.

The number of powder-average points needed for approximate convergence is adjusted according to the symmetry of the spin system:

- For MAS, γ is generally incremented in a linear fashion, with an *odd* number of angles $0 \leq \gamma < 2\pi$. This is important, since many time-domain signals are invariant for $\gamma \rightarrow \gamma + \pi$, and this condition would be fulfilled for half of the values if γ were even, resulting in a waste of calculation time. 21 γ -steps were the usual choice for dipolar-coupled systems, while in quadrupolar systems (with internal interaction frequencies exceeding 100 kHz) a considerably higher number on the order of 51–61 steps can be necessary.
- For rotational symmetry around the z-axis of the spin system, $\alpha = 0$ and a linearly incremented list with $0 \leq \beta < \frac{\pi}{2}$, with each FID weighted by $\sin \beta$, is sufficient.
- For mirror symmetry with respect to the x/z-plane, an even distribution of (α, β) over the half sphere, $(0 \leq \alpha < \pi, 0 \leq \beta < \pi)$ is sufficient. The list is obtained by using the REPULSION algorithm for the full sphere, and dividing α by 2. For most MAS experiments, a list with 96 angles over the half sphere was sufficient.

- For the general case of a full sphere, REPULSION lists with 212 and 384 (α, β) -pairs were used, and convergence was always checked with larger lists.

C.2 Multiple Tensors

If multiple couplings or different relative orientations of tensor are to be described, these relative orientations have to be specified, and expressions have to be derived to include the transformations from the PASs to the common crystal coordinate system. This can result in a large amount of messy algebra, and a more general approach was pursued here, which can be easily implemented in a computer program.

If the coordinates of the individual spins are known (they can be obtained from crystal structure data), the components of the dipolar interaction tensor in the Cartesian representation can be calculated using Eq. (1.49). The second-order irreducible spherical components are then obtained with Eqs. (A.12)–(A.14). These components form the representation in the crystal frame, $\mathbf{A}_2^{D,C}$. The powder averaging enters at this point; it is performed as Euler rotation described by Eq. (A.18). The result is the rotor frame representation, $\mathbf{A}_2^{D,R}$, in the case of MAS, or already the laboratory frame representation, $\mathbf{A}_2^{D,LAB}$, for static spectra. The $A_{20}^{D,L}$ -component is the prefactor needed for the interaction Hamiltonian (Eq. (1.41)).

CSA and quadrupolar tensors are most conveniently specified by their principal values, and a set of 3 Euler angles describing the orientation of this tensor relative to the coordinate system in which the individual spins are specified. Eqs. (A.12)–(A.14) give a prescription of how to obtain the spherical components in the PAS, and a rotation using the 3 given angles (Eq. (A.18)) yields $\mathbf{A}_2^{\lambda,R}$ (or $\mathbf{A}_2^{\lambda,LAB}$ for static spectra).

Finally, in the case of MAS, another Euler rotation using Eq. (1.70) is used to transform $\mathbf{A}_2^{\lambda,R}$ into $\mathbf{A}_2^{\lambda,L}$, which gives the $A_{20}^{\lambda,L}$ -component for any given experiment time (i.e., rotor position). This is what is done for numerical density matrix simulations. Analytical expressions in turn depend on an integrated phase (Eq. (1.82)), which appears as the argument of the trigonometric functions in the time-evolution formulae, and is also the prefactor in the average MAS Hamiltonian (Eq. (1.69)). The integration of Eq. (1.70) over a specific interval $[t_1, t_2]$ can be performed analytically, and the solution can directly be implemented in the computer

program:

$$\begin{aligned} \int_{t_1}^{t_2} A_{20}^{\lambda, LAB}(t) dt &= \int_{t_1}^{t_2} \sum_{m=-2}^2 A_{2-m}^{\lambda, R} e^{im\omega_R t} d_{-m0}^{(2)}(\beta_M) dt \\ &= \sum_{m=-2}^2 \frac{1}{im\omega_R} A_{2-m}^{\lambda, R} [e^{im\omega_R t_2} - e^{im\omega_R t_1}] d_{-m0}^{(2)}(\beta_M) \end{aligned} \quad (\text{C.2})$$

This represents the central part of the computer program used to calculate all the multi-spin spectra in the body of this work. The sums over the individual spins in time-evolution formulae for multi-spin systems (e.g. Eqs. (4.7)–(4.10)) can be conveniently implemented in loop structures of such a program.

C.3 Density Matrix Simulations

The second numerical method used is the direct integration of the quantum-mechanical master equation (Eq. (1.4)) from first principles. This approach, based on the subdivision of the time integral into finite steps, was already alluded to in Section 1.1.1. In the course of this work, a C++ computer program was developed which performs this numerical integration.

The basic time evolution formula for a propagation over a finite step reads

$$\hat{\rho}(t + \Delta t) = \hat{U}(t, \Delta t) \hat{\rho}(t) \hat{U}^{-1}(t, \Delta t). \quad (\text{C.3})$$

Δt is the central simulation parameter; its length determines the accuracy of the approximation if the Hamiltonian in the propagator is explicitly time-dependent. In general, it should be at least one order of magnitude smaller than the largest time dependence imposed by an interaction in the system (which could be the modulation of the space-parts by the MAS). For most of the simulations in this thesis, 1–2 μs were sufficient for well-converged results. Only for the simulations of quadrupolar time evolution in Chapter 5 was necessary to simulate in 100 ns steps. In the program, the spin system is represented in the product basis. It was shown in the theoretical section that all possible states of $\hat{\rho}$ and the operators describing the internal interactions can be represented by angular momentum operators, the product basis representation of which can be derived from the the spin- $\frac{1}{2}$ PAULI matrices by outer matrix

multiplication (Eq. (1.15)). The whole simulation procedure thus boils down to performing matrix multiplications, which follow the general formulae given in Chapter 1.

The propagator can be approximated by a series expansion,

$$\hat{U}(t, \Delta t) = e^{-i\hat{H}(t)\Delta t} \approx 1 + i\hat{H}(t)\Delta t + \frac{1}{2}\hat{H}(t)^2\Delta t^2 + \dots \quad (\text{C.4})$$

This is, in terms of calculation time, certainly not the most efficient of approximation of the propagator, but it is very easy to implement. The C++ program used is based on an older FORTRAN program written by I. Schnell, who found that the above expansion worked at least more efficiently than common diagonalization routines, which can also be used to obtain the exponential of a matrix. The Taylor expansion was truncated when the Euclidian norm of the propagator did not change any more by a specified amount upon adding another order.

The Hamiltonian of the system at a given time t , $\hat{H}(t)$, is the sum of all internal interactions to be considered, plus an additional rf-term describing the action of a pulse, which could be present at a specific time t . This corresponds to the most general approach of simulating finite pulses. Calculations in the δ -pulse limit are performed much more efficiently by treating the pulses as rotations in spin space, e.g. $\hat{\rho}_+ = e^{-i\frac{\pi}{2}\hat{I}_x}\hat{\rho}_-e^{i\frac{\pi}{2}\hat{I}_x}$ for the application of a 90_x° -pulse. The propagators for the set of pulses needed in the sequence can be calculated prior to the calculation of the actual pulse sequence, and, much more importantly, prior to entering the powder-average loop. A pulse is then just a simple bilinear matrix multiplication in the course of the sequence.

The program used here was generalized for spin systems of arbitrary size³ by including dynamic memory allocation. The angular momentum operators are constructed at run-time using appropriate algorithms, which allocate matrices of the proper dimension and calculate the spin operators following the form of the Hamiltonians specified in Section 1.3. The coupling parameters are calculated from the input parameters following the procedure outlined in the preceding section.

Many more topics could be discussed concerning the efficiency of the simulation, for example the re-use of propagators over cyclic parts of the pulse sequence (which corresponds

³Since the dimension of the product operator space for N spins is $\prod_i^N (2I_i + 1)$, simulations in product space, i.e. without more efficient symmetry-adapted representations of the Hamiltonians and the density matrix, are feasible only for up to about 8 spins- $\frac{1}{2}$ nuclei.

to the numerical evaluation of the propagator of the average Hamiltonian), and time-saving tricks for the simulation of (reduced) 2D spectra. The latter is the case for almost all simulations shown in the preceding chapters, where only the amplitude-modulation of the first point in the direct dimension was needed to obtain the t_1 time-domain data. A recent publication [Hodgkinson 00] gives a concise overview of the important issues relevant to the efficient simulation of solid-state NMR spectra.

C.4 Transformation of Time-domain Data

The programming environment PV-WAVE was used to perform the processing (apodization, zero-filling, phasing) of the time-domain data obtained from the numerical calculations (and experiments). Various routines, written by different people during the last decade, were used. Special emphasis is devoted to the GINA.lib (graphics interface for NMR academics), written by J. Paff. The package contains a number of very useful tools for processing and visualization of 1D and 2D NMR data.

D Description of the Sample Substances

D.1 L-Alanine

Natural-abundance L-alanine was purchased from Aldrich, the uniformly labeled sample used in Chapter 4 was bought from Isotec. A part of the crystal structure is depicted in the figure below. The shown crystal structure is based on a neutron diffraction study [Lehmann 72]. The elementary cell is orthorhombic, with the space group symmetry $P2_12_12_1$. The DIAMOND software [Bergerhoff 95] was used for the visualization of this structure and all other molecules and fragments in this thesis.

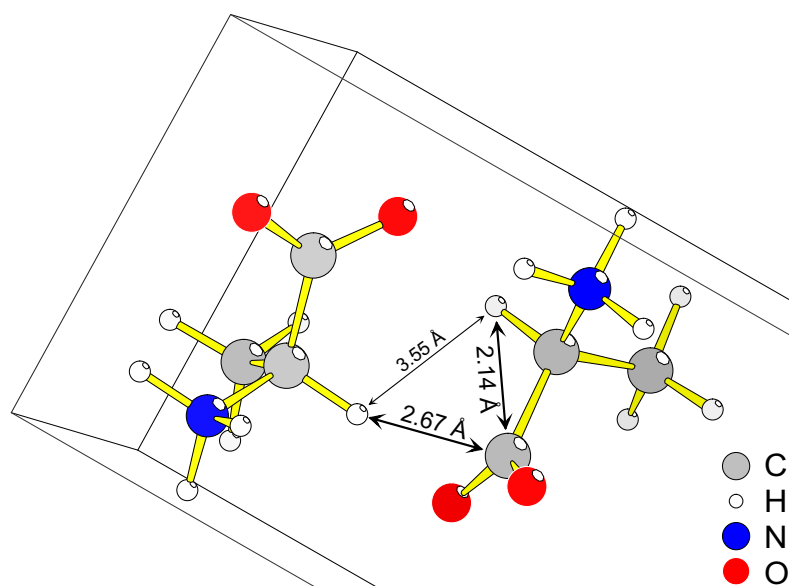


Figure D.1: Part of the crystal structure of L-alanine, showing two molecules and the closest inter- and intramolecular distances of the two CH protons and the CO carbon.

D.2 L-Tyrosine·HCl

The hydrochloride rather than pure L-tyrosine was used because of the more favorable T_1 relaxation time of the former. It was prepared by dissolving L-tyrosine (Aldrich) in dilute HCl,

and subsequent evaporation of the solvent. The procedure was repeated twice. The crystal structure data is taken from a neutron study [Frey 73]. The elementary cell is monoclinic, with the space group $P2_1$.

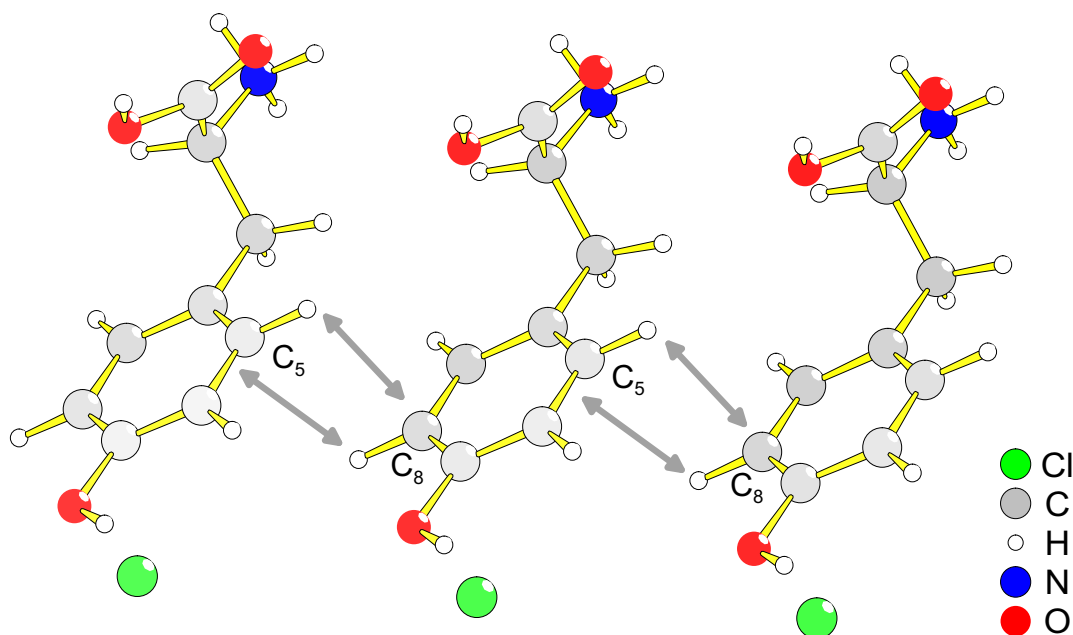


Figure D.2: Part of the crystal structure of L-tyrosine·HCl. The aromatic C_5 and C_8 positions are identified. The protons attached to these carbons experience an up-field shift, as is apparent in the correlation spectra shown on p. 64, due to ring current effects from the benzene rings in the adjacent molecules.

D.3 Ammonium Formate

Ammonium formate is well suited to study the influence of remote protons on a relatively well-isolated CH spin pair, and has the added benefit of a short T_1 . The remote protons in the ammonium groups can easily be removed by deuteration in order to obtain a reference compound.

Deuteration was performed by dissolving ammonium formate (Aldrich) in D_2O , gently heating to about $80^\circ C$, and evaporating the D_2O at this temperature under reduced pressure.

This procedure was repeated twice. The crystals were then immediately dried in an oil pump vacuum for about 20 min. Long exposure to vacuum must be avoided because of loss of the formate due to its high vapor pressure. Ammonium formate is highly hygroscopic, and thus the rotor was filled in a glove box to avoid re-exchange of water protons. The degree of deuteration is estimated to be about 95%. The T_1 relaxation times of these formates are strongly dependent on the degree of deuteration, such that recycle times were 0.5 and 5 s for the undeuterated and the deuterated compound, respectively.

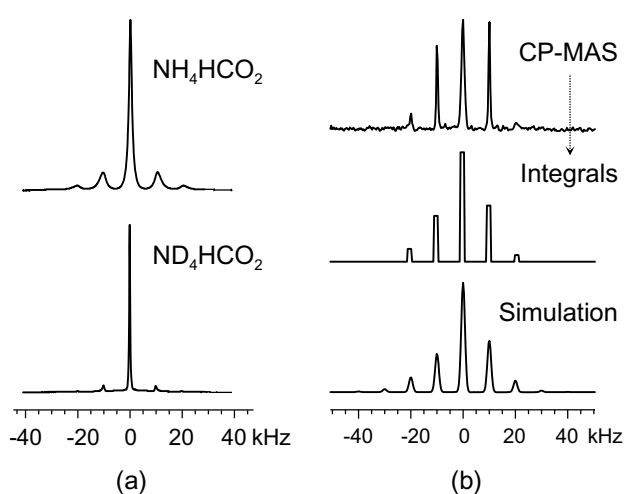


Figure D.3: ^1H SQ MAS spectra (a), and a ^{13}C CP MAS spectrum (b), along with integrals and a simulation. The spectra were obtained at 10 kHz MAS.

Therefore, the integrals of the peaks are compared with intensities from a simulation performed within the two-spin approximation including CSA. A CH-distance of 1.1 Å gave the best fit to the experimental spectrum, justifying the use of this compound as a model for a rigid spin pair.

A graphical representation of the crystal structure, as determined by X-ray diffraction [Nahringbauer 68], is given in Fig. D.4. The unit cell is monoclinic, with the space group Pc .

The samples were characterized using ^1H and ^{13}C -CP MAS spectra. In Fig. D.3a, the successful suppression of homonuclear dipolar ^1H - ^1H interactions upon deuteration is illustrated by the almost complete disappearance of dipolar spinning sidebands and the marked line narrowing. The good isolation of the CH spin pair allowed to measure a heteronuclear SQ dipolar spinning-sideband pattern of ^{13}C by simply omitting continuous wave dipolar decoupling during the acquisition interval in a CP MAS experiment (Fig. D.3b). Due to reasons not completely understood, the linewidths were different for different sideband orders.

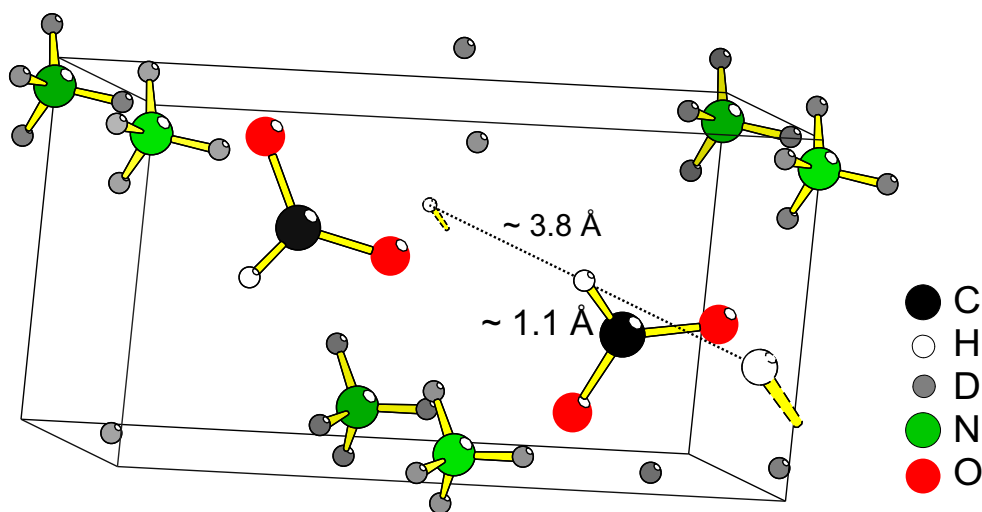


Figure D.4: One elementary cell of ammonium formate. The closest intermolecular distance between to CH-moieties is indicated.

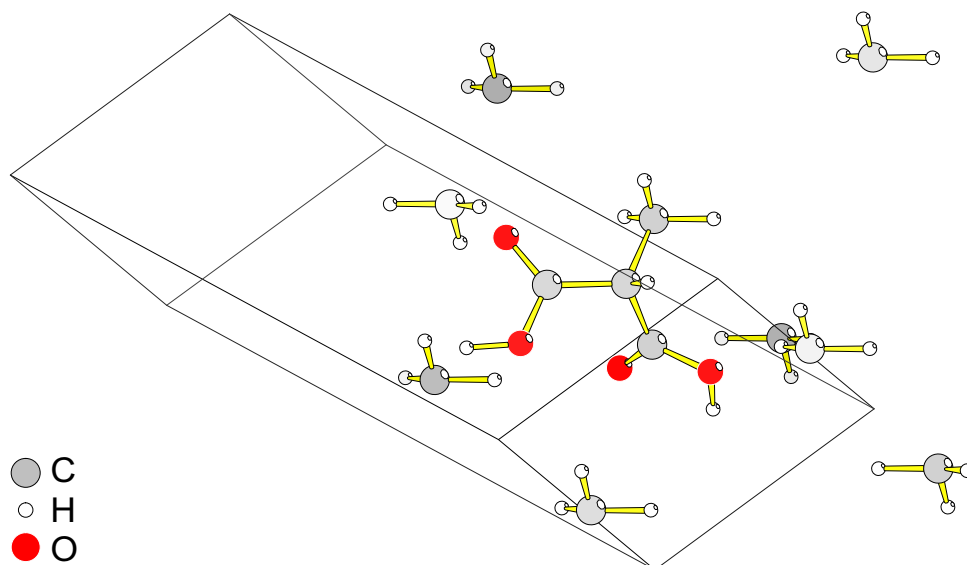


Figure D.5: Part of the crystal structure of methylmalonic acid. One molecule is depicted, along with the 8 closest methyl groups from surrounding molecules.

D.4 Methylmalonic Acid

Three different samples of methylmalonic acid were used in this thesis. Natural-abundance methylmalonic acid was bought from Aldrich, while the sample deuterated at the methyl group (>98% D), which was used for the RIDER measurements in Chapter 6, was purchased from C/D/N Isotopes. Owing to the favorable relaxation behavior of the methyl protons, the recycle time was 1 s for the former sample, whereas for the latter, transients were repeated every 30 s.

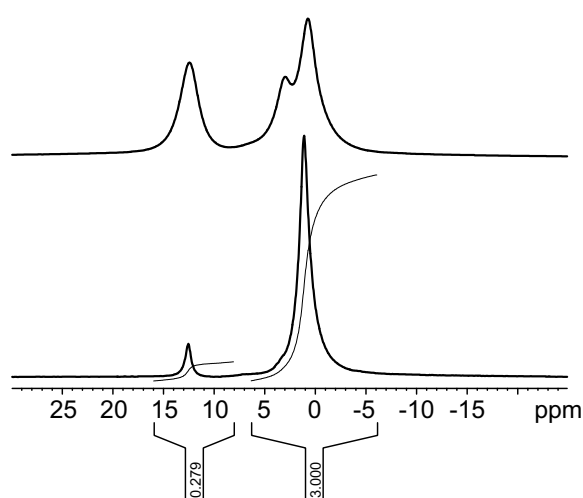


Figure D.6: ^1H SQ MAS spectra of partially deuterated and natural-abundance methylmalonic acid (25 kHz MAS).

The degree of CH/COOH deuteration was determined with ^1H SQ MAS NMR spectra (Fig. D.6). By comparison of the integrals shown in the figure, an amount of 12%(mol) of residual protons in the CH and COOH-sites was obtained.

The crystal structure shown in Fig. D.5 is based on an X-ray study [Derissen 70], in which the protons are relatively poorly located. This is the reason why, for the simulations considering the local intra- CH_3 environment, the methyl group geometry was taken from the L-alanine neutron study (Section D.1), where a more reasonable, approximately tetrahedral symmetry is exhibited.

A third sample, used for the studies of relatively well-isolated CH_3 -groups, is the “partially deuterated” sample. Methylmalonic acid is CH-acidic, which means that also the CH proton can easily be exchanged by dissolution in D_2O . The result is a sample which is in some sense the complement of the CD_3 sample. Measurements on methyl groups can be performed by ^{13}C - ^1H in the former and by ^{13}C - ^2H spectroscopy in the latter case. The sample was obtained by dissolving twice in D_2O , following essentially the same procedure and taking the precautions described in the preceding section for ammonium formate, since the sample is also hygroscopic and

decomposes easily at elevated temperature under vacuum.

D.5 Poly(vinyl alcohol)

Atactic poly(vinyl alcohol) ($M_w = 30.000 - 50.000$ g/mol) was purchased from Aldrich. The OH-deuterated compound was prepared by dissolving twice in D_2O at about $80^\circ C$ with a magnetic stirrer, and subsequent complete removal of the solvent under vacuum from the same flask.

The H_2O - and D_2O -swollen samples were prepared following the same procedure. Protonated and deuterated aPVA, respectively, were dissolved a further time, and the water was again removed under vacuum, until the solution was viscous enough to form a thin film on the inside of the flask. The film was carefully dried using a heat gun until it was completely solidified. The flask was then opened, transferred to an oven, and the film was annealed at 100° , again under vacuum, for 10 minutes.

The water content of the H_2O -swollen sample was estimated using solution-state 1H NMR spectra (Fig. D.7). The signal at 2.5 ppm is the solvent, and by shaking with D_2O , the OH-signals (centered around 4.5 ppm, with an interesting fine-structure due to the formation of hydrogen bonds) and the water peak (3.35–3.55 ppm) could be identified. From the integrals, the water content of the swollen sample was calculated to be 10.7 ± 1.0 % w/w.

The hydrated PVA film was soft and malleable, and could easily be transferred into the MAS rotors, which were stored in a desiccator while not in use to prevent re-absorption of moisture. Even though the used MAS rotors were not 100% airtight, the effects of re-absorption of water and 2H - 1H back-exchange on the spectra are assumed to be weak.

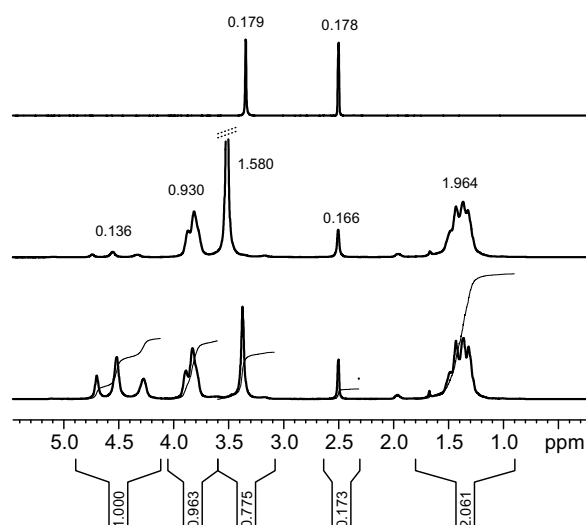


Figure D.7: 1H solution-state NMR spectra (equal numbers of scans) of the swollen aPVA sample in $DMSO-d_6$ (bottom), after shaking with D_2O (middle), and pure solvent (top slice).

E Experimental Details

E.1 Instrumentation

The NMR experiments were carried out on digital BRUKER Avance-type instruments, with B_0 -fields corresponding to ^1H resonance frequencies of 300.23 MHz (DSX300, 7 T wide bore magnet) and 700.13 MHz (DRX700, 16.4 T narrow bore magnet). Commercial 2.5 mm MAS double-resonance probes, also manufactured by BRUKER, were used for the experiments described in Chapters 3 and 4. Spinning speeds typically ranged from 15 kHz (CP MAS) to 25–30 kHz (REPT- and DIP-HMQC experiments). 90° -pulse lengths were usually $2\ \mu\text{s}$ on both channels, corresponding to $\omega_1/2\pi = 125\ \text{kHz}$, with the same field strength for the dipolar decoupling. In all experiments, TPPM dipolar decoupling [Bennett 95] was employed, using approximate 160° -pulses and a phase-modulation angle of 30° .

For the 2.5 mm MAS probeheads, the bearing gas pressure is typically 3–4 bar. At such high pressures, air friction due to the rapid air flow leads to an increase of the temperature inside the rotors. These effects have been quantified [Langer 99], and all temperatures given in Section 7.1 were corrected accordingly.

The experiments in Chapters 5, 6, and Section 7.2, were performed in the laboratory of Prof. Klaus Schmidt-Rohr at the Polymer Science and Engineering Dept, Univ. of Massachusetts, Amherst, USA. The spectrometer was also a DSX300, equipped with triple-resonance facilities. BRUKER 7 mm double- and 4 mm triple-resonance MAS probeheads were used, with spinning speeds ranging from 4 to 7 and 5 to 10 kHz, respectively. The 7 mm probe was much more sensitive in common ^{13}C - ^1H double-resonance experiments, and was used in all cases where the third (^2H) channel was not needed. Typical 90° -pulse lengths were $3\ \mu\text{s}$ for ^1H and ^{13}C , and about $3.7\ \mu\text{s}$ for ^2H , with considerable variation depending on the performance of the high-power tube amplifier.

Supporting solution-state NMR spectra were from different 500 MHz BRUKER instruments, the X-ray and DSC measurements presented in Section 7.1 were performed by M. Harbison and A. Fechtenkötter in the research group of Prof. Müllen, also at the MPI for Polymer Research.

E.2 REPT Experiments

The phase cycle is the same for all different REPT-techniques described in Chapter 3; the variants differ only in the placement of the t_1 -period. The phases are listed in Table E.1, and the individual phases are assigned to the pulses in Fig. 3.1, p. 62. The phase-cycling of the central refocusing π -pulses during the recoupling period (ϕ_6 and ϕ_7) proved necessary to remove artifacts from imperfect pulses. The phases for the recoupling π -pulse trains were kept constant for consecutive transients and cycled relative to each other according to the (xy-4) scheme [Gullion 90].

Table E.1: Phase cycle for the REPT pulse sequences.

ϕ_1	$x \bar{x} y \bar{y} \bar{x} x \bar{y} y \bar{x} x \bar{y} y x \bar{x} y \bar{y}$
ϕ_2	$y \bar{y} \bar{x} x \bar{y} y x \bar{x}$
ϕ_3	$y y \bar{x} \bar{x} \bar{y} \bar{y} x x$
ϕ_4	$\bar{x} \bar{x} \bar{y} \bar{y} x x y y$
ϕ_5	$x x y y \bar{x} \bar{x} \bar{y} \bar{y} \bar{x} \bar{x} \bar{y} \bar{y} x x y y$
ϕ_6	$y \bar{y} \bar{x} x \bar{y} y x \bar{x}$
ϕ_7	$\bar{x} x \bar{y} y x \bar{x} y \bar{y}$
ϕ_{rec}	$y y \bar{x} \bar{x} \bar{y} \bar{y} x x$

To achieve sign-sensitive detection in t_1 , the TPPI method [Schmidt-Rohr 94] was implemented by incrementing the phase of the reconversion pulse ϕ_3 by 90° for subsequent slices in t_1 .

E.3 DIP-HMSC Experiments

The phase cycles for the DIP-HMSC experiments are listed in Table E.2, with the assignment of the phases to be taken from Fig. 4.1, p. 104. The sign-sensitive detection for the DIP-HMQC and -HSQC experiments was achieved by using the STATES-TPPI method, i.e., the ^1H -MQ reconversion pulse (ϕ_5) is incremented upon advancing to the next slice, while t_1 is incremented only for every other slice. For the higher-order MQ filters, this phase increment

is $360^\circ/n$, where n is the number of subdivisions of the phase list in the table. Note that the phases were not cycled through a full CYCLOPS to suppress quadrature artifacts, in order to keep the minimum number of scans for a complete phase cycle small. This is possible on modern digital spectrometers without sacrifices in the quality of the spectra.

At very fast MAS, conventional CP proved inefficient, and a ramped CP [Metz 94] was used. Usually, a ramp with 4096 steps was applied on the ^1H channel, ranging from 90–110% of the proton B_1 -field used for a 90° pulse, which defined the B_1 -field for the Hartmann-Hahn match. The ^{13}C B_1 -field was centered on the (-1) matching sideband, i.e. $\omega_1^{13\text{C}} = \omega_1^{1\text{H}} - \omega_R$. The duration of the ramp was optimized for maximum signal, and ranged between 2 and 6 ms.

Table E.2: Phase cycle for the DIP-HMSC pulse sequences. The phases ϕ_4 and ϕ_5 (for the ^1H -MQ excitation and reconversion pulses, respectively) are specified as numbers, which have to be multiplied by $360^\circ/n$, where (n) is the number preceding the list, in order to obtain their phase. Phases in curly brackets are to be repeated. x corresponds to a 0° -phase, y to 90° , etc... The number of scans has to be an integer multiple of 32, 64 and 96 for the HMQ, ^1H -DQ and ^1H -TQ-filtered variants, respectively.

	DIP-HMQC		DIP-HSQC/HDOR	
	HMQ-filtered		^1H -DQF	^1H -TQF
ϕ_1	$x \bar{x}$			
ϕ_2	y			
ϕ_3	$x x \bar{x} \bar{x}$			
ϕ_4	(4) {1}×16 {3}×16		(8) {2}×32 {6}×32	(12) {3}×48 {9}×48
ϕ_5	(4) {1}×8 {3}×8 {3}×8 {1}×8		(8) {2}×8 {6}×8 {0}×8 {4}×8 {6}×8 {2}×8 {4}×8 {0}×8	(12) {3}×8 {7}×8 {11}×8 {9}×8 {5}×8 {1}×8 {9}×8 {1}×8 {5}×8 {3}×8 {11}×8 {7}×8
ϕ_6	$x \bar{x} \bar{x} x y \bar{y} \bar{y} y$	$x \bar{x} \bar{x} x \bar{x} x x \bar{x}$	$y \bar{y} \bar{y} y \bar{y} y y \bar{y}$	$x \bar{x} \bar{x} x \bar{x} x x \bar{x}$
ϕ_7	—	$x \bar{x} \bar{x} x$	$y \bar{y} \bar{y} y$	$x \bar{x} \bar{x} x$
ϕ_8	$\bar{y} \bar{y} y y$			
ϕ_9	$y y \bar{y} \bar{y}$			
ϕ_{10}	$x \bar{x} \bar{x} x$			
ϕ_{rec}	$x \bar{x} \bar{x} x \bar{x} x x \bar{x}$ $\bar{x} x x \bar{x} x \bar{x} \bar{x} x$		{ $x \bar{x} \bar{x} x \bar{x} x x \bar{x}$ }×2 { $\bar{x} x x \bar{x} x \bar{x} \bar{x} x$ }×2	{ $x \bar{x} \bar{x} x \bar{x} x x \bar{x}$ }×3 { $\bar{x} x x \bar{x} x \bar{x} \bar{x} x$ }×3

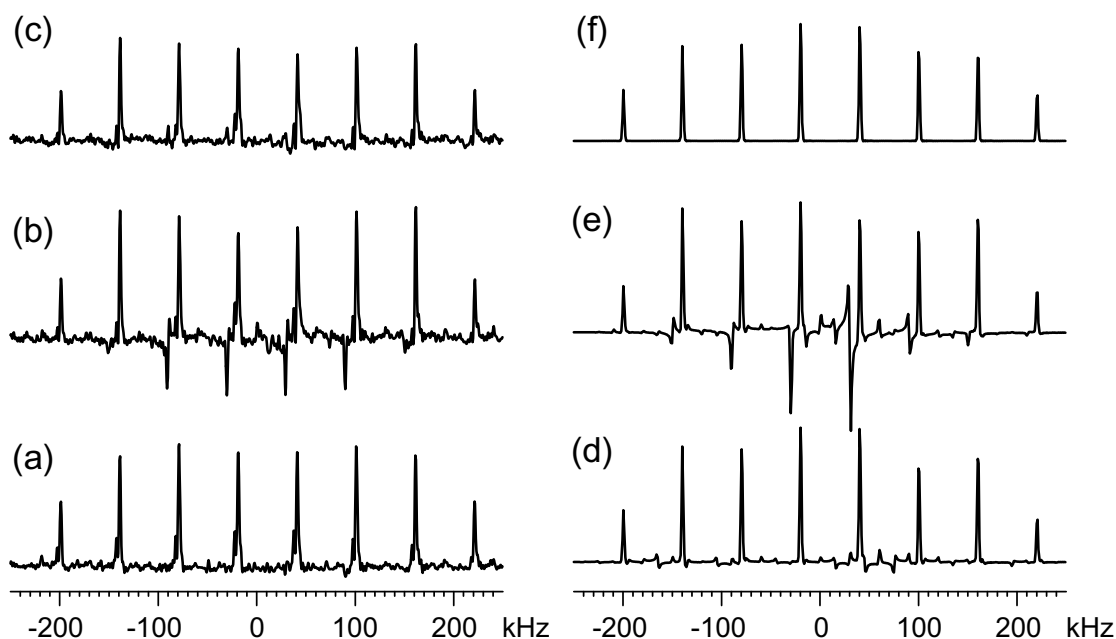


Figure E.1: Investigation of artifacts due to imperfect recoupling π -pulses in experimental (a–c) and simulated (d–f) DIP-HSQC spectra, obtained at 30 kHz MAS and $\tau_{rcpl} = 4 \tau_R$. The experimental spectra are from the CH-signal in $U\text{-}^{13}\text{C}$ L-alanine, while the density matrix simulations were performed for a single CH pair with $r_{CH} = 1.14 \text{ \AA}$ and a proton offset of 10 kHz. Spectrum (a) was acquired with 180° inversion pulses and the regular (xy-4) phase cycling in the trains, in (b) and (c), approximate 205° flip angles were used, where in (c) an improved phase cycling was applied. The simulations (d) and (e) were performed with finite ($4 \mu\text{s}$) pulses and flip angles corresponding to the experiments on the left. (f) is a from a simulation assuming δ -pulses.

It turned out that for moderate recoupling times ($4\text{--}6 \tau_R$), the phase cycling of the recoupling π -pulse trains according to the (xy-4) scheme was not effective enough to remove all artifacts in MQ spinning sideband spectra when the pulses were imperfect. Usually, pulse lengths can be determined precisely enough for this problem not to arise. The problem was, however, explored in more detail, because it is believed to be a general problem for the REPT and DIP techniques.

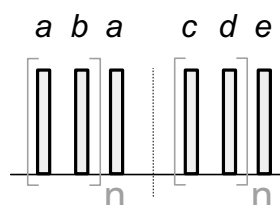
Artifacts can be seen in Fig. E.1b. The sideband pattern was acquired using an offset on the ^1H channel. It is thus shifted from the spectral center by this offset, while the artifact shows up at positions $\pm n\omega_R/2\pi$, with n being odd. It may be called a zero-frequency artifact, but it is rotor-encoded and thus appears as sidebands. A similar artifact was reported to be

presented in the earliest papers of our group on heteronuclear DQ spectroscopy [Sommer 95], where a synchronously applied BABA sequence was used, and was also observed for REPT patterns in some cases.

As mentioned, (xy-4) phase cycling usually compensates for pulse imperfections. The shown artifacts did not arise for significantly longer recoupling times, such that it is attributed to an insufficient compensation when there are too few cycles. All these observations could be supported by density matrix simulations (Fig. E.1d–f), where similar artifacts could be obtained when the flip-angles of the π -pulses were not correct. The simulated artifacts cannot be expected to match the experimental ones perfectly, since only a 2-step HMQ-selection phase cycle was simulated.⁴ This is also the reason for the weak asymmetric baseline artifacts in Fig. E.1d.

Table E.3: Improved (xy-4) phase cycling for the recoupling π -pulse trains in DIP-HQMC experiments

ϕ_a	$xxyy$
ϕ_b	$y y x x$
ϕ_c	$xxyy y y x x$
ϕ_d	$y y x x x x y y$
ϕ_e	ϕ_{10}



Possible remedies were not investigated systematically, but the additional phase cycle of the recoupling π -pulse trains shown in Table E.3 was successful in removing most of the artifacts in the spectrum in Fig. E.1c. It should again be emphasized that pulse durations can usually be determined accurately enough. The effect shown here was found because our usual way of determining pulse lengths on the ^1H channel of our 2.5 mm MAS probe was to use a CRAMPS-type sequence on adamantane. This method proved highly unsuitable due to the rather large B_1 inhomogeneity in this probe, and the artifacts shown here were our first manifestation of this problem.

⁴Usually, MQ selection in simulations is performed more efficiently by retaining only the elements in the density operator corresponding to wanted coherences before the reconversion is calculated.

E.4 ^2H -WISE and RIDER

The pulse programs used for the experiments in Chapters 5 and 6 were supplied by Klaus Schmidt-Rohr and coworkers, University of Massachusetts, Amherst, USA. The ^2H -WISE pulse program and phase cycle is largely identical to the one used for the symmetric dipolar HMQC experiment, and is described in more detail in [Sandström 99].

The RIDER/CODEX pulse sequence has been published in [deAzevedo 00]. The 64-step phase cycle consists of the regular building block of a CP experiment (8 phases for CYCLOPS and spin-temperature inversion), times 2 for storage of the sine and cosine components of the stimulated echo during τ_{mix} , times 2 for storage of the magnetization on $\pm z$ during τ_{mix} , and another factor of 2 for compensating the signal which is excited directly by the read pulse after τ_{mix} . The recoupling π -pulse phases are held constant with respect to all other phases and are again cycled according to the (xy-4) scheme. Common to the two pulse sequences mentioned above is that the ^1H dipolar coupling field during the recoupling periods was about 10–20% higher than during acquisition.

Abbreviations and Acronyms

		explained in Section
AHT	<i>average hamiltonian theory</i>	1.1.3
BABA	<i>back-to-back</i>	2.2.1
CODEX	<i>centerband-only detection of exchange</i>	6.1
COSY	<i>correlation spectroscopy</i>	Introduction
CP	<i>cross-polarization</i>	1.3.2
CSA	<i>chemical-shift anisotropy</i>	1.3.1
CW	<i>continuous-wave</i>	1.0
DQ	<i>double-quantum</i>	2.2
DRAMA	<i>dipolar recovery at the magic angle</i>	2.2.2
DSC	<i>differential scanning calorimetry</i>	7.1.1
ERM	<i>evolution rotor modulation</i>	3.3, 3.3.3
FID	<i>free induction decay</i>	1.2
FT	<i>Fourier transformation</i>	1.0
HBC	<i>hexabenzocoronene</i>	7.1
HDOR	<i>heteronuclear dipolar order rotor encoding</i>	3.2, 3.2.2
HETCOR	<i>heteronuclear correlation</i>	3.0
HMQC	<i>heteronuclear multiple-quantum correlation</i>	3.1
HMSC	<i>heteronuclear multiple-spin correlation</i>	4.0
HSQC	<i>heteronuclear single-quantum correlation</i>	3.2
INEPT	<i>insensitive nuclei enhanced by polarization transfer</i>	3.2

LC	<i>liquid crystal</i>	7.1
MAS	<i>magic-angle spinning</i>	1.4
MQ	<i>multiple-quantum</i>	2.2
NOESY	<i>nuclear Overhauser-enhanced spectroscopy</i>	Introduction
PAS	<i>principal axes system</i>	1.3.1
PVA	<i>poly(vinyl alcohol)</i>	7.2
QCC	<i>quadrupole coupling constant</i>	1.3.3
REAPDOR	<i>rotational-echo, adiabatic-passage, double-resonance</i>	5.1
REDOR	<i>rotational echo, double resonance</i>	2.1
RELM	<i>rotor encoding of longitudinal magnetization</i>	4.1
REPT	<i>recoupled polarization transfer</i>	3.1
RIDER	<i>relaxation-induced dipolar exchange with recoupling</i>	6.1
RRE	<i>reconversion rotor encoding</i>	2.2.2
SLF	<i>separated local field</i>	3.3
TEDOR	<i>transferred echo, double resonance</i>	3.2
TOSS	<i>total suppression of spinning-sidebands</i>	6.4.1
WAXS	<i>wide-angle X-ray scattering</i>	7.1.1
WISE	<i>wideline separation</i>	5.2.1
ZQ	<i>zero-quantum</i>	2.2

Bibliography

- [Abragam 61] A. Abragam. *The Principles of Nuclear Magnetism*. Oxford Univ. Press, Oxford (1961).
- [Abramowitz 72] M. Abramowitz, I. A. Stegun. *Handbook of Mathematical Functions*. Dover Publications, Inc., New York (1972).
- [Aliev 98] A. E. Aliev, E. J. MacLean, K. D. M. Harris, B. M. Kariuki, C. Glidewell. Dynamics of the Hydrogen-Bonding Arrangement in Solid Triphenylmethanol: An Investigation by Solid-State ^2H NMR Spectroscopy. *J. Phys. Chem. B* **102**, 2165–2175 (1998).
- [Andrew 58] E. R. Andrew, A. Bradbury, R. G. Eades. Nuclear Magnetic Resonance Spectra from a Crystal Rotated at High Speed. *Nature* **182**, 1659 (1958).
- [Bak 96] M. Bak, N. C. Nielsen. REPULSION, A Novel Approach to Efficient Powder Averaging in Solid-State NMR. *J. Magn. Reson.* **125**, 132–139 (1996).
- [Baum 85] J. Baum, M. Munowitz, A. N. Garroway, A. Pines. Multiple-Quantum Dynamics in Solid State NMR. *J. Chem. Phys.* **83**, 2015–2025 (1985).
- [Bennett 95] A. E. Bennett, C. M. Rienstra, M. Auger, K. V. Lakshmi, R. G. Griffin. Heteronuclear decoupling in rotation solids. *J. Chem. Phys.* **103**, 6951–6958 (1995).
- [Bergerhoff 95] Prof. Dr. G. Bergerhoff (1995). DIAMOND — Visual Information System for Crystal Structures, Gerhard-Domagk-Str. 1, D-53121 Bonn, Germany.
- [Bielecki 89] A. Bielecki, A. C. Kolbert, M. H. Levitt. Frequency-Switched Pulse Sequences: Homonuclear Decoupling and Dilute Spin NMR in Solids. *Chem. Phys. Lett.* **155**, 341–346 (1989).

- [Bielecki 91] A. Bielecki, D. P. Burum, D. M. Rice, F. E. Karasz. Solid-State Two-Dimensional ^{13}C - ^1H Correlation (HETCOR) NMR Spectrum of Amorphous Poly(2,6-dimethyl-*p*-phenyleneoxide) (PPO). *Macromolecules* **24**, 4820–4822 (1991).
- [Bloch 46] F. Bloch. Nuclear Induction. *Phys. Rev.* **70**, 460 (1946).
- [Bloom 80] M. Bloom, J. H. Davis, M. I. Valic. Spectral distortion effects due to finite pulse widths in deuterium nuclear magnetic resonance spectroscopy. *J. Can. Phys.* **58**, 1510–1517 (1980).
- [Bodenhausen 80] G. Bodenhausen, D. J. Ruben. Natural Abundance Nitrogen-15 NMR by Enhanced Heteronuclear Spectroscopy. *Chem. Phys. Lett.* **69**, 185–189 (1980).
- [Brown 99] S. P. Brown, I. Schnell, J. D. Brand, K. Müllen, H. W. Spiess. An Investigation of $\pi - \pi$ Packing in a Columnar Hexabenzocoronene by Fast Magic-Angle Spinning and Double-Quantum ^1H Solid-State NMR Spectroscopy. *J. Am. Chem. Soc.* **121**, 6712–6718 (1999).
- [Bunn 48] C. W. Bunn. Crystal Structure of Polyvinyl Alcohol. *Nature* **161**, 929–930 (1948).
- [Craats 98] A. M. van de Craats, J. M. Warman, K. Müllen, Y. Geerts, J. D. Brand. Rapid Charge Transport Along Self-Assembling Graphitic Nanowires. *Adv. Mater.* **10**, 36–38 (1998).
- [Craats 99] A. M. van de Craats, J. M. Warman, A. Fechtenkötter, J. D. Brand, M. A. Harbison, K. Müllen. Record Charge Carrier Mobility in a Room-Temperature Discotic Liquid-Crystalline Derivative of Hexabenzocoronene. *Adv. Mater.* **11**, 1469–1472 (1999).
- [de Groot 99] H. J. M. de Groot (1999). Personal communication.
- [De Paul 00] S. M. De Paul, K. Saalwächter, R. Graf, H. W. Spiess. Sideband Patterns from Rotor-Encoded Longitudinal Magnetization in MAS Recoupling Experiments. *J. Magn. Reson.* (2000). Accepted.
- [deAzevedo 99] E. R. deAzevedo, W.-G. Hu, T. J. Bonagamba, K. Schmidt-Rohr. Centerband-Only Detection of Exchange: Efficient Analysis of Dynamics in Solids by NMR. *J. Am. Chem. Soc.* **121**, 8411–8412 (1999).
- [deAzevedo 00] E. R. deAzevedo, W.-G. Hu, T. J. Bonagamba, K. Schmidt-Rohr. Principles of Centerband-Only Detection of Exchange in Solid-State NMR, and Extensions to 4-Time CODEX. *J. Chem. Phys.* (2000). Submitted.

- [Demus 98] D. Demus, J. W. Goodby, G. W. Gray, H. W. Spiess, V. Vill (eds.). Handbook of Liquid Crystals. Wiley-VCH, Weinheim (1998).
- [Derissen 70] J. L. Derissen. Crystal structure and conformation of methylmalonic acid. *Acta Cryst. B* **26**, 901 (1970).
- [Destro 88] R. Destro, R. E. Marsh, R. Bianchi. A Low-Temperature (23K) Study of L-Alanine. *J. Phys. Chem.* **92**, 966–973 (1988).
- [Ernst 87] R. R. Ernst, G. Bodenhausen, A. Wokaun. Principles of Nuclear Magnetic Resonance in One and Two Dimensions. Clarendon Press, Oxford (1987).
- [Fechtenkötter 99] A. Fechtenkötter, K. Saalwächter, M. A. Harbison, K. Müllen, H. W. Spiess. Highly Ordered Columnar Structures from Hexa-*peri*-hexabenzocoronenes — Synthesis, X-ray Diffraction, and Solid-State Heteronuclear Multiple-Quantum NMR Investigations. *Angew. Chem. Int. Ed. Engl.* **38**, 3039–3042 (1999).
- [Feike 96] M. Feike, D. E. Demco, R. Graf, J. Gottwald, S. Hafner, H. W. Spiess. Broadband Multiple-Quantum NMR Spectroscopy. *J. Magn. Reson. A* **122**, 214–221 (1996).
- [Feike 98] M. Feike, C. Jäger, H. W. Spiess. Connectivities of coordination polyhedra in phosphate glasses from P-31 double-quantum NMR spectroscopy. *J. Non-Cryst. Solids* **223**, 200–206 (1998).
- [Filip 99] C. Filip, S. Hafner, I. Schnell, D. E. Demco, H. W. Spiess. Solid-state nuclear magnetic resonance spectra of dipolar-coupled multi-spin systems under fast magic angle spinning. *J. Chem. Phys.* **110**, 423–440 (1999).
- [Frey 73] M. N. Frey, T. F. Koetzle, M. S. Lehmann, W. C. Hamilton. Precision neutron diffraction structure determination of protein and nucleic acid components. X. A comparison between the crystal and molecular structures of L-tyrosine and L-tyrosine hydrochloride. *J. Chem. Phys.* **58**, 2547–2556 (1973).
- [Friedrich 98a] U. Friedrich, I. Schnell, S. P. Brown, A. Lupulescu, D. E. Demco, H. W. Spiess. Spinning-sideband patterns in multiple-quantum magic-angle spinning NMR spectroscopy. *Mol. Phys.* **95**, 1209–1227 (1998).
- [Friedrich 98b] U. Friedrich, I. Schnell, D. E. Demco, H. W. Spiess. Triple-quantum NMR spectroscopy in dipolar solids. *Chem. Phys. Lett.* **285**, 49–58 (1998).

- [Garbow 91] J. R. Garbow, T. Gullion. Improvements in REDOR NMR Spectroscopy. Minimizing Resonance-Offset Effects. *J. Magn. Reson.* **95**, 442–445 (1991).
- [Garbow 92] J. R. Garbow, T. Gullion. The importance of precise timing in pulsed, rotor-synchronous MAS NMR. *Chem. Phys. Lett.* **192**, 71–76 (1992).
- [Geen 94] H. Geen, J.J. Titman, J. Gottwald, H.W. Spiess. Solid-state proton multiple-quantum NMR spectroscopy with fast magic angle spinning. *Chem. Phys. Lett.* **227**, 79–86 (1994).
- [Geen 95] H. Geen, J. J. Titman, J. Gottwald, H. W. Spiess. Spinning Sidebands in the Fast-MAS Multiple-Quantum Spectra of Protons in Solids. *J. Magn. Reson. A* **114**, 264–267 (1995).
- [Geen 99] H. Geen, R. Graf, A. S. D. Heindrichs, B. S. Hickman, I. Schnell, H. W. Spiess, J. J. Titman. Spin Counting with Fast MAS. *J. Magn. Reson.* **138**, 167–172 (1999).
- [Goetz 97] J. M. Goetz, J. Schaefer. REDOR Dephasing by Multiple Spins in the Presence of Molecular Motion. *J. Magn. Reson.* **127**, 147–154 (1997).
- [Gottwald 95] J. Gottwald, D. E. Demco, R. Graf, H. W. Spiess. High-resolution double-quantum NMR spectroscopy of homonuclear spin pairs and proton connectivities in solids. *Chem. Phys. Lett.* **243**, 314–323 (1995).
- [Graf 96] R. Graf, D. E. Demco, J. Gottwald, S. Hafner, H. W. Spiess. Dipolar couplings and internuclear distances by double-quantum nuclear magnetic resonance spectroscopy of solids. *J. Chem. Phys.* **106**, 885–895 (1996).
- [Graf 98a] R. Graf. *Hochauflösende Doppelquanten-NMR-Spektroskopie an amorphen Polymeren*. Dissertation, Universität Mainz (1998).
- [Graf 98b] R. Graf, A. Heuer, H. W. Spiess. Chain-Order Effects in Polymer Melts Probed by ^1H Double-Quantum NMR Spectroscopy. *Phys. Rev. Lett.* **80**, 5738–5741 (1998).
- [Graf 00] R. Graf (2000). Unpublished results.
- [Gullion 89a] T. Gullion, J. Schaefer. Detection of Weak Heteronuclear Dipolar Coupling by Rotational-Echo Double-Resonance Nuclear Magnetic Resonance. *Adv. Magn. Reson.* **13**, 57–83 (1989).
- [Gullion 89b] T. Gullion, J. Schaefer. Rotational-Echo Double-Resonance NMR. *J. Magn. Reson.* **81**, 196–200 (1989).

- [Gullion 90] T. Gullion, D. B. Baker, M. S. Conradi. New, Compensated Carr-Purcell Sequences. *J. Magn. Reson.* **89**, 479–484 (1990).
- [Gullion 92] T. Gullion, S. Vega. A simple magic angle spinning NMR experiment for the dephasing of rotational echoes of dipolar coupled homonuclear spin pairs. *Chem. Phys. Lett.* **194**, 423–428 (1992).
- [Gullion 95] T. Gullion. Measurement of dipolar interactions between spin-1/2 and quadrupolar nuclei by rotational-echo, adiabatic-passage, double-resonance NMR. *Chem. Phys. Lett.* **246**, 325–330 (1995).
- [Gullion 97] T. Gullion. Measurement of Heteronuclear Dipolar Interactions by Rotational-Echo, Double-Resonance Nuclear Magnetic Resonance. *Magn. Reson. Rev.* **17**, 83–131 (1997).
- [Haeberlen 68] U. Haeberlen, J. S. Waugh. Coherent Averaging Effects in Magnetic Resonance. *Phys. Rev.* **175**, 453–467 (1968).
- [Haeberlen 76] U. Haeberlen. High Resolution NMR of Solids, in: *Adv. Magn. Reson.*, Suppl. 1. Academic Press, London (1976).
- [Hafner 96] S. Hafner, H. W. Spiess. Multiple-Pulse Line Narrowing under Fast Magic-Angle Spinning. *J. Magn. Reson. A* **121**, 160–166 (1996).
- [Henry 85] E. R. Henry, A. Szabo. Influence of vibrational motion on solid-state line-shapes and NMR relaxation. *J. Chem. Phys.* **82**, 4753–4761 (1985).
- [Hentschel 79] R. Hentschel, H. W. Spiess. Deuterium Fourier Transform NMR in Solids and Solid Polymers. *J. Magn. Reson.* **35**, 157–162 (1979).
- [Herwig 96] P. Herwig, C. W. Kayser, K. Müllen, H. W. Spiess. Columnar Mesophases of Alkylated Hexa-*peri*-hexabenzocoronenes with Remarkably Large Phase Widths. *Adv. Mater.* **8**, 510–513 (1996).
- [Herzfeld 80] J. Herzfeld, A. E. Berger. Sideband Intensities in NMR Spectra of Samples Spinning at the Magic Angle. *J. Chem. Phys.* **73**, 6021 (1980).
- [Hester 76] R. K. Hester, J. L. Ackerman, B. L. Neff, J. W. Waugh. Separated Local Field Spectra in NMR: Determination of Structure of Solids. *Phys. Rev. Lett.* **36**, 1081–1083 (1976).

- [Hing 92] A. W. Hing, S. Vega, J. Schaefer. Transferred-Echo Double-Resonance NMR. *J. Magn. Reson.* **96**, 205–209 (1992).
- [Hing 93] A. W. Hing, S. Vega, J. Schaefer. Measurement of Heteronuclear Dipolar Coupling by Transferred-Echo Double-Resonance NMR. *J. Magn. Reson. A* **103**, 151–162 (1993).
- [Hodgkinson 00] P. Hodgkinson, L. Emsley. Numerical simulation of solid-state NMR experiments. *Progr. NMR Spectrosc.* **36**, 201–239 (2000).
- [Hohwy 98] M. Hohwy, H. J. Jakobsen, M. Edén, M. H. Levitt, N. C. Nielsen. Broadband dipolar recoupling in the nuclear magnetic resonance of rotating solids: A compensated C7 pulse sequence. *J. Chem. Phys.* **108**, 2686–2694 (1998).
- [Hohwy 99] M. Hohwy, C. M. Riensta, C. P. Jaroniec, R. G. Griffin. Fivefold symmetric homonuclear dipolar recoupling in rotating solids: Application to double quantum spectroscopy. *J. Chem. Phys.* **116**, 7983–7992 (1999).
- [Hong 97] M. Hong, J. D. Gross, R. G. Griffin. Site-Resolved Determination of Peptide Torsion Angle ϕ from the Relative Orientations of Backbone N–H and C–H Bonds by Solid-State NMR. *J. Phys. Chem. B* **101**, 5869–5874 (1997).
- [Hong 98] M. Hong, R. G. Griffin. Resonance Assignments for Solid Peptides by Dipolar-Mediated $^{13}\text{C}/^{15}\text{N}$ Correlation Solid-State NMR. *J. Am. Chem. Soc.* **120**, 7113–7114 (1998).
- [Horii 92] F. Horii, S. Hu, T. Ito, H. Odani, R. Kitamaru, S. Matsuzawa, K. Yamamura. Cross polarization / magic angle spinning ^{13}C n.m.r. study of solid structure and hydrogen bonding of poly(vinyl alcohol) films with different tacticities. *Polymer* **23**, 2299–2306 (1992).
- [Imashiro 95] F. Imashiro, S. Obara. Tacticity-Dependent ^{13}C NMR Chemical Shifts for Poly(vinyl alcohol) Models Studied by ab initio Gauge-Included Atomic Orbital Calculations. *Macromolecules* **28**, 2840–2844 (1995).
- [Jackson 75] J. D. Jackson. *Classical Electrodynamics*. Wiley, New York (1975).
- [Kayser 99] C. W. Kayser. *Molekulare Ordnung und Dynamik verschiedener Kolumnarer Diskotischer Flüssigkristalle*. Dissertation, Universität Mainz (1999).

- [Langer 99] B. Langer, I. Schnell, H. W. Spiess, A.-R. Grimmer. Temperature calibration under ultrafast MAS conditions. *J. Magn. Reson.* **138**, 182–186 (1999).
- [Lee 65] M. Lee, W. I. Goldberg. Nuclear-Magnetic-Resonance Line Narrowing by a Rotating rf Field. *Phys. Rev. A* **140**, 1261–1271 (1965).
- [Lee 95] Y. K. Lee, N. D. Kurur, M. Helmle, O. G. Johannessen, N. C. Nielsen, M. H. Levitt. Efficient dipolar recoupling in the NMR of rotating solids. A sevenfold symmetric radiofrequency pulse sequence. *Chem. Phys. Lett.* **242**, 304–309 (1995).
- [Lehmann 72] M. S. Lehmann, T. F. Koetzle, W. C. Hamilton. Precision Neutron Diffraction Structure Determination of Protein and Nucleic Acid Compounds. I. The Crystal and Molecular Structure of the Amino Acid L-Alanine. *J. Am. Chem. Soc.* **94**, 2657–2660 (1972).
- [Leisen 92] J. Leisen, M. Werth, C. Boeffel, H. W. Spiess. Molecular dynamics at the glass transition: One dimensional and two dimensional nuclear magnetic resonance studies of a glass-forming discotic liquid crystal. *J. Chem. Phys.* **97**, 3749–3759 (1992).
- [Lesage 98a] A. Lesage, D. Sakellariou, S. Steuernagel, L. Emsley. Carbon-Proton Chemical Shift Correlation in Solid State NMR by Through-Bond Multiple-Quantum Spectroscopy. *J. Am. Chem. Soc.* **120**, 13194–13201 (1998).
- [Lesage 98b] A. Lesage, S. Steuernagel, L. Emsley. Carbon-13 Spectral Editing in Solid-State NMR Using Heteronuclear Scalar Couplings. *J. Am. Chem. Soc.* **120**, 7095–7100 (1998).
- [Levante 95] T. O. Levante, M. Baldus, B. H. Meier, R. R. Ernst. Formalized quantum-mechanical Floquet theory and its application to sample-spinning in nuclear magnetic resonance. *Mol. Phys.* **86**, 1195–1212 (1995).
- [Levitt 84] M. H. Levitt, D. Suter, R. R. Ernst. Composite pulse excitation in three-level systems. *J. Chem. Phys.* **80**, 3064–3068 (1984).
- [Lowe 59] I. J. Lowe. Free Induction Decay of Rotating Solids. *Phys. Rev. Lett.* **2**, 285 (1959).
- [Maricq 79] M. M. Maricq, J. S. Waugh. NMR in Rotating Solids. *J. Chem. Phys.* **70**, 3300 (1979).

- [Maudsley 77] A. A. Maudsley, R. R. Ernst. Indirect Detection of Magnetic Resonance by Heteronuclear Two-Dimensional Spectroscopy. *Chem. Phys. Lett.* **50**, 368–372 (1977).
- [Mehring 83] M. Mehring. High Resolution NMR of Solids. Springer-Verlag, Berlin (1983).
- [Meier 86] B. H. Meier, W. L. Earl. Excitation of Multiple-Quantum Transitions Under Magic-Angle Spinning Conditions: Adamantane. *J. Chem. Phys.* **85**, 4905–4911 (1986).
- [Metz 94] G. Metz, X. Wu, S. O. Smith. Ramped-Amplitude Cross Polarization in Magic-Angle-Spinning NMR. *J. Magn. Reson. A* **110**, 219–227 (1994).
- [Minot 99] E. D. Minot, P. T. Callaghan, N. Kaplan. Multiple Echoes, Multiple Quantum Coherence, and the Dipolar Field: Demonstrating the Significance of Higher Order Terms in the Equilibrium Density Matrix. *J. Magn. Reson.* **140**, 200–205 (1999).
- [Morris 79] G. A. Morris, R. Freeman. Enhancement of Nuclear Magnetic Resonance Signals by Polarization Transfer. *J. Am. Chem. Soc.* **101**, 760–761 (1979).
- [Müller 79] L. Müller. Sensitivity Enhanced Detection of Weak Nuclei Using Heteronuclear Multiple Quantum Coherence. *J. Am. Chem. Soc.* **101**, 4481–4484 (1979).
- [Munowitz 87a] M. Munowitz, A. Pines. Principles and Applications of Multiple-Quantum NMR. *Adv. Chem. Phys.* **66**, 1 (1987).
- [Munowitz 87b] M. Munowitz, A. Pines, M. Mehring. Multiple-Quantum Dynamics in NMR: A Directed Walk through Liouville Space. *J. Chem. Phys.* **86**, 3172–3182 (1987).
- [Nahringbauer 68] I. Nahringbauer. Hydrogen bond studies. XX. The crystal structure of ammonium formate. *Acta Cryst. B* **24**, 565 (1968).
- [Naito 84] A. Naito, P. B. Barker, C. A. McDowell. Two-dimensional nuclear magnetic resonance studies on a single crystal of L-alanine. Separation of the local dipolar fields; and 2D exchange spectroscopy of the ^{14}N relaxation processes. *J. Chem. Phys.* **81**, 1583–1591 (1984).
- [Nakai 89] T. Nakai, J. Ashida, T. Terao. Influence of small-amplitude motions on two-dimensional NMR powder patterns. Anisotropic vibrations in calcium formate. *Mol. Phys.* **67**, 839–847 (1989).

- [Nielsen 94] N. C. Nielsen, H. Bilsøe, H. J. Jakobsen, M.H. Levitt. Double-quantum homonuclear rotary resonance: Efficient dipolar recovery in magic-angle spinning nuclear magnetic resonance. *J. Chem. Phys.* **101**, 1805–1812 (1994).
- [Pines 72] A. Pines, M. G. Gibby, J. S. Waugh. Proton-Enhanced Nuclear Induction Spectroscopy. A Method for High Resolution NMR of Dilute Spins in Solids. *J. Chem. Phys.* **56**, 1776–1777 (1972).
- [Pines 73] A. Pines, M. G. Gibby, J. S. Waugh. Proton-enhanced NMR of dilute spins in solids. *J. Chem. Phys.* **59**, 569–590 (1973).
- [Press 91] W. H. Press, B. P. Flannery, S. A. Teukolsky, W. T. Vetterling. Numerical Recipes in C. Cambridge University Press, Cambridge (1991).
- [Purcell 46] E. M. Purcell, H. C. Torrey, R. V. Pound. Resonance Absorption by Nuclear Magnetic Moments in Solids. *Phys. Rev.* **69**, 37 (1946).
- [Rienstra 98] C. M. Rienstra, M. E. Hatcher, L. J. Mueller, B. Q. Sun, S. W. Fesik, R. G. Griffin. Efficient multispin homonuclear double-quantum recoupling for magic-angle spinning NMR: C-13-C-13 correlation spectroscopy of U-C-13-erythromycin A. *J. Am. Chem. Soc.* **120**, 10602–10612 (1998).
- [Rose 59] M. E. Rose. Elementary Theory of Angular Momentum. Wiley, London (1959).
- [Rossum 96] B.-J. van Rossum, G. J. Boender, H. J. M. de Groot. High Magnetic Field for Enhanced Proton Resolution in High-Speed CP/MAS Heteronuclear ^1H - ^{13}C Dipolar Correlation Spectroscopy. *J. Magn. Reson. A* **120**, 274–277 (1996).
- [Rossum 97] B.-J. van Rossum, H. Förster, H. J. M. de Groot. High-Field and High-Speed CP-MAS ^{13}C NMR Heteronuclear Dipolar-Correlation Spectroscopy of Solids with Frequency-Switched Lee-Goldburg Homonuclear Decoupling. *J. Magn. Reson.* **124**, 516–519 (1997).
- [Saalwächter 99a] K. Saalwächter, R. Graf, D. E. Demco, H. W. Spiess. Heteronuclear Double-Quantum MAS NMR Spectroscopy in Dipolar Solids. *J. Magn. Reson.* **139**, 287–301 (1999).
- [Saalwächter 99b] K. Saalwächter, R. Graf, H. W. Spiess. Recoupled Polarization Transfer Heteronuclear Multiple-Quantum Correlation in Solids under Ultra-fast MAS. *J. Magn. Reson.* **140**, 471–476 (1999).

- [Saalwächter 00a] K. Saalwächter, R. Graf, H. W. Spiess. Recoupled Polarization-Transfer Methods for Solid-State ^1H - ^{13}C Heteronuclear Correlation in the Limit of Fast MAS. *J. Magn. Reson.* (2000). In preparation.
- [Saalwächter 00b] K. Saalwächter, K. Schmidt-Rohr. Relaxation-Induced Dipolar Exchange with Recoupling — A Novel MAS NMR Method for Determining Heteronuclear Distance without Irradiating the Second Spin. *J. Magn. Reson.* (2000). Submitted.
- [Sachleben 96] J. R. Sachleben, V. Frydman, L. Frydman. Dipolar Determinations in Solids by Relaxation-Assisted NMR Recoupling. *J. Am. Chem. Soc.* **118**, 9786–9787 (1996).
- [Sack 99] I. Sack, A. Goldbourt, S. Vega, G. Buntkowsky. Deuterium REDOR: Principles and Applications for Distance Measurements. *J. Magn. Reson.* **138**, 54–65 (1999).
- [Sakurada 85] I. Sakurada. Polyvinyl Alcohol Fibres. Marcel Dekker, New York (1985).
- [Sakurai 85] J. J. Sakurai. Modern Quantum Mechanics. Addison-Wesley, New York (1985).
- [Sandström 99] D. Sandström, M. Hong, K. Schmidt-Rohr. Identification and mobility of deuterated residues in peptides and proteins by ^2H - ^{13}C solid-state NMR. *Chem. Phys. Lett.* **300**, 213–220 (1999).
- [Sangill 94] R. Sangill, N. Rastrup-Andersen, H. Bildsoe, H. J. Jacobsen, N. C. Nielsen. Optimized Spectral Editing of ^{13}C MAS NMR Spectra of Rigid Solids Using Cross Polarization Methods. *J. Magn. Reson. A* **107**, 67–78 (1994).
- [Schmidt-Rohr 92] K. Schmidt-Rohr, J. Clauss, H. W. Spiess. Correlation of Structure, Mobility, and Morphological Information in Heterogeneous Polymer Materials by Two-Dimensional Wideline-Separation NMR Spectroscopy. *Macromolecules* **25**, 3273–3277 (1992).
- [Schmidt-Rohr 94] K. Schmidt-Rohr, H. W. Spiess. Multidimensional Solid-State NMR and Polymers. Academic Press, London (1994).
- [Schmidt-Rohr 99] K. Schmidt-Rohr (1999). Personal communication.
- [Schmidt 85] C. Schmidt, K. J. Kuhn, H. W. Spiess. Distribution of correlation times in glassy polymers from pulsed deuteron NMR. *Progr. Colloid Polymer Sci.* **71**, 71–76 (1985).
- [Schmidt 98] C. Schmidt, H. W. Spiess. Characterization Methods: Magnetic Resonance, pp. 595–618. Volume 1 of Demus et al. [Demus 98] (1998).

- [Schnell 98] I. Schnell, A. Lupulescu, S. Hafner, D. E. Demco, H. W. Spiess. Resolution Enhancement in Multiple-Quantum MAS NMR Spectroscopy. *J. Magn. Reson.* **133**, 61–69 (1998).
- [Schnell 99] I. Schnell. *¹H-NMR-Spektroskopie im Festkörper: Schnelle Probenrotation und Mehrquantenkohärenzen*. Dissertation, Universität Mainz (1999).
- [Sethi 91] N. K. Sethi. Carbon-13 CP/MAS Spectral Assignment With One-Dimensional Separated-Local-Field Spectroscopy. *J. Magn. Reson.* **94**, 352–361 (1991).
- [Shykind 88] D. N. Shykind, J. Baum, S. B. Liu, A. Pines. Phase-incremented multiple-quantum NMR experiments. *J. Magn. Reson.* **76**, 149–154 (1988).
- [Slichter 96] C. P. Slichter. Principles of Magnetic Resonance. Springer-Verlag, Berlin (1996).
- [Sommer 95] W. Sommer, J. Gottwald, D. E. Demco, H. W. Spiess. Dipolar Heteronuclear Multiple-Quantum NMR Spectroscopy in Rotating Solids. *J. Magn. Reson. A* **113**, 131–134 (1995).
- [Sørensen 83] O. W. Sørensen, G. W. Eich, M. H. Levitt, G. Bodenhausen, R. R. Ernst. Product Operator Formalism for the Description of NMR Pulse Experiments. *Progr. NMR Spectrosc.* **16**, 163–192 (1983).
- [Spiess 78] H. W. Spiess. Rotation of Molecules and Nuclear Spin Relaxation. In P. Diehl, E. Fluck, R. Kosfeld (eds.), *NMR Basic Principles and Progress*, Volume 15, pp. 55–214. Springer-Verlag, Berlin (1978).
- [Spiess 80] H. W. Spiess. Deuteron spin alignment: A probe for studying ultraslow motions in solids and solid polymers. *J. Chem. Phys.* **72**, 6755–6762 (1980).
- [Spiess 83] H. W. Spiess. Molecular dynamics of solid polymers as revealed by deuteron NMR. *Colloid & Polymer Sci.* **261**, 193–209 (1983).
- [Stabel 95] A. Stabel, P. Herwig, K. Müllen, J. P. Rabe. Diodelike Current-Voltage Curves for a Single Molecule — Tunneling Spectroscopy with Submolecular Resolution of an Alkylated, *peri*-Condensed Hexabenzocoronene. *Angew. Chem. Int. Ed. Engl.* **34**, 1609–1611 (1995).
- [Sun 95] B.-Q. Sun, P. R. Costa, D. Kocisko, Jr. P. T. Lansbury, R. G. Griffin. Internuclear distance measurements in solid state nuclear magnetic resonance: Dipolar recoupling via rotor synchronized spin locking. *J. Chem. Phys.* **102**, 702 (1995).

- [Terao 83] T. Terao, S. Maeda, A. Saika. High-Resolution Solid-State ^{13}C NMR of Poly(vinyl alcohol): Enhancement of Tacticity Splitting by Intramolecular Hydrogen Bonds. *Macromolecules* **16**, 1535–1539 (1983).
- [Terao 86] T. Terao, H. Miura, A. Saika. Dipolar SASS NMR spectroscopy: Separation of heteronuclear dipolar powder patterns in rotating solids. *J. Chem. Phys.* **85**, 3816–3826 (1986).
- [Torchia 82] D. A. Torchia, A. Szabo. Spin-Lattice Relaxation in Solids. *J. Magn. Reson.* **49**, 107–121 (1982).
- [Tycko 90] R. Tycko, G. Dabbagh. Measurement of nuclear magnetic dipole-dipole couplings in magic angle spinning NMR. *Chem. Phys. Lett.* **173**, 461–465 (1990).
- [Tycko 91] R. Tycko, G. Dabbagh. Double-Quantum Filtering in Magic-Angle-Spinning NMR Spectroscopy: An Approach to Spectral Simplification and Molecular Structure Determination. *J. Am. Chem. Soc.* **113**, 9444–9448 (1991).
- [Vallerien 90] S. U. Vallerien, M. Werth, F. Kremer, H. W. Spiess. Molecular dynamics and the glass transition in a columnar liquid crystal formed by a chiral discotic mesogen. *Liq. Crystals* **8**, 889–893 (1990).
- [Vega 77] S. Vega, A. Pines. Operator formalism for double quantum NMR. *J. Chem. Phys.* **66**, 5624–5644 (1977).
- [Vega 99] S. Vega (1999). Personal communication.
- [Vleck 48] J. H. van Vleck. The Dipolar Broadening of Magnetic Resonance Lines in Crystals. *Phys. Rev.* **74**, 1168 (1948).
- [Weitekamp 82] D. P. Weitekamp, J. R. Garbow, A. Pines. Determination of dipole coupling constants using heteronuclear multiple quantum NMR. *J. Chem. Phys.* **77**, 2870–2883 (1982).
- [Wu 93] X. Wu, K. W. Zilm. Complete Spectral Editing in CPMAS NMR. *J. Magn. Reson. A* **102**, 205–213 (1993).
- [Wu 94] X. Wu, S. T. Burns, K. W. Zilm. Spectral Editing in CPMAS NMR. Generating Subspectra Based on Proton Multiplicities. *J. Magn. Reson. A* **111**, 29–36 (1994).
- [Yen 83] Y.-S. Yen, A. Pines. Multiple-quantum NMR in solids. *J. Chem. Phys.* **78**, 3579–3582 (1983).

Zusammenfassung

Die aktuellen instrumentellen Fortschritte in der hochauflösenden Festkörper-NMR, insbesondere die Entwicklung von MAS-Probenköpfen für Rotationsfrequenzen von bis zu 35 kHz und Hochfeldspektrometern mit Protonen-Larmorfrequenzen von 500 MHz und mehr, ermöglichen die Durchführung von relativ einfachen ^1H Ein- und Doppelquanten-Experimenten. Mittels dieser Experimente wird durch die Korrelation der isotropen chemischen Verschiebung mit der dipolaren Kopplungskonstanten orts aufgelöst strukturelle und dynamische Information im Festkörper zugänglich. Solche Methoden werden in unserer Gruppe inzwischen routinemäßig angewendet, und das Ziel dieser Arbeit war die Übertragung der homonuklearen Doppelquantenmethodik, insbesondere die Analyse von Rotationsseitenbandenmustern in der Multiquanten- (MQ-) Dimension solcher Experimente zur Bestimmung von dipolaren Kopplungskonstanten, auf den heteronuklearen Fall. Besondere Bedeutung kam dabei ^{13}C - ^1H Systemen zu, in denen Messungen mit ^{13}C in natürlicher Häufigkeit möglich sein sollten.

Unter sehr schnellem MAS müssen die homo- und heteronuklearen dipolaren Kopplungen mittels spezieller Pulssequenzen *wiedereingekoppelt* werden, um eine effiziente Anregung der zu beobachtenden Multiquantenmoden zu erreichen. Dazu bot sich für den heteronuklearen Fall das REDOR-Experiment, bei dem im Abstand von halben Rotorperioden π -Pulse eingestrahlt werden, als unbestreitbar einfachster und robuster Ansatz an. Mit nur kleinen Modifikationen der ursprünglichen Pulssequenz kann ein *heteronukleares Multiquantenexperiment* durchgeführt werden, das in seinen wesentlichen Merkmalen mit den auf der BABA-Sequenz basierenden homonuklearen Doppelquantenexperimenten übereinstimmt. Darunter fallen das Studium des Multiquanten-Aufbauverhaltens, die Abtastung des Präzessionsverhaltens der Multiquantenkohärenz in einem zweidimensionalen Experiment und das Auftreten von Rotationsseitenbandenmustern in der Multiquantendimension dieser Experimente, aus denen die heteronukleare Dipolkopplungskonstante erhalten werden kann. Es zeigt sich, daß die ge-

nannten Ähnlichkeiten tatsächlich auf weitgehend identische Konzepte in der theoretischen Beschreibung zurückzuführen sind.

Heteronukleare MQ- (HMQ-) Spektroskopie ist ein flexibles Konzept insofern, als die HMQ-Kohärenzen unter Verwendung von Anfangsmagnetisierung einer beliebigen der beteiligten Spinspezies angeregt werden können, und zur direkten Beobachtung auch in Magnetisierung auf einem beliebigen der beiden Kanäle zurückverwandelt werden kann. Dieser Flexibilität wird bei den vorgestellten Techniken Rechnung getragen. Die wiedereingekoppelten Polarisations-Transfer Techniken (REPT, *recoupled polarization transfer*) profitieren direkt von der hohen Anfangsmagnetisierung von Protonen im thermischen Gleichgewicht und der hohen Auflösung der detektierten ^{13}C -Spins, ohne daß dabei ein Kreuzpolarisationsschritt zur Erhöhung der ^{13}C -Polarisation eingesetzt werden muß. Die vorgestellten Sequenzen eignen sich zur Messung hochaufgelöster ^{13}C - ^1H -Verschiebungs-Korrelationsspektren, und die typischen Rotationsseitenbandenmuster in der HMQ-Dimension ermöglichen in der erwarteten Weise die Bestimmung selbst von niedrigen Dipolkopplungskonstanten.

Verschiedene Varianten des ursprünglichen HMQ-Experiments werden vorgestellt, die sich durch den in der t_1 -Dimension abgefragten Kohärenztyp unterscheiden. So werden Verschiebungs-Korrelationsspektren am günstigsten mittels rotorsynchronisierter Abtastung einer Antiphasen-Kohärenz, $\hat{I}_x\hat{S}_z$, aufgenommen, während sich für das effizienteste Experiment zur Analyse der Rotationsseitenbandenmuster der heteronukleare dipolar-geordnete Zustand, $\hat{I}_z\hat{S}_z$, als in t_1 beobachtete Kohärenz ergibt. Es zeigt sich damit, daß die rotormodulierte Rekonversion als der für das Auftreten dieser Seitenbandenmuster verantwortliche Mechanismus keineswegs ein für HMQ-Kohärenzen typischer Prozess ist, sondern vielmehr auf jede der in t_1 beobachteten Kohärenzen anwendbar ist, und lediglich die Rotormodulation des Wechselwirkungs-Hamiltonoperators widerspiegelt.

Aus der theoretischen Beschreibung der REPT-Techniken ist zu folgern, daß die im Experiment angeregten HMQ-Moden in jedem Fall heteronukleare Spinpaarkohärenzen sind. Dies hat Auswirkungen auf die beobachteten Rotationsseitenbandenmuster, in denen als Folge die Intensität der Seitenbanden erster Ordnung grundsätzlich nicht verlässlich sind, da sich in diesen Beiträge von Kopplungen zu weiter entfernten Nachbarprotonen akkumulieren. Weiterhin fehlen in Verschiebungs-Korrelationsspektren von vollständig ^{13}C -isotopenmarkierten Substanzen oft Signale zu Korrelationen zwischen weit voneinander entfernten Kernspins. Dies ergibt sich zwanglos aus der theoretischen Beschreibung solcher Signale, bei denen die

Kopplung des beteiligten Protons zu einem benachbarten weiteren ^{13}C -Atom zur Dephasierung des Signals führt. Schließlich ist das spektrale Editieren von ^{13}C Spektren mittels REPT-Techniken auf relativ einfache Weise durchführbar.

Das Studium des Aufbauverhaltens der HMQ-Kohärenzen in Abhängigkeit der Wiedereinkopplungszeit ist mit den REPT-Techniken nur sehr eingeschränkt möglich. Dies wird mit der Dephasierung der beobachteten HMQ-Kohärenzen durch heteronukleare Kopplungen zu Nachbarspins begründet. Die Methode der Wahl ist dann die Klasse der symmetrischen dipolaren Multispinkorrelationstechniken (DIP-HMSC, *dipolar heteronuclear multiple-spin correlation*), die mit ^{13}C Anfangsmagnetisierung arbeiten, wie sie z.B. durch einen Kreuzpolarisationsschritt erzeugt werden kann. Die Pulssequenz ist dann symmetrisch in der Beziehung, daß sowohl während der Anregungs- als auch während der Rekonversionszeit in ^{13}C transversale Kohärenzen beteiligt sind. Diese Techniken ähneln dem ursprünglichen REDOR-Experiment dahingehend, daß eine Korrektur des Signals mittels eines Referenzexperiments absolute HMQ-Intensitäten zugänglich macht, die nicht mehr von Relaxationseffekten abhängen und auch nicht mehr kritisch von Kopplungen zu benachbarten Heterospins beeinflusst werden. Weiterhin können, in Analogie zu REPT, Verschiebungs-Korrelations- und Seitenbandenexperimente durchgeführt werden.

Der interessanteste Aspekt dieser Klasse von Experimenten ist jedoch die Tatsache, daß die Evolution von transversalen ^{13}C -Kohärenzen auch die Anregung höherer Multispin-HMQ-Moden des Typs $\hat{S}_x \prod_i \hat{I}_x^{(i)}$ ermöglicht, für die eine Selektion der Kohärenzordnung im I-Spin Unterraum mittels eines Phasenzklus implementiert werden kann. Dazu wurde ein heteronukleares Spin-Counting-Experiment durchgeführt und ein ausführlicher Vergleich der Eigenschaften dieses Experiments mit den bekannten homonuklearen Spin-Counting-Experimenten angestellt. Verschiebungs-Korrelationsexperimente und die Aufnahme von Rotationsseitenbandenmustern mit der Selektion einer spezifischen Quantenordnung im Protonen-Unterraum sind ebenfalls durchführbar, und die Resultate stimmen gut mit der analytischen Beschreibung dieser Spektren überein.

Für die Experimente an ^{13}C - ^1H -Systemen lässt sich zusammenfassen:

- Die Verwendung von schnellem MAS mit $\nu_R > 20$ kHz führte in allen Fällen zu einem vernachlässigbaren Einfluß der homonuklearen ^1H - ^1H Kopplung, die sich direkt sichtbar nur noch in endlichen Linienbreiten in den Verschiebungs-Korrelationsspektren

äußert. Das Erscheinungsbild der Spektren wie die absoluten HMQ-Intensitäten und die Struktur der Rotationsseitenbandenmuster kann gut unter alleiniger Berücksichtigung der heteronuklearen Kopplung erklärt werden, was einen theoretisch gut handhabbaren Formalismus zur Folge hat, in dem sich die beobachteten Phänomene auf der Basis einer Summe von Paarwechselwirkungen beschreiben lassen.

- Sämtliche in dieser Arbeit vorgestellten ^{13}C - ^1H -Korrelationsexperimente basieren auf einfachen, der NMR-Spektroskopie in Lösung entlehnten Konzepten. Diese setzen das Vorhandensein gut lokalisierter heteronuklearer Paarwechselwirkungen voraus, die sich hier aus der erfolgreichen Unterdrückung homonuklearer Kopplungen durch das sehr schnelle MAS ergeben.
- Die REPT-Techniken sind die effizientesten Vertreter heteronuklearer Korrelationstechniken für Standardanwendungen in ^{13}C - ^1H -Systemen. Dies ist anhand einiger erfolgreicher Anwendungen auf die Untersuchung von Struktur und Dynamik in diskotischen Mesophasen mit ^{13}C in natürlicher Häufigkeit illustriert.
- Der Multispin-Charakter der in den DIP-HMSC-Experimenten angeregten Kohärenzen lässt auf fruchtbare Anwendungen dieser Techniken in der Strukturaufklärung hoffen. Vielversprechende Kandidaten sind hier die Dreispinkorrelationen (ein ^{13}C , zwei ^1H), messbar in zweidimensionalen Verschiebungs-Korrelationsspektren von ^{13}C mit der Summe der zwei chemischen Verschiebungen der zwei benachbarten Protonenspins, und das heteronukleare Spin-Counting mit seiner besonderen Eigenschaft, die lokale Umgebung eines spezifischen ^{13}C -Spins abzutasten.

Eine REDOR-Wiedereinkopplungssequenz eignet sich auch zur Durchführung von MAS-Experimenten, in denen ^{13}C chemische Verschiebungen mit ^2H Quadrupol-Breitlinienspektren korreliert werden können. Ein bereits existierendes Experiment konnte durch die Einführung von Composite-Pulsen dahingehend verbessert werden, daß nun Spektren mit höherem Signal-zu-Rausch Verhältnis und ohne Phasenfehler in der t_1 -Dimension erhalten werden. Die Technik wurde erfolgreich zur Identifikation eines bislang nicht beschriebenen Bewegungsprozesses der Wasserstoffbrückenbindungen in den kristallinen Anteilen von ataktischem Polyvinylalkohol eingesetzt.

Die durch die begrenzte Anregungsbreite von Radiofrequenzpulsen endlicher Länge

stark eingeschränkte Anwendbarkeit dieser Technik auf die meisten Quadrupolkerne mit Spin $I > \frac{1}{2}$ kann durch Anwendung des relaxationsinduzierten dipolaren Austauschexperiments mit Wiedereinkopplung (RIDER, *relaxation-induced dipolar exchange with recoupling*) vollständig umgangen werden. Mit dieser dem REDOR-Experiment sehr ähnlichen Methode sind heteronukleare Dipolkopplungskonstanten zwischen ^{13}C und einem beliebigen Quadrupolkern zugänglich, ohne daß auf letzteren überhaupt Pulse eingestrahlt werden. Die Methode nutzt die Relaxation des Quadrupolkerns zur Beobachtung der heteronuklearen Kopplung aus und ermöglicht nicht nur präzise Messungen schwacher Kopplungskonstanten, sondern lässt auch Aussagen über Relaxationsprozesse der Mehrquantenübergänge des Quadrupolkerns zu.

Zukünftige Arbeiten sind vor allem auf dem Gebiet von Dynamik und Ordnungsprozessen in Polymerschmelzen über dem Glaspunkt geplant, in denen die Messungen dipolarer ^{13}C - ^1H Restkopplungen mit der erhöhten chemischen Selektivität durch Detektion von ^{13}C im Prinzip die Beobachtung von Unterschieden in der Dynamik von Segmenten der Polymerkette mit verschiedener Konfiguration oder Konformation ermöglichen sollte. Außerdem steht noch eine vertiefte experimentelle und theoretische Erforschung des Wechselspiels zwischen dem Wiedereinkopplungsprozess und molekularer Dynamik auf derselben Zeitskala (des „intermediate motional regime“) aus. Vorläufige Messungen weisen auf eine Veränderung der Seitenbandenmuster und einen späteren Zusammenbruch der Anregungseffizienz der Multiquantensequenz hin, sobald Bewegungen auf der Zeitskala des Experiments einsetzen. Diese Arbeiten sind unabdingbar für ein besseres Verständnis und den möglichen Einsatz der in dieser Arbeit besprochenen Techniken zum detaillierten Studium solcher langsameren Bewegungsprozesse.

Danksagung

Die Liste der Personen, ohne die diese Arbeit in ihrer vorliegenden Form nicht zustande gekommen wäre, ist lang. Noch deutlich länger ist die Liste derjenigen, die meine letzten zweieinhalb Jahre am MPI für Polymerforschung (und an der UMass in Amherst) zu einer sehr schönen und anregenden Zeit haben werden lassen, und ohne die das Anfertigen dieser Arbeit nicht auch nur annähernd so viel Spaß gemacht hätte. Ich danke

- *Prof. H. W. Spiess* für die in jede Richtung offene und interessante Aufgabenstellung, die Organisation einer motivierten und motivierenden Arbeitsgruppe und einer Infrastruktur, die in der mir bekannten Forschungslandschaft ihresgleichen sucht, sein stetes Interesse und vor allem seine Begeisterungsfähigkeit, und schließlich für die Möglichkeit, viele der durchgeführten Arbeiten auch im internationalen Rahmen vorstellen und diskutieren zu können.
- *Prof. Klaus Schmidt-Rohr* für die Idee, daß NMR ein interessantes Forschungsgebiet sein könnte, für die ersten Schritte am Festkörper-Spektrometer (im winter term 94/95 in Amherst), insbesondere für genau die richtigen Ratschläge zur richtigen Zeit („...ich dachte da macht man am besten REDOR.“), unzählige anregende und lehrreiche Gespräche und einen in jeder Beziehung gelungenen und schönen Sommer 1999 in Amherst. Many thanks also to *Hiro Kaji* and the research group of KSR, to *Charlie Dickinson* for teaching his insightful and stimulating NMR course, and to *Prof. Muthukumar and his group* for computer support.
- *Robert Graf* für wertvolle Vorarbeit, den „start-up“ in die Welt der Multiquanten, die gute und fruchtbare Zusammenarbeit, das Betreuen eines Spektrometerpools, der trotz einer inzwischen ins Unermeßliche gesteigerten Komplexität noch immer stetig an Anwenderfreundlichkeit gewinnt, und schließlich für viele kulinarische Bereicherungen, seine Freundschaft und die notwendige Ruhe im Forschungsalltag.
- *Ingo Schnell* für seine Unvoreingenommenheit dahingehend, daß man sich auch als Chemiker vor der Theorie nicht zu ängstigen braucht, seine ebenfalls umfangreiche Vorarbeit, viele wichtige Denkanstöße in Sachen Programmierung and Multiquantenspektroskopie und die Einsicht, daß schnelles MAS (fast) alle Probleme löst.
- *Susan DePaul* and *Steven Brown* for their collaboration on a number of interesting projects, a lot of insightful discussions, the American and British touch to everyday life in the Spiess-

group, and for their steady patience while proof-reading ever increasing amounts of German/British/American pidgin English.

- *Martha Harbison* und *Andreas Fechtenkötter*, sowie vielen anderen Mitstreitern der Graphit- und Dendrimerfraktionen der Gruppe von Prof. Müllen, für die Bereicherung dieser Arbeit mit tatsächlichen *Anwendungen* und den damit verbundenen Ausflug in die wahre Welt der Forschung, daneben für viele Tassen Kaffee, Gläser Bier und Whiskey, und die Einsicht, daß wer hart arbeitet auch feste feiern darf.
- Our never dwindling source of theoretical support from Romania, namely *Prof. Dan Demco*, *Claudiu Filip* and *Adonis Lupulescu*, for initial impulses and many useful hints and stimulating discussions.
- *Stephan Büchner*, der uns, was vielleicht inzwischen auch seine Meinung ist, viel zu früh verlassen hat, für logisch-analytische Unterstützung, und die vielen interessanten Gespräche und willkommenen Ablenkungen aus dem Einerlei des Büroalltags.
- *Michael Wind*, *Stefan Reinsberg* und *Burkhard Doliwa*, ersterem für die Mitarbeit bei den Dendrimeren, letzteren für rechnerische Kompetenz und allen für so einige nette Abende („Na, habt ihr Lust auf Kino ...?“) und Skiurlaube.
- *Manfred Wilhelm* für seinen unerschöpflichen Ideenfundus, und für den Anstoß und die erste Fühlungnahme in Bezug auf einen ertragreichen Sommeraufenthalt in Amherst.
- *Hans-Peter*, *Manfred* und *Frank* für die unentbehrliche und *raichliche* Unterstützung durch *HehnTronics™*, die eidgenössische Bastelkam'r und den *Rechner-Keller*.
- *Volker Macho* und der Computercrew, sowie *Christian Holm*, für reichlich Rechenzeit und den großen Einsatz, mit dem sie das inzwischen doch sehr selbständig denkende Hausnetz in Zaum halten. Dank gilt auch *Heiko Schmitz* und *Mathias Pütz* für die Vorarbeit und die Unterstützung beim Schreiben einiger C++-Routinen.
- *Ute Pawelzik* und der Chemiegruppe für etliche Probenpräparationen und die Möglichkeit, ein echtes Chemielabor noch ab und zu von innen sehen zu dürfen.
- Last but not least *meinen Eltern* für jede nur erdenkliche Freiheit, die großzügige Unterstützung und den Rückhalt, ohne den ich neun Jahre Chemiestudium nicht so guter Dinge überstanden hätte.

Lebenslauf

Name: Kay Saalwächter
Geburtsdatum: 17.12.1970
Geburtsort: Aachen

Schulbildung:

1977 bis 1981 Grundschule: Pestalozzi-Schule, Ingelheim
1981 bis 1990 Staatl. Sebastian-Münster-Gymnasium, Ingelheim
25.5.1990 Abitur

Wehrdienst: 1.7.1990 bis 27.6.1991

Studium:

WS 1991/92 bis SS 1993 Grundstudium Chemie (Diplom) and der Johannes Gutenberg-Universität Mainz
16.8.1993 Diplom-Vorprüfung
WS 1993/94 bis SS 1997 Hauptstudium an der Albert-Ludwigs-Universität Freiburg
August 1994 bis Juni 1995 2 Semester Auslandsstudium an den Departments of Chemistry / Polymer Science, University of Massachusetts, Amherst, USA
Januar bis September 1997 Diplomarbeit zum Thema „*Cellulose in neuen koordinierenden Lösungsmitteln — Untersuchung der Lösungsstruktur mittels statischer / dynamischer Lichtstreuung und rheologischen Methoden*“ bei Prof. W. Burchard, Institut für Makromolekulare Chemie, Universität Freiburg
29.10.1997 Diplom, Schwerpunkt: Makromolekulare Chemie
seit November 1997 Promotion auf dem Gebiet Physikalische Chemie / Kernresonanzspektroskopie zum Thema „*Heteronuclear Recoupling Methods in Solid-State NMR*“ bei Prof. H. W. Spiess, Max-Planck-Institut für Polymerforschung, Mainz
Juni bis August 1999 DAAD-Stipendium (HSP-III) für einen Forschungsaufenthalt bei Prof. K. Schmidt-Rohr, Polymer Science and Engineering Dept., University of Massachusetts, Amherst, USA

Tätigkeiten:

10.7.1995 bis 15.9.1995 Aushilfskraft im NMR-Labor der Abt. F&E Analytik, Boehringer Ingelheim KG
November/Dezember 1995 wissenschaftliche Hilfskraft im AK Prof. Gronski, Institut für Makromolekulare Chemie, Universität Freiburg

Sonstiges:

14.10.1998 Steinhofer-Preis 1998 der Universität Freiburg „für hervorragende wissenschaftliche Leistungen in der Diplomarbeit“

